Guest-induced flexibility in crystals

by

Anneli Heyns

(Supervisor: Prof. L. J. Barbour)

Submitted in partial fulfilment of the requirements for the degree

Doctor of Philosophy

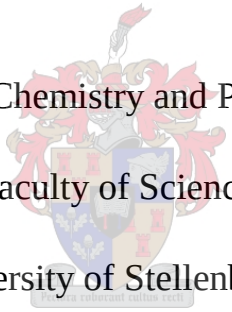

Department of Chemistry and Polymer Science

Faculty of Science

University of Stellenbosch

March 2012

Stellenbosch University http://scholar.sun.ac.za

Declaration

By submitting this thesis electronically, I Anneli Heyns hereby declare that the entirety of the work contained herein is my own, original work, that I am the owner of the copyright thereof (unless to the extent explicitly stated otherwise) and that I have not previously in its entirety or in part submitted it for obtaining any qualification.

.....

Anneli Heyns

Copyright © 2012 Stellenbosch University

All rights reserved

Stellenbosch University http://scholar.sun.ac.za

Abstract

The primary goal of the work presented here was to prepare both organic and metal-organic porous crystals (using crystal engineering strategies) in order to study the guest-induced flexibility of such seemingly rigid materials.

The first section describes the structural modification of a known oxacalix[4]arene compound and the ability of the novel derivatives to encapsulate guest molecules in the solid state. Although it was not possible to obtain porous guest-free forms of any of the hosts, an apohost phase of a 2,3-naphthalene-derivative was obtained from dimethyl sulfoxide. This host uses the same principle as a molecular tweezer by capturing the guests between its offset eclipsing naphthalene moieties; a series of solvate structures were obtained. The flexible nature of the host molecule, when enclosing guests of different shapes and sizes, has been illustrated by a systematic conformational study.

The work dealing with metal-organic compounds was shown to be the more successful of the two parts and forms the largest portion of the work. A series of discrete metallocycles was synthesised and their ability to function as porous materials was investigated. In all instances the metallocyclic hosts included the solvent of crystallisation within the ring. Desolvation of the included solvent did not occur as a single-crystal to single-crystal process and in some instances desolvation coincided with decomposition of the metallocyclic host even though the guests are situated within continuous channels. Although it was not possible to examine the permeability of the empty host, single-crystal to single-crystal guest exchange occurs rapidly when exposing the acetonitrile solvated metallocycle to several solvents. Significant adjustment of the host conformation, as well as the guest-accessible volume, accompanies the uptake of the different guests. Remarkably, this exchange process can also occur upon exposure to small gaseous guests such as I_2, CO_2, C_2H_2 and C_2H_3Cl.

The physico-chemical properties of a known seemingly nonporous metallocycle were investigated in order to formulate a mechanism of transport from one discrete cavity to the next. Crystals of the apohost were shown to be permeable to a series of solvents despite the lack of conventional channels in the host structure. Accurate sorption isotherms measured at four different temperatures revealed host:guest ratios that are comparable to the host:guest ratio inferred from the single-crystal structures. The thermodynamic parameters of sorption ΔH_{ad} and ΔS_{ad} could be derived from the isotherms and revealed essential information on the affinity of the hosts for particular guests. Significant deviation in the centroid-to-centroid distance between the imidazole

Stellenbosch University http://scholar.sun.ac.za

rings suggest that the transport of molecules is facilitated by “flapping” of the imidazole rings. The extent of the host flexibility was explored by studying the permeation of relatively large volatile *solids* such as naphthalene and *p*-dichlorobenzene. Kinetic sorption isotherms in conjunction with precise single-crystal data revealed a possible mechanism of transport, which was confirmed by molecular mechanics calculations.

Opsomming

Die primêre doel van die werk wat hier aangebied word, is om die soepelheid van skynbaar rigiede gasheerkonformasies, wanneer die gasheer verskillende gasmolekules omsluit, te ondersoek. Gedurende die studie is kristalmanipulasie strategieë gebruik om beide organiese- en organometaliese poreuse gasheermateriale voor te berei.

In die eerste afdeling ondersoek ons die strukturele modifisering van 'n bekende oxacalix[4]arene verbinding asook die vermoë van die nuwe gasheermateriale om gasmolekules in die vastetoestand te omsluit. Hoewel ons nie in staat was om poreuse gasvrye vorms van enige van die gasheermateriale voort te bring nie, is ‘n gasvrye fase van 'n 2,3-naftaleenafgeleide verbinding vanuit ‘n dimetielsulfoksiedoplossing verkry. Hierdie gasheer maak gebruik van dieselfde beginsel as 'n molekulêre “knyper” om die gasmolekules tussen sy naftaleen arms vas te vang en 'n reeks gas-gasheerstrukture is gevolglik verkry. Die dinamiese aard van die gasheermolekuul, wanneer dit gasmolekules met verskillende vorms en groottes omsluit, is deur 'n sistematiese konformasiestudie geïllustreer.

Die organometalliese afdeling was meer suksesvol, siende dat poreuse materiale wel geproduseer is, en vorm dus die grootste deel van die studie. Gedurende hierdie deel is ‘n reeks metallosiklieseverbindings gesintiseer en hulle potensiaal om as poreuse spesies te funksioneer is ondersoek. Die oplosmiddel waarvan die metallosikliese kristalle gegroei is, is in alle gevalle binne die kompleksringholte vasgevang as ‘n gasspesie. Desorpsiestudies het bewys dat die gasspesies eers by hoë temperature vrygelaat word en in sekere gevalle vind desorpsie van die oplosmiddel en ontbinding van die metallosikliese verbinding gelyktydig plaas, alhoewel die gasspesies in oop kanale vasgehou word. Die deurdringbaarheid van die gasvrye metallosiklieseKomplekse kon dus nie met behulp van enkelkristaldiffraksie bestudeer word nie, maar die tegniek het bewys dat enkelkristal-tot-enkelkristal gasuitruiling spoedig plaasvind wanneer ‘n asetonitrielgevulde metallosikliese kristal blootgestel word aan ‘n reeks ander oplosmiddels. Uitruiling van die gas molekules vind plaas deur middel van noemenswaardige modifikasie van die gasheerkonformasie en die gastoeganklike spasie. Die buitengewone verwisseling van klein gasagtige molekules soos

Stellenbosch University http://scholar.sun.ac.za

CO_2, I_2, C_2H_2 en C_2H_3Cl is ook as ‘n enkelkristal-tot-enkelkristal proses, met behulp van ‘n hoë druk gassel, bestudeer.

Gedurende die finale gedeelte van die studie is die fisiese-chemiese eienskappe van ‘n skynbaar-nieporeuse metallosikliese verbinding bestudeer sodat ‘n meganisme van die beweging van gas molekules van een holte na die volgende voorgestel kon word. Aangesien dit reeds voorheen bevind is dat dié verbinding poreus is vir klein gasagtige molekules, is die deurdringbaarheid van ‘n reeks groter oplosmiddels as gaste ondersoek deur middel van enkelkristaldiffraksie, desorpsiestudies en sorpsiestudies. Akkurate sorpsie isoterme is by vier verskillende temperature gemeet en toon dat die gas:gasheer verhoudings vergelykbaar is met die verhoudings afgelei van die enkelkristalstrukture. Verder is termodinamiese parameters soos ΔH_{ad} en ΔS_{ad} ook bereken en waardevolle inligting in verband met die affiniteit van die metallosikliese gasheer kon oorgedra word. Merkwaardige veranderinge in die posisies van die imidasoolringe het voorgestel dat die meganisme van gasoordrag moontlik ‘n proses behels waarin die gasheer die imidasool ringe “flapper”. Die aard van die gasheer dinamika is uitgebeeld deur die deurlaatbaarheid van groot vlugtige vaste stowwe soos naftaleen en *p*-dichlorobenseen te bestudeer. Kinetiese sorpsie isoterme en akkurate enkelkristal data in samewerking met molekulêre meganika berekeninge het dié voorgestelde meganisme van vervoer bevestig.

Stellenbosch University http://scholar.sun.ac.za

Acknowledgments

Completing this thesis (and degree) would not have been possible without the help, love and support of numerous people. Although I was not the most pleasant person to be around during the writing-up stages, knowing that you were all behind me meant a great deal and got me through it all!

Firstly, I would like to sincerely thank my supervisor Len Barbour for giving me the amazing opportunity to work in his research group. You have been a great mentor and the almost four years under your guidance has supplied me with immense enthusiasm and admiration for all the aspects of chemistry and research.

My colleagues and fellow students in the Supramolecular Materials Group (who I now all consider my friends – Tia, Jacobs, Jan Gertenbach, Dinubandu Das, Tanya le Roex, Delia Haynes, Catharine Esterhuysen, Matteo Lusi, Vincent Smith, Prashant Bhatt, Leigh Loots, Storm Potts, Eustina Batisai, Ilné Grobler, Marike Du Plessis, Charl Bezuidenhout, Guillaume Greyling, Helené Wahl, Sean Robinson, Malcolm Applewhite and Marlene Milani), thank you for making every day at the office special. I am really going to miss the lovely working environment and coffee time will never be the same without you! Special thanks need to go out to Jan Gertenbach, who would immediately drop everything to help out (whether it's a personal or a work related problem), and Tia Jacobs for all of her help during the initial stages of this project.

Thank you to my friends Storm, Leigh, Shani, Ingrid and Mareta, for always encouraging me, suffering with me and for all the other fun times.

I would like to thank my parents and my sisters for showering me with love and support and lastly, Gerdus for loving me no matter what.

Stellenbosch University http://scholar.sun.ac.za

Publications

CrystEngComm:

Solid-state structural studies of oxacalix[2]arene[2]naphthalene as a molecular tweezer

(A. Kleyn, T. Jacobs, L. J. Barbour, *CrystEngComm*, 2011, **13**, 3175-3180)

Conferences

1 Western Cape SACI Student Symposium (2010), University of Cape Town, South Africa

2 Pacific Basin Chemistry Society Conference (*Pacifichem* 2010), Honolulu, Hawaii, USA
Presented two posters: Solid-state structural studies of oxacalix[2]arene[2]naphthalene as a molecular tweezer; Permeability and Reversible Guest Exchange of a Seemingly Nonporous Metallocycle

3 Western Cape SACI Student Symposium (2009), University of Stellenbosch, South Africa

4 INDABA 6 (Structure and Properties, 2009), Berg-en-dal, Kruger National Park
Poster presentation: Inclusion Chemistry of a Novel Hexa-Host

5 12th Seminar on Inclusion Compounds (2009), Stellenbosch University, South Africa
Poster presentation: Inclusion Chemistry of a Novel Hexa-Host

6 39th National SACI Convention (2008), University of Stellenbosch, South Africa

Stellenbosch University http://scholar.sun.ac.za

List of symbols and abbreviations

ASU	Asymmetric unit
B2MB	1, 4-bis(2-methylimidazole-1-ylmethyl)benzene
BZ	Benzene
CIF	Crystallographic Information File
CCD	Charge-coupled device
$CHCl_3$	Chloroform
CS_2	Carbon Disulfide
CSD	Cambridge Structural Database
Cy	Cyclohexane
0D	Zero-dimensional (referring to a molecular solid – i.e. one consisting of discrete molecular building blocks)
1D	One-dimensional
2D	Two-dimensional
3D	Three-dimensional
DCM	Dichloromethane
DIOX	1,4-Dioxane
DMAC	Dimethyl acetamide
DMF	Dimethyl formamide
DMSO	Dimethyl sulfoxide
DNA	Deoxyribonucleic acid
Co^{2+}	Cobalt(II)
CPK	Corey-Pauling-Koltun colouring guide
Cu^{2+}	Copper(II)
DSC	Differential scanning calorimetry
G	Guest
$\Delta G°_{ad}$	Gibbs free energy of sorption
H	Host
$\Delta H°_{ad}$	Isosteric enthalpy of sorption
H_2O	Water
Im	Imidazole

Stellenbosch University http://scholar.sun.ac.za

IR	Infra-red
IUPAC	International Union of Pure and Applied Chemistry
k	Equilibrium constant
MeOH	Methanol
Me_2CO	Acetone
MeCN	Acetonitrile
MIL	Materials of institut Lavoisier
MOFs	Metal organic frameworks
NMP	N-methyl pyrrolidone
NBZ	Nitrobenzene
P	Absolute pressure
P_0	Saturation pressure
P/P_0	Relative pressure
PXRD	Powder X-ray diffraction
RES	Structure resource file
RNA	Ribonucleic acid
$\Delta S°_{ad}$	Isosteric entropy of sorption
SBUs	Secondary building units
SCD	Single-crystal X-ray diffraction
T	Temperature
TBC4	*tert*-butylcalix[4]arene
T_{on}	Onset temperature
TGA	Thermogravimetric analysis

Stellenbosch University http://scholar.sun.ac.za

Atom colour key

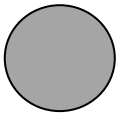

Carbon

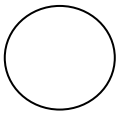

Hydrogen

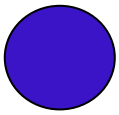

Nitrogen

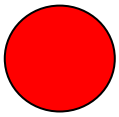

Oxygen

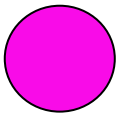

Sulfur

Copper

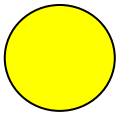

Chlorine

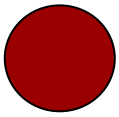

Bromine

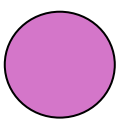

Cobalt

Fluorine

Stellenbosch University http://scholar.sun.ac.za

Table of contents

Stellenbosch University http://scholar.sun.ac.za

Stellenbosch University http://scholar.sun.ac.za

Stellenbosch University http://scholar.sun.ac.za

Chapter 1
Concepts in supramolecular chemistry

1.1 Supramolecular chemistry

The term "supramolecular chemistry" was introduced in 1978 by the Nobel laureate J. M. Lehn. He defined supramolecular chemistry as the "chemistry beyond the molecule", referring to the association of two or more molecules held together by non-covalent bonds.[1] Although supramolecular chemistry is a rather young discipline, its concepts may be traced back to the beginnings of modern chemistry. The discovery of intermolecular forces (first postulated in 1873 by van der Waals) followed by the "Übermolecule" (*i.e.* supermolecule – see Figure 1.1a) notion recognised by Wolf in the 1930s,[2-4] shifted the focus of current research from conventional molecular chemistry to investigating the formation of entities of higher complexity. An prominent highlight in the expansion of supramolecular chemistry was the development of X-ray crystallography, which would eventually allow the structural characterisation of such *supermolecules*. For more detail on the history and development of supramolecular chemistry, the author recommends the printed works *Supramolecular Chemistry* (pages 2-8)[5] and *The Encyclopedia of Supramolecular Chemistry Volumes 1-2* by J. W. Steed[6] and J. L. Atwood and *Comprehensive Supramolecular Chemistry Volumes 1-6* edited by J. M. Lehn.[7]

As it is practiced today, supramolecular chemistry straddles more than one discipline and enduring examples of collaborations between physicists, crystallographers, synthetic organic chemists and biologists can be found in the literature. However, the focus of this introductory chapter is on the fundamental concepts of supramolecular chemistry and its subfields and not to provide a comprehensive historical overview. For this reason five interdisciplinary concepts hace been selected (relevant to the present manuscript) that will be discussed in more detail in the following sections. More comprehensive descriptions will follow as required in Chapters 3-5.

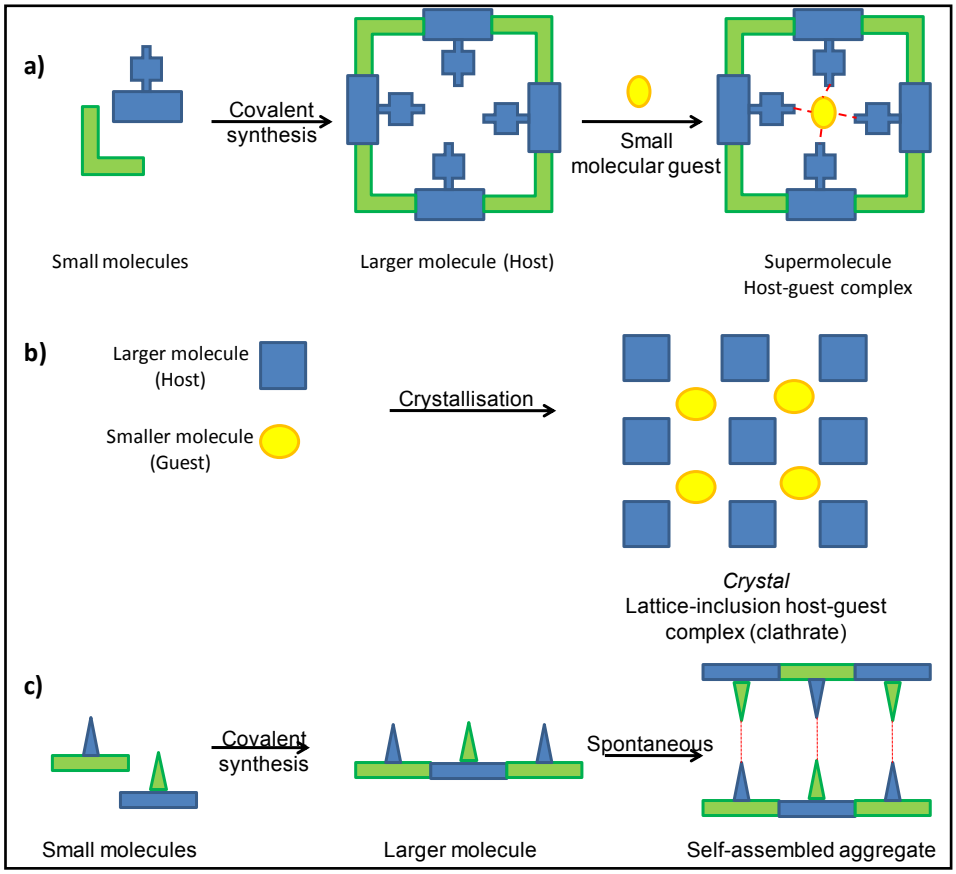

Figure 1.1 The construction of a supramolecular system starting from molecular building blocks. a) Formation of a host-guest complex; b) creation of a clathrate crystal; c) self assembly of complementary molecules.*

1.2 Crystal engineering

Covalent bonds are the primary design elements in organic chemistry and studies of these bonds have progressed to the stage where it is now possible to synthesise even highly complex biomolecules by organic synthesis.[8] The next step is to design "beyond" the molecule by strategic exploration of the non-covalent bonds between molecules. In order to comprehensively define *crystal engineering*, the term *crystal* requires some description. In the context of this manuscript a *crystal* refers to a crystalline material consisting of a systematic arrangement (according to the shape, symmetry and favourable non-covalent interactions) of a conceptually infinite number of atoms, molecules or supermolecules in the solid state. Different packing motifs of such units results in different crystal structures.

* The figure was adapted from *Core Concepts in Supramolecular Chemistry and Nanochemistry* by Steed *et al.*, 2007

Stellenbosch University http://scholar.sun.ac.za

While supramolecular chemistry aims to understand the structure and properties of systems that consist of more than one molecule, *crystal engineering* is "the bottom-up" construction of such functional materials, "starting from molecular or ionic building blocks assembled by means of noncovalent interactions".[9] Schmidt was the first to use the term *crystal engineering* when he characterised the interrelationship between the crystal structure and the reactivity of photodimerisation products in the solid state.[10] Crystal engineering has expanded into a rich field with industrial applications such as the improvement of novel industrial heterogeneous catalysts and the development of storage matrices for gases (*e.g.* hydrogen and methane).

The crux of crystal engineering nowadays is based on Desiraju's extended concept of *supramolecular synthons*[11] that can be applied to form novel crystalline materials (synthons were first introduced by Corey in 1967).[12] Synthons assemble into *tectons* (*i.e.* molecular components of a crystal connected *via* synthons) and can be defined as recurring intermolecular motifs within solid-state structures (see Figure 1.2). Non-covalent interactions are the "glue" that refines the sensible positioning of specific functional groups into supramolecular synthons. Supramolecular construction thus reduces significantly to the detection and utilisation of robust and transferable (*e.g.* between structures) supramolecular synthons.

The Cambridge Structural Database (CSD) is an indispensible research tool for sourcing the frequency of occurrence and the distance-dependence of certain synthons.[13-14] The CSD is a library (of over half a million entries) that contains structures of organic molecules, organometallic molecules and supramolecular assemblies; it allows us to elucidate supramolecular synthon patterns long after the structure was originally determined. At this stage, crystal engineering does not necessarily lead to crystal structure prediction (*i.e.* a purely theoretical route to determining crystal packing).[15] Despite recent advances in supramolecular synthesis, the ability to alter the properties of solids *via* precise control over the structure still presents a difficult task since the slightest change in the molecular structure may result in an unwanted dramatic difference in the crystal structure.

The remainder of this section includes an overview of some of the relevant non-covalent forces, as well as some example strategies, structures and accomplishments that have been reported in crystal engineering of organic molecular solids and organic-inorganic hybrid materials.

Stellenbosch University http://scholar.sun.ac.za

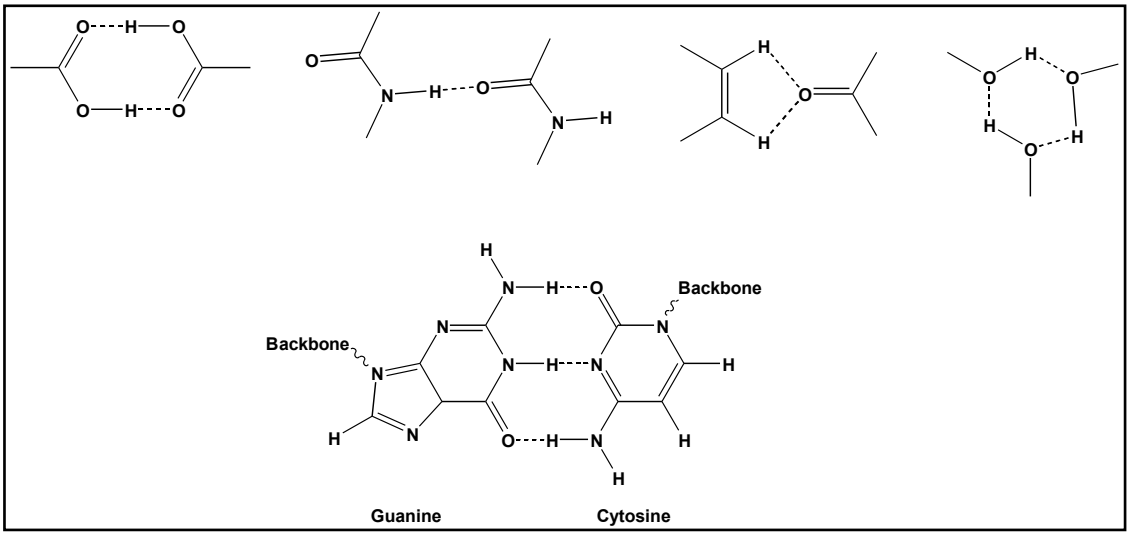

Figure 1.2 Schematic diagrams of selected synthons (top). For a detailed list the reader can consult the review on this topic recently updated by Desiraju.[11] An example of hydrogen bonding is depicted in the base pairing of guanine and cytosine to form a tecton (shown at the bottom of the figure).

1.2.1 Noncovalent (*i.e.* intermolecular) interactions

As mentioned earlier, intermolecular interactions can be viewed as the heart of modern crystal engineering.[16] Crystallisation from the gas or liquid phase is essentially an unfavourable process, and the system needs to gain substantial enthalpy (through balancing of the attractive and repulsive forces between molecules in the crystal) in order to triumph over a dramatic decrease in entropy. Thus, the existence of intermolecular bonds is related to the energetic stability of the supramolecular aggregate.[16] Noncovalent interactions can be subdivided into two categories, *viz* directional and non-directional forces.[5] While both hydrogen bonds and coordination bonds are still the major components of current crystal engineering research, we will also discuss other weaker interactions that have shown vast promise in constructing functional materials.

It is also important to note that, as a consequence of the overall contributions from intermolecular interactions, molecules tend to pack as close as possible to one another. This phenomenon was described by Kitaigorodskii as the close-packing principle.[17] With regard to molecular recognition, close-packing has been simplified as "bumps must fit into holes"[18] and "empty space is an energetic waste".[19] Ultimately, the overall packing motif of a crystal must therefore reach a compromise between optimising the attractive interactions and minimising repulsive interactions in conjunction with the shapes of the molecules.

1.2.1.1 Directional forces

Directionality implies topological control and selectivity, which consequently guarantee that the process of supermolecule or crystal formation (Figure 1.2b) would be reproducible.[9] Moreover, with regard to directional forces, there is a correlation between the length and the strength of the bond.[9]

Hydrogen bonds

When defining a hydrogen bond (concerning crystal engineering), Etter's elaboration[20] on the Pauling definition of a bond[21] is still appropriate:

A hydrogen bond is an interaction that directs the association of a covalently bound hydrogen atom with one or more other atoms, groups of atoms, or molecules into an aggregate structure that is sufficiently stable to make it convenient for the chemist to consider it as an independent chemical species.

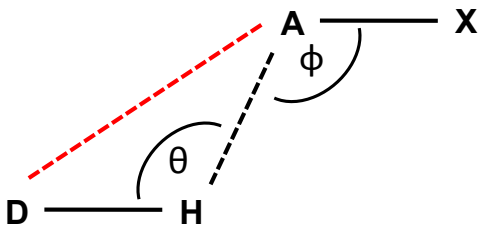

Figure 1.3 Schematic illustration of the important geometric parameters of a hydrogen bond. The D···A distance (shown as a red dashed line) is the principal parameter for identification of hydrogen bonds in this study.

In simple terms the hydrogen bond is thought of as a stable electrostatic interaction between a D–H donor and an A acceptor, where D and A are electronegative atoms (*i.e.* electron-rich, for example O, N, S, Cl and F – Figure 1.3).[9] The long-range nature of the hydrogen bond permits more than one acceptor to be bonded to a donor atom. Such geometries are generally referred to as bifurcated (*i.e.* two acceptors – Figure 1.4(a)) and trifurcated (*i.e.* three acceptors) hydrogen bonds. In some instances an acceptor group can simultaneously be bonded to two distinct donor groups, resulting in an A-X bifurcated acceptor (Figure 1.4(b)). For neutral molecules, hydrogen bonds are usually thermodynamically stronger (*e.g.* by 10-65 $kJ.mol^{-1}$) than van der Waals interactions (see below), but weaker than conventional covalent bonds.[8, 22] Figure 1.3 shows that the characteristic

Stellenbosch University http://scholar.sun.ac.za

geometry of a hydrogen bond D–H···A–X is given by distances A···D and H–D, angles HAX (Φ) and AHD (θ), as well as the planarity of the system.[11]

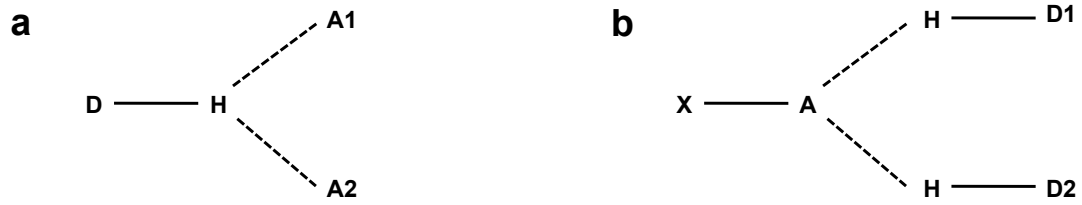

Figure 1.4 Illustrations of bifurcated donor (a) and bifurcated acceptor (b) hydrogen bonding systems.

Hydrogen bonds can be subdivided into three groups, according to the strengths of the interactions: strong, moderate and weak (Table 1.1). The strength of a strong hydrogen bond can be considered as being of the same order as a weak covalent bond; the hydrogen atom is more or less in the centre between the donor and the acceptor. As seen in Table 1.1, strong hydrogen bonds have an almost linear bond angle θ. This angle can decrease significantly, and can be almost perpendicular in certain weak hydrogen bonds, for example a C–H···π interaction between acetylene molecules where the C–H bond is directed perpendicularly towards the π-system.[15, 23]

The most commonly used criteria for identification of a hydrogen bond are the distance H···A (*e.g.* shorter than the sum of their van der Waals radii) and the angle θ (*e.g.* > 110°). However, according to the SHELX-97 manual "It is difficult to locate hydrogen atoms accurately using X-ray data because of their low scattering power, and because the corresponding electron density is smeared out, asymmetrical, and is not centered at the position of the nucleus. In addition hydrogen atoms tend to have larger librational amplitudes than other atoms."[24] For this reason, the presence of a hydrogen bond will exclusively be reported by the D···A distance (Figure 1.3).

Stellenbosch University http://scholar.sun.ac.za

Table 1.1 Properties of hydrogen bond interactions.[†]

Interaction/property	**Strong**	**Moderate**	**Weak**
D–H···A	mainly covalent	Mainly electrostatic	Electrostatic
Bond energy/ kJ mol^{-1}	60-120	16-60	<12
Bond length/ Å			
H···A	1.2-1.5	1.5-2.2	2.2-3.2
D···A	2.2-2.5	2.5-3.2	3.2-4.5
Bond angle (θ)/ °	175-180	130-180	90-150
Examples	HF complexes	Acids	C–H···Cl
	$H_5O_2^+$	Alcohols	C–H···π
	-	DNA/RNA	C–H···O

Coordination bonds

Coordination bonds are ion-dipole interactions, which range in strength from 50-200 kJ.mol^{-1}. Ion-dipole interactions usually occur between positively charged ions (such as Na^+) and polar molecules (*e.g.* H_2O and methanol). Coordination bonds have mostly electrostatic nature in instances where they occur between non-polarisable metal cations (e.g. Cu^{2+} and Co^{2+}) and hard bases (e.g. R-Cl$^-$ and R-N$^-$).

Halogen bonds

The early works of Schmidt utilised halogen-halogen bonds in crystal design.[10] Although the nature of such interactions is a subject of debate at this time, halogen-halogen interactions most certainly display directionality, as shown by Desiraju *et al*.[25] Halogen bonds occur between pairs of halogen atoms (X···X, X = Cl, Br, I) or between halogen atoms and electron-pair donors (*e.g.* O, N), whereby the halogen atom in the latter acts as an electron-pair acceptor. Halogen bonding concerning iodine is the strongest interaction, followed by halogen bonds with bromine and chlorine. Thus, the strength of the bond is related to the electron-withdrawing strength of the halogen.[15] Additionally, it has been noted that the nature of fluorine permits it to preferentially associate *via* C–H···F hydrogen bonds rather than through F···F halogen bonds.[18]

[†] Adapted from *Core Concepts in Supramolecular Chemistry and Nanochemistry*, John-Wiley & Sons, Ltd, **2007** by J. W. Steed, D. R. Turner, K. J. Wallace,

1.2.1.2 Non-directional forces

Unlike directional forces, the actions of non-directional (*i.e.* non-selective) forces within structural environments cannot always be predicted since they do not possess specific topologies.[9] The latter factor also influences the strength of such interactions. Furthermore, non-directional interactions can stabilise a wide range of molecular coupling compared to directional forces, which are rigid and can only occur between mutually complementary species.[15]

π–π Stacking

Interactions that arise between two aromatic rings (often in circumstances where one ring is moderately electron rich and the other is electron poor) are defined as π–π stacking. Other π-systems such as alkenes and alkynes are also known to interact *via* π–π stacking. There are two general types of π–π stacking: face-to-face (Figure 1.5(a) and (b)) and edge-to-face (Figure 1.5(c)), although intermediate geometries might also occur. Face-to-face interactions occur between two parallel aromatic rings separated by ~3.5 Å in an offset fashion. A repulsive interaction arises when the ring systems are eclipsed (Figure 1.5(a)). Edge-to-face stacking can be considered as weak hydrogen bonds (see 1.2.1.1) and are also accountable for the distinguishing herringbone packing motif, which is a common feature in the crystal structures of aromatic hydrocarbons such as benzene (Figure 1.5(d)). Edge-to-face interactions are thought to take place as a result of the attraction between the negatively charge π-electron cloud of one aromatic system and the positively charged σ-nature of an adjacent ring. The reader is advised to consult the excellent work by Hunter and Sanders on *The Nature of π–π Interactions*[26] if additional information is required.

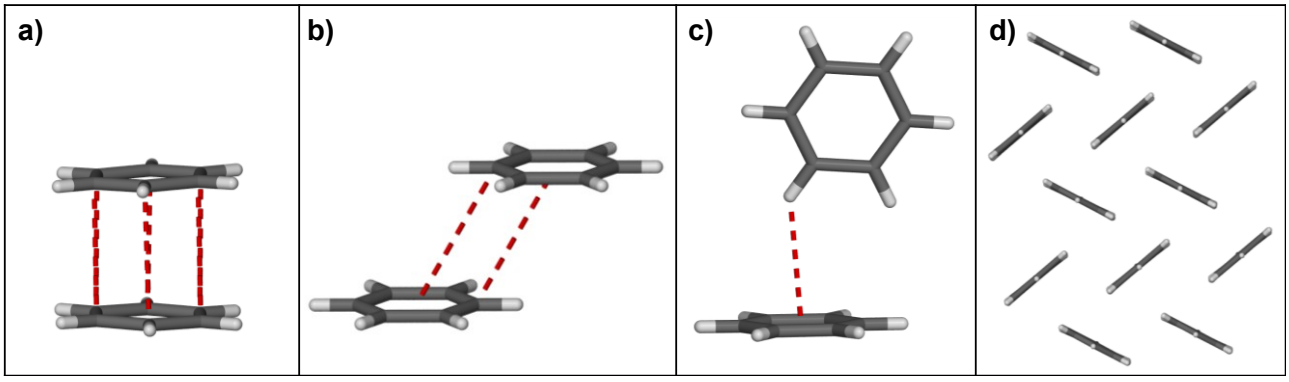

Figure 1.5 Examples of π–π stacking taken from the CSD. a) edge-to-face; b) eclipsed face-to-face (repulsive); c) off-set face-to-face; d) herringbone packing arrangement.

Stellenbosch University http://scholar.sun.ac.za

van der Waals Forces

van der Waals forces are dispersion effects that arise from the polarisation of an electron cloud by the proximity of a nearby nucleus. These attractive forces can be divided into two components, namely *London interactions* and *exchange-repulsion* terms. Fluctuations of the electron distributions result in the formation of dipoles such that partial positive charges will be attracted to partial negative charges. The attractive force (London dispersion) has an r^{-6} dependence on the distance between the atoms. On the other hand, exchange-repulsion correlates with the shape of the molecule and balances dispersion at short range (decreasing with r^{-12}). van der Waals interactions are particularly important in systems where small molecules are encapsulated in a crystalline lattice (*i.e.* inclusion compounds – Section 1.3).

1.2.2 Design strategies and recent advances

One of the aims of crystal engineering is to make crystals by design. Crystal engineering can be subdivided into two main areas: organic molecular materials and coordination networks.

The ability of organic molecules to undergo very selective reactions is starting to play a larger role in solid-state supramolecular chemistry. Crystal engineering has been utilised to design systems in which the two reaction partners are in close proximity such that a solid-state reaction can occur. An example of this methodology is the self-association of *trans*-1,2-bis(4-pyridyl)ethylene and resorcinol (*via* an O–H···N hydrogen bond synthon) to bring two double bonds in close proximity to each other (Figure 1.6); remarkably, UV radiation yields the cyclobutane derivative via [2+2] cycloaddition of the two double bonds.[27] Many research groups aim to reduce the environmental contamination caused by volatile organic solvents; numerous porous metal-organic complexes have been synthesised using solvent-free techniques.[28-29]

Stellenbosch University http://scholar.sun.ac.za

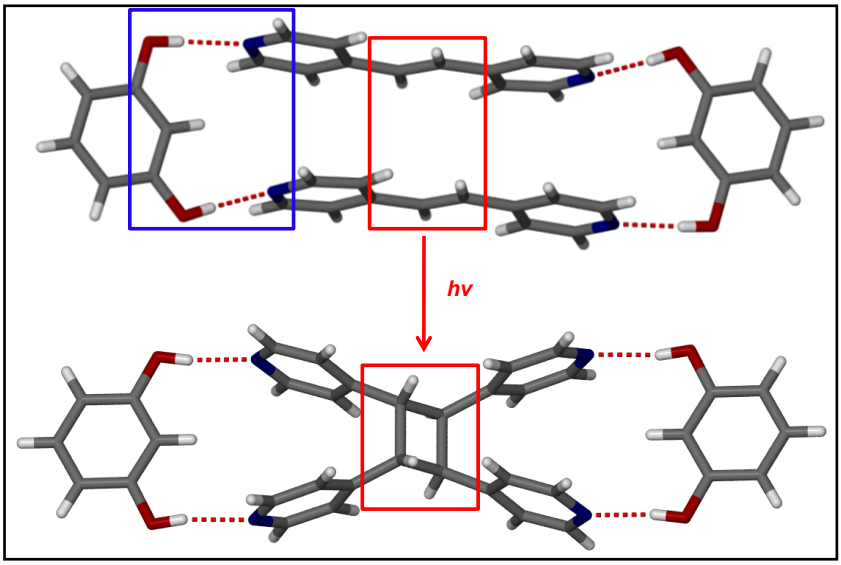

Figure 1.6 Crystal engineering of *trans*-1,2-bis(4-pyridyl)ethylene and resorcinol (top) holds the two double bonds in close proximity for [2+2] photodimerisation reaction (outlined in red rectangles) to yield the cyclobutane derivative (bottom). The supramolecular synthon is indicated with a blue rectangle.[27]

To date, the design of organic systems rather than inorganic aggregates has dominated supramolecular chemistry and crystal engineering. However, the realisation that the incorporation of metals into supramolecular systems introduces added structural variety (*e.g.* increased flexibility and structural variability) produced an explosion of coordination polymer reports in the literature. The term c*oordination polymer* refers to an infinite arrangement of metals bridged by organic ligands. In recent times, many research groups have aimed to construct artificial coordination polymers that resemble natural zeolites, owing to the remarkable catalytic, guest-exchange and absorption properties of the latter (see Sections 1.3 and 1.5.1). Metal-organic frameworks (MOFs), a subdivision of coordination polymers, are most frequently constructed using *reticular synthesis*. Reticular synthesis (first developed by the Yaghi group)[30] involves combining metal clusters (*i.e.* secondary building units, SBUs in Figure 1.7(a)) and organic linkers to form a neutral three-dimensional (3D) network. SBUs symbolise defined structural motifs such as octahedra, tetrahedra and cuboids and are generated *in situ* during the synthesis of the MOF. The renowned MOF-5 (see Figure 1.7(b)) was generated in this manner.

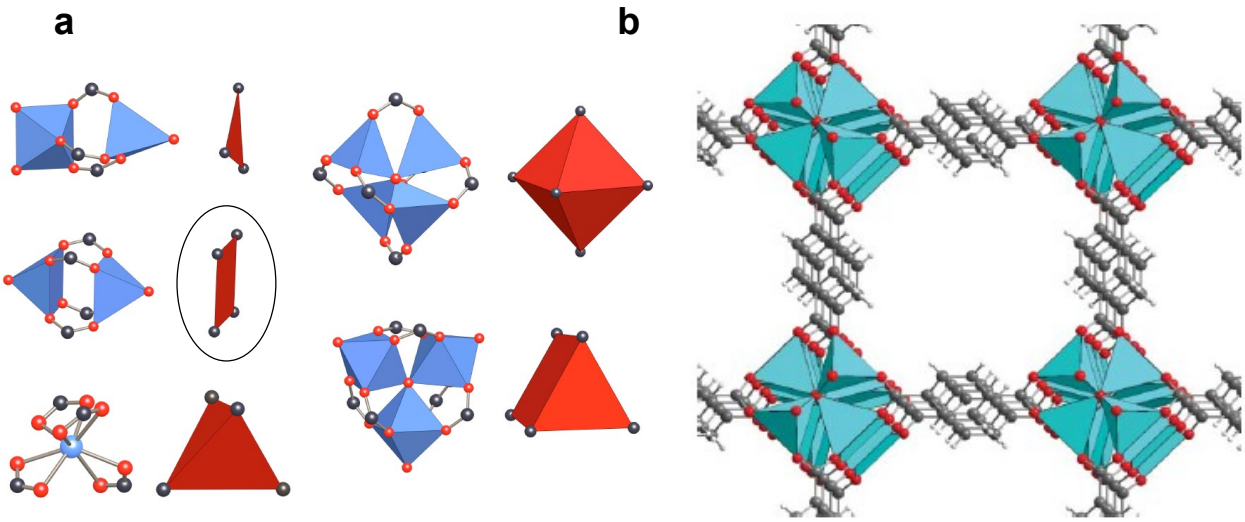

Figure 1.7 (a) Examples of SBUs using carboxylates with rigid geometries. Oxygen atoms are represented as red spheres and carbon atoms as black spheres. Metal-oxygen polyhedra are coloured blue, and the polyhedra defined by carboxylate carbon atoms (SBUs) are red.[30] (b) The structure of MOF-5, which is synthesised using benzene-1,4-dicarboxylic acid with octahedral carboxylate SBUs as nodal points.

1.3 Inclusion compounds

Because supramolecular chemistry entails a complexation process that mostly relies on the non-covalent interactions discussed in 1.2.1, it is important to first clarify some of the terminology used throughout this thesis. It is generally accepted that a large molecular entity possessing considerable open space in its molecular conformation or packing arrangement (*i.e.* hole or cavity), is termed the *host*. The host molecule can then non-covalently bind to another, usually smaller molecule (*i.e.* guest) to produce a host-guest complex (*i.e.* supermolecule in Figure 1.1a) or *inclusion compound*. The *binding-site* is therefore a particular region of the host or guest that is of the correct size, geometry and functionality to effectively interact with other molecules.[5, 15] According to Cram, the host has a convergent binding-site and the guest has a divergent binding-site.[31]

The first known host-guest complex is thought to be that of solidified chlorine encapsulated by hydrogen-bonded water molecules (*i.e.* a *clathrate hydrate* with formula $Cl_2 \cdot 10H_2O$[32] – discussed below), which was reported by Davy in 1811.[33] Further progress in host-guest chemistry sprung from the development of the *lock-and-key* principle by Fisher in 1894. This principle was derived from his work on the binding of substrates (*i.e. key*) by enzymes (*i.e. lock*) owing to the complementary size and shape of the substrate relative to the enzyme binding-site. However, the lock-and-key analogy is not a particularly good description of biological systems because enzymes

Stellenbosch University http://scholar.sun.ac.za

are highly flexible and thus conformationally dynamic.[15] Koshland addressed this constraint by postulating the *induced-fit* model whereby the binding-site of the enzyme precisely adapts to fit the shape of the substrate. Following the discovery of X-ray diffraction, and after the first structural elucidation of a host-guest complex was reported by H. M. Powell in 1948, a door opened to an unexplored aspect of supramolecular chemistry.[34]

Much of current supramolecular chemistry has sprung from developments in macrocyclic chemistry, in particular, the tremendous contributions of both Cram (on cyclophanes – Figure 1.8(a))[31] Lehn (on cryptands – Figure 1.8(b)).[35-36] and Supramolecular chemistry has, since the discovery of macrocycles, grown above and beyond simple molecular recognition and catalysis.[36]

Modern host compounds can be classified into two broad categories: *cavitands* and *clathrands*.[5] Cavitands (*e.g.* cryptands, cyclophanes and calixarenes – see Figure 1.8) are defined as molecular containers owing to their imposed concave surfaces (*i.e.* cavities) present in both solution and the solid state.[5] These molecules are capable of forming stable complexes (*i.e. cavitates*) with cations (in solution) and neutral guest molecules (in the solid state). Neutral guest molecules are associated with the host *via* weak intermolecular forces (see section 1.2.1). Although calixarenes (Figure 1.8(c)) are formally members of the cyclophane family (*i.e.* contain bridged aromatic rings), their distinct bowl-shaped conformation and their ability to form stable inclusion compounds with any appropriate solvent have made them one of the most studied classes of organic macrocycles. The term *calixarene* was introduced by Gutsche because of their resemblance to the bowl-shaped conformation of a *calix crater*, a Greek vase.[36-37]

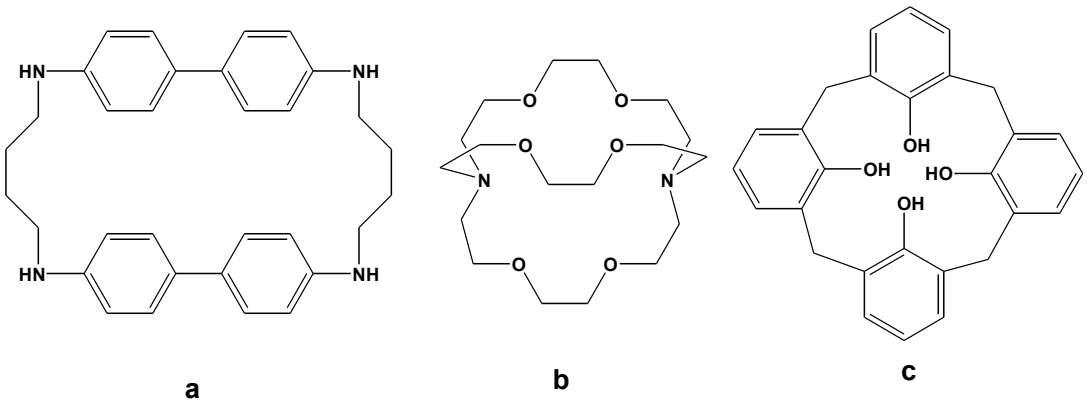

Figure 1.8 Schematic structures of a) a cyclophane,[38] b) Lehn's cryptand[35] and c) Gutsche's calixarene[37]

Stellenbosch University http://scholar.sun.ac.za

On the other hand, clathrands have "extramolecular" cavities (*i.e.* interstitial voids – see Figure 1.1(b)) and are only formed in the solid state. The word *clathrate* is derived from the Latin word *clathrus*, meaning "surrounded on all sides".[15] The term clathrate was first used by Powell to describe β-hydroquinone derivatives.[39] Other well-known examples include Dianin's compound,[40] urea and thiourea clathrates (Figure 1.9).[41] The distinction between cavitates and clathrates is illustrated in Figures 1.1(a) and (b), respectively. As the name suggests, *clathrate hydrates* are formed from hydrogen-bonded water molecules (as hosts) with small gas or liquid guests trapped within their neutral interstitial cavities.[15] A lot of recent research interest has been devoted to hydrates of natural gases, which have potential applications as fuel reserves. They are also unwanted by-products in oil production since they block natural gas pipelines.

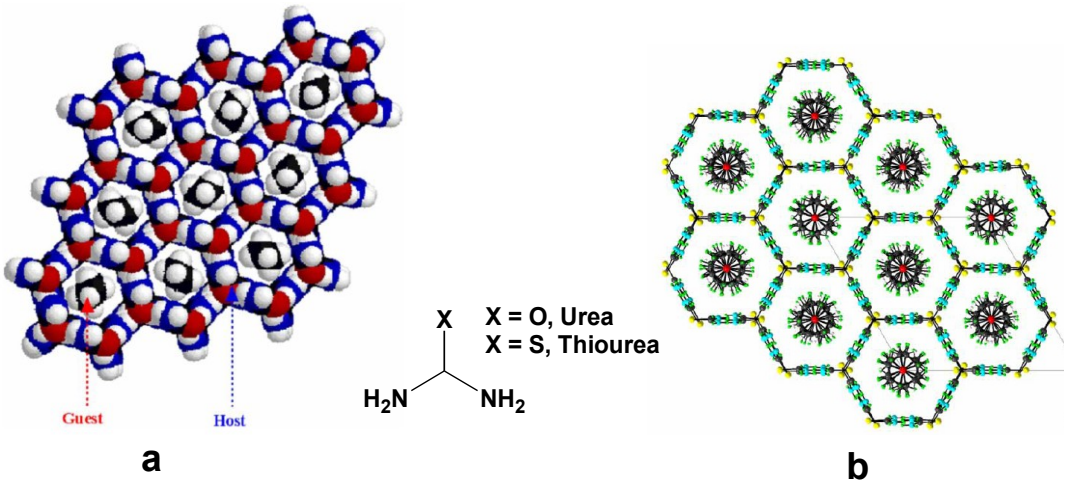

Figure 1.9 Crystal structures of (a) urea and (b) thiourea clathrates viewed along the channel axis. The guest molecules are, respectively, hexadecane and 1–bromoadamantane.[41] A general representation of the molecular structures of urea and thiourea is also shown in the middle of the figure.

Apart from clathrate hydrate inclusion compounds, many inorganic host-guest complexes (such as zeolites) feature predominantly in already implemented industrial applications of inclusion compounds. Zeolites are naturally occurring materials which predominantly consist of aluminosilcate frameworks that contain cavities or channels (see Figure 1.10). The empty space in zeolites gives rise to many useful properties such as guest-exchange, separation and catalysis.[15, 42] Many synthetic zeolites have recently been synthesised to fulfil some of the properties displayed by natural zeolites. For example, zeolite ZSM-5 is readily utilised in the industrial separation of xylene isomers (see Figure 1.10).

Stellenbosch University http://scholar.sun.ac.za

MOFs also form stable inclusion compounds by encapsulating the reaction mixture solvent within their large pores. The properties of MOF inclusion compounds will be discussed in more detail in Section 1.5.1 and Chapters 4 and 5.

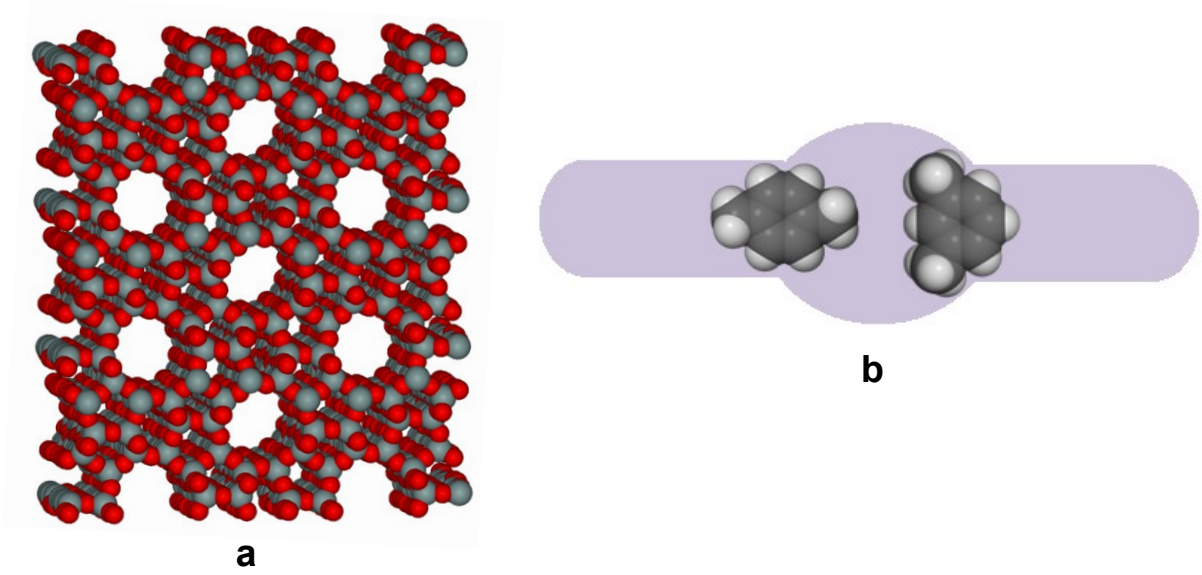

Figure 1.10 (a) The structure of ZSM-5 viewed along the large continuous channels. (b) A cartoon representation of the separation of *p*-xylene and *m*-xylene within the pores of ZSM-5; *p*-xylene can diffuse through the pores, whereas *m*-xylene cannot.

The process of guest inclusion (Figure 1.11) can generally be represented by the following equation:[43]

$$\mathrm{H}\,(s, \alpha) + n\mathrm{G}\,(l,g) \rightleftharpoons \mathrm{H{\cdot}G}_n\,(s, \beta)$$

where α is the pure phase of the host H, β the phase of the inclusion compound and n the host:guest ratio. Figures 1.11(a) and (b) shows the formation of a host-guest crystal (β-phase) by self-assembly from solution (refer to the next section). However, this process (Figure 1.11 (a) and (b)) can also occur from the solid or vapour phase. Decomposition (Figure 1.11c, d and e) of the host-guest complex (β-phase) is usually achieved by heating above the release temperature of the guest and the resulting apohost phase (α, γ or β_0) is dependent on the nature of the host material. With regard to the recent trend of constructing porous compounds by design, the most favourable inclusion compound would be one that yields a β_0-phase apohost (*i.e.* porous) upon removal of the guest.

Stellenbosch University http://scholar.sun.ac.za

However, most host molecules would prefer to rearrange themselves to form a close-packed structure with no guest molecules trapped in the lattice (Figure 1.11c). Another unfavourable consequence of guest release is that, for most materials, this process occurs with concomitant loss in crystal quality such that single-crystal X-ray diffraction (SCD) methods are no longer feasible. Other methods such as differential scanning calorimetry (DSC) and thermogravimetric analysis (TGA), in combination with powder X-ray diffraction (PXRD), may then be used to study inclusion compound decomposition. In particular, accurate host:guest ratios can be determined from the TGA thermogram; DSC measurements indicate the occurrence of various thermal events such as the onset temperature (T_{on}) of guest release, a polymorphic phase transformation or melting of the host or guest compound.[44] The term *polymorphism* is used in many disciplines and highlights the diversity of nature. In the present context, it refers to a material that can exist in more than one solid form (*e.g.* conformational polymorphs of the α-phase apohost).[45]

It has been shown that some inclusion compounds (mostly MOFs) can tolerate guest removal without concomitant phase transformation to a nonporous α-phase. If this process occurs without significant loss in the single-crystallinity, it can be referred to as a *single-crystal to single-crystal* transformation. Although this is an especially uncommon phenomenon for organic materials, single-crystal structures of calixarene-type hosts containing void spaces larger than 25 $Å^3$ have been reported.[46-53] These compounds, together with other porous materials, will be discussed in more detail in section 1.5.1. For the supramolecular chemist, single-crystal to single-crystal transformations are a powerful means of obtaining information on the structure-related properties such as the mechanism of guest uptake and release, to mention only one.

Stellenbosch University http://scholar.sun.ac.za

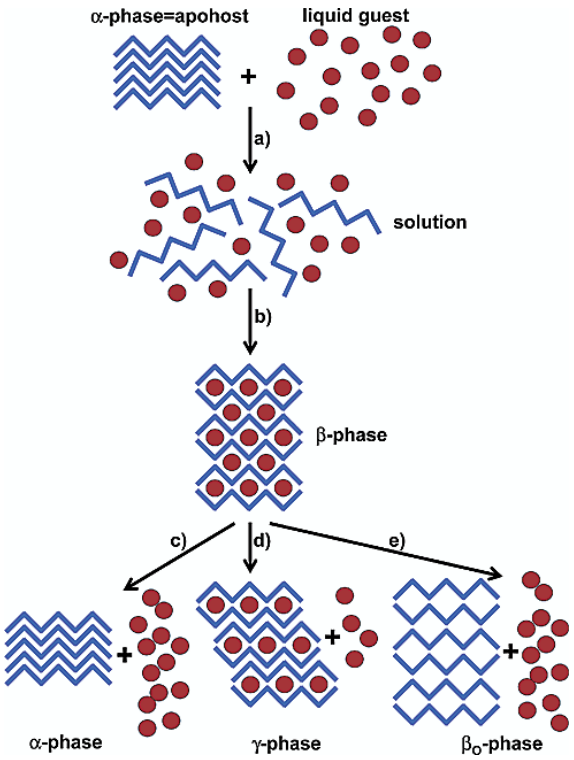

Figure 1.11 The growth (a and b) and decomposition (c, d and e) of a host-guest complex (*β*-phase).[43]

1.4 Self-assembly

Self-assembly is the spontaneous reversible association of two or more components to form a larger, non-covalently bound aggregate – Figure 1.1(c).[15] The renowned double helix of deoxyribonucleic acid (DNA), which is comprised of two strands associated by hydrogen bonds and π–π stacking interactions, is an excellent example of self-assembly.[15] None of the species involved in forming the aggregate therefore act as either a host or a guest. Although the process of self-assembly typically occurs spontaneously, it can be influenced by solvation and templation effects, as well as the nucleation process or the crystallisation conditions. For this reason, fine control over the assembly of molecules into ordered solids remains a relatively elusive outcome and we are rarely able to predict the structure of the crystalline product as yet.[8]

Stellenbosch University http://scholar.sun.ac.za

1.5 Sorption

Fontana[54] and Scheele[55] recognised the increase in the concentration of molecules from a gaseous phase on a solid surface (charcoal) in 1777. It was only in 1881 that this phenomenon (*i.e.* the physical adherence or bonding of ions and molecules onto the surface of another phase) was defined as *adsorption*.[56-57] The quantitative study of *diffusion* (*i.e.* the tendency of a system to occupy all of its accessible states) started in the 1850's with the works of Fick and Graham.[58]

Absorption, on the other hand, is the incorporation of a substance (*i.e.* absorptive) in one state into another material (*i.e.* absorbent) of a different state (e.g. liquids being absorbed by a solid or gases being absorbed by a liquid).[59] One of the principal distinguishing features observed experimentally between *adsorption* and *absorption* is that the former is always exothermic, whereas the latter can be either endo- or exothermic.[60] Adsorption can be subdivided into two main categories, namely *physisorption* and *chemisorption*.[59] Physical adsorption involves relatively weak intermolecular forces between adsorbent and adsorptive, while chemisorption involves the formation of a chemical bond between the host and the guest.[61] Further discussion will focus exclusively on physisorption since the inclusion complexes presented in this manuscript are solely stabilised by intermolecular forces. Moreover, to avoid confusion, in this thesis the term *sorption* (in conjunction with the general terms *sorbent, sorbate* and *sorptive*) will be used to describe the combined action of adsorption and absorption. We will refer to the process of removing the sorbed molecules as *desorption*. At constant temperature, the relationship between the amount sorbed and the equilibrium pressure of the gas/vapour is defined as a sorption isotherm. Sorption *hysteresis* occurs when the sorption and desorption curves do not coincide.[62] The majority of experimental physisorption isotherms can be categorised into six types (Figure 1.12), according to the International Union of Pure and Applied Chemistry (IUPAC) classification.[62-63]

Stellenbosch University http://scholar.sun.ac.za

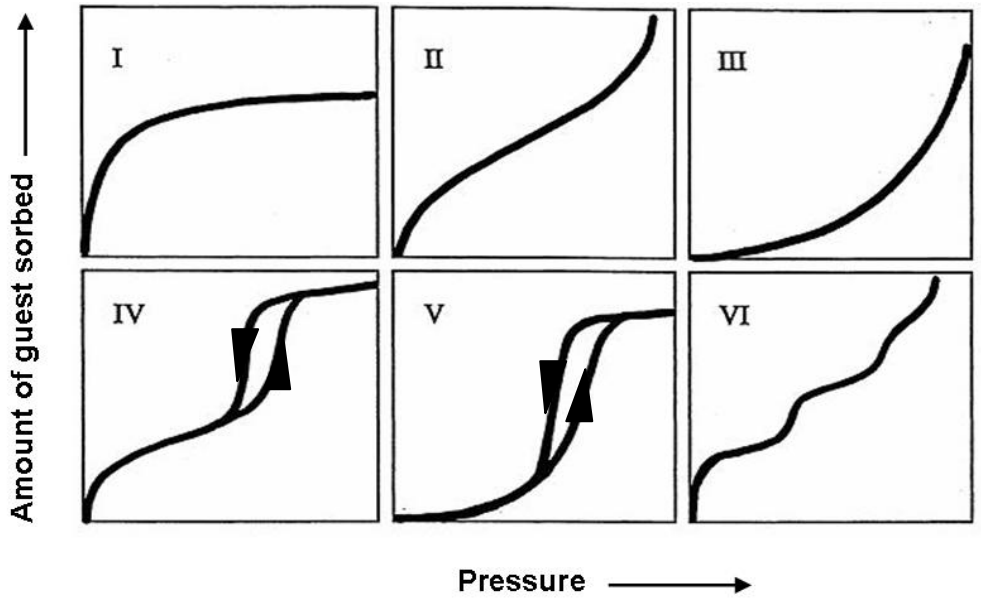

Figure 1.12 Types of physisorption isotherms, according to the IUPAC classification. [62-63]

Type I isotherms are reversible and show a characteristic plateau towards saturation (*i.e.* limiting sorption), indicating that most of the guest uptake occurs at low relative pressures. The appearance of an approximately linear plateau indicates a very small external surface area which, in turn, enhances host-guest interactions owing to the molecular dimensions of the micropores. The limiting sorption is correlated with the vacant micropore volume. *Type II* isotherms have a smooth shape (*i.e.* non-stepwise character) over the whole P/P_0 range. Non-porous or macroporous sorbents usually exhibit reversible *Type II* sorption behaviour, which means that unrestricted monolayer-multilayer sorption takes place at high relative pressure. *Type III* isotherms are easily distinguishable from Type I or II isotherms, since most sorption occurs at the higher P/P_0 range. A reversible profile is also displayed over the whole pressure range, which is a typical feature of weak host-guest interactions being present. *Type IV* isotherms are related to Type II isotherms, except they are not reversible and display hysteresis as a result of emptying and filling the mesopores by capillary condensation. Similar to the shape of Type III isotherms, the shape of *Type V* isotherms (not reversible) is indicative of weak sorbent-sorbate interactions. Type V isotherms are not common. *Type VI* isotherms have a stepped profile and are associated with layer-by-layer sorption on a uniform non-porous surface. The steps are dependent on the system and the temperature.

It is important to note that the isotherm models in Figure 1.12 were derived from studies using sorbents that have instantly recognisable pores (*e.g* zeolites). Therefore, materials that are not porous in the conventional sense[48] may deviate from the IUPAC specifications (or produce an

intermediate isotherm between two classes). The concept of porosity of seemingly nonporous materials[49-51, 64] will be discussed in more detail below.

1.5.1 Porosity

Sorption and diffusion studies of guest molecules can provide information on the volume and size of the sorption site, and the heat (energy) of sorption.[59] The most widely accepted definition of *porous* is any material containing cavities, channels or interstices – Figure 1.13.[63] Although *permeability* and *porosity* go hand in hand, there is a slight distinction between their precise definitions. Indeed, *permeability* is a measure of the ease with which molecules are transported through the pores and is controlled by factors such as the packing, shape and the nature of the molecules.[64] Porous materials can be subdivided into three categories based on pore dimensionality: microporous (<15 Å), mesoporous (15-500 Å) and macroporous (>500 Å).[65]

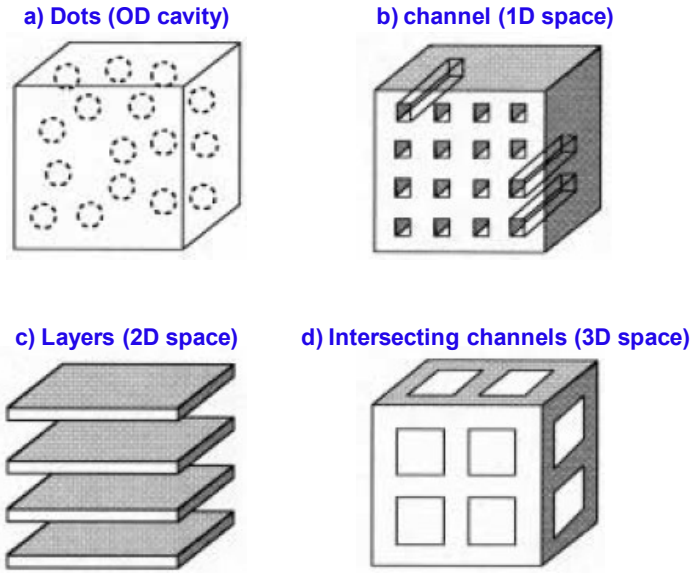

Figure 1.13 The four types of pores are illustrated. a) 0D cavities (circles) are usually nonporous as the guests are completely surrounded by the wall molecules, but it has been shown that several seemingly nonporous materials are indeed porous. b) Channels (1D), c) layers (2D) and d) intersecting channels (3D).[66]

It has become apparent from recent studies by Kitagawa,[67-68] Yaghi[30] and Barbour[47-49, 64] that, with regard to the molecular scale, the conventional definition of porosity should be revisited. Barbour recommended that the following guidelines should be considered when identifying a crystal as being porous:

Stellenbosch University http://scholar.sun.ac.za

1. the material should display permeability to guest species
2. a particular phase of the material should be designated as porous
3. *in principle*, the host phase should remain unchanged upon guest uptake

It can be inferred from these reports that, in the context of molecular crystals, a more suitable definition of *porous* involves any material that has been shown to take up guest molecules *via* sorption experiments.

Guest uptake can be monitored using many different procedures, of which the most common are the measurement of volumetric isotherms (indirect technique based on the determination of the volume of guest sorbed from the gas phase) and gravimetric sorption isotherms (direct method that relies on the measurement of the weight of the sorbent).[59] In order to comply with the industrial standards, precise sorption data has to be measured over a wide pressure and temperature range.

In view of the molecular scale, Barbour described three types of porosity: conventional porosity, porosity "without pores" and virtual porosity.[48] These three concepts will now be described, together with suitable examples.

Conventional porosity

Conventional porosity refers to materials such as zeolites (section 1.3) which retain their porous host framework, even after removal of the included guest molecules. These materials usually contain permanent channels or pores, which are reversibly accessible to the sorbate molecules (Figure 1.13b-d). As mentioned earlier, crystal engineering is the method of choice for designing potentially porous crystals. Unfortunately, molecules in crystals tend to minimise the interstitial space, in order to effectively participate in favourable intermolecular interactions (i.e. close-packing principle – 1.2.1.1) and void space larger than 25 $Å^3$ is a rare occurrence.[47-48] It is for this reason that molecular crystals have been neglected as potentially porous materials. However, one advantage of using molecular crystals rather than amorphous porous materials is that they can be studied using X-ray diffraction. X-ray diffraction provides accurate structural information (such as host-guest and guest-guest interactions) which allows us to investigate certain properties of crystals, and with the help of crystal engineering, design "improved" porous materials.

The synthesis and development of MOFs marked the beginning of a new era in the study of conventional porous materials. The metals in MOFs introduce rigidity to the frameworks (which are directly analogous to zeolites) and the guest molecules can therefore be removed without a concomitant phase transformation to a nonporous phase (Figure 1.11c). Kitagawa categorised

Stellenbosch University http://scholar.sun.ac.za

functional MOFs into three classes (according to the nature of the host phase that results upon desolvation), namely 1st generation, 2nd generation and 3rd generation (Figure 1.13).[66] The 1st *generation* compounds include microporous frameworks, which only show porosity when guest molecules are present in the framework. These materials show irreversible framework collapse on removal of guest molecules. The *2nd generation* compounds have stable and robust porous frameworks, which show permanent porosity upon removal of the guest molecules. The *3rd generation* compounds have flexible frameworks, and adjust their channels or pores reversibly in response to external stimuli (*e.g.* light, electric field and guests).

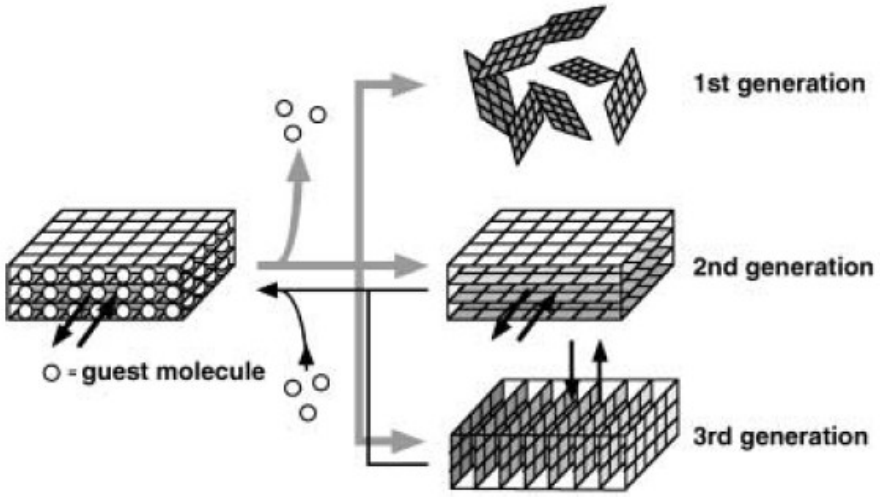

Figure 1.14 The different classes of functional MOFs. The guest desolvation process is reversible for 2nd and 3rd generation MOFs.[66]

The number of reports on flexible frameworks is rising substantially, because of their uncomplicated syntheses and the crystalline nature of their dynamic frameworks, which permits studying their properties (*i.e.* porosity) using X-ray diffraction.[69-75] Additionally, flexible porous materials can also be applied to molecular sensing, non-linear optical properties and magnetism, apart from the properties exhibited by conventional MOFs, such as catalysis and gas storage. The groups of Férey[69, 71-73, 75] and Kitagawa[66] have dominated the field of flexible porous compounds. In particular, Férey *et al.* have developed an exciting group of 3rd generation porous MOFs, namely MILs (Materials of Institute Lavoisier).[69-75] These compounds are known for their reversible flexible frameworks and it has been shown that their frameworks can endure a reversible increase of more than 40% in the unit cell volume (*i.e.* breathing – see Chapter 5) upon sorption of specific guest molecules. The different states of these dynamic frameworks are usually associated with

Stellenbosch University http://scholar.sun.ac.za

tremendous variation in the pore volume (see Figure 1.13). Due to the enormous strain on the framework induced by its flexibility, it is very rare for breathing transitions to occur as single-crystal to single-crystal processes.[76] Chapter 5 describes the extent to which guest-induced flexibility in a seemingly nonporous crystal can be exploited. For more information on functional MOFs and their dynamic frameworks, the author recommends the outstanding reviews by Kitagawa[66] and Ferey.[71-72]

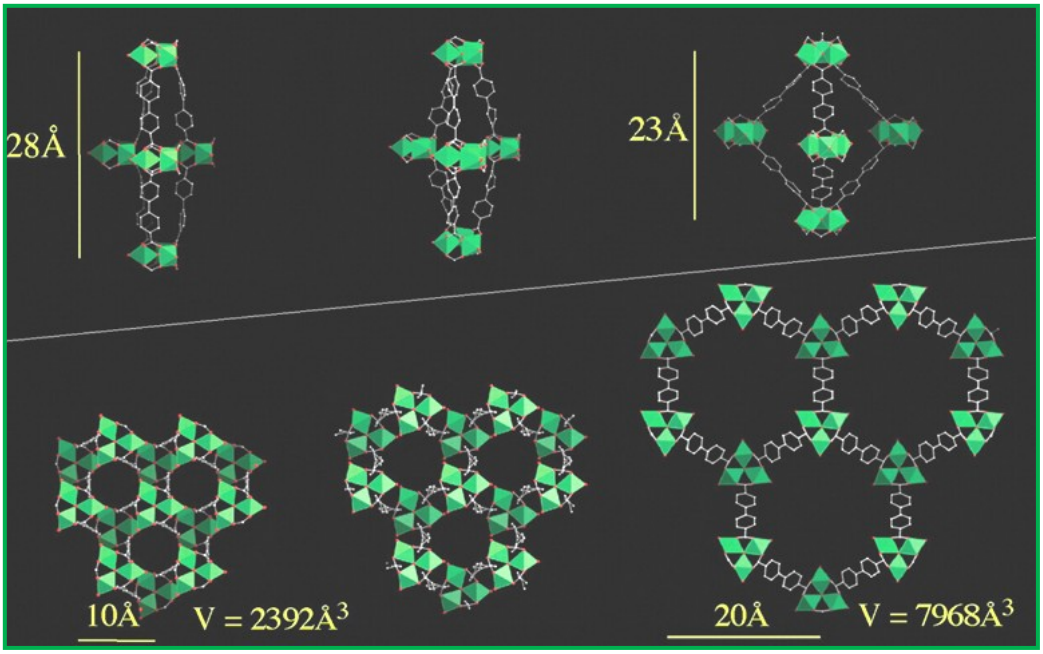

Figure 1.15 Progression of the flexibility (breathing) in MIL-88D (*i.e.* chromium(III)naphthalenedicarboxylate complex). A projection along [001] is shown for the dehydrated closed-pore form (left), the as-synthesised hydrated structure (middle) and the open extended pore (right). The "open" pore can be obtained by exchanging the water guests for solvent molecules.[74]

Virtual porosity

Virtual porosity results from the misconceptions relating to two crucial features of reporting porosity. Firstly, it entails deleting carefully selected atoms from the asymmetric unit of the crystal structure. In most cases, these are atoms of small guest molecules, counterions and bridging ligands between metals that are located within the virtual pores. In the second instance, the use of capped-stick diagrams rather than space-filling representations provides an illusion that the material is porous.

Porosity "without pores" (*i.e.* transient porosity)

Although this form of porosity is a reasonably new phenomenon, it has been reported for both organic and hybrid organic-inorganic materials.[47, 50-51, 77] Porosity *"without pores"* suggests that the material contains lattice voids larger than 25 $Å^3$, but channels or layers connecting these discrete cavities are not apparent. Guest species can still permeate the crystal despite the absence of conventional pores. In principle, transient porosity does not completely obey the 3rd guideline for identifying porous materials, because the host must adjust to some extent in order to make space for the incoming guest. Most of the reports on the single-crystal to single-crystal permeability of seemingly nonporous crystals have come from Atwood *et al*.[46-47, 49-53, 78-79] and Barbour *et al.,*[64] but a recent report by Takamizawa and Kohbara described the permeability of CO_2 through a "closed-pore crystal" (Figure 1.16).[77] It was hypothesised, after considering these reports, that the host dynamics create temporary openings through which guest diffusion can occur.[48] Since this concept is of particular relevance to some of the work presented in this manuscript, additional discussions will follow in the appropriate chapters.

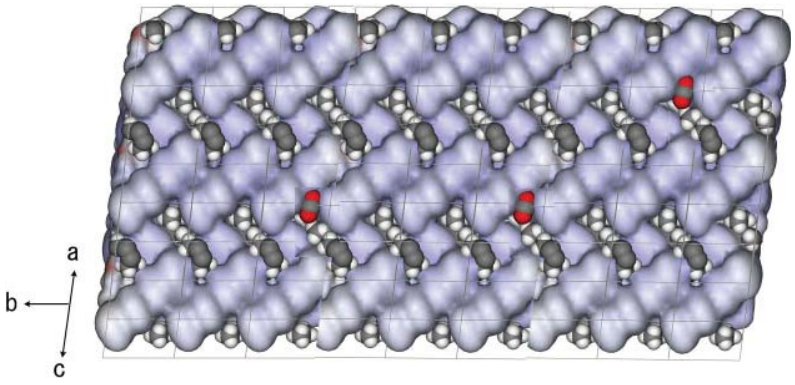

Figure 1.16 A perspective view of the CO_2-containing isolated cavities in a Rh_2benzoate complex crystal.[80]

1.5.2 Thermodynamics and kinetics of sorption

Growing interest in designing functional porous solids has led to an increasing number of commercially available sorption analysers (*i.e.* instruments that measure guest uptake as a function of the relative pressure). Thermodynamic parameters of equilibrium states (*i.e.* no hysteresis) can be determined from the sorption isotherms. In this context, *equilibrium* implies that any point on the sorption isotherm can be reached by increasing (sorption) or decreasing (desorption) the guest pressure.[81] *Thermodynamics* only concerns the initial (*i.e.* empty) and the final (*i.e.* saturated)

states of the system and relates the equilibrium constant of the process to the free energy of sorption ($\Delta G°_{ad}$). The free energy $\Delta G°_{ad}$ is given by the following equation:[59]

$$\Delta G°_{ad} = \Delta H_{ad} - T\Delta S°_{ad}$$

where ΔH_{ad} is the enthalpy of sorption, $\Delta S°_{ad}$ is the entropy of sorption and T is the isothermal experimental temperature. Measurement of ΔH_{ad} is one of the most fundamental thermodynamic characterisation methods for porous solids and is useful in optimising the sorption process. The simplest means of obtaining $\Delta H°_{ad}$ and $\Delta S°_{ad}$ is by the isosteric method. The methodology of the isosteric method is explained in Chapter 5. Decreasing ΔH_{ad} values toward the saturation pressure of the sorbate are expected for energetically heterogeneous sorbents. Although it is a rare occurrence, an increase in ΔH_{ad} values as $P/P_0 \rightarrow 1$ usually indicates the presence of cooperative guest-guest interactions (*i.e.* lateral interactions).[59] The $\Delta H°_{ad}$ value at zero equilibrium loading pressure ($P/P_0 = 0$) gives an indication of the affinity of a host system for a guest and can be related to various interaction energies.[59, 82]

Thermodynamic data enable us to predict the outcome of certain sorption reactions. However, thermodynamic data do not reveal any information on how the process will progress with time (*i.e.* kinetics), although both the *kinetics* of sorption and of desorption are vital aspects of physisorption chemistry.[43] Both of these reactions can be monitored by measuring the mass change as a function of time.[83] The extent of the reaction (α) is defined as

$$\alpha = (m_0 - m_t)/(m_0 - m_f)$$

where m_0 is the initial mass, m_t is the mass at time t, and m_f is the final mass. By plotting α as a function of time (Figure 1.17 (a)), various models can be fitted to the kinetic curve. These models (*e.g.* first-order **F1**, contracting area **R2** or contracting volume **R3**)[59] each correspond to a particular reaction mechanism. The activation energy E_a can be derived by employing the corresponding rate constant k in the Arrhenius equation.

$$k = A \exp(-E_a/RT)$$

Thus, activation energy E_a can easily be calculated from the negative slope of the plot of ln k versus $1/T$ (see Figure 1.17 (b)). Experimental measurement of the kinetic parameters of sorption did not form part of the present study; however it is important to understand the differences between

kinetics and thermodynamics to be able to derive credible thermodynamic information from experimental sorption isotherms, and the processes governing solid-gas reactions.

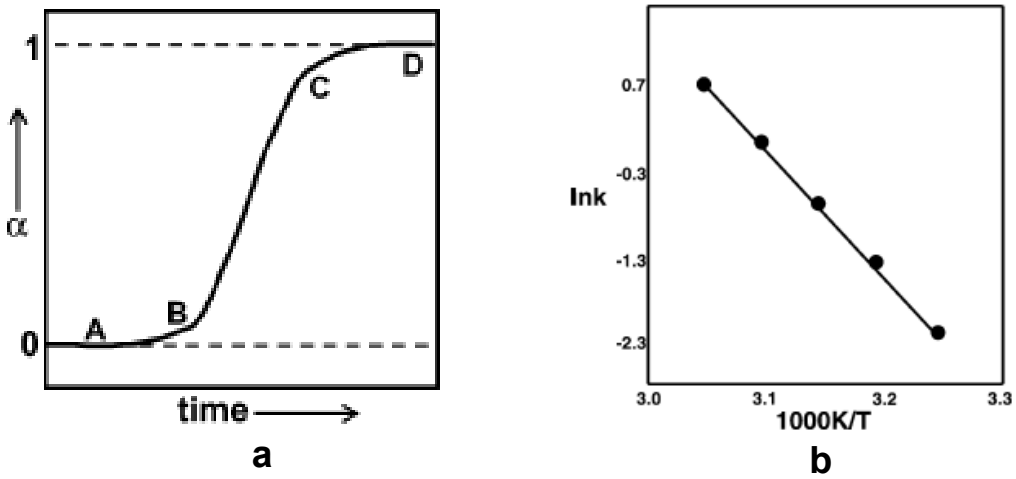

Figure 1.17 (a) Representation of an α-time plot. (b): A typical ln *k* versus T^{-1} plot.[43, 83-85]

1.6 Thesis Outline

The primary aim of this study is to explore the solid-state physico-chemical aspects and thus the structure-property relationships involved in guest-induced flexibility of supramolecular crystals. These molecular crystals were specifically designed (molecules synthesised according to crystal engineering strategies) to obtain hosts that can readily encapsulate a variety of guests.

Chapter 2 contains detailed descriptions of the methodologies and techniques used during the study. *Chapter 3* describes modification of a known oxacalixarene host in order to study its inclusion capabilities. During this study a novel oxacalix[2]arene[2]naphthalene[86] host molecule (Figure 1.18) was synthesised and crystallised from a number of solvents, and a series of solvate structures was produced. Guest desorption trends are discussed and the flexible nature of the host molecule, when enclosing guests of different shapes and sizes, has been illustrated by a systematic conformational study.

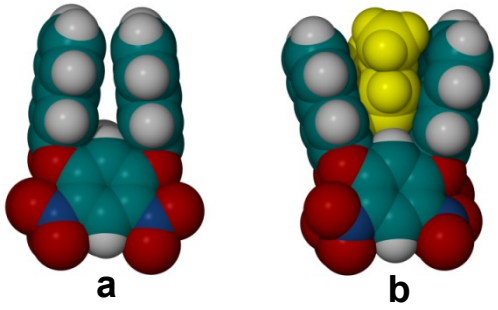

Figure 1.18 (a) The apohost and (b) the dimethyl formamide solvate of oxacalix[2]arene[2]naphthalene in space-filling representations .

Chapter 4 explores the self-assembly of four novel "doughnut-shaped" metallocycles (see Figure 1.19) by the reaction of Co^{2+} or Cu^{2+} halides and imidazole-based coordinating ligands in the appropriate solvents. The utilisation of these metallocycles is based on the design strategy that molecules with "awkward" shapes will be unable to close-pack in the solid state, resulting in void space that can accommodate small solvent molecules. Additionally, incorporation of the metal induces some rigidity to the complex. The rigidity of the metal in conjunction with the flexibility of the methylene bridges of the organic ligand is thought to produce the right balance between flexibility and rigidity to permit single-crystal to single-crystal desolvation of the guest molecule to yield potentially porous crystals.

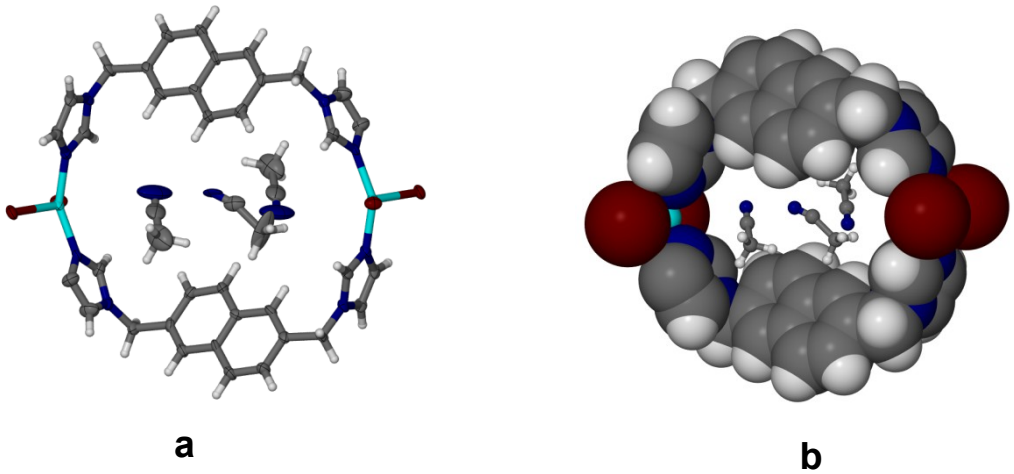

Figure 1.19 (a) The single-crystal structure of the acetonitrile-included $CuBr_2$ metallocycle showing the ellipsoids with 50% probability. (a) A space-filling representation of the acetonitrile-included $CuBr_2$ metallocycle, illustrating the "doughnut-shaped" molecular conformation.

Throughout *Chapter 5* the main emphasis is on the determination and interpretation of equilibrium states, as well as the thermodynamics of vapour sorption in a seemingly nonporous

Stellenbosch University http://scholar.sun.ac.za

metallocycle. This metallocycle displayed significant flexibility upon encapsulation of certain guests. The first part of the investigation focused on the permeability of the material to a series of solvents at the solid-vapour interface; all adducts were characterised structurally using single-crystal X-ray diffraction, and sorption isotherms at four different temperatures were recorded for each in order to determine the thermodynamic parameters ($\Delta H°_{ad}$ and $\Delta S°_{ad}$). The sorption isotherms are described in terms of the IUPAC classification and plots of guest occupancy (*i.e.* fraction of host:guest ratio) versus the relative pressure P/P_o yielded information on the affinity for each particular guest. The second part of the study is concerned with the single-crystal to single-crystal sorption of volatile organic solids such as naphthalene and *p*-dichlorobenzene (Figure 1.20). *Chapter 6* summarises the results and conclusions of the work presented in Chapters 3, 4 and 5.

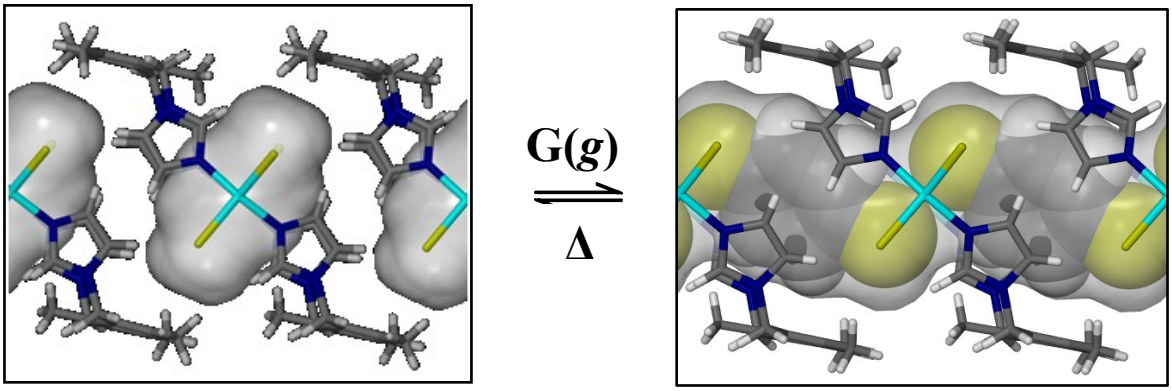

Figure 1.20 The formation of a continuous channel upon exposing the "empty" metallocycle to *p*-dichlorobenzene vapour.

Stellenbosch University http://scholar.sun.ac.za

1.7 References

[1] J. M. Lehn, *Angew. Chem. Int. Ed. Engl.* **1988**, *27*.

[2] K. L. Wolf, H. Dunken, K. Merkel, *Z. Physik. Chem.* **1940**, *B46*, 287-312.

[3] K. L. Wolf, H. Frahm, H. Harms, *Z. Physik. Chem.* **1937**, *B36*, 237-287.

[4] K. L. Wolf, R. Wolff, *Angew. Chem. Int. Ed.* **1949**, *61*, 191-201.

[5] J. W. Steed, J. L. Atwood, *Supramolecular Chemistry*, John Wiley & Sons Ltd, West Sussex, **2000**.

[6] J. L. Atwood, J. W. Steed, in *Encyclopedia of Supramolecular Chemistry, Vol. 1*, Pergamon, New York, **2004**, 158.

[7] J. M. Lehn, in *Comprehensive Supramolecular Chemistry, Vol. 1-10*, Pergamon, New York, **1996**.

[8] C. B. Aakeröy, D. S. Leinen, in *Crystal Engineering: From molecules and crystals to materials* (Ed.: D. Braga), **1999**.

[9] D. Braga, F. Grepioni, in *Encyclopedia of Supramolecular Chemistry*, **2004**, 357-363.

[10] G. M. J. Schmidt, *Pure Appl. Chem.* **1971**, *27*, 647.

[11] G. R. Desiraju, *Angew. Chem. Int. Ed. Engl.* **1995**, *34*, 2311.

[12] E. J. Corey, *Pure Appl. Chem.* **1976**, *14*, 19.

[13] F. H. Allen, J. E. Davies, J. J. Galloy, O. Johnson, O. Kennard, C. F. Macrae, E. M. Mitchell, G. F. Mitchell, J. M. Smith, D. G. Watson, *J. Chem. Inf. Comput. Sci.* **1991**, *31*.

[14] D. Braga, *Chem. Commun.* **2003**, *2751*.

[15] J. W. Steed, D. R. Turner, K. J. Wallace, *Core Concepts in Supramolecular Chemistry and Nanochemistry*, John-Wiley & Sons, Ltd, **2007**.

[16] C. B. Aakeröy, N. R. Champness, C. Janiak, *CrystEngComm* **2010**, *12*, 22-43.

[17] A. I. Kitaigorodskii, *Organic Chemical Crystallography*, Consultant Bureau, **1961**.

[18] A. D. Bond, W. Jones, *Supramolecular Organization and Materials Design*, Cambridge University Press, **2002**.

[19] A. Gavezzotti, *Crystal Symmetry and Molecular Recognition*, John Wiley & Sons, Chichester, **1997**.

[20] M. C. Etter, *Acc. Chem. Res.* **1990**, *23*, 120.

[21] U. L. Pauling, *The Nature of the Chemical Bond, Vol. 6*, 3 ed., Cornell University Press: Ithaca, NY, **1960**.

Stellenbosch University http://scholar.sun.ac.za

[22] C. B. Aakeröy, *Chem. Soc. Rev.* **1993**, 379.

[23] G. Desiraju, in *Encyclopedia of Supramolecular Chemistry, Vol. 1* (Eds.: J. L. Atwood, J. W. Steed), Marcel Dekker Inc., **2004**.

[24] G. M. Sheldrick, *SHELX-97 Manual*, http://linux.uni-ac.gwdg.de/SHELX/, **1997**.

[25] V. R. Pedireddi, D. S. Reddy, B. S. Goud, D. C. Craig, A. D. Rae, G. R. Desiraju, *J. Chem. Soc., Perkin Trans. 2* **1994**, *2353*.

[26] C. A. Hunter, K. K. M. Sanders, *J. Am. Chem. Soc.* **1990**, *112*, 5525.

[27] L. R. MacGillivray, J. L. Reid, J. A. Ripmeester, *J. Am. Chem. Soc.* **2000**, *122*, 7817-7818.

[28] A. L. Garay, A. Pichon, S. L. James, *Chem. Soc. Rev.* **2007**, *36*, 846-855.

[29] A. Pichon, A. Lazuen-Garay, S. L. James, *CrystEngComm* **2006**, *8*, 211-214.

[30] O. M. Yaghi, M. O'Keefe, N. W. Ockwig, H. K. Chae, M. Eddaodi, J. Kim, *Nature* **2003**, *423*, 705-714.

[31] D. J. Cram, *Angew. Chem. Int. Ed. Engl.* **1986**, *25*, 1039.

[32] M. Q. Faraday, *J. Sci.* **1823**, *15*, 71.

[33] H. Davy, *Phil. Trans. Roy. Soc.* **1811**, *101*.

[34] H. M. Powell, *J. Chem. Soc.* **1948**, 61.

[35] B. Dietrich, J. M. Lehn, J. P. Pederson, *Tetrahedron Lett.* **1969**, *2885*.

[36] J. L. Atwood, J. E. D. Davies, D. D. Macnicol, F. Vögtle, in *Comprehensive Supramolecular Chemistry, Vol. 1* (Ed.: J. M. Lehn), Pergamon, **1996**.

[37] C. D. Gutsche, J. F. Stoddart, *Monographs in Supramolecular Chemistry* **1989**.

[38] H. Stetter, E. E. Roos, *Chem. Ber.* **1955**, *88*, 6675.

[39] H. M. Powell, *J. Chem. Soc. Dalton. Trans.* **1948**, *61*.

[40] J. L. Flippen, J. Karle, I. L. Karle, *J. Am. Chem. Soc.* **1970**, *92*.

[41] K. D. M. Harris, *Supramol. Chem.* **2007**, *19*, 47-53.

[42] R. Sozostak, *Molecular sieves*, 2nd ed., Blackie Academic and Professional, London, UK, **1998**.

[43] L. R. Nassimbeni, *Acc. Chem. Res.* **2003**, *36*, 631-637.

[44] M. E. Brown, *Vol. 1*, **2001**.

[45] J. Bernstein, in *IUCr Monographs on Crystallography*, Oxford Science Publications, **2002**, 2, 74-75.

Stellenbosch University http://scholar.sun.ac.za

[46] J. L. Atwood, L. J. Barbour, A. Jerga, *Science* **2002**, *296*, 2367-2369.

[47] J. L. Atwood, L. J. Barbour, A. Jerga, B. L. Schottel, *Science* **2002**, *298*, 1000-1002.

[48] L. J. Barbour, *Chem. Commun.* **2006**, 1163-1168.

[49] S. J. Dalgarno, P. K. Thallapally, L. J. Barbour, J. L. Atwood, *Chem. Soc. Rev.* **2007**, *36*, 236-245.

[50] P. K. Thallapally, L. Dobrzańska, T. R. Gingrich, T. B. Wirsig, L. J. Barbour, J. L. Atwood, *Angew. Chem. Int. Ed.* **2006**, *45*, 6506-6509.

[51] P. K. Thallapally, G. O. Lloyd, J. L. Atwood, L. J. Barbour, *Angew. Chem. Int. Edit.* **2005**, *44*, 3848-3851.

[52] P. K. Thallapally, G. O. Lloyd, T. B. Wirsig, M. W. Bredenkamp, J. L. Atwood, L. J. Barbour, *Chem. Commun.* **2005**, 5272-5274.

[53] P. K. Thallapally, T. B. Wirsig, L. J. Barbour, J. L. Atwood, *Chem. Commun.* **2005**, 4420-4422.

[54] F. Fontana, *Mem. Mat. Fis. Soc. Ital* **1777**, *1*, 679.

[55] C. W. Scheele, *Chemische Abhandlung vor der Luft und dem Feuer* **1773**.

[56] H. Kayser, *Wied. Ann. Phys.* **1881**, *12*, 526.

[57] H. Kayser, *Wied. Ann. Phys.* **1881**, *14*, 141.

[58] A. Fick, *Phil. Mag.* **1855**, *10*, 30.

[59] F. Rouquerol, J. Rouquerol, K. Sing, *Adsorption by Powders and Porous Solids* **1999**, *Academic Press, San Diego*.

[60] C. Tien, *Adsorption Calculations and Modeling, Butterworth-Heinemann Series in Chemical Engineering, Butterworth-Heinemann* **1994**, *USA*.

[61] M. Suzuki, *Adsorption Engineering, Chemical Engineering Monographs 25* **1990**, *Kondansha Ltd and Elsevier Publishers B.V*.

[62] K. S. W. Sing, D. H. Everett, R. A. W. Haul, L. Moscou, R. A. Pierotti, J. Rouquerol, T. Siemieniewska, *Pure Appl. Chem.* **1985**, *57*, 603-619.

[63] J. Rouquerol, D. Avnir, C. W. Fairbridge, D. H. Everett, J. H. Haynes, N. Pernicone, J. D. F. Ramsay, K. S. W. Sing, K. K. Unger, *Pure Appl. Chem.* **1994**, *66*, 1739-1758.

[64] L. Dobrzańska, G. O. Lloyd, H. G. Raubenheimer, L. J. Barbour, *J. Am. Chem. Soc.* **2006**, *128*, 698-699.

[65] A. Nangia, in *Encyclopedia of Supramolecular Chemistry, Vol. 2*, 1 ed. (Eds.: J. L. Atwood, J. W. Steed), Marcel Dekker, Inc., Amsterdam, **2004**, 967-972.

Stellenbosch University http://scholar.sun.ac.za

[66] S. Kitagawa, R. Kitaura, S. I. Noro, *Angew. Chem. Int. Ed.* **2004**, *43*, 2334-2375.

[67] S. Kitagawa, T. Nakamura, S.-I. Noro, *Chem. Commun.* **2006**, 701.

[68] S. Kitagawa, R. Kitaura, S.-I. Noro, *Angew. Chem. Int. Ed.* **2004**, *43*, 2334.

[69] S. Bourrelly, B. Moulin, A. Rivera, G. Maurin, S. Devautour-Vinot, C. Serre, T. Devic, P. Horcajada, A. Vimont, G. Clet, M. Daturi, J. C. Lavalley, S. Loera-Serna, R. Denoyel, P. L. Llewellyn, G. Ferèy, *J. Am. Chem. Soc.* **2010**, *132*, 9488-9498.

[70] T. Devic, P. Horcajada, C. Serre, F. Salles, G. Maurin, B. Moulin, D. Heurtaux, G. Clet, A. Vimont, J. M. Greneche, B. Le Ouay, F. Moreau, E. Magnier, Y. Filinchuk, J. Marrot, J. C. Lavalley, M. Daturi, G. Ferèy, *J. Am. Chem. Soc.* **2010**, *132*, 1127-1136.

[71] G. Ferèy, *Chem. Soc. Rev.* **2008**, *37*, 191-214.

[72] G. Ferèy, C. Serre, *Chem. Soc. Rev.* **2009**, *38*, 1380-1399.

[73] A. H. Fuchs, A. Boutin, M. A. Springuel-Huet, A. Nossov, A. Gedeon, T. Loiseau, C. Volkringer, G. Ferèy, F. X. Coudert, *Angew. Chem. Int. Edit.* **2009**, *48*, 8314-8317.

[74] C. Serre, C. Mellot-Draznieks, S. Surble, N. Audebrand, Y. Filinchuk, G. Ferèy, *Science* **2007**, *315*, 1828-1831.

[75] T. K. Trung, N. A. Ramsahye, P. Trens, N. Tanchoux, C. Serre, F. Fajula, G. Férey, *Microporous Mesoporous Mater.* **2010**, *134*, 134-140.

[76] T. K. Maji, G. Mostafa, R. Matsuda, S. Kitagawa, *J. Am. Chem. Soc.* **2005**, *127*, 17152-17153.

[77] S. Takamizawa, M. Kohbara, *Dalton Trans.* **2007**, 3640-3645.

[78] J. L. Atwood, L. J. Barbour, A. Jerga, *Angew. Chem. Int. Ed. Engl.* **2004**, *43*, 2948-2950.

[79] J. L. Atwood, L. J. Barbour, P. K. Thallapally, T. B. Wirsig, *Chem Commun (Camb)* **2005**, 51-53.

[80] S. Takamizawa, E.-i. Nataka, T. Akatsuka, R. Miyake, Y. Kakizaki, H. Takeuchi, G. Maruta, S. Takeda, *J. Am. Chem. Soc.* **2010**, *132*, 3783-3792.

[81] T. M. Letcher, *Chemical Thermodynamics for Industry*, Royal Society of Chemistry, **2004**.

[82] R. M. Barrer, *Zeolites and Clay Minerals as Sorbents and Molecular Sieves*, London: Academic Press Inc., **1978**.

[83] L. R. Nassimbeni, *Supramol. Chem.* **2000**, *12*, 161-167.

[84] L. J. Barbour, K. Achleitner, J. R. Greene, *Thermochim. Acta* **1992**, *205*, 171-177.

[85] M. R. Caira, L. R. Nassimbeni, F. Toda, D. Vujovic, *J. Chem. Soc., Perkin Trans. 2* **2001**, 2119-2124.

Stellenbosch University http://scholar.sun.ac.za

[86] A. Kleyn, T. Jacobs, L. J. Barbour, *CrystEngComm* **2011**, *13*, 3175-3180.

Stellenbosch University http://scholar.sun.ac.za

Chapter 2
Experimental methods

Completion of the work presented here involved numerous routine methods and instrumental techniques. Many of these techniques (*e.g.* NMR, ATR-IR, ESI-MS and UV-VIS) are well documented and for this reason will not be discussed in this chapter. Several other techniques that are specific to this field will be discussed in more detail and, where needed, a more comprehensive description will follow in Chapters 3, 4 and 5.

2.1 Single-crystal X-ray diffraction (SCD)

Single-crystal X-ray diffraction data were collected using a Bruker SMART Apex I diffractometer equipped with a Mo fine-focus sealed tube ($\lambda = 0.71073$ Å) and a 0.5 mm MonoCap collimator. The detector was upgraded to the Apex II model during the late stages of this work. Temperature control was maintained using an Oxford Cryosystems cryostat (700 Series Cryostream Plus). In general, the mother liquor was decanted before carefully removing several crystals from the vial using a spatula. Crystal quality was assessed according to its ability to rotate plane-polarized light, its transparency and its morphology. A suitable crystal was mounted on a commercially available MiTeGen MicroMount™[1] using paratone oil. Data were collected using omega scans, and recorded using a charge couple device (CCD) area detector with a detector to crystal distance of 60 mm. Data reduction and absorption corrections were carried out using the subprograms SAINT[2] and SADABS[3-4] of the APEX II software package. Space groups were assigned based on systematic absences and intensity statistics using XPREP. Most structures were solved by direct methods using SHELXS-97[5] and non-hydrogen atoms were refined anisotropically by means of full-matrix least squares calculations on F^2 by SHELXL-97[5] and the X-Seed[6] graphical user interface. Challenging structures involved using a combination of Patterson methods and structure expansion prior to routine structure refinement. In all cases, hydrogen atoms were placed in calculated positions using riding models. Publication quality images were generated using the programme POV-Ray[7]. Crystallographic supplementary data (.res and .cif files) can be found in the attached CD.

Stellenbosch University http://scholar.sun.ac.za

2.2 Powder X-ray diffraction (PXRD)

A PANalytical X'PERT-PRO (PANalytical, Almelo, Netherlands) diffractometer was employed for high resolution powder X-ray diffraction studies. Intensity data were collected using Cu-K_α radiation (λ = 1.5418 Å). Samples were gently crushed (using a spatula) before being carefully transferred onto a zero-background sample holder, taking special care to randomly distribute the particles. In the case of variable temperature measurements, a specifically designed conducting sample holder was used. The data collection protocol typically consisted of a step size of 0.012º within the 2θ range of 3°- 60°. Powder patterns calculated from single-crystal data were generated using the program LAZY-Pulverix.[8] Calculated diffractograms were compared to the experimental patterns to confirm that the single-crystal structure is representative of the bulk sample. All diffractograms were plotted with Microsoft Excel.

2.3 Volumetric sorption isotherms

All vapour sorption isotherms were collected on a Micromeretics® Accelerated Surface Area and Porosimetry System 2020 (ASAP 2020 – Figure 2.1).[9] The method employs the principles of gas sorption manometry whereby the instrument measures the pressure in a calibrated container (*i.e.* constant volume) and at a stable temperature. The ASAP analyser is equipped with two independent vacuum pumps, one for sample preparation and one for sample analysis, allowing the two steps to occur concurrently without interruption and provides an oil-free environment for the sorption measurements. The instrument is fitted with inline cold traps and a sample saturation pressure (P_{sat}) tube. The vapour pressure of the sorbate P_0 (at the analysis temperature) is measured throughout the experiment using the P_{sat} transducer, allowing the vapour pressure to be monitored at each data point. Pressure measurements are accurately recorded by a 1 mmHg transducer and can only be measured in the range of 0-950 mmHg. Higher pressures are unnecessary for vapour sorption studies, since sorption experiments with organic vapours only allow pressures up to that of the vapour pressure at each the desired temperatures. The four desired temperatures (0 , 10, 20, 30 ºC) used in the study were controlled and maintained to an accuracy of +/- 0.05 °C using a Grant refrigerated recirculation bath equipped with a locally-developed removable dewar, which fits around the sample tube. This device is compatible with the elevator of the ASAP. The system software monitors and controls the analyser in real time and also facilitates manual control of the mechanical valves (Figure 2.2.). A specific analysis protocol was set up before each analysis.

Stellenbosch University http://scholar.sun.ac.za

Parameters such as the accurate sample density, sample mass, experimental temperature and the P_{sat} of the solvent at the analysis temperature are required by the analysis program. Some of the sorbate (solvent) properties are listed in Table 5.2 in Chapter 5. All solvents were dried, pre-distilled and degassed before each set of experiments. Each sample was initially placed under vacuum for 24 hours at 70 ºC to ensure that all traces of solvent were removed prior to the next sorption measurement. After data collection, the software automatically saves a report consisting of data points collected (mmol guest per gram of host) corresponding to each equilibrium pressure point. All isotherms were plotted as mmol guest per mmol of host (*i.e.* occupancy) against either the relative pressure or the absolute pressure using Microsoft Excel.

Figure 2.1 A photograph of an ASAP 2020 analyser.

Stellenbosch University http://scholar.sun.ac.za

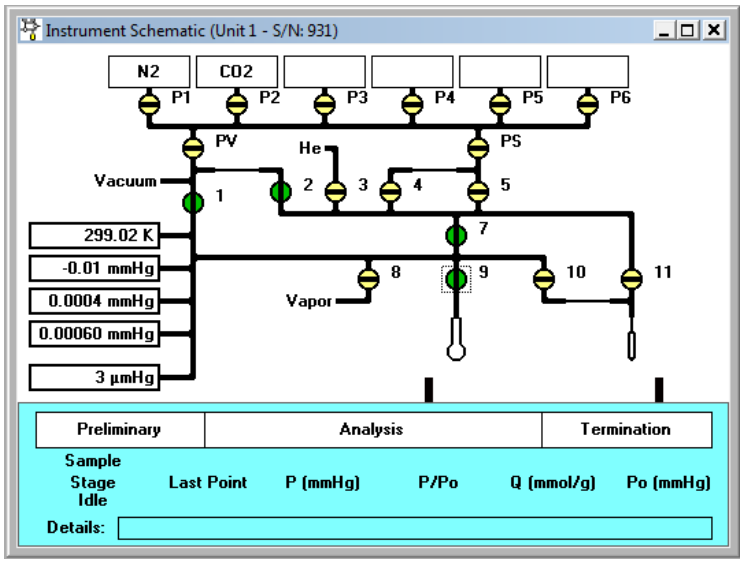

Figure 2.2 The instrument schematic with which the user can manually control the mechanical valves of the ASAP 2020. Green circles indicate "open" valves and yellow circles designate "closed" valves.

2.4 Thermogravimetric analysis (TGA)

Thermogravimetric analysis was carried out on a TA Instruments Q500 thermogravimetric analyser. Using the software interface an analysis protocol was set up, which generally consisted of heating the sample from ambient to a specified temperature (up to 600 °C) at a rate of 10 ºC.min^{-1}. Samples of mass 1-7 mg were transferred into an aluminium pan before analysis. The balance and sample were purged with dry N_2 gas flowing at a rate of 50 cm^3.min^{-1}. Interpretation and analysis of the data were carried out using TA Instruments Universal Analysis program. All figures were prepared with Microsoft Excel.

2.5 Differential scanning calorimetry (DSC)

Differential scanning calorimetry was carried out using a TA Instruments Q100 differential scanning calorimeter. Samples were prepared by crimping the sample pan and lid tightly (hermetic conditions). A reference pan was prepared in the same manner for each analysis. Analyses were generally carried out in the temperature range -60-400 ºC and a general experimental procedure consisted of heating/cooling the sample while the heat flow into or out of the sample, relative to the reference, was measured as a function of time and temperature in a controlled atmosphere. N_2 gas, flowing at a rate of 50 ml. min^{-1} was used to purge the furnace. The resulting thermograms were

Stellenbosch University http://scholar.sun.ac.za

analysed using TA Instruments Universal Analysis program and figures were prepared with Microsoft Excel.

2.6 Viewing intermolecular interactions

The presence of intermolecular interactions was established by analysing the crystal structures using a combination of the programs CrystalExplorer[10] and Mercury 2.4. Mercury is a structure visualisation component of the CSD[11-12] which allows one to locate and display intermolecular and/or intramolecular hydrogen bonds, short van der Waals contacts, and other contacts specified by the user. During the present study, the option to display multiple structures simultaneously was also very useful, since least-squares overlays of similar structures could be performed.

CrystalExplorer is a relatively recent and novel "toolkit for crystal engineering" and makes use of the *Hirshfeld surface* to indicate the locations of intermolecular interactions. The *Hirshfeld surface*[13] (named after F. L. Hirshfeld)[14] of a molecule in a crystal represents the regions in the crystal where the electron distribution for the *promolecule* (*i.e.* electron distribution sum of spherical atoms for the molecule) exceeds the corresponding sum of the neighbouring molecules or the *procrystal* (*i.e.* electron distribution of a sum of spherical atoms for the crystal).[15-16] The wave function for the Hirshfeld surface and a graphical example of such a surface is depicted on the left of Figure 2.3. Although there are many ways of visualising the Hirshfeld surface (*e.g.* closest internal contact surface (d_i) and closest external contact surface (d_e)), only the d_{norm} distance (normalised combination of both d_i and d_e surfaces and their van der Waals radii – Figure 2.3(b)) was used to determine the nature of short contacts during the present study (Figure 2.4). Short contacts are easily observable using the colour code shown in Figure 2.4(a). Another useful feature of CrystalExplorer, with regard to the present study, is the 2D-fingerprint of the Hirshfeld surface (*i.e.* fingerprint plot), which is essentially a visual summary of the frequency of the intermolecular interactions present in a crystal.[16] High quality images of the d_{norm} surfaces and the fingerprint plots were generated from the .cif files (obtained from structure refinement in X-Seed) and by using the "export graphics" option in CrystalExplorer. For more information on the features of CrystalExplorer the reader can consult the software manual available online.[10]

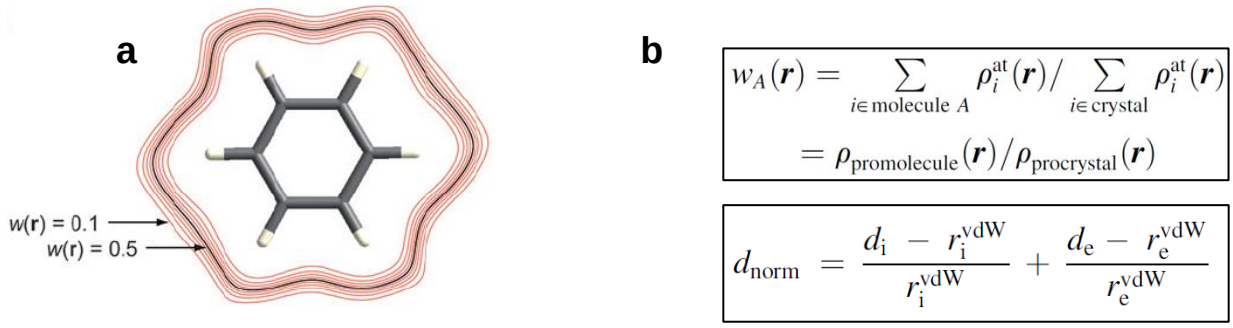

Figure 2.3 (a) Outline of the wave function $w_A(r)$ surrounding a benzene molecule in the crystal. (b) Equations representing the Hirshfeld surface wave function (top) and the d_{norm} function (bottom). [10]

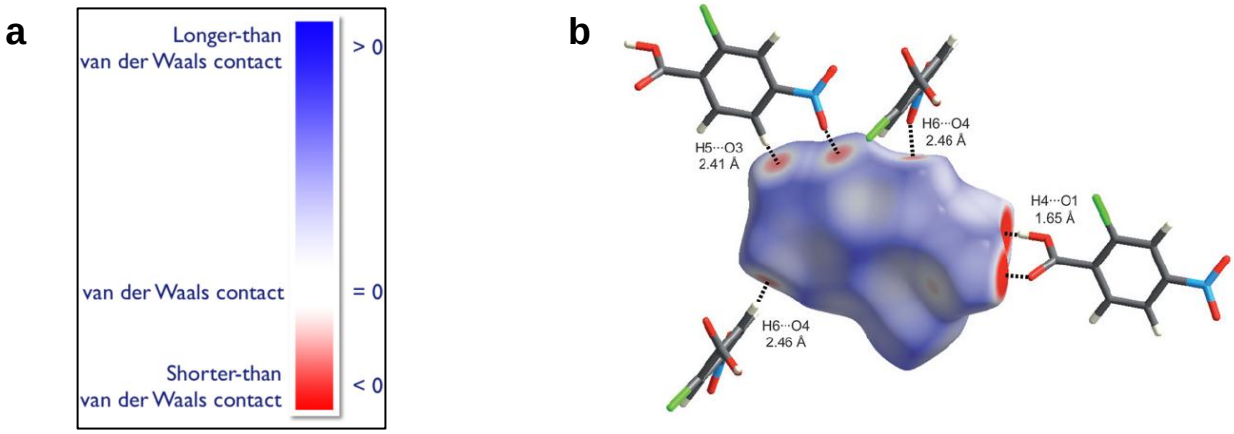

Figure 2.4 (a) The scale used to denote intermolecular interactions using the d_{norm} surface. Short contacts appear as red and white surfaces on a blue background. (b) The d_{norm} Hirshfeld surface of 2-chloro-4-nitrobenzoic acid (form I). Four adjacent molecules related to the surface *via* close contacts are also shown. [10]

2.7 Miniature gas cell for collecting intensity data

When we consider the formation of a solid-gas host-guest complex under equilibrium conditions (Section 1.3), the extent of inclusion will depend on the overpressure of the guest. Therefore, in order to collect SCD data of the gas-loaded material the crystal must be kept under a constant pressure of the gas in question throughout the duration of the intensity data collection experiment. To overcome this practical challenge, a reusable gas cell (Figure 2.5) was constructed. This gas cell is sufficiently compact to facilitate routine data collections using a standard diffractometer (Figure 2.5) and can also withstand relatively high pressure (~ 80 bar). The specific model of the gas cell shown in Figure 2.5 is a modification of two earlier versions that did not allow routine data collections, and *centering* of the crystal in the X-ray beam was difficult in some instances. For more

Stellenbosch University http://scholar.sun.ac.za

information on the construction and methodology of the previous gas cell models the reader can consult the theses of Jacobs[17] and Lloyd.[18]

The updated gas cell consists of three components (Figures 2.5 and 2.6): a) a stainless steel fitting that attaches a glass capillary to the gas cell, b) a brass gas cell coated with nickel, and c) a valve stem threaded at both ends. A steel lock nut is used for simple height adjustment of the crystal mounted within the gas cell. Figure 2.6 shows a cross section view of the gas cell, which has a port for gas loading, a valve stem and a port that fits the steel fitting. Typically, the assembly of the gas cell comprises gluing a suitable crystal to the end of a microfiber, which is then glued within a glass capillary with an outside diameter of 3 mm. The glass capillary is flame-sealed at the narrow end prior to inserting the microfiber. Epoxy resin is used to seal the glass capillary to the steel fitting in order to render a leak-proof connection. Loading the gas cell with the particular gas was achieved by attaching the gas cell to a manifold using a detachable steel arm. The required pressure to the gas cell can be controlled using the regulator and determined with an accurate test gauge. The gas cell is then opened for ~20 sec before closing it again and the procedure repeated again after 30 min. The pressure within the gas cell is not measured during the data collection and it is assumed to be that indicated by the test gauge when the gas cell is sealed. The miniature gas cell fits onto a standard goniometer head (Figure 2.5) such that a typical data collection strategy can be executed. SCD data for measurements using the gas cell were collected using a Bruker APEX II DUO equipped with a multilayer monochromater. All data collections were carried out using the Mo Incoatec IμS microsource (λ = 0.71073 Å). In most cases intensity data were collected at room temperature. However, guest molecules could not always be modelled in a sensible manner owing to the high thermal motion associated with the gaseous guests at this temperature. For such systems, data collections were carried out at lower temperature, taking special care not to expose the gas to temperatures below its critical point.

Stellenbosch University http://scholar.sun.ac.za

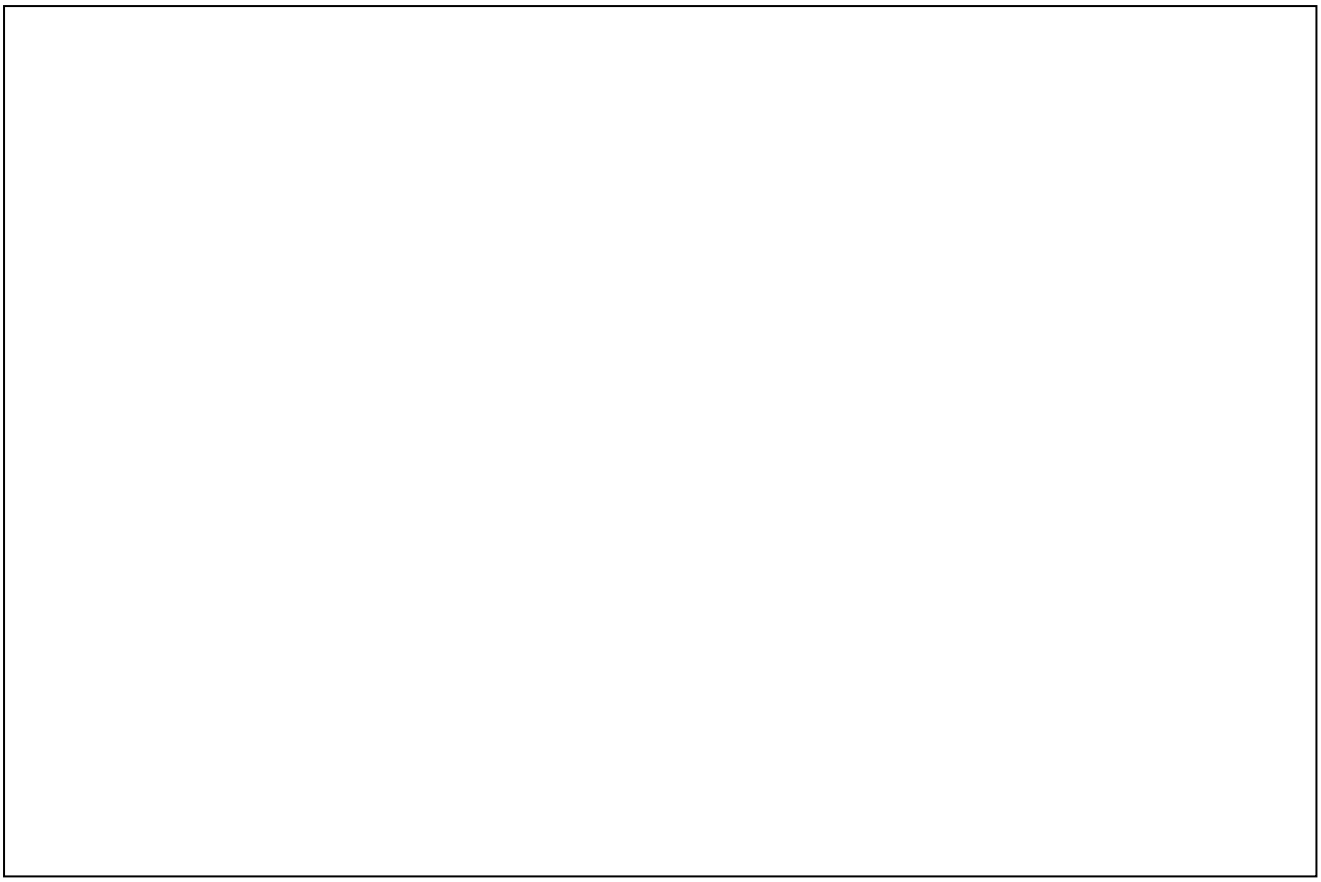

Figure 2.5 A photograph of the miniature gas cell fitted onto a goniometer head (left). The essential parts are indicated with yellow arrows. The gas cell (highlighted in yellow) fitted onto the single-crystal X-ray diffractometer is shown on the right.

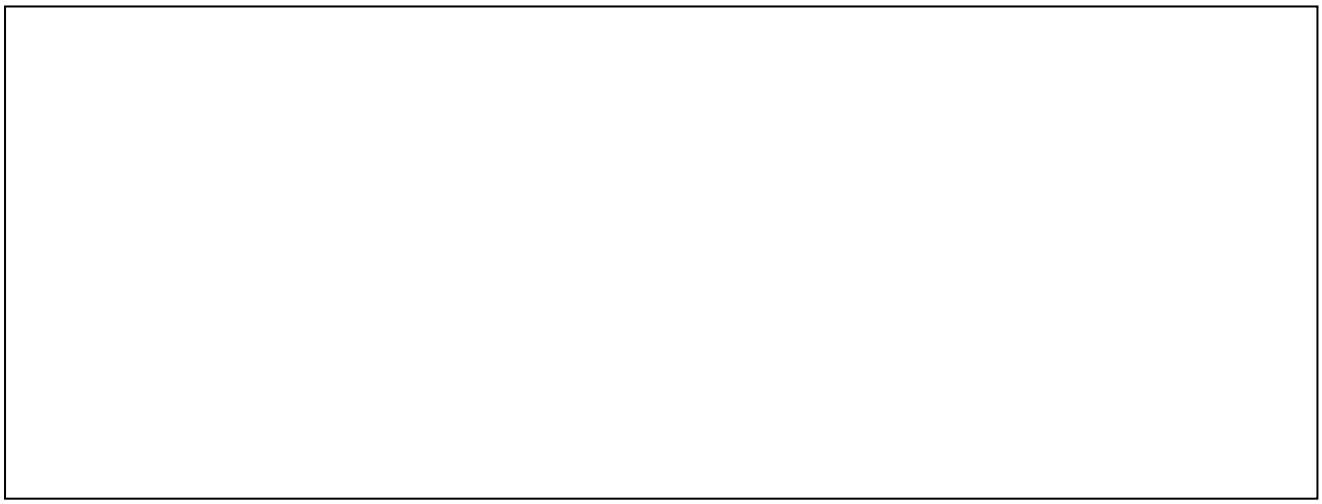

Figure 2.6 Cross section of the gas cell.

Stellenbosch University http://scholar.sun.ac.za

2.8 Calculation and graphical representation of the solvent-accessible volume

The guest-accessible volume[19] is that which is reversibly accessible to solvents or other guest molecules and this concept was first developed by Richards in 1971 for use in protein chemistry.[20] During this study the solvent-accessible volumes for all relevant structures were calculated using MSROLL[21-23] (accessible via the program X-Seed). Guest molecules accommodated within the space unoccupied by the host molecules were deleted prior to each calculation and the void in question was blocked at both ends by placing a "dummy" atom such as iodine. However, the volume of the "dummy" atom is not taken into account when calculating the guest-accessible volume. This is because the guest-accessible volume per unit cell is determined by subtracting the free volume mapped between two "dummy" atoms at the ends of one unit cell from the free volume mapped between two "dummy" atoms at the ends of two adjacent unit cells.

The solvent-accessible surface can be graphically represented as the Connolly surface using MSROLL[21-23] and POV-Ray.[6, 24] The Connolly surface calculation involves a modified version[20] of the "rolling ball" algorithm first developed in 1973 by Shrake and Rupley.[25] This adapted algorithm uses a sphere (whose radius can be specified) to "probe" the volume of the host molecules beyond their van der Waals radius (Figure 2.7 and Table 2.1). It is important to note that the choice of the probe radius (generally 1.4 or 1.5 Å) has an effect on the observed volume (*e.g.* a smaller probe radius reports a larger volume) – the probe radius can be increased systematically until the accessible surface does not extend beyond the centre of the accessible volume being determined.[18] Thus, the calculation is also greatly affected by the assigned atomic van der Waals radii (see Table 2.1). MROLL[21-23] outputs a .cav file, which can be imported into X-Seed[6] in order to render high-quality figures of the void space (Figure 2.7) using POV-Ray.[6-7, 24] If a particular region of a guest molecule protrudes beyond the Connolly surface (see Figure 2.7), it is usually an indication that a strong host-guest interaction is present at that location.

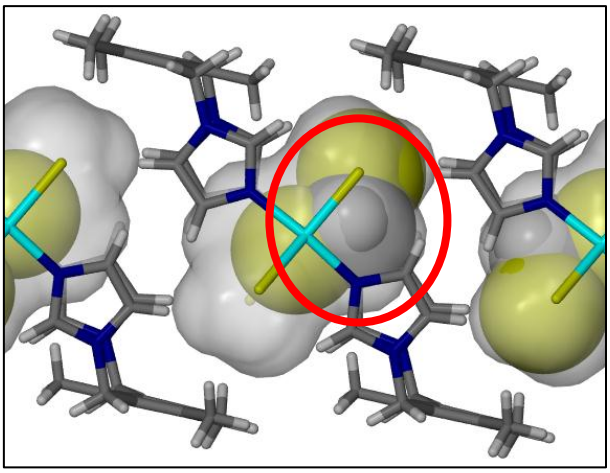

Figure 2.7 An example of the solvent-accessible volume mapped as the Connolly surface (semi-transparent grey surface with V = 125 Å^3, using a probe radius = 1.4 Å). The dichloromethane guest molecules are shown as van de Waals spheres (*i.e.* space-filling representation) and the regions of the guest protruding (depicted by the red circle) the accessible surface indicates the locations of intermolecular interactions (e.g. a C–H···Cl hydrogen bond is shown).

Table 2.1 van der Waals radii used during this study. [26]

Atom	Radius (Å)	Atom	Radius (Å)
H	1.20	Br	1.93
C	1.70	I	1.98
N	1.55	Co^{2+}	0.65
O	1.50	Cl	1.80
S	1.80	F	1.40
Cu^{2+}	0.68		

2.9 Confirming the host:guest ratios using electron counts

The occupancies of the guest, and consequently the host:guest ratios, in the single-crystal structures were determined using the SQUEEZE[27] routine of the software PLATON.[26, 28] SQUEEZE calculates the number of electrons present within the accessible volume. This calculation therefore outputs "the contribution of a (heavily) disordered solvent to the calculated structure factors by back-Fourier transformation of the continuous density found in a masked region of the difference map. The masked region is defined as the solvent accessible region left by the ordered part of the structure."[29] We can therefore identify the guest on the basis of its number of electrons (*e.g.* methanol has 18 e^-), as well as determine the occupancy of the guest by calculating the ratio of the experimental electron count to the expected electron count of the guest molecule(s). These

Stellenbosch University http://scholar.sun.ac.za

calculations are carried out in the triclinic systems and it should be noted that "the number of recovered electrons in the void is strongly dependent on the quality of the low-angle reflections".[29] It is for this reason that the miniature gas cell was designed in order to allow routine (*i.e.* unrestricted) data collection strategies to be used.

The included-guest molecules were deleted from the model prior to running SQUEEZE. The void volume and the electron count, among other values, are written to the "PLATON.sqf" output file. SQUEEZE calculations were carried out for all structures that contain guest molecules situated in both discrete cavities or continuous channels (Chapters 4 and 5).

Stellenbosch University http://scholar.sun.ac.za

2.10 References

[1] Mitegen, 95 Brown Rd - Suite 183, NY 14850, **2004**

[2] SAINT, Version 6.45, Bruker AXS Inc., Madison, WI, **2003**.

[3] SADABS, Version 2.05, Bruker AXS Inc., Madison, WI, **2002**.

[4] R. H. Blessing, *Acta Crystallogr., Sect. A: Found. Crystallogr.* **1995**, *51*, 33.

[5] G. M. Sheldrick, *Acta Crystallogr., Sect. A: Found. Crystallogr.* **2008**, *64*, 112-122.

[6] L. J. Barbour, *J. Supramol. Chem.* **2001**, *1*, 189-191.

[7] V. POV-Ray™ for Windows, Persistence of Vision Raytracer Pty. Ltd., Williamstown, Australia, 2004, http://www.povray.org.

[8] K. Yvon, W. Jeitschko, E. Parthe, *J. Appl. Crystallogr.* **1977**, *10*, 73-74.

[9] D. Orr, *Micromeritics Instrument Corporation*, Georgia, **1062**.

[10] M. A. Spackman, D. Jayatilaka, in *CrystalExplorer Manual*, http://ra.bcs.uwa.edu.au/CrystalExplorer/wiki/index.php/Main.

[11] F. H. Allen, J. E. Davies, J. J. Galloy, O. Johnson, O. Kennard, C. F. Macrae, E. M. Mitchell, G. F. Mitchell, J. M. Smith, D. G. Watson, *J. Chem. Inf. Comput. Sci.* **1991**, *31*.

[12] D. Braga, *Chem. Commun.* **2003**, *2751*.

[13] M. A. Spackman, C. P. G. Byrom, *Phys. Lett* **1997**, *267*, 215-220.

[14] F. L. Hirshfeld, *Theor. Chim. Acta* **1977**, *44* 129-138.

[15] J. J. McKinnon, D. Jayatilaka, M. A. Spackman, *Chem. Commun.* **2007**, 3814-3816.

[16] M. A. Spackman, D. Jayatilaka, *CrystEngComm* **2009**, *11*, 19-32.

[17] T. Jacobs, *Design and Construction of Novel Porous Materials (PhD Thesis), in Department of Chemistry & Polymer Science*, Stellenbosch University, **2007**.

[18] G. O. Lloyd, *Crystal Engineering of Porosity (MSc Thesis), in Department of Chemistry & Polymer Science*, Stellenbosch University, **2006**.

[19] L. J. Barbour, *Chem. Commun.* **2006**, 1163-1168.

[20] F. M. Richards, *Annu. Rev. Biophys. Bioeng.* **1977**, *6*, 151-176.

[21] M. L. Connolly, *Science* **1983**, *221*, 709-713.

[22] M. L. Connolly, *J. Mol. Graphics* **1993**, *11*, 139-143.

[23] M. L. Connolly, *J. Appl. Cryst.* **1983**, *16*, 548-558.

[24] J. L. Atwood, L. J. Barbour, *Cryst. Growth Des.* **2002**, *3*, 3-8.

[25] A. Shrake, J. A. Rupley, *J. Mol. Biol.* , **1973**, *79*, 351-371.

[26] PLATON, Utrecth University, Utrecht, The Netherlands, **2008**.

Stellenbosch University http://scholar.sun.ac.za

[27] P. van der Sluis, A. L. Spek, *Acta Crystallogr., Sect. A: Found. Crystallogr.* **1990**, *46*, 194-201.

[28] A. L. Spek, *J. Appl. Crystallogr.* **2003**, *36*, 7-13.

[29] P. van der Sluis, A. L. Spek, *SQUEEZE Manual* **1990**.

Stellenbosch University http://scholar.sun.ac.za

Chapter 3
Oxacalix[4]arenes

3.1 Introduction

Calix[4]arenes are well known for assuming a bowl-shaped (*i.e.* cone-shaped)[1] molecular conformation when the lower rim comprises hydroxyl functionalities (Figure 3.1(a)). While these hosts were initially synthesised to function as molecular receptors, they have been utilised in many other innovative and exciting applications such as chiral separation, temperature-sensing devices, antioxidants and pressure-sensitive recording materials.[2] In particular, *p-tert*-butylcalix[4]arene (**TBC4**) is a versatile inclusion compound that has been shown to have several guest-induced structural motifs.[3]

Ripmeester[4] showed that a solvent-free structure of **TBC4** can be crystallised from a tetradecane solution. This **TBC4** apohost form crystallises in $P2_1/c$ and the structure consists of a close-packed arrangement of molecules – calix[4]arene molecules interdigitated by each inserting a *tert*-butyl group into the cavity of a neighbouring molecule. Furthermore, a low density polymorph (space group symmetry: $P2_1/n$) of pure **TBC4** can be prepared by sublimation under reduced pressure at 270 °C.[3] Remarkably, the bilayer-type packing motif contains voids each with a volume of approximately 235 $Å^3$. In the structure of **TBC4**, the calixarene molecules that define the cavity are not perfectly eclipsed and potential channels leading to the capsule are blocked by *tert*-butyl groups of adjacent molecules (see Figure 3.1(b)). Regardless of the nonporous nature (*i.e.* lacking conventional channels or pores) of **TBC4**, it has been shown that immersing the $P2_1/n$ crystals in liquid vinyl bromide results in a single-crystal to single-crystal phase transition to an efficiently packed structure (space group symmetry: $P4/n$) that incorporates one molecule of vinyl bromide per **TBC4** cavity. The vinyl bromide **TBC4** inclusion compound is isostructural to the toluene solvate with regard to the host packing arrangement. Further studies revealed that the $P2_1/n$ apohost phase of **TBC4** is porous to small gas molecules such as CO_2, N_2, C_2H_2 and O_2.[5-10] It was later noted that a single-crystal to single-crystal phase transformation (from $P2_1/n$ to $P4/n$) occurs upon exposure to >10 bar of CO_2 pressure.[11] For more details on the developments regarding **TBC4**, a recent review by Dalgarno *et al.* is recommended.[12]

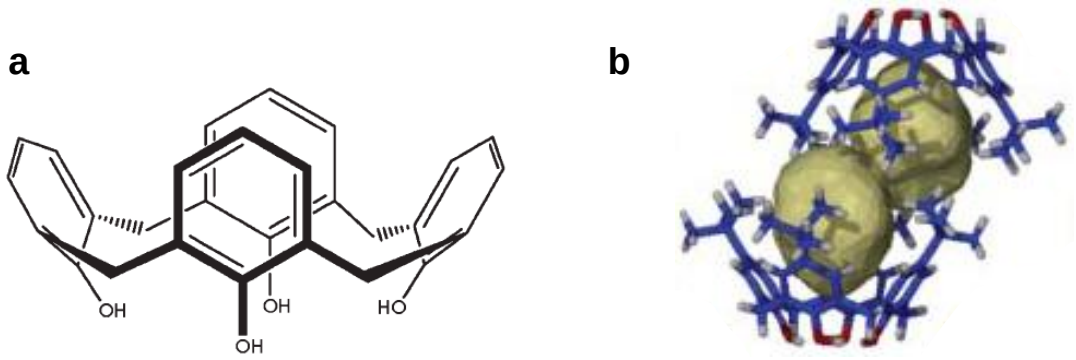

Figure 3.1 (a) Schematic of the bowl-shaped conformation of calix[4]arene. (b) The solvent-accessible capsule formed between two offset facing *tert*-butylcalix[4]arene molecules.[9]

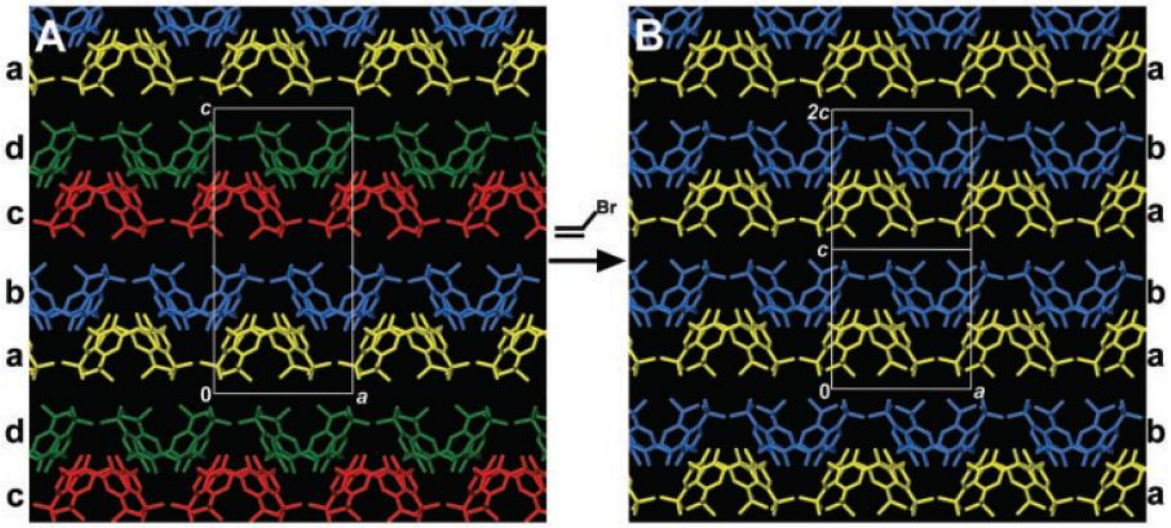

Figure 3.2 Differences in the packing (shown along [010]) that occur upon exposing sublimed crystals of **TBC4** (*i.e.* $P2_1/n$ phase) to vinyl bromide. The two phases have related unit cell parameters and the bilayer arrangements are ab/cd (**A**) and ab/ab (**B**).[13]

Besides the efficient functionalisation of calixarenes at both the endo[14] and exo-positions of the central annulus, heteroaromatic arene units have been incorporated into the calixarene framework, giving rise to a new family of tetrameric macrocycles, namely heterocalix[4]arenes. Since these heteroatoms have different electronic and steric effects to carbon, such a replacement is expected to substantially change the conformational properties (*e.g.* ring sizes and bond angles of the bridging atoms).[15-16] Heterocalix[4]arenes, such as calixpyrroles and calixpyridines have attracted particular interest as supramolecular receptors,[16-17] and have been studied intensively for their unusual conformations[18] and tunable cavities.[19]

On the other hand, heteracalix[4]arenes differ from heterocalix[4]arenes in that, in the former, the methylene linkages are replaced by heteroatoms. Although heteracalix[4]arenes are less common, they possess inherently different properties such as size, conformational preferences and host-guest relationships that might give rise to a new unexplored field of host-guest chemistry. When the linking bridges consist of oxygen, sulfur or nitrogen atoms, they are referred to as oxacalix[4]arenes, thiacalix[4]arenes and azacalix[4]arenes, respectively (Scheme 3.1).[20]

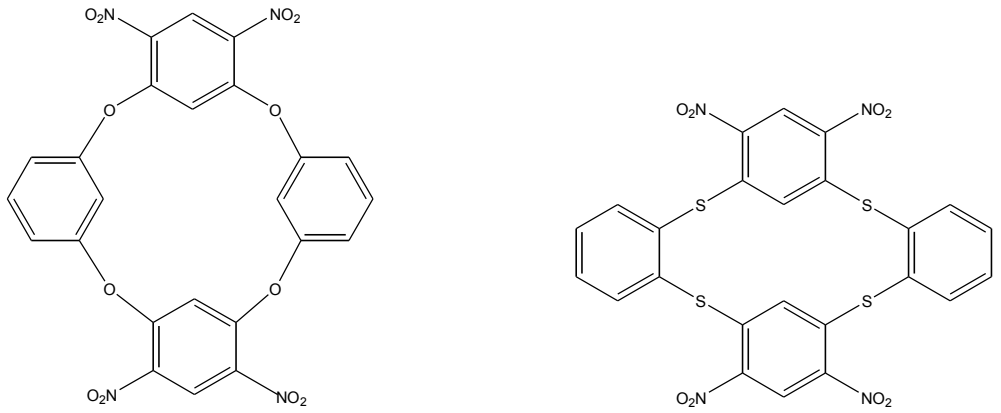

Scheme 3.1 Examples of an oxacalix[4]arenes (**A**) and a thiacalix[4]arenes (**B**).

The history of oxacalix[4]arene macrocycles dates back to 1966 when Sommer and Staab[21] synthesised the first oxacalixarene (**A**, Scheme 3.1) by the single-step reaction of resorcinol and 1,5-dichloro-2,4-dinitrobenzene. Introduction of the *ortho/para*-nitro groups activates the ring for direct nucleophilic aromatic substitution reactions (S_NAr). Hydrogenation and subsequent deamination of **A** afforded the unsubstituted oxacalix[4]arene.[21] More than ten years later Lehmann[22] discovered that the yield of the tetrametric macrocycles such as **A** can be improved by using 1,5-difluoro-2,4-dinitrobenzene instead of the dichloro-derivative as formerly used by Sommer and Staab. The carbon-fluorine bond was found to be more reactive with regard to the S_NAr reaction mechanism.[22]

The structure of **A** was provided by both mass spectrometry and ^{1}H nuclear magnetic resonance (NMR) spectroscopy, though characterisation of these types of compounds was hindered by the low solubility in NMR solvents. The ^{1}H NMR spectra of oxacalix[4]arenes revealed high-field resonances for the intra-annular protons of the electrophilic component (*i.e.* dinitrobenzene moiety), which is attributed to a shielding effect of the neighbouring aromatic rings. This suggests that **A** preferentially adopts a saddle-shaped conformation in

solution. The saddle-shaped conformation is characterised by a distorted 1,3-alternate arrangement of different moieties above and below the central plane defined by the bridging heteroatoms (Figure 3.3). This particular conformation is enforced by maintaining conjugation between the bridging oxygen atoms and the initial electron-poor nitro-bearing aromatic rings. Lehmann speculated that oscillation of the dinitro rings would allow conformational mobility, which is vital when studying porosity and solvent-inclusion complexes.[13]

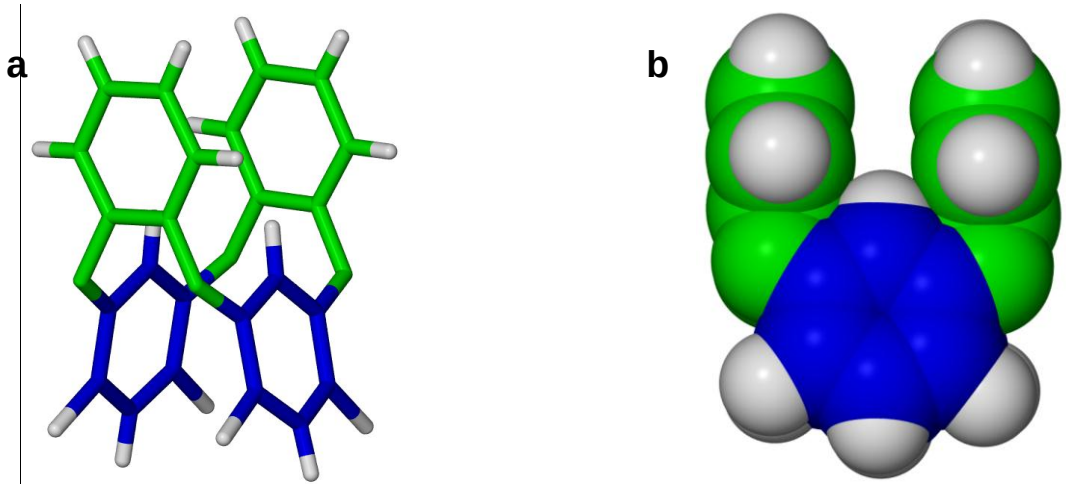

Figure 3.3 The saddle-shaped (1,3-alternate) conformation of oxacalix[4]arenes shown in (a) capped-sticks and (b) space-filling representation. Aromatic rings are shown in green (above) and blue (below) to indicate the positions above or below the mean plane through heteroatom bridges. Hydrogen atoms are shown in CPK colours.

Accurate variable temperature studies (30-150 ºC) of thiacalix[4]arenes (**B,** Figure 3.2) showed no significant changes in the NMR spectra, suggesting considerable rigidity of these ring systems. These thiacalix[4]arenes were first reported in 1981 and also adopt the established saddle-shaped conformation as well as forming stable solvates with dimethylformaide, dimethylsulfoxide and dichlorobenzene in solution.[23] To date, no single-crystal structures have been reported for **B**. Useful information on the stability of these solvates was provided by a careful study of their mass spectra.[23]

In the ensuing three decades heteracalix[4]arenes did not attract much attention, most likely owing to their limited solubility, which hindered the synthesis, purification and characterisation of these compounds. However, recent reports (especially by the groups of Champers,[24] Wang[19] and Katz[25]) showed that this barrier can be overcome, thus expanding the scope of possibilities in heteracalixarene chemistry. Katz *et al.* described several host-guest complexes that were obtained by introducing hydrogen-bond donors into the concave

cavity of the resulting oxacalix[2]arene[2]naphthyridines, although no corresponding apohost (*i.e.* solvent-free) structures were characterised.[26] In general, emphasis has mostly been placed on the synthesis of new oxacalixarenes[25, 27] and reports on solid-state structural studies[28-29] of oxacalix[4]arenes are scarce in any context.

We are interested in studying solid-state structure-property relationships (*e.g.* polymorphism,[30] guest polar ordering,[31] isostructurality, negative thermal expansion[32] and porosity[5-6, 8-10, 13, 33]) of organic materials. This chapter describes the solid-state structure-property relationships of novel oxacalix[4]arenes (Scheme 3.2) produced by structural modification of a known calixarene derivative (**C1**).

As part of the present study, three oxacalix[4]arenes **C1**-**C3** were synthesised. The common feature of these compounds is that the dinitro rings are connected (via the ether linkages) to different aromatic moieties in an alternating fashion (Scheme 3.2). Although **C1** had previously been synthesised, the single-crystal structure was unknown. Our interest in these molecules relates to their "awkward" molecular conformation, which we expected to arrange in a similar manner to the molecules in the porous phase of **TBC4**, resulting in vacant interstitial space. The ether linkages were inserted to facilitate guest inclusion via low energy C–O–C angle flexibility, thus creating an ideal material for the study of permeability to small guests. In particular, we compare the effect of increasing the ring-size (*i.e.* **C1** versus **C3**) and introducing longer arms (*i.e.* **C1** versus **C2**) on the solid-state guest inclusion ability of oxacalix[4]arenes (Scheme 3.2). Additionally, single-crystal X-ray diffraction analysis allows us to compare subtle deviations in the host conformations (not feasible by NMR), as well as to explain the thermal stability of the inclusion compounds on the basis of their associated host-guest interactions.

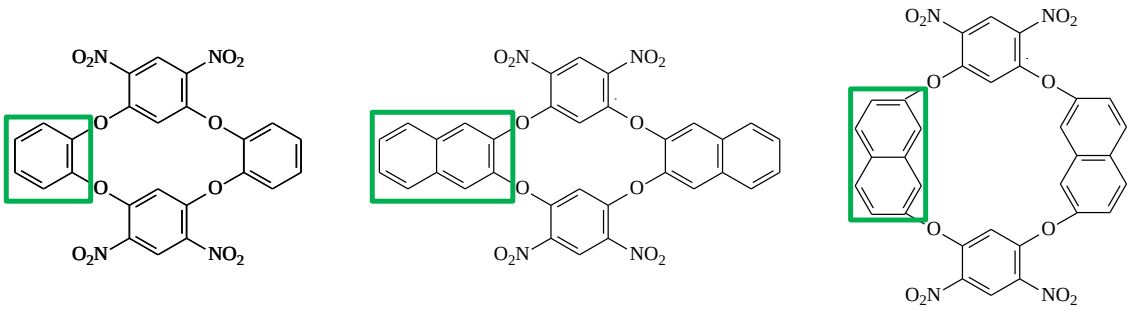

Compound **C1** Compound **C2** Compound **C3**

Scheme 3.2 Schematic diagrams for compounds **C1**-**C3**. The compounds were obtained by using 1,2-dihydroxybenzene (**C1**), 2,3-dihydroxynaphthalene (**C2**) and 2,7-dihydroxynaphthalene (**C3**) as the nucleophilic reaction partners (the "arms" are indicated with a green rectangle in each case). A modified literature procedure was followed.[27]

3.2 Results and discussion

3.2.1 Characterisation by means of single-crystal X-ray diffraction, powder X-ray diffraction and thermal analysis

This section contains detailed structure descriptions of the crystals obtained from studying compounds **C1**-**C3**. Host conformations are discussed and compared with regard to the ∠C–O–C, the dihedral angle between opposite dinitro rings and the dihedral angle between opposite arms (Tables 3.2 and 3.4). In order to investigate the thermal stability of the crystals, thermal analyses were carried out by means of TGA and DSC. In some cases other analyses such as PXRD were carried out to support the thermal stability results. Compounds **C1**-**C3** are discussed in separate sections.

3.2.1.1 Compound C1

In an attempt to obtain the single-crystal structure of the previously reported **C1,** crystals were grown by slow evaporation of a solution prepared by dissolving 20 mg of **C1** in varying amounts of different high boiling solvents. Only high boiling solvents (*e.g.* dimethylformamide, dimethylacetamide, nitrobenzene, N,N-methylpyrridole, *m*-dichlorobenzene and dimethylsulfoxide) were used since compound **C1** is relatively insoluble in the common low-boiling solvents. Crystals suitable for single-crystal X-ray diffraction analysis were obtained from dimethyl sulfoxide (DMSO), dimethyl formamide (DMF), dimethyl acetamide (DMAC), N-methyl pyrrolidone (NMP) and nitrobenzene (NBZ). Identical structures were obtained from several different solvents, even though different crystal morphologies were observed.

Single-crystal X-ray diffraction revealed that the molecular conformation of **C1** (Figure 3.4) is indeed saddle-shaped, as previously characterised by Lehman in solution.[10] Surprisingly, none of the solvents of crystallisation were included in the crystal structures, since several solvate structures have been reported for the thiacalix[4]arene analogue of **C1**.[34]

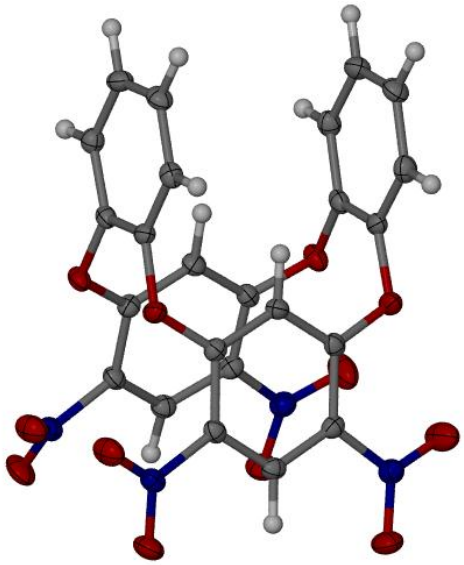

Figure 3.4 The ASU of **C1a**. The thermal ellipsoids are shown with 50% probability.

Careful inspection of the vial containing crystals grown from DMSO revealed three different morphologies: hexagonal prisms (**C1a**), thin plates (**C1b**) and blocks (**C1c**). Single-crystal X-ray diffraction revealed that the block-shaped crystals crystallise in the monoclinic Sohnke space group $P2_1$ while the plate-shaped crystals as well as the hexagonal-shaped crystals crystallise in the centrosymmetric monoclinic space group $P2_1/n$. Structures **C1a (=C1b)** and **C1c** are therefore concomitant polymorphs.[35] The structures of the crystals obtained from DMF, DMA, NMP and NBZ are identical to those of **C1a** and **C1b**. The crystallographic data for **C1a** and **C1c** are summarised in Table 3.1.

In both **C1a** (Figure 3.4) and **C1c** (Figure 3.5), the asymmetric unit (ASU) consists of one complete molecule with the saddle-shaped conformation. The molecules in **C1c** differ slightly in conformation when compared to the molecules in **C1a** (see Figure 3.5 and Table 3.2). Relative to **C1a**, the major conformational differences in **C1c** include an increase in the angle between the dinitrobenzene rings (15.5° in **C1a** and 24.1° in **C1c**) and a decrease in the dihedral angle between the benzenoid arms (3.4° in **C1a** and 1.7° in **C1c**). The different orientations of the nitro groups also contribute to the formation of the different structures (Figures 3.5 and 3.6). The latter factors suggest that **C1a** and **C1c** are conformational polymorphs in addition to being concomitant polymorphs.[35]

As suggested by the different space groups, the molecules in **C1a** and **C1c** assume different packing motifs (Figure 3.6). Molecules in **C1c** are eclipsed, with their nitro groups facing the same direction within a column, and this orientation is reversed in the adjacent columns. The resulting chessboard arrangement of molecules is shown in Figure 3.6(b). The

conformation of **C1** in **C1a** allows considerable interdigitation of the benzenoid arms, resulting in a densely packed structure (Figure 3.6(a)). Interdigitation is facilitated by molecules organised in an offset head-to-tail fashion by alternating face-to-face π···π interactions (centroid···centroid ≈ 4.23(1) and 3.88(3) Å) between benzenoid moieties of neighbouring molecules. It is also important to note that, in both structures, the orientations of the nitro groups are influenced by intermolecular interactions with adjacent molecules.

Differences between **C1a** and **C1c** are also apparent from the fingerprint plots shown in Figure 3.7. Supporting analyses using powder X-ray diffraction illustrates that the bulk material (as-synthesised) is overwhelmingly representative of **C1a**, as shown in Figure 3.8.

Since crystallisation from DMSO afforded only a small number of **C1c** crystals, PXRD and DSC analyses could not be carried out exclusively for this phase, owing to the large sample sizes required for these experiments. Thermal analyses of **C1a** were carried out on the as-synthesised product. The TGA thermogram of **C1a** shows that decomposition occurs above 350 °C. The DSC thermogram of **C1a** shows peaks for a wide temperature range (-60 to 350 °C).

Table 3.1 Crystallographic data for structures **C1a** and **C1c**.

	C1a	**C1c**
Empirical formula	$C_{24}H_{12}N_4O_{12}$	$C_{24}H_{12}N_4O_{12}$
Formula weight	548.38	548.38
Temperature/K	100(2)	173(2)
Wavelength/Å	0.71073	0.71073
Crystal system	monoclinic	monoclinic
Space group	$P2_1/n$	$P2_1$
a /Å	8.9306(7)	10.667(2)
b /Å	12.8384(1)	10.500(2)
c /Å	19.1458(2)	10.820(2)
α /°	90.00	90.00
β /°	101.3410(1)	115.06(3)
γ /°	90.00	90.00
Volume/Å^3	2152.3(3)	1097.8(4)
Z	4	2
Calculated density/g cm^{-3}	1.692	1.659
F_{000}	1120	560
Reflections collected	12419	6071
Independent reflections	4666 [R_{int} = 0.0164]	3214 [R_{int} = 0.0194]
Data/restraints/parameters	4666 / 0 / 361	3214 / 1 / 361
Goodness-of-fit on F^2	1.162	0.854
Final *R* indices [I□>□2σ(I)]	*R*1 = 0.0360, *wR*2 = 0.1329	*R*1 = 0.0299, *wR*2 = 0.0963
R indices (all data)	*R*1 = 0.0416, *wR*2 = 0.1412	*R*1 = 0.0313, *wR*2 = 0.0985

Table 3.2 Selected conformational parameters for **C1a** and **C1c**.

	C1a	**C1c**
Average ∠C–O–C / °	115.47	117.28
Distance between benzenoid arms / Å	4.67	4.63
Dihedral ∠ between dinitrobenzenoid rings / °	15.52 (3)	24.11 (1)
Dihedral ∠ between benzenoid arms / °	3.41 (5)	1.65 (2)

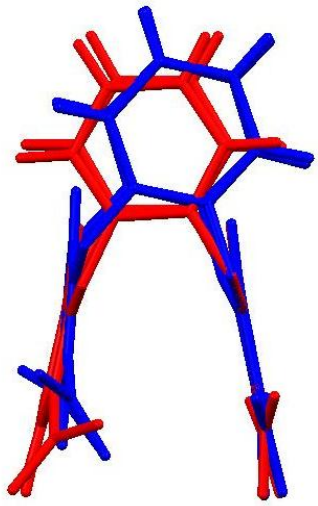

Figure 3.5 Structure overlay of **C1a** and **C1c** showing the differences in conformation between the two phases. The anticipated saddle-shaped conformation of **C1a** is shown in red and the distorted conformation of **C1c** in blue.

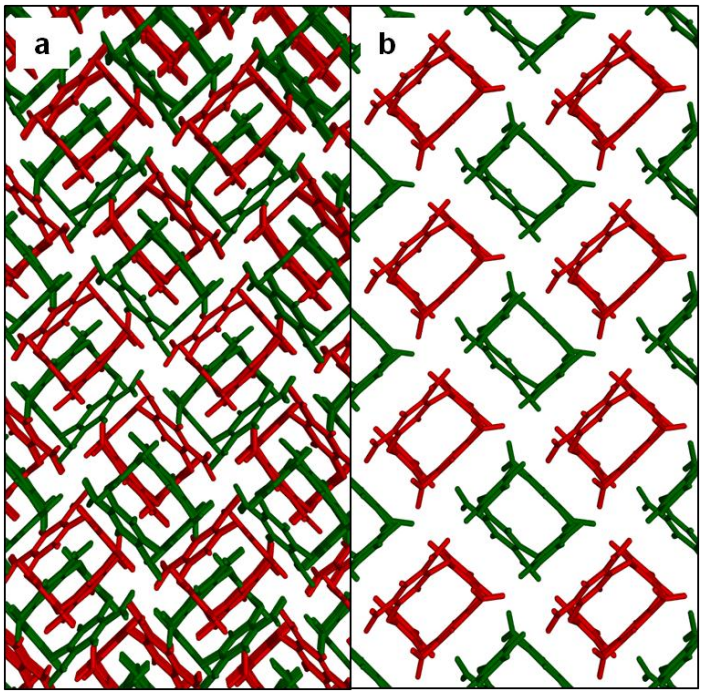

Figure 3.6 Packing motifs in (a) **C1a** and (b) **C1c**. Colours: red, nitro groups directed towards the viewer; green, nitro groups directed away from the viewer.

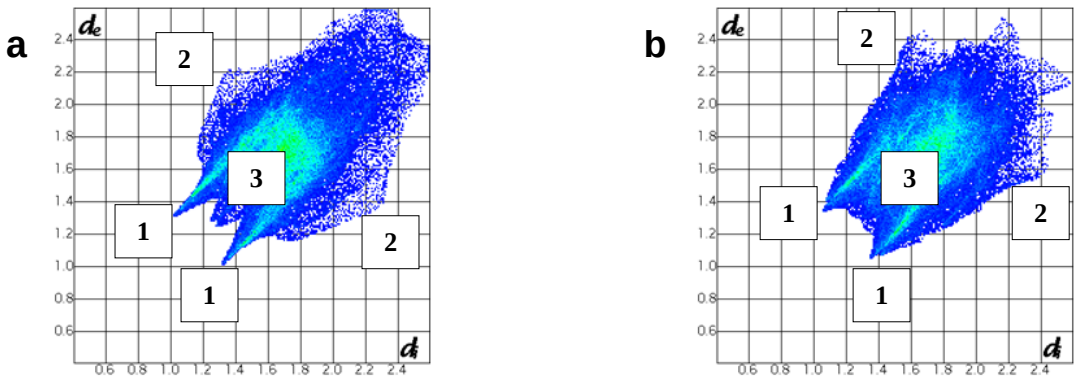

Figure 3.7 Fingerprint plots generated from the Hirshfeld surface by means of CrystalExplorer[36-38], (a) **C1c** and (b) **C1a**. The intermolecular interactions are numbered **1**-**3**. **1**: O···H interactions; **2**: C···H interactions; **3**: H···H interactions.

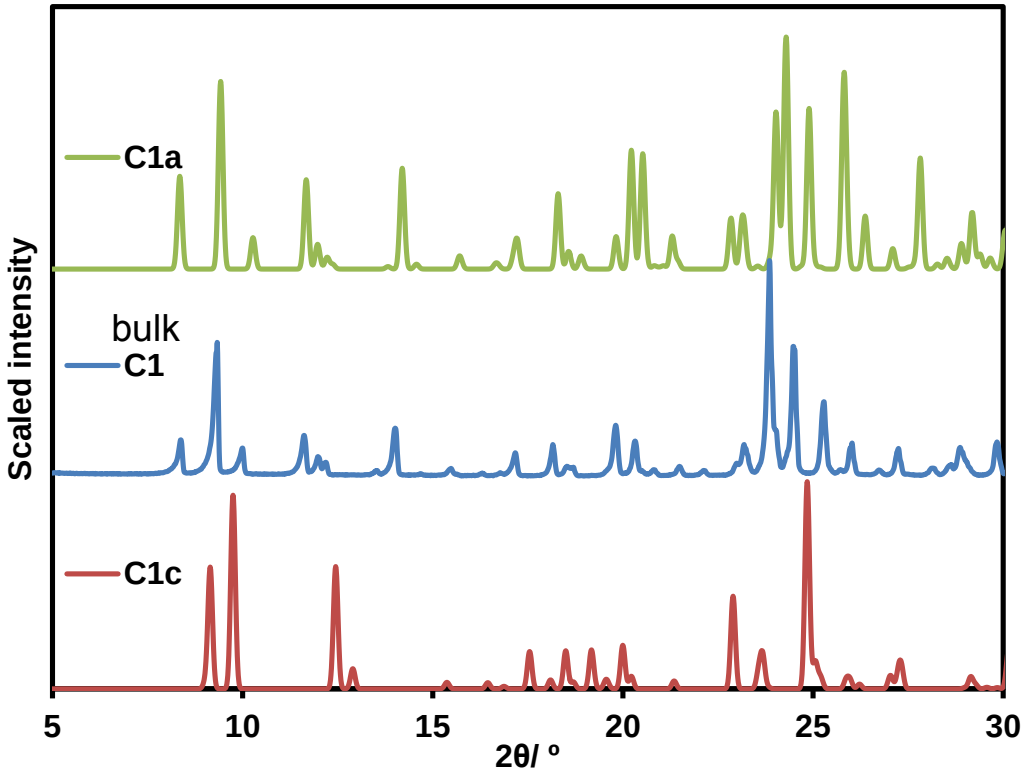

Figure 3.8 The experimental PXRD pattern for the bulk material (blue) and the simulated patterns for **C1a** (green) and **C1c** (red)**.**

3.2.1.2 Compound C2

The next step was to investigate the effect (*e.g.* on host-guest complexation and porosity) of modifying the initial oxacalix[4]arene compound **C1** by increasing the arm length of the nucleophilic reaction partner. Scheme 3.2 shows that the molecular framework of **C2** is

similar to that of **C1**, except that the benzenoid moiety is replaced by a 2,3-naphthalene moiety.

The solubility of **C2** in various high boiling solvents such as DMSO, DMF, NBZ, ethanolamine, diethyl formamide (DEF), DMA, dibutyl formamide (DBF), NMP, ethanol-nitrobenzene was tested. Crystals suitable for SCD were obtained from DMSO (**C2a**), DMF (**C2·DMF**), DMAC (**C2·DMAC**), NMP (**C2·NMP**) and nitrobenzene (**C2·NBZ**). With the exception of the crystal grown from DMSO, solvent molecules are encapsulated by **C2** in all cases. As anticipated, the host adopts a saddle-shaped conformation in each of the complexes. Relative to the apohost **C2a**, significant changes in the molecular geometry of **C2** occur upon solvent complexation. The major differences involve twisting and "opening" of the napthalenyl arms to yield a V-shaped molecular conformation, rather than the C-shape of the apohost. The crystallographic data for structures **C2a** to **C2·NBZ** are listed in Table 3.3.

Although **C2** is a macrocycle, the napthalenyl arms employ the same working principle as molecular tweezers when it encloses a guest molecule.[39] Molecular tweezers (MTs),[40] sometimes referred to as molecular clips, are usually non-cyclic macromolecular complexes with open cavities capable of binding guests. They are of fundamental interest as synthetic receptors in the bioorganic field[41] and have also attracted attention with regard to molecular recognition of anions in solution.[42] In its 1,3-alternate conformation, **C2** has induced flexibility by virtue of low-energy bond angle distortions about the ether linkages.[15] This allows the pincers (*i.e.* the napthalenyl arms) to separate slightly, thus enabling insertion of an appropriately sized guest molecule without significantly altering the packing arrangement relative to that of the apohost.[20]

The apohost structure is essential when studying the properties of molecules that can occlude guest molecules upon crystallisation since the formation and subsequent stabilisation of a solvate depends on the structure of the solvent-free host.[43] Knowing the conformation of the empty host can provide valuable insight when studying other solid-state properties such as polymorphism,[30] porosity[13] and molecular recognition.[17] It is often difficult to prepare solvent-free single crystals when molecules have a strong tendency to crystallise as solvates. Solvent molecules can provide extra stability to the crystal through hydrogen bonding or packing affects.[43-44] Consequently, desolvation under reduced pressure and thermal treatment usually results in structural rearrangement with concomitant loss of single-crystallinity.[45] In many cases the apohost structure can be produced by careful choice of solvent of crystallisation,[46] sublimation,[13] or melt-crystallisation.[30, 47-48] Obtaining the apohost is especially complicated when the host does not sublime or melt, and finding the correct

solvent for crystallising a guest-free structure can then be time consuming and expensive. A systematic study, involving growing crystals from a range of solvents containing varying amounts of **C2**, was carried out over a period of 12 months.

The apohost structure **C2a** was obtained from a saturated solution of **C2** in DMSO. The molecules crystallise in the Sohnke space group $P2_1$ and adopt a distorted saddle-shaped molecular conformation similar to that previously reported for **C1c** and other related molecules.[5] The ASU of **C2a** (Figure 3.9(a) and (b)) consists of one molecule located in a general position, and Z = 2. Although **C2** adopts the 1,3-alternate conformation, the molecule is slightly distorted such that it does not possess precise C_{2v} symmetry. The cofacial napthalenyl arms in **C2a** are eclipsed and inclined towards each other to approximate a C-shape (Figure 3.9(b)); the centroid···centroid distance between the uppermost rings is 4.0 Å and the dihedral angle between their least-squares planes is 12.0° (Table 3.4). The average length for bond A is 1.37 Å and the C-O-C angle is 115.0° in the V-shaped apohost structure. These values are similar to those of **C1a** and are shown in Table 3.2 and 3.4, respectively.

The packing arrangement of **C2a** can be described as a chessboard array of columns running parallel to [101]; the molecules within each column are eclipsed with their nitro groups facing the same direction, and this orientation is reversed in adjacent columns (Figure 3.9(e)). We note that this arrangement also precludes interstitial inclusion of solvent molecules. The powder diffractogram (Figure 3.10) calculated from the SCD structure of **C2a** is consistent with the experimental diffractogram of the as-synthesised phase.

Table 3.3 Crystallographic data for structures **C2a** to **C2·NBZ**.

	C2a	**C2·DMF**	**C2·DMAC**	**C2·NMP**	**C2·NBZ**
Empirical formula	$C_{32}H_{16}N_4O_{12}$	$C_{35}H_{23}N_5O_{13}$	$C_{36}H_{25}N_5O_{13}$	$C_{37}H_{25}N_5O_{13}$	$C_{44}H_{26}N_6O_{16}$
Formula weight	648.49	721.58	735.61	747.62	894.71
Temperature/K	100(2)	100(2)	100(2)	100(2)	100(2)
Wavelength/Å	1.54184	0.71073	0.71073	0.71073	0.71073
Crystal system	monoclinic	monoclinic	monoclinic	monoclinic	triclinic
Space group	$P2_1$	Cc	Cc	Cc	$P\bar{1}$
a /Å	10.8413(4)	11.982(3)	11.918(3)	12.2118(13)	11.6967(1)
b /Å	10.7317(3)	21.272(6)	21.169(5)	21.065(2)	13.1380(1)
c /Å	12.4040(4)	12.948(3)	13.550(3)	13.1639(15)	13.3989(1)
α /°	90	90	90	90	92.2940(1)
β /°	112.033(4)	110.586(3)	110.775(2)	110.508(2)	96.5760(1)
γ /°	90	90	90	90	112.5370(1)
Volume/Å^3	1337.75(8)	3089.6(14)	3196.2(13)	3171.7(6)	1881.4(3)
Z	2	4	4	4	2
Calculated density/g cm^{-3}	1.610	1.551	1.529	1.566	1.579
F_{000}	664	1488	1520	1544	920
Reflections collected	6183	28640	15197	14103	17703
Independent reflections	3567	3521	5622	6960	8090
	[R_{int} = 0.0384]	[R_{int} = 0.0392]	[R_{int} = 0.0323]	[R_{int} = 0.0462]	[R_{int} = 0.0162]
Data/restraints/parameters	3567 / 1 / 433	3521 / 4 / 503	5622 / 13 / 538	6960 / 18 / 557	8090 / 0 / 595
Goodness-of-fit on F^2	0.833	1.061	1.099	1.050	1.029
Final R indices [I□>□2σ(I)]	R1 = 0.0387	R1 = 0.0392	R1 = 0.0526	R1 = 0.0462	R1 = 0.0336
	wR2 = 0.0924	wR2 = 0.1066	wR2 = 0.1573	wR2 = 0.1005	wR2 = 0.0880
R indices (all data)	R1 = 0.0622	R1 = 0.0456	R1 = 0.0537	R1 = 0.0605	R1 = 0.0383
	wR2 = 0.1040	wR2 = 0.1112	wR2 = 0.1582	wR2 = 0.1068	wR2 = 0.0922

Stellenbosch University http://scholar.sun.ac.za

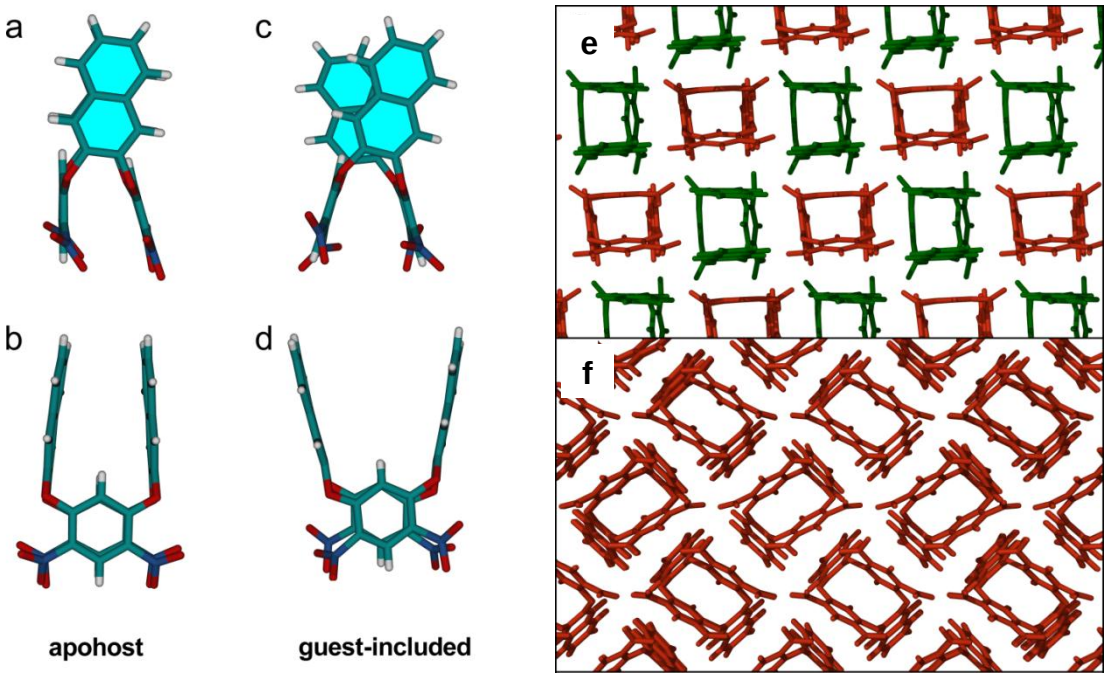

Figure 3.9 (a-d) Perspective views showing the conformations of **C2** in its uncomplexed (a and b) and complexed forms (c and d). The host molecule in (a) and (b) shows the uncomplexed conformation as observed in the apohost phase **C2a**: (a) front view and (b) side view. The molecule in (c) and (d) shows the opened and twisted pincer arms as observed in the DMF solvate phase **C2·DMF**: (c) front view and (d) side view. Packing of the host molecules in **C2a** (e) as viewed along [101] and **C2·DMF** (f) as viewed along [100]. Molecules are shown in capped-stick representation. Colours: red, nitro groups directed towards the viewer; green, nitro groups directed away from the viewer. Guest molecules are omitted for clarity.[39]

Table 3.4 Selected conformational properties of **C2a**, **C2·DMF**, **C2·DMAC**, **C2·NMP**, and **C2·NBZ**.

	C2a	**C2·DMF**	**C2·DMAC**	**C2·NMP**	**C2·NBZ**
Average ∠C–O–C / °	115.00	119.89	118.37	118.43	119.02
Distance between pincer arms / Å [a]	4.00	6.72	6.80	6.69	6.95
Dihedral ∠ between benzenoid rings / °	15.96(4)	45.37(5)	36.39(3)	29.99(3)	31.18(1)
Dihedral ∠ between pincer arms / °	9.59(5)	27.76(3)	29.64(4)	26.78(3)	30.73(1)

[a] Centroid···centroid distance between uppermost rings of the napthalenyl pincers

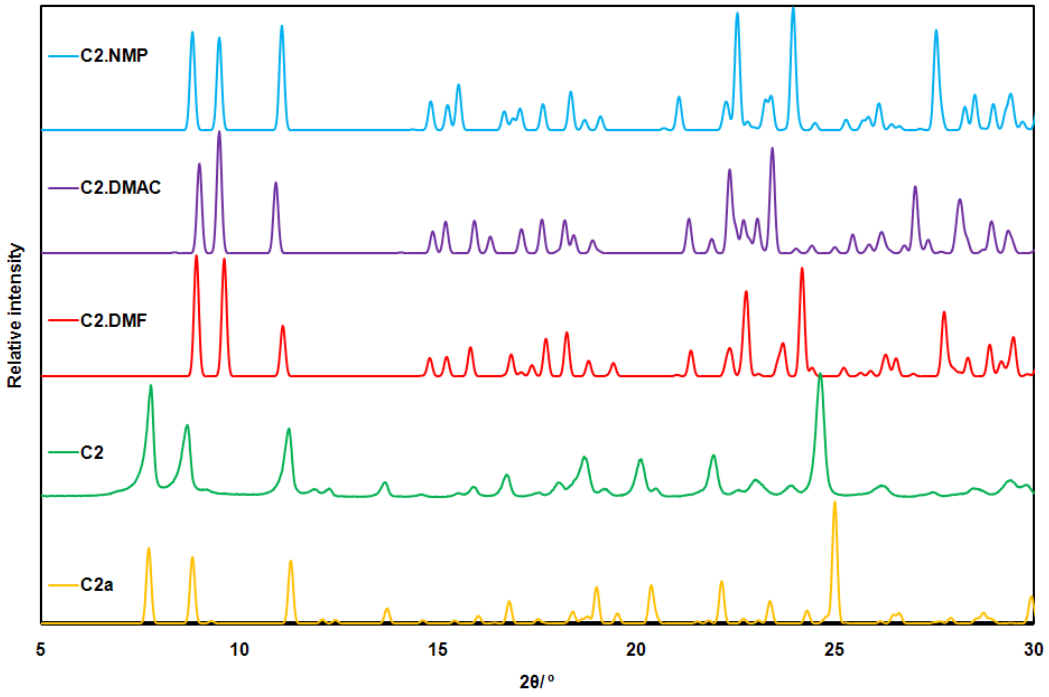

Figure 3.10 Experimental powder diffractogram of as-synthesised **C2** (green) and simulated traces for the apohost phase **C2a** (yellow) crystallised from DMSO and the solvate phases **C2·DMF** (red), **C2·DMAC** (purple) and **C2·NMP** (blue).[39]

The solvate **C2·DMF** crystallises in the polar monoclinic space group *Cc* with Z = 4. The ASU consists of one host as well as a disordered DMF guest molecule, with all molecules located in general positions. Relative to the apohost, significant changes in the molecular geometry of **C2** occur upon solvent complexation. The major differences involve twisting and "opening" of the napthalenyl arms (Figure 3.9(c) and (d)) to yield a V-shaped molecular conformation, rather than the C-shape of the apohost. The symmetry of the host molecule is approximately C_{2v} in its uncomplexed form (*i.e.* in **C2a**), but reduces to C_2 when a planar guest is accommodated between the napthalenyl pincers (Figure 3.9(c)). In order to accommodate the guest in **C2·DMF**, the centroid···centroid distance between the uppermost rings of the pincers increases to 6.7 Å and the dihedral angle between their least-squares planes is 26.1° (Table 3.4). Separation of the pincer groups strains the ether linkages between adjacent rings (C–O–C angles given in Table 3.4), and this causes the molecule to buckle such that the napthalenyl arms can no longer eclipse each other (Figure 3.9 (c)). This results in a C_2 conformation that is inherently chiral, and this phenomenon is observed in all of the solvated structures described here.

Stellenbosch University http://scholar.sun.ac.za

The guest molecule in **C2·DMF** is disordered over two positions (Figure 3.11), but the two sites differ significantly in occupancy (85:15). Both instances of the disordered guest are located between the napthalenyl pincers of the V-shaped host (Figure 3.11). We postulate that the bias in favour of one orientation over the other is due to less favourable van der Waals contacts between the guest in the 15% orientation and the surrounding host molecules.

As observed for **C2a**, the complexes stack in an eclipsed fashion to form an approximately square array of columns (running parallel to [100], see Figure 3.9(f)), except in **C2·DMF** the nitro groups are all oriented in the same direction (*i.e.* polar arrangement of columns). This polar arrangement, along with placement of the guest molecules within the tweezer arms of the host, is shown in Figure 3.12. The guest interacts with the host via a weak bifurcated hydrogen bond between the inner annulus protons of the host and the carbonyl oxygen of DMF ($C_{donor}\cdots O_{acceptor}$ = 3.15(4) and 3.34(4) Å – Table 3.5).

SCD analysis reveals that the yellow crystals obtained from DMAC (**C2·DMAC**) have the same space group as **C2·DMF**, that is *Cc*. Once again the ASU consists of one host molecule and a disordered guest molecule, and Z = 4. Furthermore, the twofold (55:45) disorder of the DMAC guest molecules is similar to that of DMF in **C2·DMF** (Figure 3.11). Moreover, examination of the packing reveals that **C2·DMF** and **C2·DMAC** are isostructural with respect to the arrangement of the host molecules (i.e. isoskeletal[49] and a detailed structure description is therefore not necessary (see Figures 3.11 and 3.12).

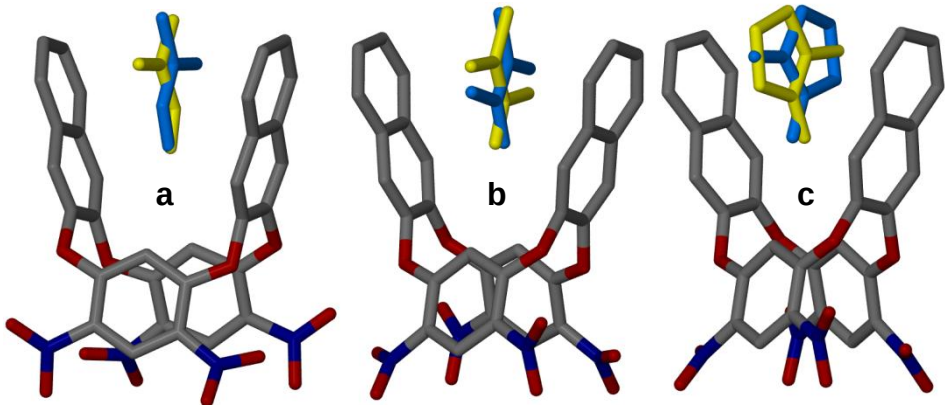

Figure 3.11 Perspective views of the isoskeletal solvates (a) **C2·DMF**, (b) **C2·DMAC** and (c) **C2·NMP** showing the two-fold disorder of the respective guest molecules (situated between the pincer arms). In each case the more favourable position of the guest is shown in yellow and the less favourable orientation in blue. All non-hydrogen atoms are shown in capped-stick representation and all hydrogen atoms are omitted for clarity.

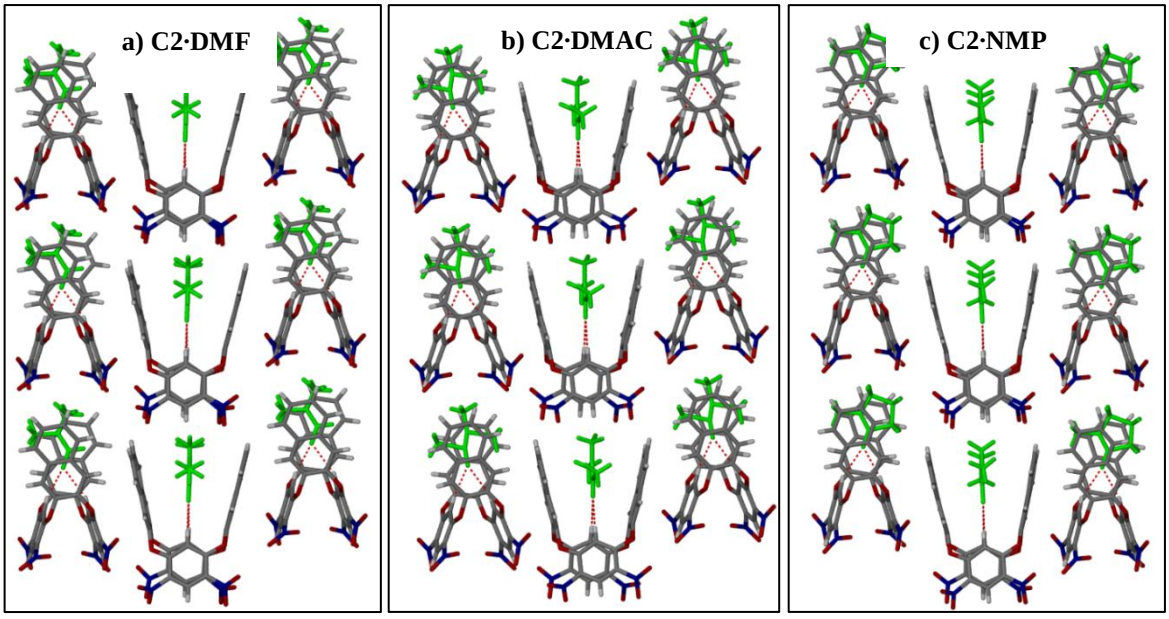

Figure 3.12 (a-c) Capped-stick illustrations of the isoskeletal solvates of **C2** showing the hydrogen bond between the host and the guest in each case. Only one of the possible guest disorder orientations (coloured green) is shown in each case.

Crystals obtained from NMP (**C2·NMP**, space group *Cc*), are also isostructural to **C2·DMF** and **C2·DMAC** with respect to the packing of the host molecules. As observed for DMF in **C2·DMF**, the guest molecule is disordered (Figure 3.11) over two unequally distributed positions (82:18). Owing to the similarities shared with **C2·DMF** and **C2·DMAC**, no further discussion of the packing of **C2·NMP** is necessary (see Figures 3.11 and 3.12).

The solvate **C2·NBZ** crystallises in the centrosymmetric space group $P\bar{1}$ and the host conformation is similar to that of the solvates **C2·DMF** to **C2·NMP**. However, the ASU consists of one host molecule and two NBZ guest molecules – one of the guest molecules is situated between the napthalenyl pincers of the host molecule and the other is situated adjacent to the host molecule.

Packing analysis of **C2·NBZ** shows that neighbouring host molecules arrange in an up-down fashion to create 1D strands that progress parallel to [011]. The chains are stabilised by the formation of slightly offset face-to-face π-π stacking interactions between the napthalenyl pincers of adjacent host molecules. The chains stack to form layers (Figure 3.13) parallel to (1-11); the host molecules in adjacent strands within each layer are arranged in an offset head-to-head or tail-to-tail fashion, and the three dimensional arrangement results in the formation of a 2D network of solvent accessible channels. The two unique guest molecules associate with each other by means of an edge-to-face π-π interaction, with the

Stellenbosch University http://scholar.sun.ac.za

closest $C_{donor}\cdots$centroid distance being 3.5 Å. A bifurcated C-O···H hydrogen bond ($C_{donor}\cdots O_{acceptor}$ = 3.541(2) and 3.468(1) Å – Table 3.5) binds the nitrobenzene molecule tightly inside the void. The remaining nitrobenzene molecule is located between neighbouring chains and is closely associated with the nitrobenzene in the void via an edge-to-face π-π stacking interaction with centroid···centroid ≈ 3.49 Å.

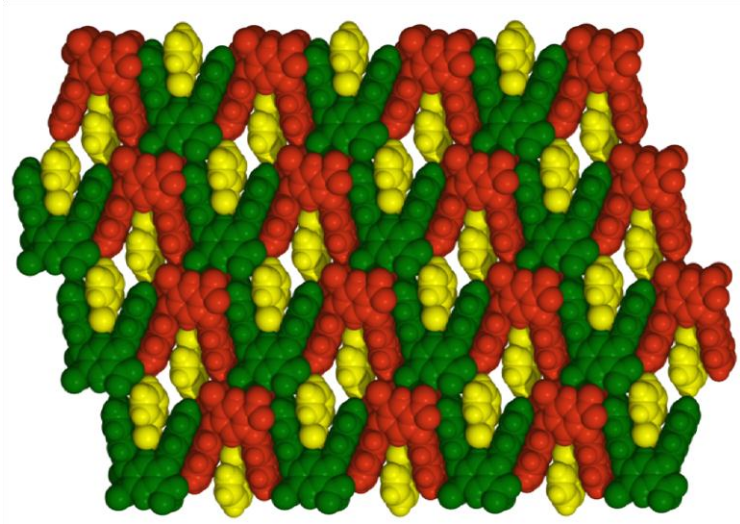

Figure 3.13 Perspective view of **C2·NBZ** showing offset head-to-head and tail-to-tail packing of the host molecules to form layers parallel to (1-11). Colours: red, host nitro groups directed upwards; green, host nitro groups directed downwards; yellow, complexed nitrobenzene guest molecules. Interstitial nitrobenzene guest molecules have been omitted for clarity.[39]

It is interesting to note that crystallisation from DMSO produces an apohost structure while the other solvents yield solvates. It is also noteworthy that, in the cases of DMF, DMAC, NMP and NBZ, the guest molecules are planar and can thus easily be accommodated between the napthalenyl arms of the conformationally flexible host. Owing to the lone pair of electrons on its sulfur atom, DMSO is not planar and therefore not suitable as a guest that can be bound in a tweezer-like fashion.

Stellenbosch University http://scholar.sun.ac.za

Table 3.5 Hydrogen bonding parameters for host-guest interactions in solvates **C2·DMF**, **C2·DMAC** and **C2·NBZ** (we only report donor-acceptor distances since calculated hydrogen positions are not reliable when refined against X-ray data).

	D-H···A	D···A / Å
C2·DMF	C18-H31···O8A	3.340(4)
	C18-H31···O8B	3.358(1)
	C36-H36···O8A	3.315(4)
	C36-H36···O8B	3.221(1)
C2·DMAC	C18-H18···O5A	3.369(6)
	C18-H18···O5B	3.568(8)
	C36-H36···O5A	3.347(6)
	C36-H36···O5B	3.207(8)
C2·NMP	C18-H18···O1A	3.357(4)
	C18-H18···O1B	3.572(16)
	C36-H36···O1A	3.325(4)
	C36-H36···O1B	3.192(1)
C2·NBZ	C18-H18···O1A	3.328(2)
	C36-H36···O1A	3.467(2)

Thermal analyses of **C2a** were carried out using the as-synthesised powder. These measurements shows that the apohost phase is stable within the temperature range -60 to 300 °C and that decomposition of **C2a** occurs above 320 °C. A summary of the thermal stability results for complexes of **C2** is given in Table 3.6. TGA of **C2·DMF** reveals a mass loss of 10.3 weight percent for desolvation, with an onset temperature (T_{on}) of 102.4 ºC. This corresponds to a host to guest ratio of 1:1, which is consistent with the SCD structure **C2·DMF**. DSC shows an endothermic peak at T_{on} = 104.3 ºC as a result of the loss of DMF. The TGA thermogram of **C2·DMAC** shows a single-step desorption event (mass loss = 6.2%), which corresponds to the endotherm at T_{on} = 105.3 °C in the DSC thermogram. Similarly, a desolvation weight loss of 11.3% is observed for **C2·NMP**, corresponding to an endotherm at T_{on} = 146.7 °C. Slow heating of **C2·DMF**, **C2·DMAC** and **C2·NMP** to 100 ºC on a hot-stage microscope consistently afforded a yellow powder, indicating that desolvation does not proceed as a single-crystal to single-crystal process for any of these solvates. Indeed, PXRD analysis confirms that desolvation results in the formation of phase **C2a** in each case. Reversibility of the solid-vapour desorption process was investigated by exposing desorbed

Stellenbosch University http://scholar.sun.ac.za

C2·DMF to **C2·NMP** to their respective solvent vapours. After four weeks no weight gain was observed, and the guest desorption-process thus appears to be irreversible for these systems. The TGA and DSC thermograms for the isoskeletal solvates **C2·DMF** to **C2·NMP** are shown in Figures 3.14 and 3.15.

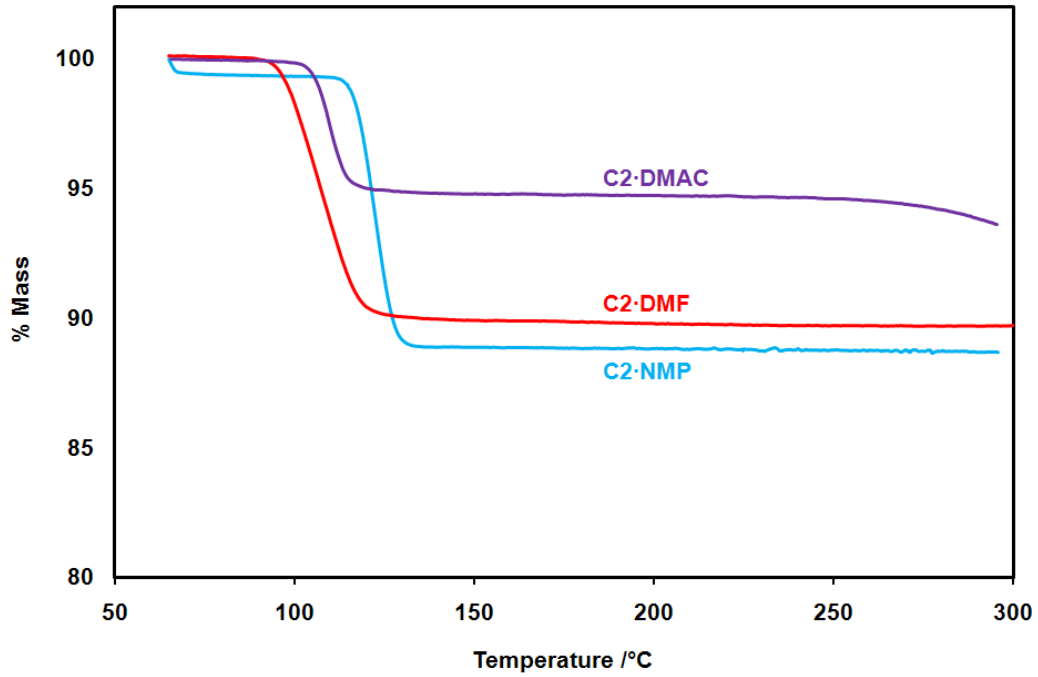

Figure 3.14 TGA thermograms of the isoskeletal solvates **C2·DMF** (red), **C2·DMAC** (purple) and **C2·NMP** (blue) show single solvent loss steps in all three solvates. In each case the mass loss corresponds to a host:guest ratio of 1:1, the guests being DMF (red), DMAC (purple) and NMP (blue), respectively. Decomposition takes place above 300 °C, therefore the abscissa is only plotted to this temperature.

Nitrobenzene is easily removed from **C2·NBZ** and the yellow crystals crack upon gentle heating. TGA reveals a 36.9% weight-loss (Figure 3.18) that can be ascribed to the loss of two molecules of NBZ, corresponding to the 1:2 host:guest ratio observed in the SCD structure. Unlike the DSC thermograms of the isoskeletal solvates **C2·DMF**-**C2·NMP**, that for **C2·NBZ** shows two endothermic peaks (Figure 3.16). Based on supporting PXRD evidence (Figure 3.17) it is reasonable to presume that the peak at T_{on} = 69 ºC corresponds to desolvation of both crystallographically unique NBZ guests, and the second peak (T_{on} = 155 ºC) is due to a temperature-induced phase transformation from an as-yet unknown guest-free phase to apohost phase **C2a**.

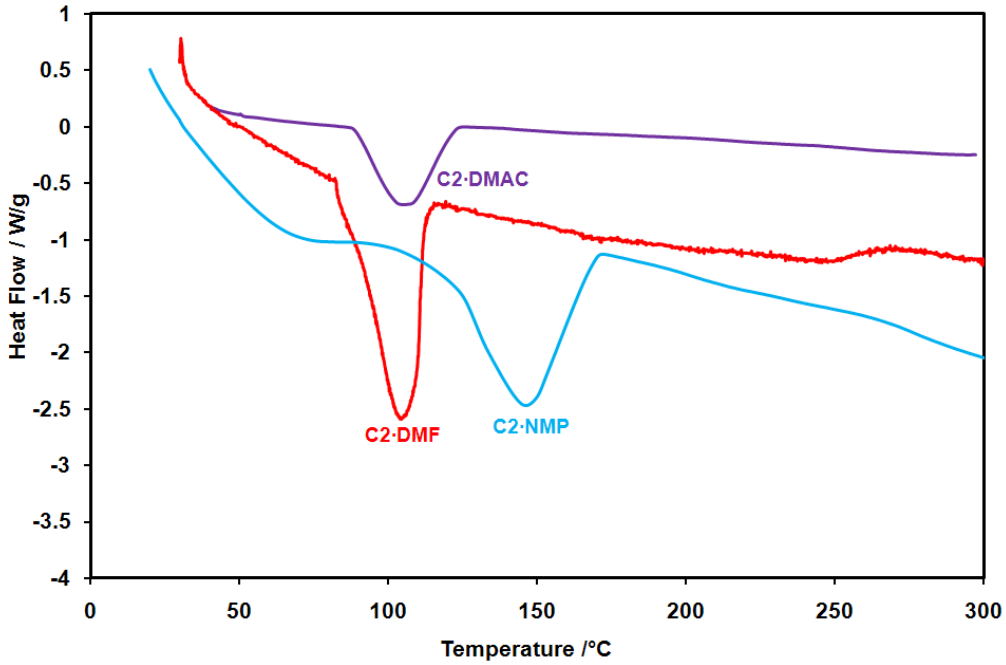

Figure 3.15 DSC thermograms showing the endotherms corresponding to the desolvation of solvates **C2·DMF** (red), **C2·DMAC** (purple) and **C2·NMP** (blue). Onset temperatures (T_{on}) associated with each of the endotherms are listed in Table 3.5.

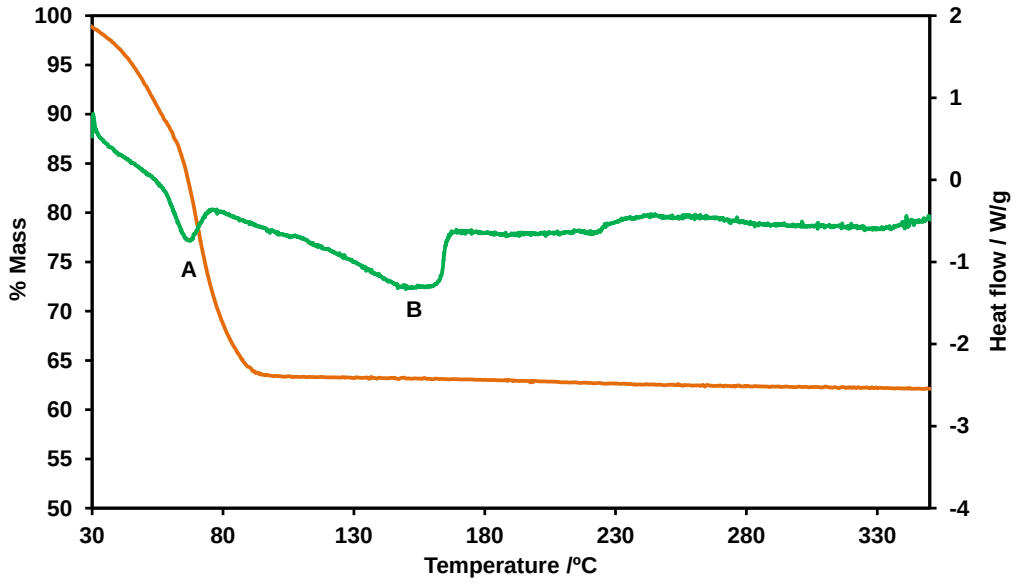

Figure 3.16 TGA and DSC of the NBZ solvate **C2·NBZ**. The 36.9% weight loss between ambient temperature and 90 °C is consistent with the loss of two nitrobenzene molecules per host and corresponds to peak A of the DSC trace. According to variable-temperature PXRD an as-yet unknown guest free phase is formed upon loss of nitrobenzene, and this phase undergoes a polymorphic phase transition to **C2a** upon further heating (peak B). We note that the sample heating conditions were not identical for the two experiments: TGA was carried out with the sample purged with nitrogen gas while DSC was carried out with the sample in a sealed pan.

Stellenbosch University http://scholar.sun.ac.za

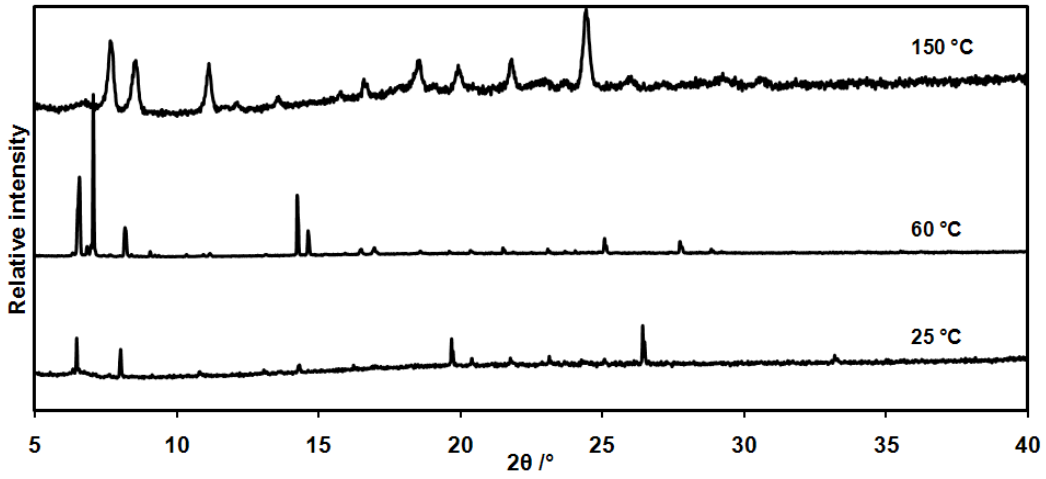

Figure 3.17 Variable temperature PXRD diffractograms of the as-yet unknown apohost phase of **C2a** (60 ºC) and the solvate **C2·NBZ** (25 ºC). Desolvation of both crystallographically unique NBZ guests yields the unknown guest-free phase (150 ºC). Heating the unknown guest-free phase results in apohost phase **C2a**.

Table 3.6 Thermoanalytical data for complexes **C2·DMF** to **C2·NBZ**.

	TGA		DSC
Solvate	**Mass loss / %**	**Host:Guest**	T_{on} **/ ºC**
C2·DMF	10.3	1:1	100.7
C2·DMAC	6.2	1:1	105.3
C2·NMP	11.3	1:1	146.7
C2·NBZ	36.9	1:2	69.8

3.2.1.3 Compound C3

The final stage in the study of the ability of novel oxacalix[4]arenes to form host-guest complexes involved increasing the cavity size by utilising 2,7-napthalenyl moieties. It was initially thought that a solvate would be obtained if these molecules stack one over the other, creating a guest-filled channel along the cavities of the **C3** molecules.

Following the synthesis and characterisation of compound **C3**, complex formation was investigated by means of crystallisation from DMF, DMSO and nitrobenzene. Unfortunately, crystals suitable for SCD were obtained exclusively from DMF, which yielded two different crystal morphologies; blocks (**C3a**) and thin needles (**C3b**). We were unable to collect X-ray diffraction data of the needle-shaped crystals **C3b** since these crystals were

Stellenbosch University http://scholar.sun.ac.za

very thin and did not produce enough high angle reflection data to be able to even determine the unit cell parameters. Figure 3.18 shows that the experimental pattern obtained from the bulk material **C3** is possibly a mixture of the phases represented in **C3a** and **C3b**.

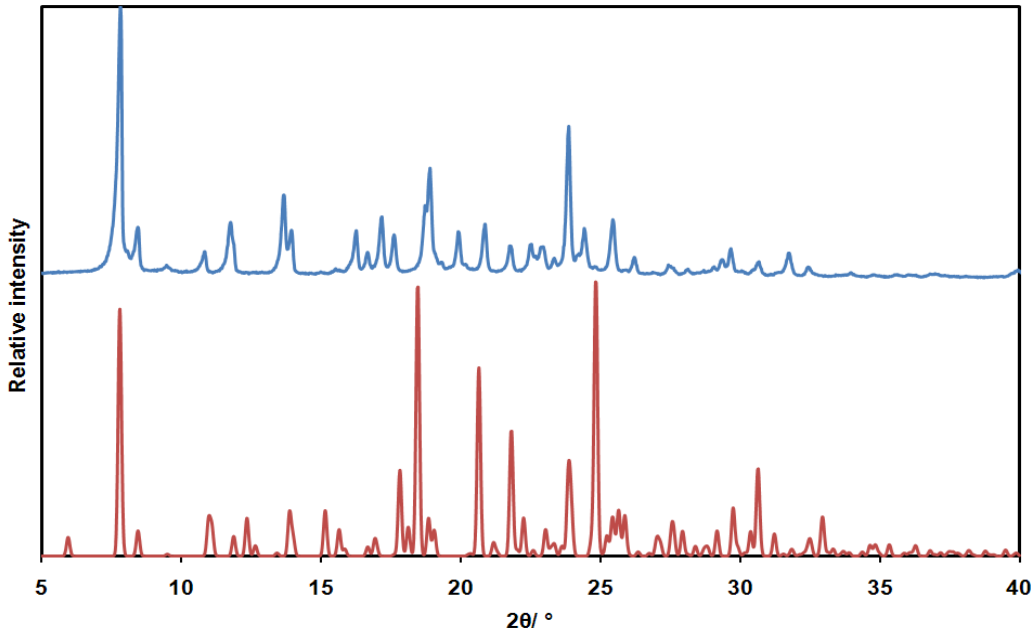

Figure 3.18 Comparison of the calculated diffractogram of **C3a** (blue) and the experimental diffractogram of **C3** (red).

C3a crystallises in the triclinic space group $P\bar{1}$ with two crystallographically unique molecules in the ASU. The two unique molecules differ slightly in their conformations, resulting in the formation of crystallographically different columns (Figure 3.19). Molecules within the same column are associated via face-to-face π-π stacking between benzenoid rings (centroid···centroid ≈ 4.51 and 4.55 Å - Figure 3.19). Furthermore, each column is associated with the adjacent crystallographically different columns via edge-to-face π-π stacking between napthalenyl rings (C_{donor}···centroid ≈ 3.49 Å). Figure 3.20 shows the chessboard arrangement of crystallographically different columns. We note that the 3D packing arrangement of **C3a** also precludes the presence of interstitial solvent molecules.

Stellenbosch University http://scholar.sun.ac.za

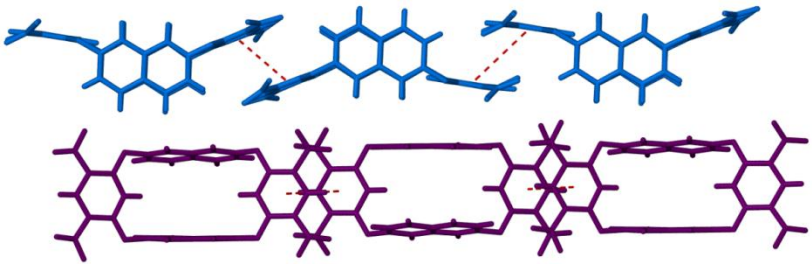

Figure 3.19 Perspective view of the columns in **C3a**. Crystallographically different molecules are shown in blue and purple. The π-π stacking interactions between the benzenoid rings of identical molecules are indicated with dashed lines.

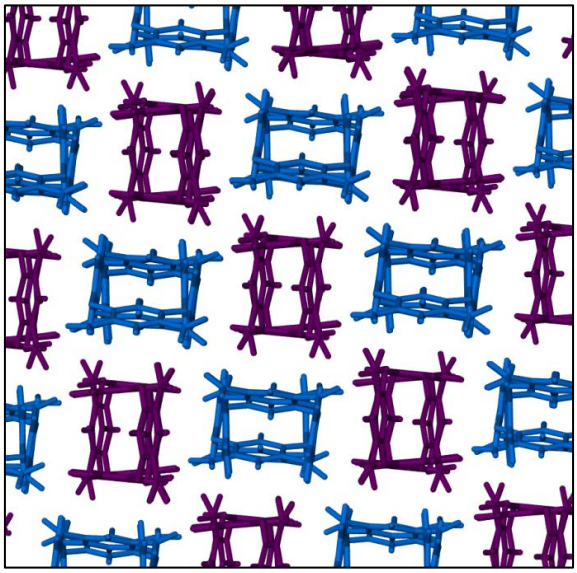

Figure 3.20 A view along the columns in **C3a**, showing the chessboard packing arrangement of the crystallographically different columns (coloured purple and blue).

The overall conformation of the molecules in **C3a** is saddle-shaped with regard to the 1,3-alternate arrangement of the moieties (above and below the central plane defined by the ether linkages). However, the conformation is distorted relative to the conformations in **C1c** and **C2a** since the dinitro-rings are oriented at a dihedral angle ≈ 148.3° in **C3a** compared to 16.0° in **C2a** and 24.1° in **C1c**. Furthermore, **C3a** crystallises without included solvent molecules. This increase in the dihedral angle between the benzenoid rings is facilitated by the eclipsed napthalenyl arms (distance between napthalenyl arms ≈ 4.47 Å)[*], which are orientated at a dihedral angle of 8.52° (Figure 3.21).

[*] Measured as the centroid···centroid distance between naphthalene rings

Stellenbosch University http://scholar.sun.ac.za

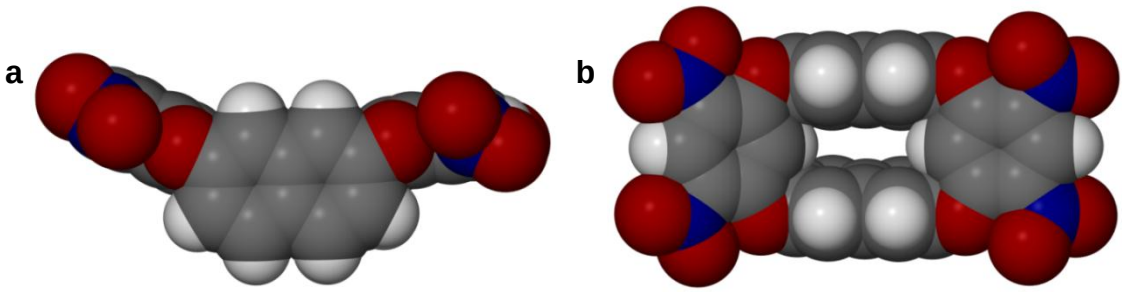

Figure 3.21 Perspective views of the host conformation (in space-filling representation) in **C3a** shown (a) perpendicular to the napthalenyl rings and (b) along the cavity.

Thermal stability studies of **C3a** were carried out on the bulk material, which is overwhelmingly representative of **C3a**. The TGA thermogram of **C3a** shows no significant mass loss (corresponding to desolvation of solvent molecules) prior to decomposition of **C3** above 300 °C (Figure 3.22). The apohost phase **C3a** was found to be stable for the temperature range -60 to 350 °C; there are no endothermic peaks present in the DSC thermogram.

Thermogravimetric studies of **C3b** shows a thermogram similar to that of **C3a** (Figure 3.22). However, unlike the DSC thermogram of **C3a**, the DSC thermogram (Figure 3.22) of **C3b** shows an evident endotherm at approximately 130 °C. This endotherm is thought to be a result of a phase transformation, since solvent molecules do not appear to be present in **C3b**.

Stellenbosch University http://scholar.sun.ac.za

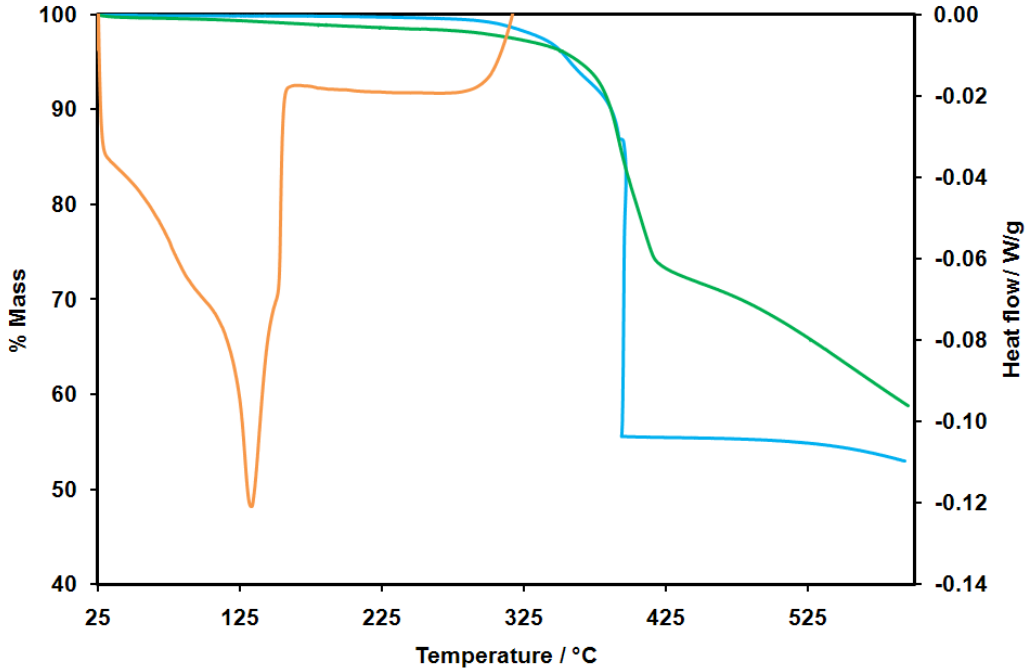

Figure 3.22 TGA and thermograms of **C3a** (blue) and **C3b** (green) and the DSC thermogram of **C3b** (orange). The small mass loss starting at room temperature is attributed to DMF solvent present on the surface of the crystals of **C3b**. The DSC thermogram of **C3b** shows that heating **C3b** results in a phase transformation (endothermic peak at ~ 130 °C).

3.3 General conclusions

Oxacalix[4]arenes are established members of the calixarene family and can more often than not be recognised by their 1,3-alternate (*i.e.* saddle-shaped) conformations. It was initially thought that we can benefit from the "awkwardly-shaped" molecular conformations of oxacalix[4]arenes since they should pack inefficiently in the solid-state, resulting in voids that can be occupied by guest molecules. Moreover, Lehman speculated that oscillation (*i.e.* flexibility induced by the heteroatoms) of the dinitro rings should facilitate guest exchange and/or uptake. Our preliminary aim was to alter one component of a known oxacalix[4]arene[50] **C1** in order to investigate the effect on the complex formation capability. Indeed, the molecular conformation (and consequently the packing of the molecules) was successfully engineered by both increasing the size of the cavity (**C3**) and elongating the arm length of opposite moieties (**C2**) of **C1**. We therefore synthesised three oxacalix[4]arenes **C1**-**C3** (Scheme 3.2). Although we were unable to obtain porous phases of **C1**-**C3**, other interesting structure-property relationships were revealed.

Stellenbosch University http://scholar.sun.ac.za

The synthesis of **C1** was reported elsewhere, but the crystal structure was unknown previously. We report the formation of concomitant conformational polymorphs **C1a** and **C1c** when **C1** is crystallised from DMSO. Both polymorphs comprise molecules in the saddle-shaped conformation, but differ in their packing arrangements.

In the solid state **C2** assumes the 1,3-alternate conformation, allowing it to function as a molecular tweezer by utilising its napthalenyl moieties as pincer arms. An apohost phase **C2a** was crystallised from DMSO and single-crystal X-ray diffraction analysis reveals that the pincer arms are pinched together (*i.e.* C-shaped) rather than interdigitating in its open V-shaped form. The packing arrangement in **C2a** is similar to that of molecules in **C1c**. Solvate crystals of **C2** were obtained from DMF (**C2·DMF**), DMAC (**C2·DMAC**), NMP (**C2·NMP**) and NBZ (**C2·NBZ**) and these were also analysed by means of single-crystal X-ray diffraction. Three of the solvate phases are isoskeletal with a host:guest ratio of 1:1, and with the guest molecules located between the pincer arms. The nitrobenzene solvate has a host:guest ratio of 1:2 – one of the guest molecules is complexed by the pincer arms while the second is situated interstitially. In each of the solvates we observe weak C–H···O bifurcated hydrogen bonds between the host and guest. Although DMSO is capable of participating in a similar host-guest interaction, we suggest that the non-planarity of the guest overrides this consideration.

Single-crystal X-ray diffraction revealed that crystallising **C3** from DMF produces a tightly packed structure without the inclusion of solvent molecules, which is opposite to what we initially proposed. It was shown that increasing the cavity size results in **C3** molecules adopting a more planar saddle-shaped conformation when compared to **C1** and **C2**. In conclusion, we have shown that guest complexation for **C1**-**C3** type compounds in the solid state can be facilitated by elongating the arms, which then operate as pincers to encapsulate the guests.

Stellenbosch University http://scholar.sun.ac.za

3.4 Experimental section: Synthesis and characterisation

3.4.1 Compound C1

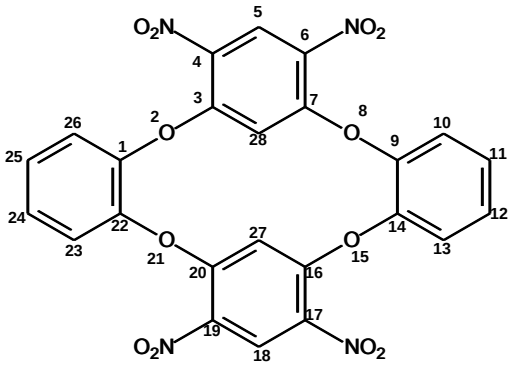

To 2 mmol of catechol dissolved in 20 ml DMF were added 2 mmol (408mg) 1,3-difluoro-4,6-dinitrobenzene and 4.4 mmol (440 mg) triethylamine. The mixture was heated under reflux and after cooling, a few drops of water added. The reaction mixture was kept overnight at 4 °C for precipitation to occur. The resulting precipitate (yellow/white) was purified by washing with methanol and acetone. The pure product was dried for 8 hrs at 100 ºC under vacuum. The crystalline product was characterised by means of NMR, ESI-MS, DSC, TGA, ATR-IR, PXRD and SCD. Crystals were grown by the slow evaporation of solvent by dissolving 20 mg of product in varying amounts of several high boiling solvents. Crystals suitable for SCD were obtained from DMF, DMA, nitrobenzene, NMP and DMSO.

4,6,17,19-Tetranitro-2,8,15,21-tetraoxacalix[2]arene[2]benzene (**C1**) 91% yield M.p.: >350 ºC (dec.); IR (ATR-IR, cm^{-1}): ν_{max} 3093 (sp^2 CH stretch), 1591 and 1351 (C-NO_2), 1284 (C-O stretch), 768 (sp^2 aromatic out of plane stretch); ^{1}H-NMR (DMSO-D_6, 400MHz): δ 5.68 (2H, s, ArH), 7.44-7.60 (8H, ArH), 8.70 (2H, 2, ArH); $^{13}C\{^1H\}$-NMR (DMSO-D_6, 400 MHz): δ 106.2, 125.4, 125.7, 129.2, 131.9, 143.2, 153.2 ppm; MS (ES^+): m/z 583 (M^+ + H_2O), 565 (100%, M^+).

3.4.2 Compound C2

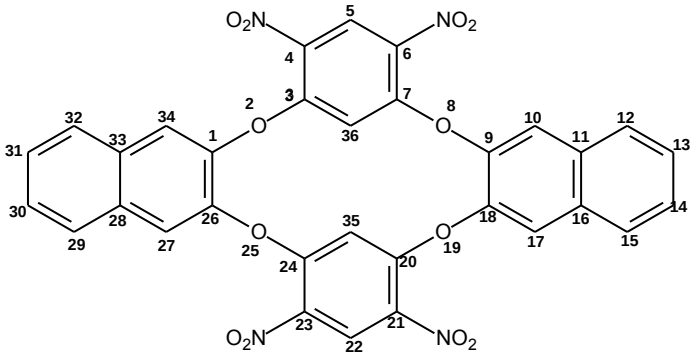

To a solution of 2 mmol (320 mg) 2,3-dihydroxynaphtalene in 20 ml DMF were added 2 mmol (408 mg) 1,3-difluoro-4,6-dinitrobenzene and 4.4 mmol (440 mg) triethylamine. The reaction mixture was then stirred under reflux for 30 min. A few drops

Stellenbosch University http://scholar.sun.ac.za

of water were added after the mixture was allowed to cool to room temperature. Precipitation was achieved by cooling at 4 °C overnight. The resulting precipitate (yellow/white) was be purified by rinsing with methanol and acetone. The pure product was dried for 8 hrs at 100 ºC under vacuum. The crystalline product was characterized by means of NMR, ESI-MS, DSC, TGA, ATR-IR, PXRD and SCD. Crystals were grown by the slow evaporation of solvent by dissolving 20 mg of product in varying amounts of different high boiling solvents. High boiling solvents that were investigated include DMSO, DMF, Nitrobenzene, ethanolamine, DEF, DMA, DBF, NMP, ethanol-nitrobenzene. Crystals of single-crystal analyses quality were obtained from DMSO, DMF, DMA, NMP and NBZ.

4,6,21,23-Tetranitro-2,8,19,25-tetraoxacalix[2]arene[2]naphthalene (**C2**) 82% yield M.p.: >300 ºC (dec.); IR (ATR-IR, cm^{-1}): ν_{max} 3063 (sp^2 CH stretch), 1594 and 1352 (C-NO_2), 1288 (C-O stretch), 837 (sp^2 aromatic out of plane stretch); ^{1}H-NMR (DMSO-D_6, 400MHz): δ 6.03 (2H, s, ArH), 7.48-7.51 (4H, dd, J = Hz, ArH), 7.79-7.81 (4H, dd, J = Hz, ArH), 8.08 (4H, s, ArH), 8.76 (2H, s, ArH); ^{13}C{^{1}H}-NMR (DMSO-D_6, 400 MHz): δ 153.5, 141.29, 132.17, 131.12, 127.62, 127.35, 125.72, 123.22, 106.3 ppm; MS (ES^+): m/z 648, M^+, 666, M^+ + H_2O, 665 (100%, M^+ + OH^-).

3.4.3 Compound C3

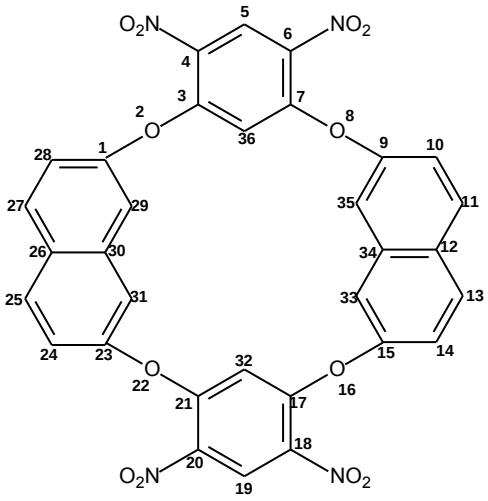

2,7-dihydroxynaphtalene (2 mmol, 320 mg), 1,3-difluoro-4,6-dinitrobenzene (2 mmol, 408 mg) and triethylamine (4.4 mmol, 440 mg) were suspended in 20 ml DMF. The mixture was then stirred (30 min) under reflux. A few drops of water were added to the cooled reaction mixture prior to treatment at a temperature of 4 °C to achieve precipitation. The resulting precipitate (yellow/white) was be purified by washing with methanol and acetone prior to recrystallisation from DMF. The pure product was dried for 8 hrs at 100 ºC under reduced pressure. The crystalline product was characterised by means of NMR, ESI-MS, DSC, TGA, ATR-IR, PXRD and SCD. Crystals were grown by the slow evaporation of solvent by dissolving 20 mg of product in varying amounts of different high boiling solvents. Crystals suitable for SCD were obtained from DMF.

Stellenbosch University http://scholar.sun.ac.za

4,6,18,20-Tetranitro-2,8,16,22-tetraoxacalix[2]arene[2]naphthalene (**C3**) 70% yield M.p.: >320 ºC (dec.); IR (ATR-IR, cm^{-1}): ν_{max} 3063 (sp^2 CH stretch), 1594 and 1352 (C-NO_2), 1288 (C-O stretch), 837 (sp^2 aromatic out of plane stretch); ^{1}H-NMR (DMSO-D_6, 400MHz): δ 6.59 (2H, s, ArH), 7.35 (4H, dd, J = 2.4, 8.9 Hz, ArH), 7.60 (4H, d, J = 2.4 Hz, ArH), 7.98 (4H, d, J = ArH), 9.05 (2H, s, ArH); ^{13}C{^{1}H}-NMR (DMSO-D_6, 400 MHz): δ 110.3, 114.4, 119.6, 125.2, 128.2, 130.9, 134.2, 134.5, 152.9, 154.5 ppm; MS (ES^+): m/z 711, M^+, 693 (100%, M^+).

Stellenbosch University http://scholar.sun.ac.za

3.5 References

[1] C. D. Gutsche, J. F. Stoddart, *Monographs in Supramolecular Chemistry* **1989**.

[2] J. L. Atwood, J. W. Steed, in *Encyclopedia of Supramolecular Chemistry, Vol. 1*, Pergamon, New York, **2004**, 158.

[3] J. L. Atwood, L. J. Barbour, G. O. Lloyd, P. K. Thallapally, *Chem. Commun.* **2004**, 922-923.

[4] E. Brouwer, K. A.Udachin, G. D.Enright, J. Ripmeester, K. J. Ooms, P. A. Halchuk, *Chem.Commun.* **2001**, 565.

[5] P. K. Thallapally, L. Dobrzańska, T. R. Gingrich, T. B. Wirsig, L. J. Barbour, J. L. Atwood, *Angew. Chem. Int. Ed.* **2006**, *45*, 6506-6509.

[6] P. K. Thallapally, G. O. Lloyd, T. B. Wirsig, M. W. Bredenkamp, J. L. Atwood, L. J. Barbour, *Chem. Commun.* **2005**, 5272-5274.

[7] P. K. Thallapally, G. O. Lloyd, J. L. Atwood, L. J. Barbour, *Angew. Chem. Int. Edit.* **2005**, *44*, 3848-3851.

[8] J. L. Atwood, L. J. Barbour, A. Jerga, *Angew. Chem. Int. Ed. Engl.* **2004**, *43*, 2948-2950.

[9] P. K. Thallapally, T. B. Wirsig, L. J. Barbour, J. L. Atwood, *Chem. Commun.* **2005**, 4420-4422.

[10] J. L. Atwood, L. J. Barbour, P. K. Thallapally, T. B. Wirsig, *Chem Commun (Camb)* **2005**, 51-53.

[11] K. A. Udachin, I. L. Moudrakovski, G. D. Enright, C. I. Ratcliffe, J. A. Ripmeester, *Phys. Chem. Chem. Phys.* **2008**, *10*, 4636-4643.

[12] S. J. Dalgarno, P. K. Thallapally, L. J. Barbour, J. L. Atwood, *Chem. Soc. Rev.* **2007**, *36*, 236-245.

[13] J. L. Atwood, L. J. Barbour, A. Jerga, B. L. Schottel, *Science* **2002**, *298*, 1000-1002.

[14] R. K. Juneja, K. D. Robinson, C. P. Johnson, J. L. Atwood, *J. Am. Chem. Soc.* **1993**, *115*, 3818-3819.

[15] Y. Yasukawa, K. Kobayashi, H. Konishi, *Tetrahedron Lett.* **2009**, *50*, 5130-5134.

[16] M.-X. Wang, *Chem. Commun.* **2008**, 4541-4551.

[17] D.-X. Wang, Q.-Y. Zheng, Q.-Q. Wang, M.-X. Wang, *Angew. Chem. Int. Ed.* **2008**, *47*, 7485-7488.

[18] M. V. Baker, M. J. Bosnich, D. H. Brown, L. T. Byrne, V. J. Hesler, B. W. Skelton, A. H. White, C. C. Williams, *J. Org. Chem.* **2004**, *69*, 7640-7652.

Stellenbosch University http://scholar.sun.ac.za

[19] M.-X. Wang, H.-B. Yang, *J. Am. Chem. Soc.* **2004**, *126*, 15412-15422.

[20] W. Sliwa, *Chem. Heterocycl. Compd.* **2004**, *40*, 683-700.

[21] N. Sommer, H. A. Staab, *Tetrahedron Lett.* **1966**, *7*, 2837-2841.

[22] P. A. Lehmann F, *Tetrahedron* **1974**, *30*, 727-733.

[23] K. v. Deuten, W. Hinrichs, T. Weiss, G. Klar, Turpin, Letchworth, ROYAUME-UNI, **1985**.

[24] R. D. Chambers, P. R. Hoskin, A. Khalil, P. Richmond, G. Sandford, D. S. Yufit, J. A. K. Howard, *J. Fluorine Chem.* **2002**, *116*, 19-22.

[25] J. L. Katz, M. B. Feldman, R. R. Conry, *Org. Lett.* **2004**, *7*, 91-94.

[26] J. L. Katz, B. J. Geller, P. D. Foster, *Chem. Commun.* **2007**, 1026-1028.

[27] C. Capici, D. Garozzo, Giuseppe Gattuso, Angela Messina, Anna Notti, Melchiorre F. Parisi, I. Pisagatti, S. Pappalardo, *ARKIVOC* **2009**, *viii* 199-211.

[28] C. Zhang, C. F. Chen, *J. Org. Chem.* **2007**, *72*, 3880-3888.

[29] H. Konishi, T. Mita, Y. Yasukawa, O. Morikawa, K. Kobayashi, *Tetrahedron Lett.* **2008**, *49*, 6831-6834.

[30] D. Das, L. J. Barbour, *J. Am. Chem. Soc.* **2008**, *130*, 14032-14033.

[31] T. Jacobs, M. W. Bredenkamp, P. H. Neethling, E. G. Rohwer, L. J. Barbour, *Chem. Commun.* **2010**, *46*, 8341-8343.

[32] D. Das, T. Jacobs, L. J. Barbour, *Nat. Mater.* **2010**, *9*, 36-39.

[33] J. L. Atwood, L. J. Barbour, A. Jerga, *Science* **2002**, *296*, 2367-2369.

[34] E. E. Boros, C. W. Andrews, A. O. Davis, *J. Org. Chem.* **1996**, *61*, 2553-2555.

[35] J. Bernstein, in *IUCr Monographs on Crystallography*, Oxford Science Publications, **2002**, 2, 74-75.

[36] J. J. McKinnon, D. Jayatilaka, M. A. Spackman, *Chem. Commun.* **2007**, 3814-3816.

[37] M. A. Spackman, D. Jayatilaka, in *CrystalExplorer Manual*, http://ra.bcs.uwa.edu.au/CrystalExplorer/wiki/index.php/Main.

[38] M. A. Spackman, C. P. G. Byrom, *Phys. Lett* **1997**, *267*, 215-220.

[39] A. Kleyn, T. Jacobs, L. J. Barbour, *CrystEngComm* **2011**, *13*, 3175-3180.

[40] C. W. Chen, H. W. Whitlock, *J. Am. Chem. Soc.* **1978**, *100*, 4921-4922.

[41] F.-G. Klarner, B. Kahlert, *Acc. Chem. Res.* **2003**, *36*, 919-932.

[42] J. M. Hermida-Ramon, M. Mandado, M. Sanchez-Lozano, C. M. Estevez, *Phys. Chem. Chem. Phys.*, *12*, 164-169.

Stellenbosch University http://scholar.sun.ac.za

[43] T. Hosokawa, S. Datta, A. R. Sheth, N. R. Brooks, V. G. Young, D. J. W. Grant, *Cryst. Growth Des.* **2004**, *4*, 1195-1201.

[44] S. A. Barnett, D. A. Tocher, M. Vickers, *CrystEngComm* **2006**, *8*, 313-319.

[45] J. L. Atwood, J. E. D. Davies, D. D. MacNicol, F. Vögtle, in *Comprehensive Supramolecular Chemistry*, *Vol. 6* (Ed.: G. A. Jeffrey), Pergamon Press, Oxford, **1996**.

[46] R. Bishop, A. N. M. M. Rahman, J. Ashmore, D. C. Craig, M. L. Scudder, *CrystEngComm* **2002**, *4*, 605-609.

[47] B. Sarma, S. Roy, A. Nangia, *Chem. Commun.* **2006**, 4918-4920.

[48] G. S. McGrady, M. Odlyha, P. D. Prince, J. W. Steed, *CrystEngComm* **2002**, *4*, 271-276.

[49] G. O. Lloyd, J. Alen, M. W. Bredenkamp, E. J. C. de Vries, C. Esterhuysen, L. J. Barbour, *Angew. Chem. Int. Edit.* **2006**, *45*, 5354-5358.

[50] A. Lehmann, *Tetrahedron* **1974**, *30*, 727-733.

Stellenbosch University http://scholar.sun.ac.za

Chapter 4
Design and characterisation of novel metallocycles

4.1 Introduction

The engineering of empty space (*i.e*. porosity) in crystalline solids has become highly topical over the past decade, having applications in gas storage, sensing and separation (*i.e*. selective sorption), as well as molecular recognition.[1] The main impediment to creating new porous materials to function in the abovementioned applications is that molecules generally tend to close-pack such that interstitial voids larger than 25 $Å^3$ do not occur readily. Thus far, microporous zeolites have been exploited as the preeminent porous materials for industrial applications. However, there are numerous disadvantages associated with zeolites.[2-3] Previous strategies for engineering porous crystals have involved preparing solvent-templated structures, and then extracting the solvent molecules without causing the resulting metastable apohost framework to collapse. In most cases removal of the solvent in molecular (*i.e.* zero-dimensional) solids results in reorganisation of the host molecules into a close-packed nonporous phase.[4] A more recent approach is to utilise metal-organic frameworks (MOFs) as porous solids, owing to their characteristic long-range rigidity and consequential structural integrity.[5] MOFs are designed to mimic the natural occurring zeolites[2-3, 6] and generally consist of rigid organic ligands coordinated to transition metal centres (see Chapter 1 for a more elaborate description of MOFs). MOF synthesis allows for tuning of properties in a more versatile way than what is possible for purely inorganic frameworks of conventional porous materials. The two major advantages of using MOFs over zeolites is that interpenetration of frameworks does not occur often, and in most cases, removal of the solvent does not proceed via a phase change to a nonporous phase. Additionally, the existence of inorganic and organic moieties in the structure allows hydrophilic and hydrophobic surfaces to coexist along the pores, which may have some influence on the guest uptake/removal properties. Much effort has also been devoted to designing flexible porous materials that adapt their frameworks to accommodate a guest of specific shape or size (see Chapter 5). For a detailed overview on the developments in MOF chemistry, the recent reviews by Ferèy[7] and Kitagawa[5] should be consulted.

We mainly focus on the self-assembly of transition metals and ditopic imidazole-based ligands[8-13] to form discrete (0D) dinuclear metallocycles. Most of these metallocycles (*i.e.* cyclic hosts) have approximately “doughnut-shaped” molecular conformations, which

prevents them from interdigitating or close-packing in the solid-state. The packing is usually characterised by metallocycles stacking one above the other to form one-dimensional columns. The rigidity of the host permits removal of the solvent molecules (*i.e.* guests) without concomitant transformation to an interdigitated host phase. For a limited number of metallocyclic systems, desolvation occurs without significant loss in single-crystallinity; *i.e.* a single-crystal structure of an empty host (*i.e.* apohost) phase can be characterised. Using analytical techniques such as single-crystal X-ray diffraction, we can obtain valuable information on the host-guest as well as the guest-guest interactions.

As part of our ongoing studies of metallocycles, two analogous $[Ag_2L_2]$ complexes had previously been prepared from equimolar solutions (in acetonitrile) of ligand to Ag^+ salt (see scheme 4.1). [13-14]

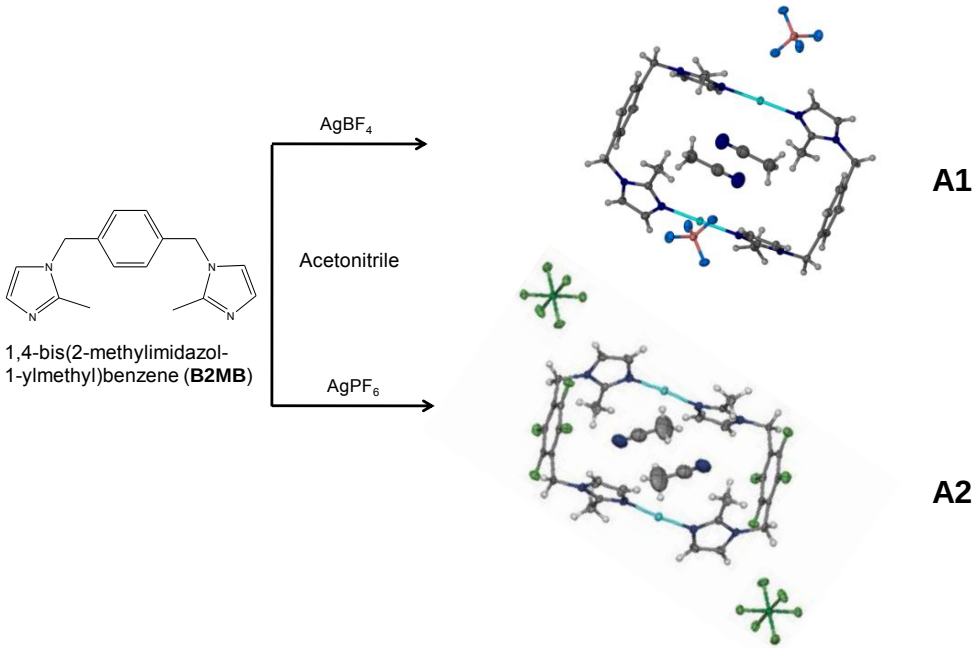

Scheme 4.1 Formation of $[Ag_2(B2MB)_2](BF_4)_2{\cdot}2CH_3CN$ (**A1**) and $[Ag_2(B2MB)_2](PF_6)_2{\cdot}2CH_3CN$ (**A2**).

The overall structures of the metallocycles shown in Scheme 4.1 are similar in that the metallocycles stack in such a way that their apertures align to form continuous solvent-filled channels. Thermogravimetric analysis and single-crystal X-ray diffraction showed that the acetonitrile guests can be released under mild conditions to obtain an apohost phase in both instances. The apohost phases are identical to the solvent-included structures (relating to the host packing). Furthermore, the CO_2 sorption capabilities of the two metallocycles were compared using a gravimetric sorption analyser. Although both materials appear to follow

classical Type I sorption behaviour, **A2** can accommodate more than two CO_2 molecules per host compared to **A1**, which has a maximum capacity of two CO_2 molecules per host in the measured range. Single-crystal structures of these CO_2-included complexes were unknown, owing to the practical challenge that the crystal must be exposed to a constant pressure of the relevant gas at all times during intensity data collection.

In order to test the extent of the permeability of **A2**, single crystals were exposed to a bulkier guest (*e.g.* acetone vapour) and single-crystal X-ray diffraction confirmed the presence of the acetone molecules.

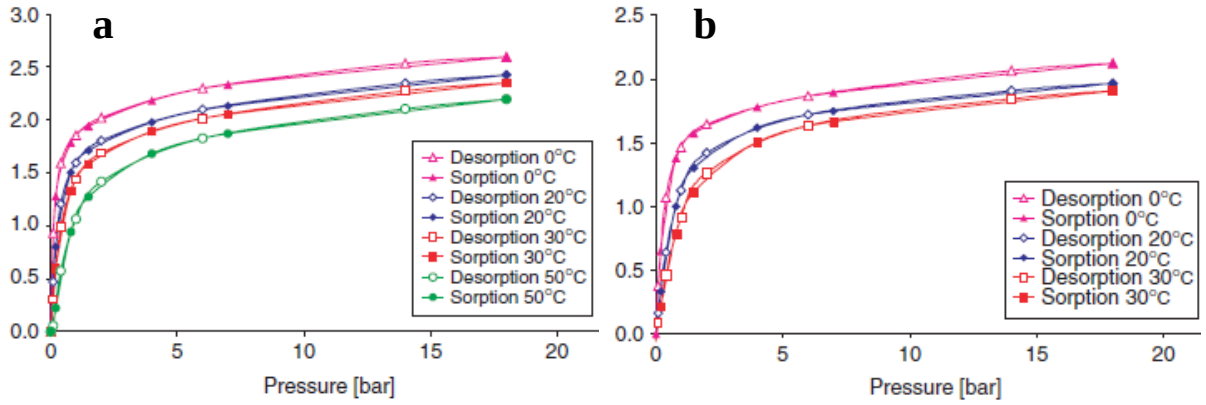

Figure 4.1 Sorption and desorption isotherms for **A2** (a) and **A1** (b). The ordinate indicates the uptake of CO_2 as the molar ratio of guests per host (*i.e.* occupancy).

In order to investigate the structural aspects of solid-gas interactions, an environmental gas cell was developed with the aim of facilitating X-ray intensity data collection under controlled gas pressures. Exploratory gas cell work was initially carried out using a metallocycle similar to **A1**,[15] and was then extended using a $[Cd_2L_2]$ metallocycle – for a more detailed description of this work, the reader may consult the PhD thesis of T. Jacobs.[16]

Jacobs' study[16] was based on the self-assembly of five analogous molecular hexagons from different metal ions and the novel ligand 4,4′-bis(2-methylimidazol-1-ylmethyl)biphenyl (**L** in Scheme 4.2). The reaction of **L** with different cadmium(II) halides yielded three discrete metallocycles $[Cd_2\mathbf{L}_2X_4]\cdot 2CH_3OH$ (X = Cl, Br and I). Removal of the methanol guests occurs without rearrangement of the host molecules (Figure 4.2(a)) and three novel porous

compounds were characterised.

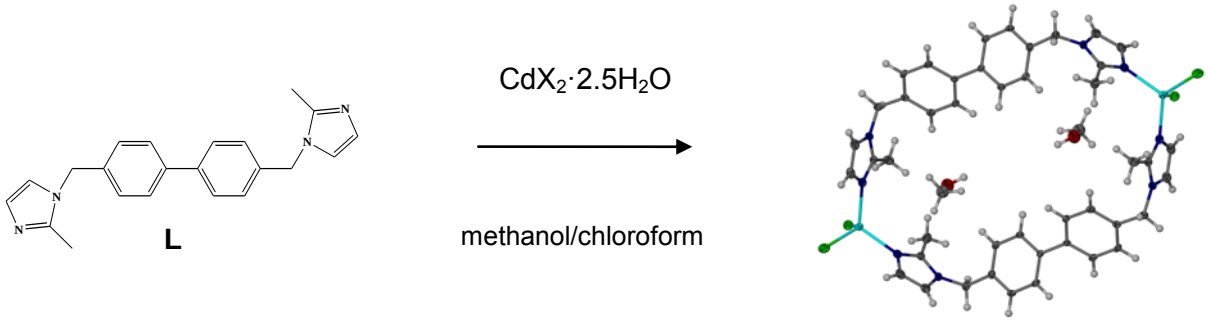

Scheme 4.2 Formation of $[Cd_2L_2X_4]\cdot 2CH_3OH$ (X = Cl, Br and I).[16]

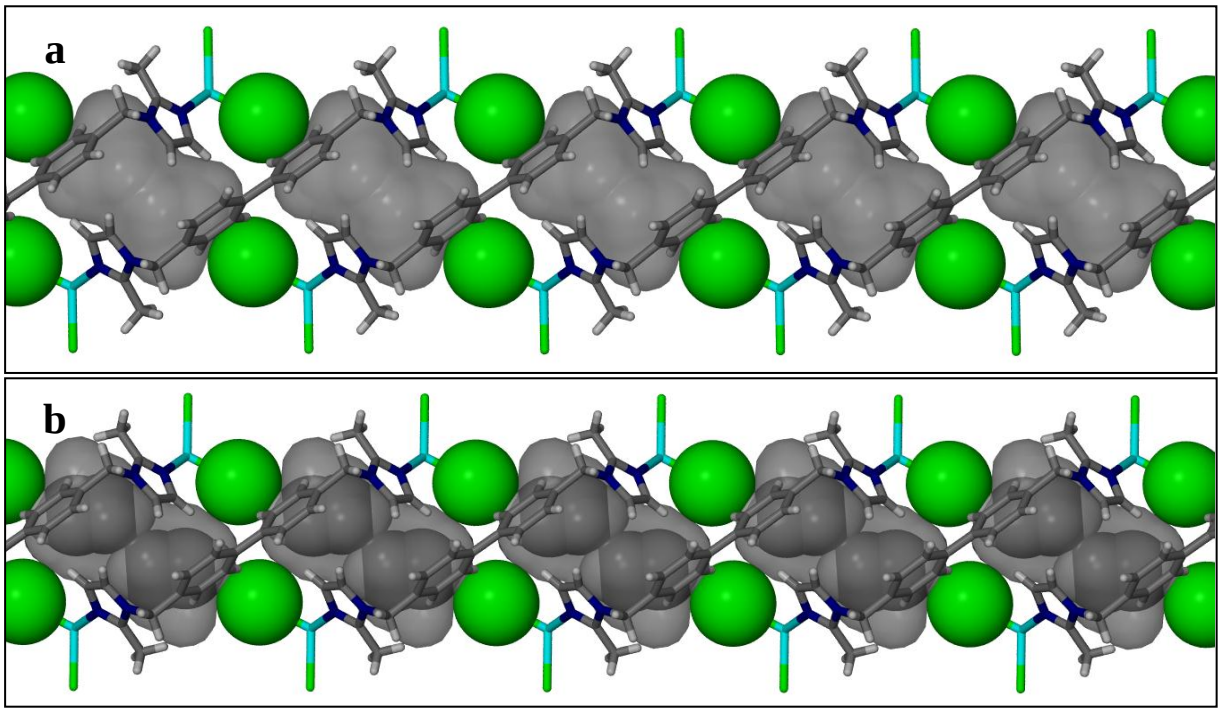

Figure 4.2 Empty voids in $[Cd_2\mathbf{L}_2Cl_4]$ (semi-transparent grey surfaces, volume ≈ 117 Å^3) after removal of the guest molecules (a) – structure determined under vacuum. In situ exposure of the crystals to gas pressure yielded gas-loaded structures – only the C_2H_2 included structure (b), is shown but a similar structure for CO_2 was determined. [16]

It was shown that $[Cd_2\mathbf{L}_2Cl_4]$ is permeable to C_2H_2 (Figure 4.2 (b)) and CO_2; single-crystal structures revealing the positions of the guests were obtained. An acetylene gas sorption isotherm was determined for $[Cd_2\mathbf{L}_2Cl_4]$ using a locally-developed volumetric gas sorption instrument. Gas sorption isotherms for CO_2 were recorded at variable temperatures using a commercial gravimetric gas sorption instrument. Although sorption behaviours of the two investigated gases differ only slightly, the high level of structural detail obtained during

this study allowed rationalisation of these differences in terms of host-guest interactions, as well as packing considerations. A maximum occupancy of two guest molecules per cavity (Figures 4.2 and 4.3) was established in both cases.

It is of further interest that the uptake of gas and diffusion of solvent occurs despite the apparent lack of channels linking the voids: a plausible explanation for this involves the spontaneous formation of short-lived channels as a result of dynamic motion of the framework components. Indeed, the atomic displacement parameters indicate that the Cl^- ions guarding the gates between successive cavities and the imidazole (*Im)* moieties undergo the largest displacement, suggesting a continuous gating process that allows gas molecules to pass through. This proposed mechanism of gas transport was supported by kinetic studies of CO_2 sorption, which suggested a non-activated diffusion model at 1.4 bar gas pressure.[16]

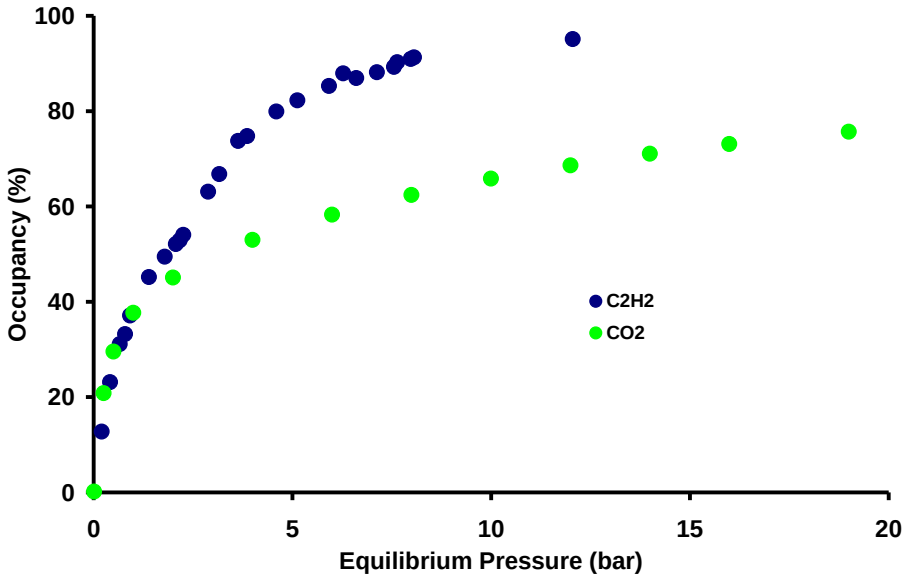

Figure 4.3 The sorption of C_2H_2 and CO_2 by $[Cd_2\mathbf{L}_2Cl_4]$ at 22 ºC (100% occupancy implies two guest molecules per cavity)

The work presented in the next two chapters is an extension of the abovementioned studies. As part of the present study the following seven ligands were synthesised (Scheme 4.3):

- 6,7–bis (imidazole-1-yl-methyl)-quinoxaline (**L1**)[17]
- 1,3-bis-(2-methyl-imidazol-1-ylmethyl)-2-hydroxy-5-methylbenzene (**L2**)[18]
- 2,6-bis-(2-methyl-imidazol-1-ylmethyl)-pyridine (**L3**)[19]
- 2,6-bis-(imidazol-1-ylmethyl)-pyridine (**L4**) [19]

- 1,3-bis-(2-methyl-imidazol-1-ylmethyl)-2,4,6-trimethylbenzene (**L5**)
- 1,3-bis-(imidazol-1-ylmethyl)-2,4,6-trimethylbenzene (**L6**)[20]
- 2,6–bis (imidazole-1-yl-methyl)-naphthalene (**L7**)[21]

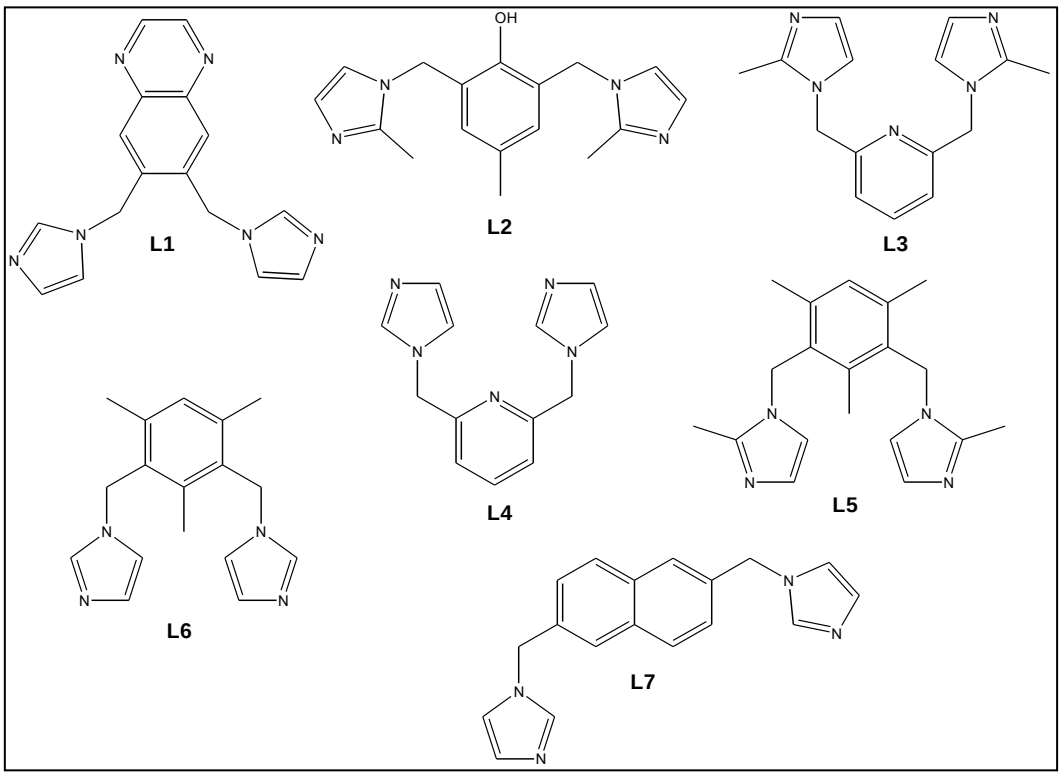

Scheme 4.3 Schematic diagrams of the ligands **L1**-**L7** synthesised during this study.

Although the crystal structures for some of the pure ligands have not been reported as yet, only **L5** is a novel compound. It is further of interest that **L1**-**L7** have not been utilised in the preparation of porous metallocycles. The initiative behind constructing novel porous materials using **L1**-**L7** is the rigidity of the spacer, flexibility of the methylene bridging arms (bearing the imidazole-derived coordinating groups) and the ability of the these groups to coordinate to transition metal salts. Further discussion in the next two chapters will be limited to compounds containing **L3**, **L6** and **L7**, since coordination compounds prepared from **L1**, **L2**, **L4** and **L5** did not yield promising porous materials.

Reaction of the three ligands (**L3**, **L6** and **L7**) with chloride or bromide salts of cobalt(II) and copper(II) (in the appropriate solvent system) resulted in discrete neutral metallocycles that stack to form linear columns parallel to a particular cell axis. As observed for previously reported structures of analogous imidazole-derived coordination compounds, porous metallocycles were obtained when **L3**, **L6** and **L7** assumed an approximate C-shape.

The metallocycles enclose solvent molecules; indeed, the solvent molecules are thought to template the formation of these ring-like structures.[10] Previous studies have shown that the nature of the solvent (*e.g.* molecular shape, size, polarity or chirality) can influence the overall conformation of the complex.[11]

The primary aim of the work described in this chapter was to investigate the guest-exchange ability of discrete metallocycles. Observations regarding the influence on the host conformation when exchanging the included solvent molecule for a guest of different size, shape and chemical nature are discussed, along with the influence of the different host-guest and guest-guest interactions. Finally, the study was extended to incorporate the exchange of acetonitrile for small gaseous guests (I_2, CO_2, vinyl chloride and C_2H_2).

4.2 Results and discussion

4.2.1 Synthesis and characterisation of self-assembled metallocycles

The ligands **L3**, **L6** and **L7** were synthesised using a modified literature procedure.[22] Crystal data for **L3** and **L7** can be found in Section 4.4.1. A series of metallocycles (**M1** – **M5** shown in Scheme 4.4) was prepared via self-assembly of one of the ligands (**L3**, **L6** and **L7**) with a specific metal halide salt. The metallocycles enclose the solvent of crystallisation in all cases. In some instances, the host selectively includes one solvent over the other and in other complexes, a mixture of solvents is included. This section will cover details of the crystallisation and synthetic conditions, in conjunction with characterisation by means of crystal structure determination and thermal stability. It is important to note that **M1**-**M5** signify the metallocyclic host compounds and not the single-crystal structures of the complexes. The single-crystal structures will be denoted by **M1**-**M5**, followed by the mnemonic (Table 4.1) for the encapsulated solvent (*e.g.* **M1·MeCN**). The reader should take note that the synthesis of metallocycle **M5** has previously been reported and further discussion on the characterisation and structure-property relationships of **M5** will ensue in Chapter 5.[23]

Table 4.1 A list of the mnemonics that correspond to the solvents enclosed within the metallocycles.

Mnemonic	Solvent
H_2O	Water
MeOH	Methanol
MeCN	Acetonitrile
Me_2CO	Acetone
DCM	Dichloromethane
$CHCl_3$	Chloroform
CS_2	Carbon Disulfide
BZ	Benzene
Cy	Cyclohexane
Diox	1,4-Dioxane

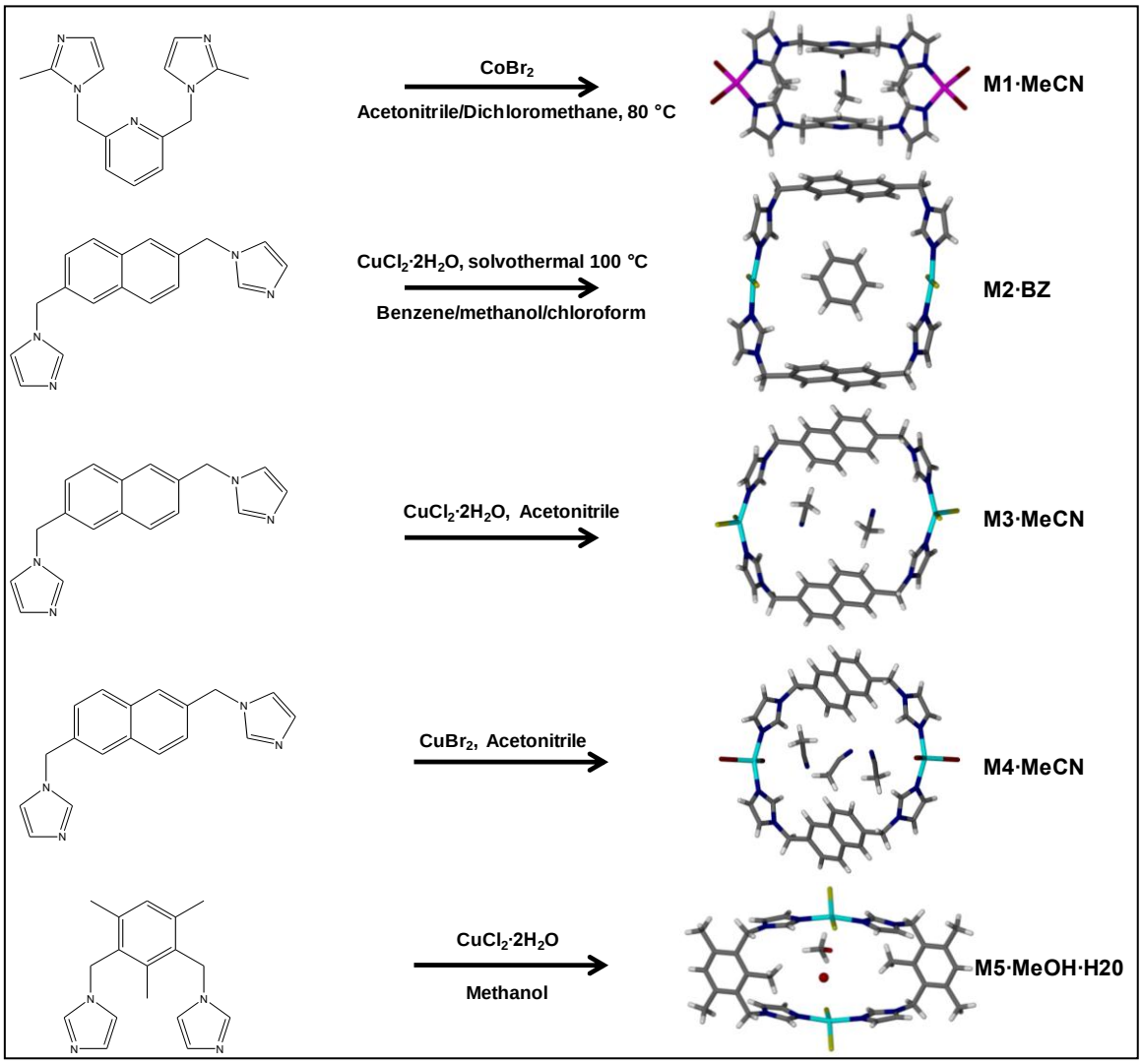

Scheme 4.4 Crystallisation conditions of the five parent compounds discussed in this thesis. Each metallocycle is shown with its corresponding encapsulated solvent, which is thought to template the formation of the cyclic hosts. **M3·MeCN** and **M4·MeCN** are isostructural with respect to the host packing.

Crystals of **M1·MeCN** were prepared using the layering method; dilute equimolar solutions of $CoBr_2$ (in acetonitrile) and **L3** (in dichloromethane) were slowly mixed by diffusion prior to heating the mixture at 80 °C. Blue needle-shaped crystals formed almost immediately upon cooling to room temperature. Structure determination of the crystals revealed a metallocycle in the monoclinic space group *C*2/*m*, with a = 14.482(6) Å, b = 22.703(9) Å, c = 7.084(7) Å, β = 116.46(2)°. It has already been noted that the positions of the four 2-methylimidazole rings relative to the mean plane of the metallocycle can be used to describe the overall conformation of the cyclic molecules.[10] Methyl groups can be directed either up (U) or down (D) with respect to the mean plane of the metallocycle. With reference to the metallocycle in Figure 4.4(a), the groups are assigned by starting with the 2-methyl group in the bottom left corner of the metallocycle, and proceeding clockwise. Using this convention, metallocycle **M1** is assigned the conformation UUDD in **M1·MeCN** (Figure 4.4). The metallocycles form infinite columns along [001]. Each Co^{2+} centre is in a tetrahedrally-distorted square planar coordination environment, allowing the two pyridine moieties of **M1** to interact via a very weak π-π interaction (centroid···centroid ≈ 5.20 Å). Thus, the pyridine rings are eclipsed along [100]. The C-shaped conformation of **L3** forces the methyl groups of the imidazole moieties to point towards the interior of **M1**. These factors contribute to hardly any vacant space being available within the ring of the metallocycle.

The packing arrangement of **M1** is facilitated by a C–H···N hydrogen bond between acetonitrile molecules and the *para*-hydrogen atom of the pyridine ring (C_{donor}··· $N_{acceptor}$ = 3.54(2) Å). Acetonitrile guests are located within a channel, which is enclosed between four infinite columns of stacked **M1** molecules; columns are linked by strong π-π interactions between *Im* rings of neighbouring molecules (centroid···centroid ≈ 3.39 Å).

Although **M1** forms a metallocycle as described above, crystals produced from a solution (kept at room temperature instead of 80 °C) identical to that from which **M1·MeCN** was grown, have a different crystal morphology. These large blocked-shape crystals crystallise in the monoclinic space group $P2_1/c$. In this structure, **L3** assumes a C-shape but precludes formation of a discrete metallocycle, contradicting our initial assumption that metallocycle formation relies exclusively on the shape of the ligand. Instead, a polymeric chain structure **P1** is formed (see Figure 4.5). In **P1**, steric hindrance between 2-methyl-imidazole moieties of neighbouring ligands presumably prevents the π-π stacking interaction (in **M1·MeCN**) between **L3** molecules. **P1** encapsulates dichloromethane molecules that are situated between the one-dimensional strands propagating along [010].

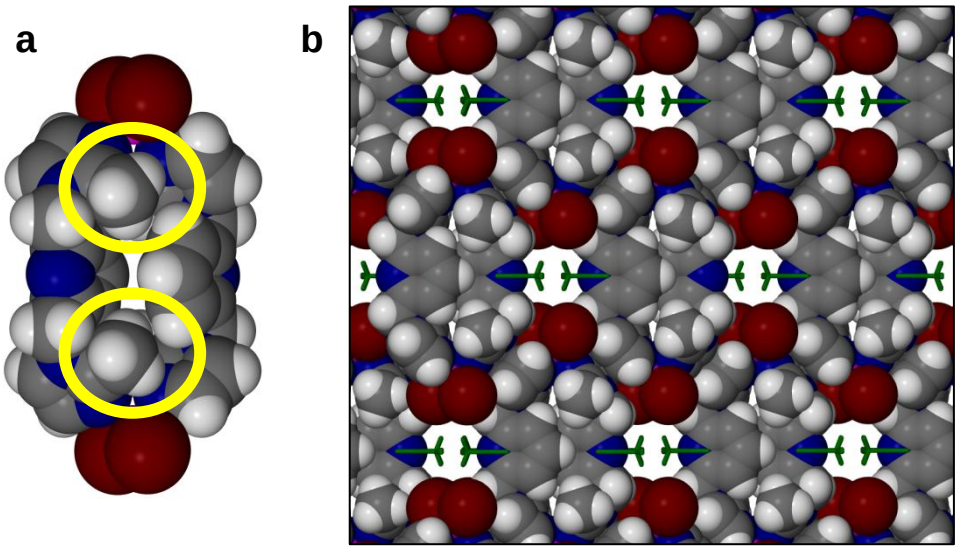

Figure 4.4 (a): Space-filling image showing the UUDD conformation of **M1** and illustrating the restricted space within the metallocycle. The locations of the two "up" methyl groups are indicated with yellow circles. (b): Perspective view of **M1·MeCN** along [001] showing the positions of the acetonitrile guests in the channels; the hosts are shown in space-filled representation and the guests have been coloured green for clarity.

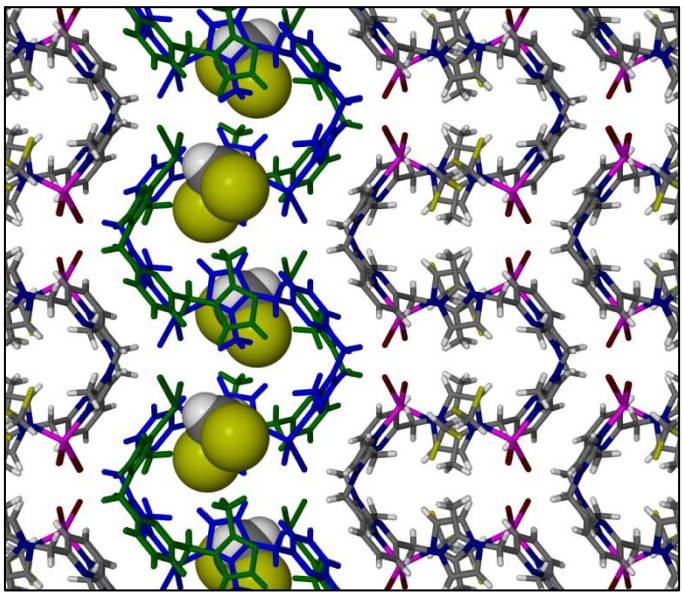

Figure 4.5 A perspective view of the packing motif of **P1** along [001]. The blue strand propagates with the 2-methyl imidazole groups always pointing along [0-10]; the green strand propagates with its 2-methyl imidazole groups pointing along [010]. Dichloromethane guests are disordered over two sites of equal occupancy. Only one of the disordered sites for the guests (in space-filled representation) is displayed within the strands shown in blue and green.

In order to study the removal of the solvent molecules from the host structure, **M1·MeCN** was subjected to thermal analysis. TGA shows that desolvation of the acetonitrile

guests occurs readily, starting at room temperature (Figure 4.6). The host:guest ratio was deduced by determining the percentage mass loss as a result of desolvation (4.4% mass loss ≈ 1 guest per metallocycle). DSC measurements on **M1·MeCN** reveal an endotherm with an onset temperature of 76.9 °C; this coincides with the desolvation of the guest. It appears that guest release occurs with a concomitant phase change to a nonporous (i.e. close-packed) structure, a process that is most likely facilitated by host distortion. This phase transformation was investigated by means of powder X-ray diffraction on the as-synthesised (guest-included) phase, which confirmed that the bulk material is representative of the single-crystal structure **M1·MeCN**. As anticipated, a different phase was obtained upon heating **M1·MeCN** to 150 °C. In an attempt to reproduce the phase in **M1·MeCN**, the high temperature phase was immersed in 2 mL acetonitrile for several minutes before recording another powder diffractogram. Indeed, the **M1** phase is reproduced upon uptake of acetonitrile (see Figure 4.8), but other solvents such as methanol and acetone could not induce reversion to a host phase similar to that observed for **M1·MeCN**. It appears that methanol and acetone are not sorbed. This is consistent with our initial statement that the acetonitrile guest is a key factor for stabilising the arrangement of metallocycles in **M1·MeCN** through C–H···N hydrogen bonds. To determine whether desorption of **M1·MeCN** can proceed as a single-crystal to single-crystal transformation, selected crystals of **M1·MeCN** were heated at 80 °C for 48 hours. Inspection (*e.g.* using a microscope) of the outward appearance of the crystals revealed that they crack and break apart upon heating. A single-crystal structure could therefore not be determined and, owing to peak broadening and a lack of peak intensity in the powder diffractogram, the structure of the high temperature phase could not be deduced by powder X-ray diffraction.

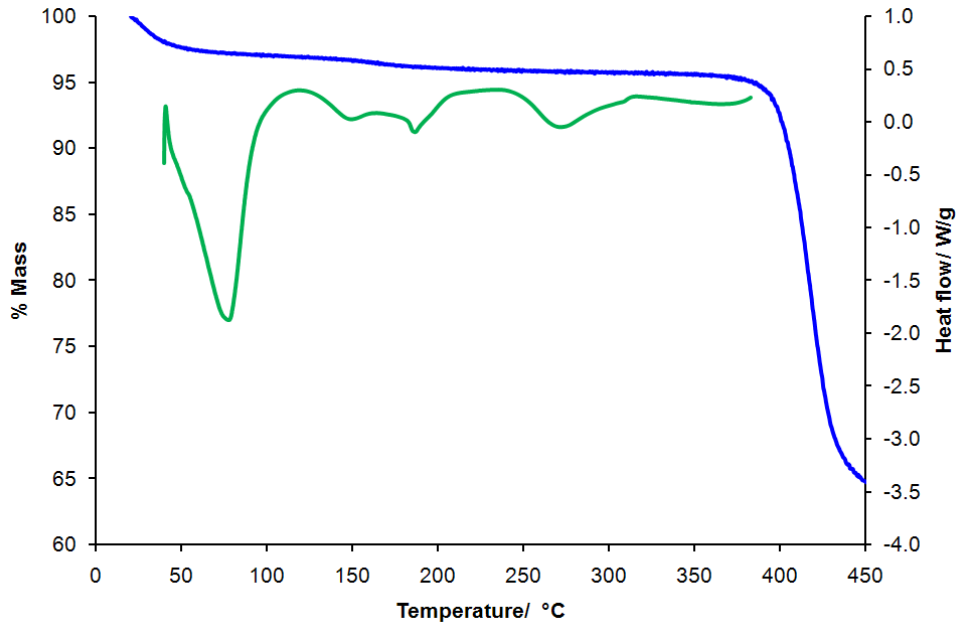

Figure 4.6 Thermogravimetric analysis (blue) for **M1·MeCN** indicates that desolvation of the acetonitrile guests starts at room temperature. The DSC thermogram (green) of **M1·MeCN**, showing that guest release between 60 and 80 °C occurs with a concomitant phase change. Decomposition of the host takes place above 400 °C.

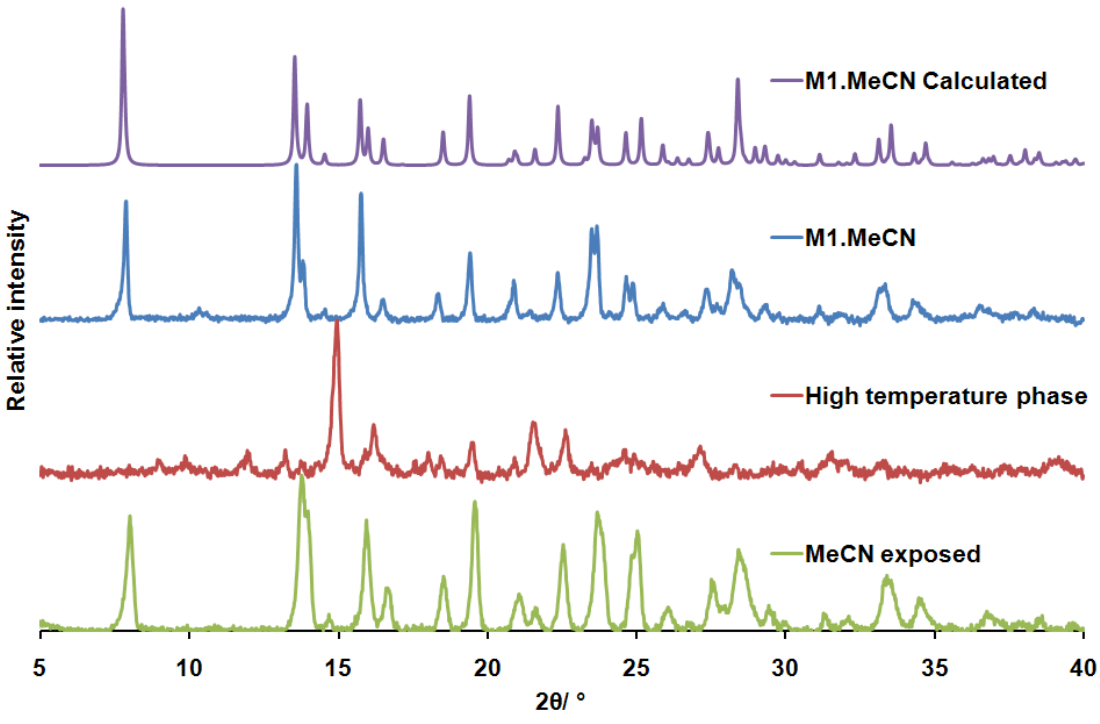

Figure 4.7 Diffractograms of **M1·MeCN**, as well as, the high temperature phase of **M1** both before and after exposure to acetonitrile. The calculated diffractogram for **M1·MeCN** is also depicted.

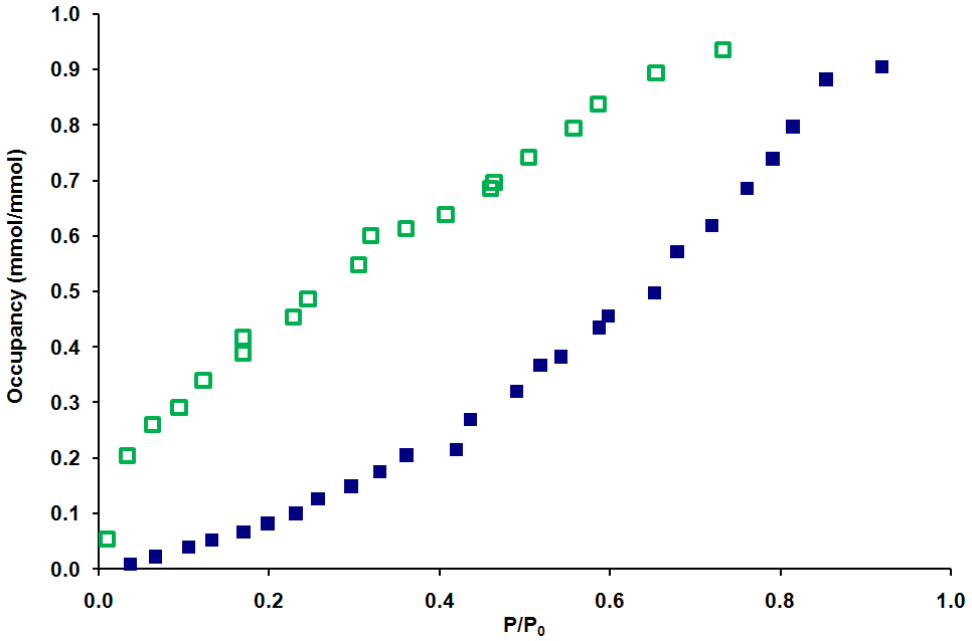

Figure 4.8 The acetonitrile sorption (solid blue squares) and desorption (open green squares) isotherms of **M1**. A maximum occupancy of one is reached at $P/P_0 = 1$. The desorption profile shows hysteresis.

Solvothermal treatment of **L7** (in benzene/chloroform) and $CuCl_2{\cdot}2H_2O$ (in methanol) produced green plate-shaped single crystals; space group $P2_1/c$ (a = 13.179(5) Å, b = 14.609(5) Å, c = 10.590(5) Å, β = 97.517(1)°). The ASU consists of half a host and half a benzene guest. The coordinated groups in **M2·BZ** are arranged in a distorted square-planar fashion around the Cu^{2+} centre. The approximate square molecular shape favours π···π stacking (centroid···centroid ≈ 4.07 Å) between neighbouring metallocycles. When viewed along [001], metallocycles pack to form brick-wall type layers. These layers overlap such that the space within the ring (occupied by benzene guests) is blocked off by adjacent layers and no continuous channels are present in **M2·BZ** (Figure 4.9(a)). Mapping the solvent-accessible space reveals that the benzene guests are located within discrete pockets, each formed between four adjacent metallocycles. Location of the benzene guest within the ring is influenced by two primary host-guest interactions; C–H···Cl hydrogen bonds ($C_{donor}\cdots Cl_{acceptor}$ = 3.980(1) Å), and C–H···π contacts (C_{donor}···centroid ≈ 4.18 Å). Thermoanalytical measurements for **M2·BZ** were not carried out owing to a lack of sufficient quantities of sample. Attempts at removing the benzene guest (*e.g.* heating **M2·BZ** at 150 °C or exchanging benzene for acetone) were unsuccessful. The contributions of the strong host-guest interactions are a plausible reason for the stability of **M2·BZ** and additional experiments were not carried out.

Interestingly, layering of **L7** (in benzene/chloroform) and $CuCl_2 \cdot 2H_2O$ (in methanol) produced yellow block-shaped crystals after several days. Single-crystal X-ray diffraction revealed that these crystals (**M3·Mix**) are crystallographically different from the green crystals of **M2·BZ**. Structure elucidation revealed a "doughnut"-shaped metallocycle **M3**. This complex crystallises in *C*2/*c*, with cell parameters a = 26.721(2) Å, b = 14.316(9) Å, c = 12.693(8) Å, β = 117.962(1)°. Unlike **M2·BZ**, the coordinated groups are arranged in a distorted tetrahedron around the Cu^{2+} centre. This results in the metallocycle **M3** having an overall oval molecular shape. As anticipated, these metallocycles arrange in columns along a crystallographic axis (*i.e.* [001]), resulting in a different packing arrangement than that observed for **M2·BZ.** Figure 4.9 shows the differences in the packing arrangements of **M2·BZ** and **M3·Mix**.

Stacking effects in **M3·Mix** are achieved by weak C–H···Cl hydrogen bonds between the methylene bridges/naphthalene rings and the chloride ions of **M3** within the same column ($C_{donor}\cdots Cl_{acceptor} \approx$ 3.635 and 3.938 Å, respectively). This creates a remarkable stacking arrangement such that (within a column) adjacent metallocycles are not related by purely translational symmetry (*e.g.* along [001] for **M3·Mix**) as is the case with some previously studied metallocycles.[16, 23] Inefficient packing of metallocycles results in the formation of solvent-filled channels along [001]. We were unable to model the solvent molecules present in the channels. We speculate that the positions of guest molecules within the channel of **M3·Mix** could not be determined owing to a mixture of solvent molecules being present in the same channel, as well as corresponding guests having several optimal positions. For this reason we examined crystal growth of metallocycle **M3** using a single solvent solution.

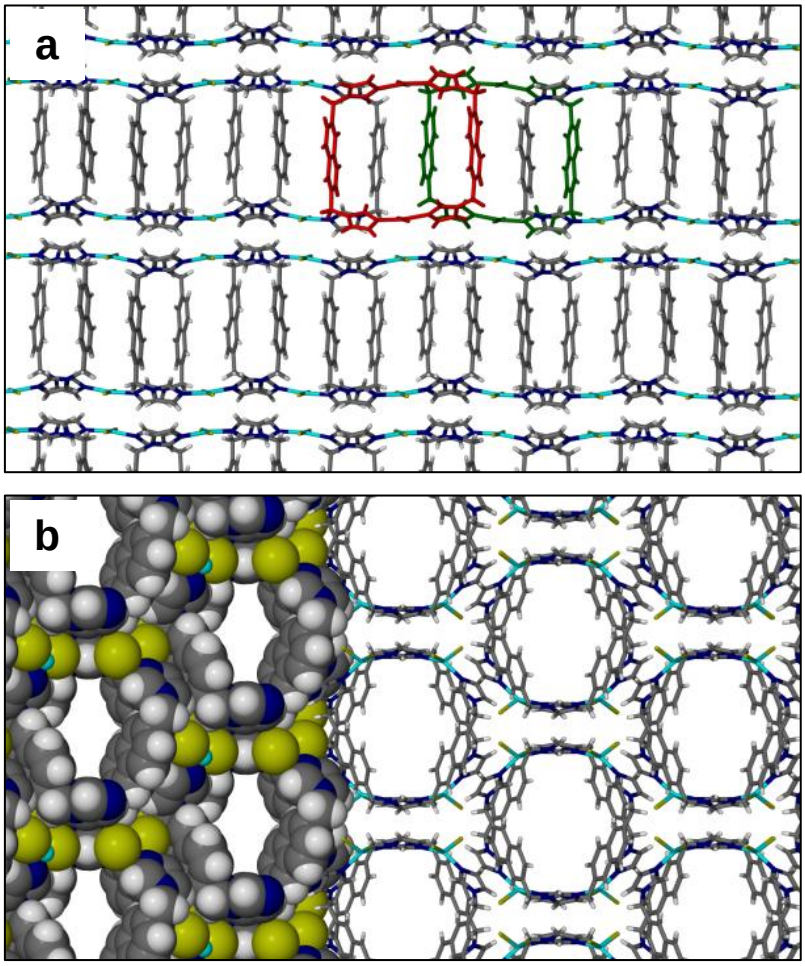

Figure 4.9 Packing diagrams for (a) **M2·BZ** and (b) **M3·Mix** both shown along [001]. (a) The red metallocycle forms part of the layer that is above the metallocycle displayed in green. Benzene guests are situated in between these layers, but are omitted from this figure for clarity. (b) Discrete stacked columns result in an inefficient packing arrangement. The left half of the figure is shown in space-fill to point out formation of continuous channels along [001].

Slow evaporation of a solution containing **L7** and $CuCl_2 \cdot 2H_2O$ in acetonitrile (Scheme 4.4) yielded crystals of the same colour and morphology as **M3·Mix**. Indeed, the resulting metallocycle **M3·MeCN** is isoskeletal to **M3·Mix**, except that in **M3·MeCN** the acetonitrile guest molecules could easily be modelled within the complex ring. The ASU consists of half a metallocycle and one acetonitrile molecule, giving a host:guest ratio of 1:2. Another acetonitrile guest is generated adjacent (*i.e.* in a head to tail fashion) to the unique guest molecule via inversion symmetry. Guest molecules are distributed in an orderly fashion along the length of a continuous channel (V = 486 Å^3 per unit cell, probe r = 1.5 Å) propagating parallel to the crystallographic *c*-axis. The solvent-filled channels occupy approximately 12% of the total cell volume. The electron count (120 e^- per unit cell) within the channel

(calculated using the SQUEEZE[24] routine of PLATON[25]) is consistent with the presence of four acetonitrile molecules (119 e^- per unit cell).

Apart from weak C–H···π contacts (C_{donor}···centroid ≈ 3.81 and 4.49 Å), no additional interactions appear to hold the acetonitrile guests within the aperture of the host (see Figure 4.10).

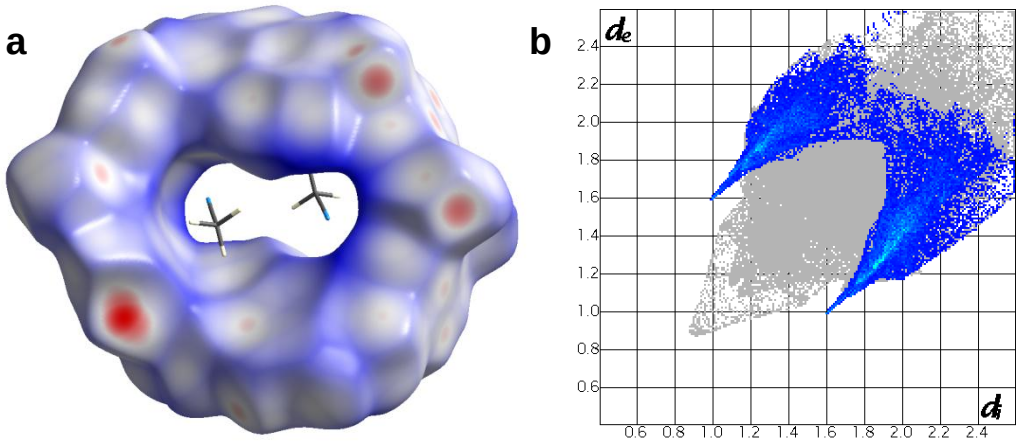

Figure 4.10 (a): The Hirshfeld surface of **M3** in **M3·MeCN**. Blue/white colours on the interior surface of **M3** indicate that no strong host-guest interactions are present in this complex. The intense red surfaces identify the sites of the strong C–H···Cl hydrogen bonds that govern the stacking of metallocycles along [001]. (b): These hydrogen bonds make up more than 21% of the total interaction contribution, as experienced by the metallocycle in **M3·MeCN**.

The absence of significant host-guest interactions is rather unusual, especially since desolvation of the guest molecules does not yield an empty host phase (*e.g.* similar to the apohost structures previously reported for related metallocycles).[13-14, 23] Instead, the TGA thermogram of **M3·MeCN** displays an almost horizontal line (*i.e.* stable mass) until 160 °C, above which the abrupt mass loss attributed to guest desolvation coincides with decomposition of **M3·MeCN** above 200 °C. Although single-crystal data of the empty phase could not be collected, the yellow-green powder obtained from heating the crystals **M3·MeCN** at 120 °C for three days appears to be partially desolvated (Figure 4.11). Powder X-ray diffraction confirmed that the phase of the partially desolvated material is highly similar to that of **M3·MeCN**. Figure 4.12(a) shows a possible arrangement of the acetonitrile guest molecules within the channel in **M3·MeCN**.

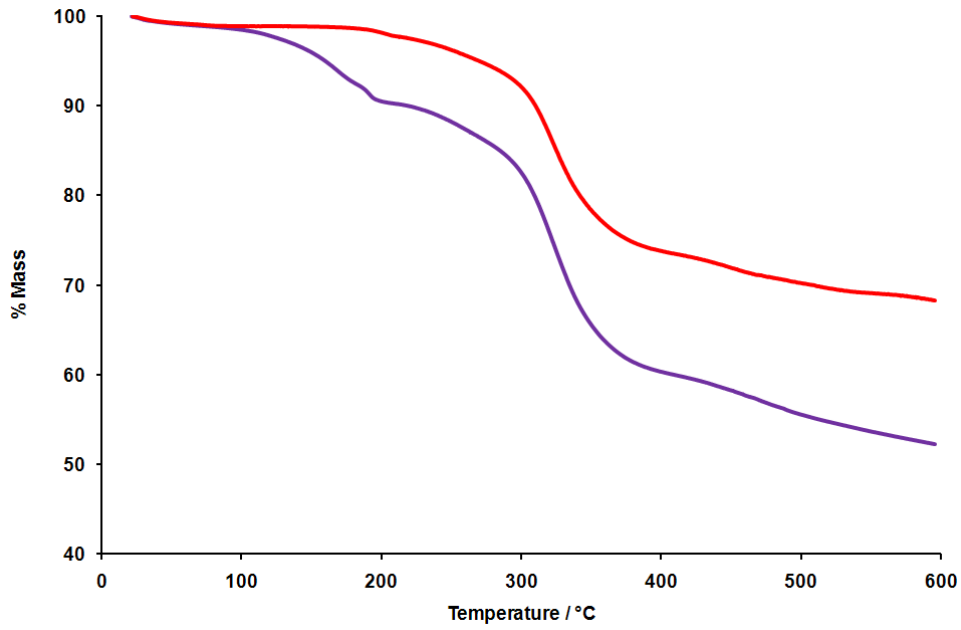

Figure 4.11 TGA thermograms of **M3·MeCN** (purple) and partially desolvated **M3·MeCN** (red). Desolvation of **M3·MeCN** occurs above 100 °C and coincides with decomposition (above 200 °C) of the metallocycle. Heating **M3·MeCN** at 120 °C yielded the thermogram for partially desolvated **M3·MeCN** (red), showing almost no mass loss below 200 °C. Although the TGA results for only **M3·MeCN** are shown here, similar behaviour was observed for **M4·MeCN**.

The acetone solvate crystals **M3·Me$_2$CO** were obtained from an acetone solution containing equimolar amounts of **L7** and $CuCl_2 \cdot 2H_2O$. Structure determination revealed that the ASU of **M3·Me$_2$CO** comprises half a metallocycle and two acetonitrile molecules, each of which is disordered over two positions of equal occupancy. Once again, **M3·Me$_2$CO** is isostructural to **M3·MeCN** with respect to the host packing, though minor deviations in the cell parameters occur upon formation of **M3·Me$_2$CO** (a = 26.340(7) Å, b = 14.467(3) Å, c = 12.745(9) Å, β = 118.294°, V = 4276.89 Å^3). As anticipated, the unit cell volume increases with inclusion of the larger guest molecule.

A conventional channel (V = 515 Å^3 per unit cell, probe r = 1.5 Å in Figure 4.12(b)) analogous to the channel in **M3·MeCN**, accommodates the guest molecules within the host interior (Figure 4.12(b)). The host:guest ratio is 1:2 as confirmed by the electron count (146 e^- per unit cell). The host does not appear to prefer one guest position over another and acetone guests are arbitrarily positioned within the channel. In contrast to the included acetonitrile guests, acetone molecules are connected to the host in **M3·Me$_2$CO** via weak C–H···O hydrogen bonds (C_{donor}···$O_{acceptor}$ ≈ 3.291(3) Å), as well as C–H···π contacts (C_{donor}···centroid

≈ 3.60 Å). Additionally, guest-guest interactions structured by a C–H···O hydrogen bonded spiral contribute to the overall stabilisation of the inclusion complex **M3·Me$_2$CO** (C_{donor}····$O_{acceptor}$ ≈ 3.361(2) Å).

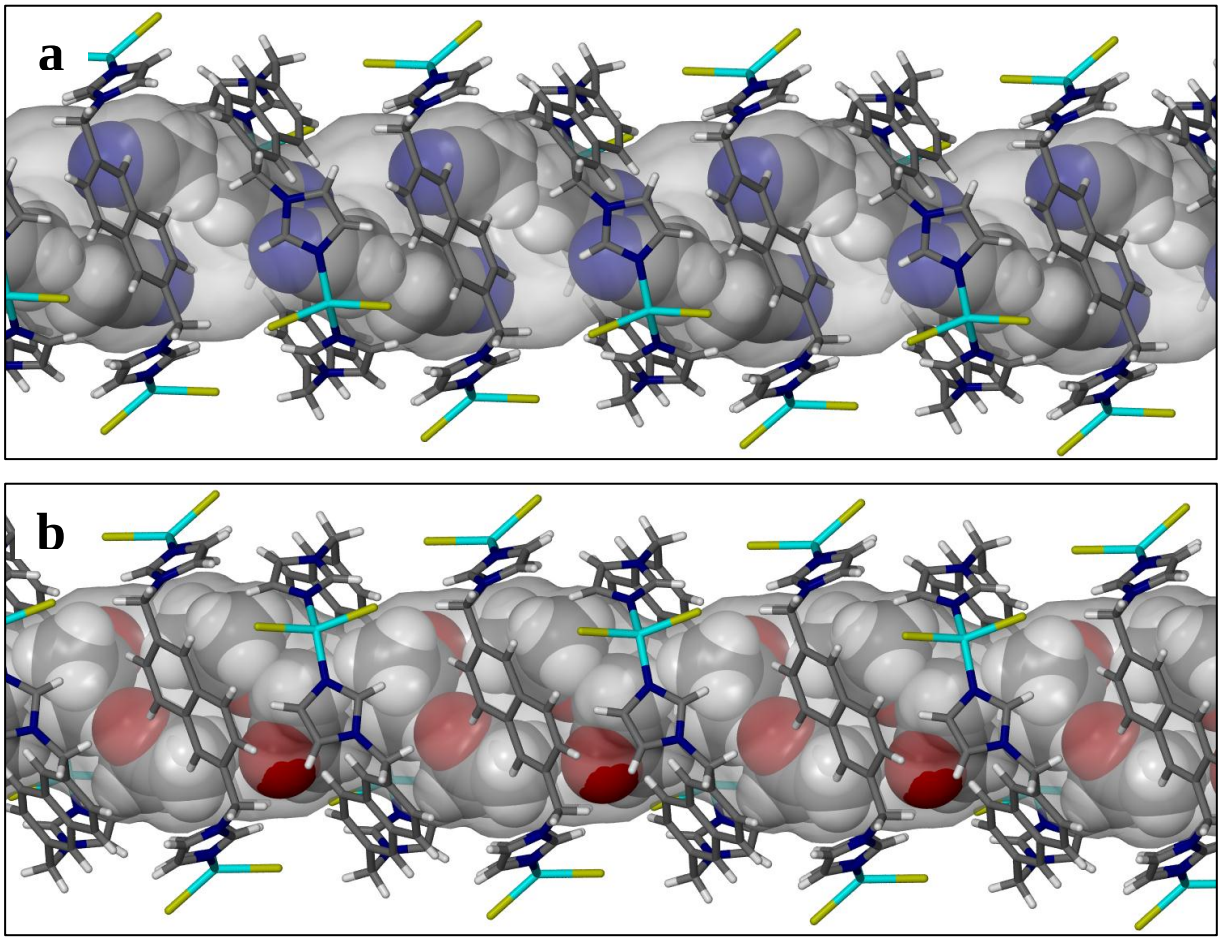

Figure 4.12 Columnar stacking of metallocycles in (a) **M3·MeCN** and (b) **M3·Me$_2$CO**. The host molecules are shown as capped-sticks and guest molecules (acetonitrile and acetone in **M3·MeCN** and **M3·Me$_2$CO**, respectively) in space-filling representation. The Connolly surface of the solvent-filled channels (V = 485 and 515 Å^3 per unit cell for **M3·MeCN** and **M3·Me$_2$CO**, respectively using a probe r = 1.5 Å) is illustrated as a semi-transparent grey surface. In the acetone-filled channel of **M3·Me$_2$CO**, only one of the possible arrangements of the acetone molecules is shown. This arrangement is facilitated by strong guest-guest interactions and a C–H···O hydrogen bond (indicated by the oxygen atom protruding slightly from the Connolly surface) with the metallocycle.

Crystals obtained from a solution of **L7** and $CuBr_2$ in acetonitrile (Scheme 4.4) were characterised using single-crystal X-ray diffraction, which revealed a metallocycle analogous to **M3·MeCN** with regard to the packing of the host molecules. **M4·MeCN** also crystallises in the space group $C2/c$, but slight adjustment to the β angle occurs upon varying the halogen

anion bonded to the Cu^{2+} centre (β = 119.2 ° in **M4·MeCN**, β = 117.6 ° in **M3·MeCN**). In contrast to the unique component in **M3·MeCN**, the ASU of **M4·MeCN** contains half a host molecule situated across an inversion centre at Wyckoff position *a*, and two acetonitrile guests. Space group symmetry requires one of the unique acetonitrile guests to be disordered over two positions of equal occupancy, resulting in a host:guest ratio of 1:3. The other acetonitrile guest is situated in a position favourable for interacting with the naphthalene rings of the host (C_{donor}····centroid ≈ 4.46 Å). Figure 4.13 shows that the guest molecules are situated within continuous channels with a guest-accessible volume of 519 $Å^3$ per unit cell, and the host:guest ratio calculated from the number of electrons (140 e^- per unit cell) corresponds to the model for **M4·MeCN**. The efficient packing of the guests within the channel is facilitated by a spiral of guest-guest C–H···N interactions (C_{donor}···$N_{acceptor}$ = 2.961(1) and 3.206(3) Å). Compound **M4·MeCN** displays identical behaviour to that of **M3·MeCN** (Figure 4.12) upon desolvation and an apohost structure could therefore not be characterised.

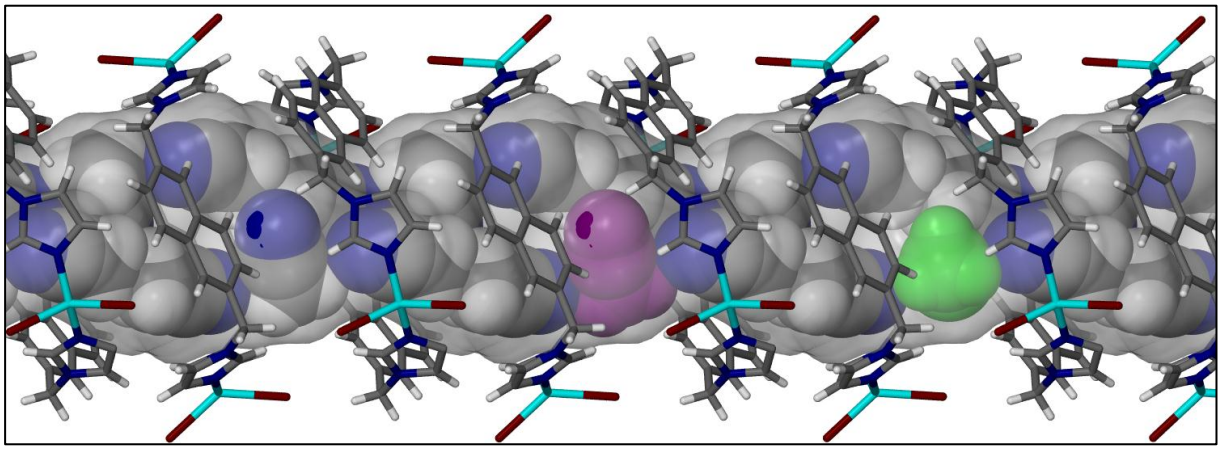

Figure 4.13 An acetonitrile-filled channel in **M4·MeCN**. The guest molecules are shown in space-filling representation within the Connolly surface of the channel (semi-transparent grey surface, V = 515 $Å^3$ per unit cell, using a probe r = 1.5 Å). The disordered sites are indicated in purple (nitrogen directed towards the outside of the channel) and green (nitrogen directed towards the interior of the channel).

Although we were unable to obtain porous apohost structures of **M1·MeCN**, **M2·BZ**, **M3·MeCN** or **M4·MeCN**, the high thermal stability (along with the retention of monocrystallinity) of inclusion complexes **M3·MeCN** and **M4·MeCN** eliminate the need for *in situ* experiments when investigating the structural consequences of reversibly exchanging acetonitrile for a different guest. Single-crystal X-ray diffraction thus permits us to monitor

changes in the host conformation in order to accommodate the new guests, by determining the nature of the host-guest and guest-guest interactions. Supporting techniques such as UV-Vis spectroscopy contribute by revealing slight changes in colour (not always visible with the naked eye) that can be explained with regard to the effect that the size of the guest can have on the host conformation. Furthermore, the shape and size of the guest-accessible space can provide information on the selectivity for a particular guest species.

4.2.2 Guest-induced chromatic changes in M3·MeCN

The main techniques to monitor and characterise solid-state guest-exchange processes are IR, NMR, PXRD, TGA, DSC and single-crystal X-ray diffraction. **M3·MeCN** contains Cu^{2+} and is therefore not suitable for NMR. To the best of our knowledge, guest-induced phase changes do not occur, which renders PXRD ineffective for characterising guest-exchange processes in **M3·MeCN**. Furthermore, SCD requires good quality single crystals in order to accurately model the guest, and the thin needles of **M3·MeCN** are not of sufficient quality for high resolution data. Although thermogravimetric analysis does not yield the molecular structure, TGA thermograms can indicate whether or not the guest-exchange process occurred. Consequently, an estimated host:guest ratio can be deduced.

TGA was carried out on partially desolvated powdered samples of **M3·MeCN** (heated at 120 °C for 3 days) which were exposed to one of the following vapours: methanol, acetonitrile, acetone, chloroform, benzene or 1,4-dioxane (see Figure 4.14). In all instances desolvation begins at room temperature, but a clear guest loss step is not observed since desolvation of the guests coincides with decomposition of the host. These results are presented in Table 4.2.

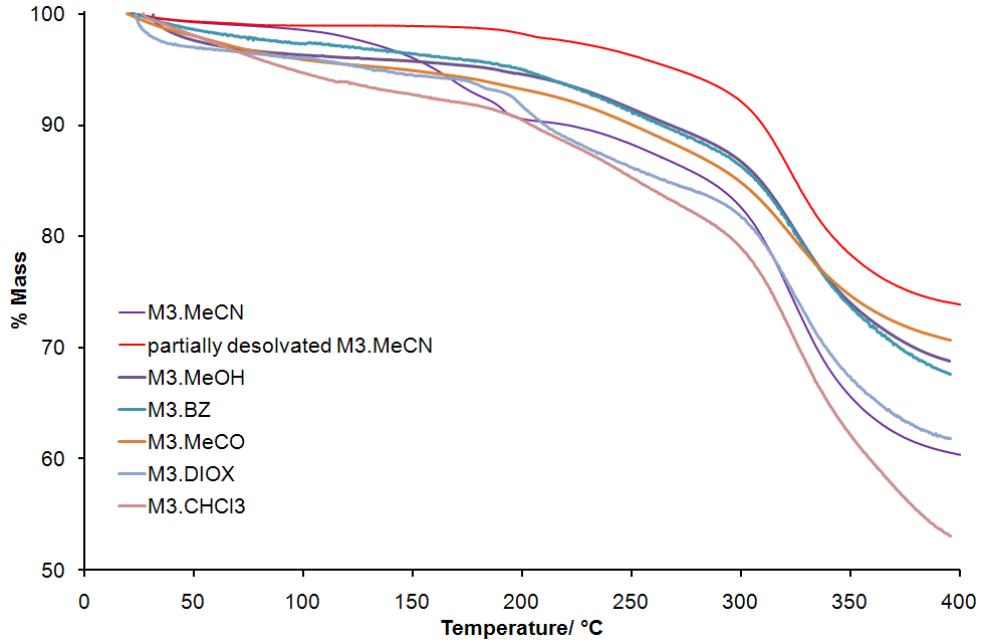

Figure 4.14 Thermogravimetric analyses for the products of the guest-exchange process of **M3·MeCN**.

After characterisation of the guest-exchange products (by means of TGA), we noticed that hazy changes in the colour (*e.g.* different shades of green and yellow) of the partially desolvated **M3·MeCN** precipitate occur upon exposure to the different solvents. The guest-dependent photoinduced reflectance spectra offer a facile technique to characterise such colour changes induced by solid-state guest-exchange processes.

The guest-exchange ability of metallocycle **M3·MeCN** was examined by monitoring the wavelength and intensity (*e.g.* as % reflectance) of the exited Cu^{2+} reflectance band, using solid-state UV-Vis at room temperature. The yellow-green powder **M3·MeCN** was exposed to one of the guest vapours (*e.g.* acetonitrile, acetone, 1,4-dioxane, chloroform, benzene or methanol) for 24 hours. All experiments were carried out by irradiating the samples at 320 nm and collecting reflectance spectra between wavelengths 190 – 1100 nm. Although none of the vapours caused significant changes in colour when in contact with partially desolvated **M3·MeCN**, evident changes in the photoinduced reflectance maxima (see Figure 4.15) occur upon guest-exchange. These results, together with the thermogravimetric measurements, confirm that guest-exchange is indeed taking place (see Table 4.2).

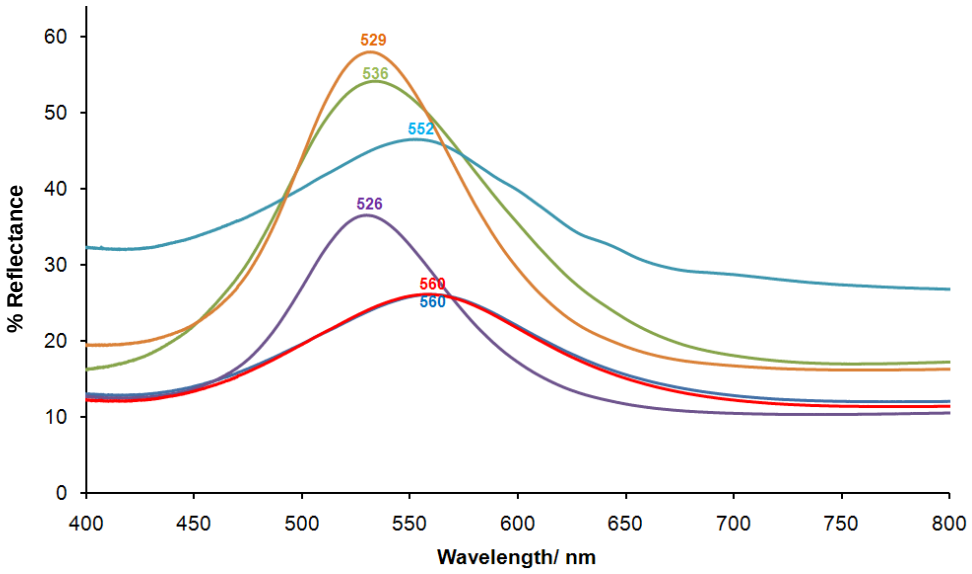

Figure 4.15 Photoinduced solid-state reflectance spectra recorded for partially desolvated **M3·MeCN** (red) after exposure to methanol (light blue), acetonitrile (purple), acetone (green), chloroform (orange) and benzene (dark blue), respectively. The maximum reflectance bands are indicated using the same colour scheme.

Host-guest compounds **M3·MeCN** to **M3·Bz** (Table 4.2) all exhibit green reflectance bands between 500 and 560 nm upon excitation at λ = 320 nm. The deviations in the wavelength corresponding to the reflectance maxima are attributed to changes in the host conformation as a consequence of the related host-guest interactions.[26] It would be interesting to compare these reflectance shifts with single-crystal structures of the host-guest complexes since the shifts to either the blue (*e.g.* left on the abscissa) or yellow reflectance (*e.g.* right on the abscissa) can then be correlated to a specific solid-state structural change in the host. Similar luminescent properties have been observed for a porous three-dimensional Cd(II) MOF.[26]

Table 4.2 A summary of the TGA and UV-Vis spectroscopy results for the guest-exchange processes of **M3·MeCN**.

Inclusion compound	TGA (% mass loss)	Host:guest	Max Reflectance (nm)
Partially desolvated M3·MeCN	~ 0	1:<2	560
M3·MeOH	5.9	1:2	560
M3·MeCN	7.3	1:2	627
M3·Me_2CO	10.1	1:2	536
M3·$CHCl_3$	10.3	1:1	529
M3·BZ	7.4	1:1	552
M3·DIOX	10.2	1:1	563

4.2.3 Single-crystal to single-crystal guest-exchange

As mentioned in section 4.2.1, desolvation of **M3·MeCN** and **M4·MeCN** coincides with decomposition of the host, and a porous apohost structure could not be characterised. Guest-exchange processes in **M3·MeCN** could not be investigated using single-crystal X-ray diffraction, owing to the poor quality of the crystals. However this was not the case for **M4·MeCN**.

In order to investigate the guest-exchange capability of **M4·MeCN**, single-crystals of **M4·MeCN** were immersed in a vial containing one of the solvents acetone, methanol, dichloromethane, chloroform, benzene, cyclohexane or carbon disulphide (Table 4.1). Single-crystal data were collected after two days of exposure to the solvent. Following structure solution, the data were compared to the acetonitrile solvate structure **M4·MeCN** as a reference for studying changes in the metallocycle conformation that are triggered by subtle supramolecular interactions. The guest-exchange process is demonstrated by the following equation:

$$\mathbf{H{\cdot}MeCN}(s) + n\mathbf{G}(l) \rightarrow \mathbf{H{\cdot}G_n}(s) + \mathbf{MeCN}(l)$$

where **H·MeCN** represents an acetonitrile-included host-guest complex. The guest **G** (*e.g.* solvents in Table 4.1, present in excess during the process) replaces the acetonitrile guest **MeCN**, resulting in the formation of a new solid host-guest complex **H·G_n**.

This process occurred rapidly in all instances without a change in the space group symmetry. In all cases X-ray diffraction analysis proved to be unambiguous and no further analytical techniques were deemed necessary. Although measuring the kinetics of the exchange process would have been a welcome addition to the study, these measurements are very difficult to make and were not attempted. Structures of the new inclusion complexes have been evaluated in terms of deviation of the angle between the mean plane of the metallocycle (*i.e.* plane through the atoms N–Cu–N on either side of the molecule, see Figure 4.16) and the symmetry-related naphthalene rings. Disorder of these rings was not observed, implying that the "tilt" angle (Φ) is fixed throughout a particular structure. Although deviation in the $Cu^{2+}\cdots Cu^{2+}$ and the centroid···centroid distance between imidazole rings (*i.e.* *Im*···*Im*) occurs to some extent in all structures, it will only be mentioned in extreme instances. A summary of these parameters, among others, is shown in Table 4.3. The crystallographic data for structures **M4·MeCN** to **M4·Cy** are listed in Tables 4.4.

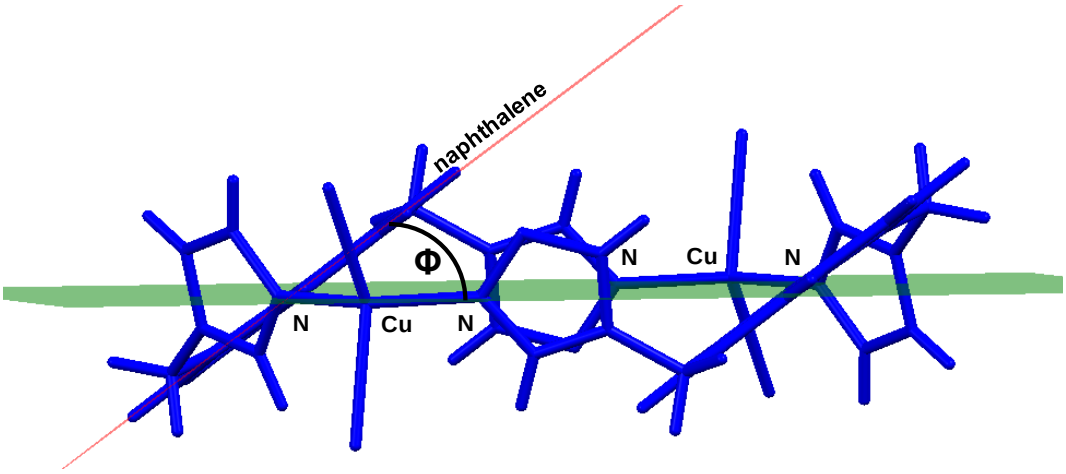

Figure 4.16 A side view of **M4** in **M4·MeCN** (guest molecules are omitted) indicating the position of ∠Φ. The angle is determined by calculating the mean planes through a naphthalene ring (shown in red) and N–Cu–N atoms on either side of the metallocycle (shown in green).

4.2.3.1 M4·H_2O

The **M4·H_2O** structure was problematic with regard to modelling the guest molecules in a sensible manner. The metallocyclic host can easily be modelled and significant electron density peaks appear within the complex ring. These peaks could not be modelled as acetonitrile molecules. The electron count (208 e^- per unit cell) within the accessible space (553 $Å^3$ per unit cell) implies that the electron density peaks are not due to included

acetonitrile molecules (see Table 4.3). The total electron count amounts to 10 H_2O molecules per host. Since the single-crystal data were inconclusive, thermogravimetric analysis was carried out. Figure 4.17 reveals a mass loss of 15.5%, which corresponds to a 1:10 host:guest ratio for **M4·H_2O**.

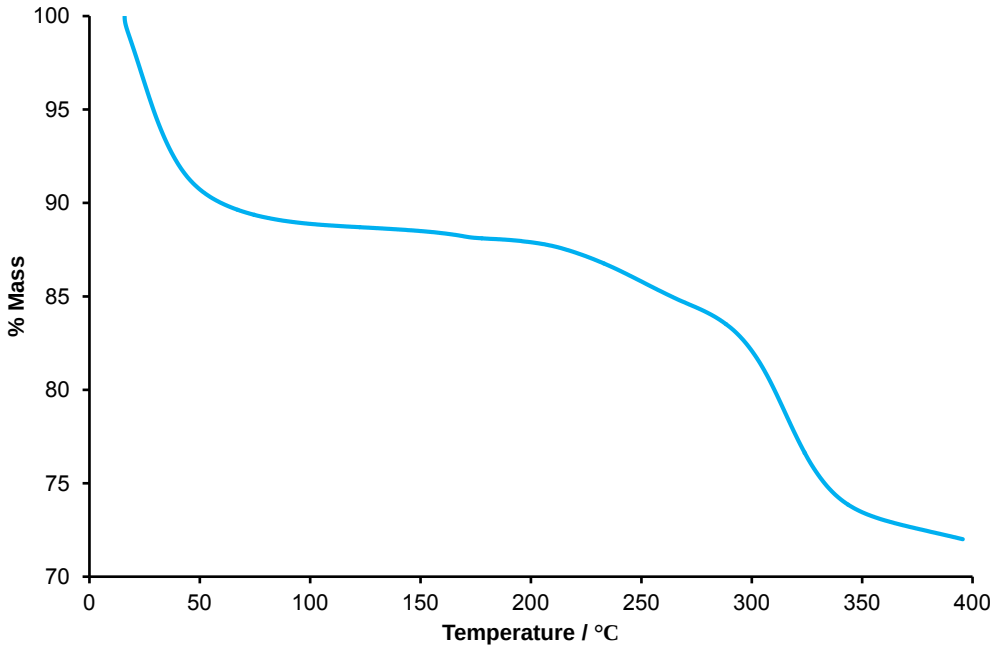

Figure 4.17 TGA thermogram of **M4·H_2O**.

4.2.3.2 M4·MeOH

It was only after several attempts that the pure (*i.e.* dry) methanol-included complex **M4·MeOH** was obtained, owing to the concomitant inclusion of H_2O molecules. Strong hydrogen bonds between H_2O and methanol guests appear to be the driving force for the sorption of the binary adduct rather than the exclusive sorption of methanol. The structure of **M4·MeOH** is remarkably similar to that of **M4·MeCN**; the ASU consists of half a host, one fully occupied methanol guest and one half-occupancy methanol molecule that is disordered over two positions. The two-fold disordered guests are related to each other via the symmetry operator (-*x*,*y*,½-*z*) and there is no evidence for one site being favoured over the other; this results in a host:guest ratio of 1:3. Methanol has approximately the same size and shape as acetonitrile, and therefore the overall molecular conformations of metallocycles in **M4·MeOH** and **M4·MeCN** are comparable, apart from a small increase in the angle between the mean plane of the metallocycle and the naphthalene rings (Φ_{MeCN} = 36.22°, Φ_{MeOH} =

37.39°). Interestingly, in the structure of **M4·MeOH**, guest molecules do not interact with the Cu^{2+} ions or the organic spacer. The oxygen atoms of the guests are all pointing towards the interior of the channel (V = 513 Å^3 per unit cell, probe r = 1.5 Å in Figure 4.18). This might indicate that the methanol guest is not of adequate size for efficient interaction with the host, and guests therefore preferentially interact with one another. A hydrogen-bonded spiral (*i.e.* O_1–H···O_2–H···O_3) of methanol guests occupies the solvent-accessible channels ($O1_{acceptor}$····$O2_{donor}$ = 2.593(2), $O2_{acceptor}$····$O3_{donor}$ = 3.243(2) and $O3_{acceptor}$····$O1_{donor}$ = 2.712(2) Å).

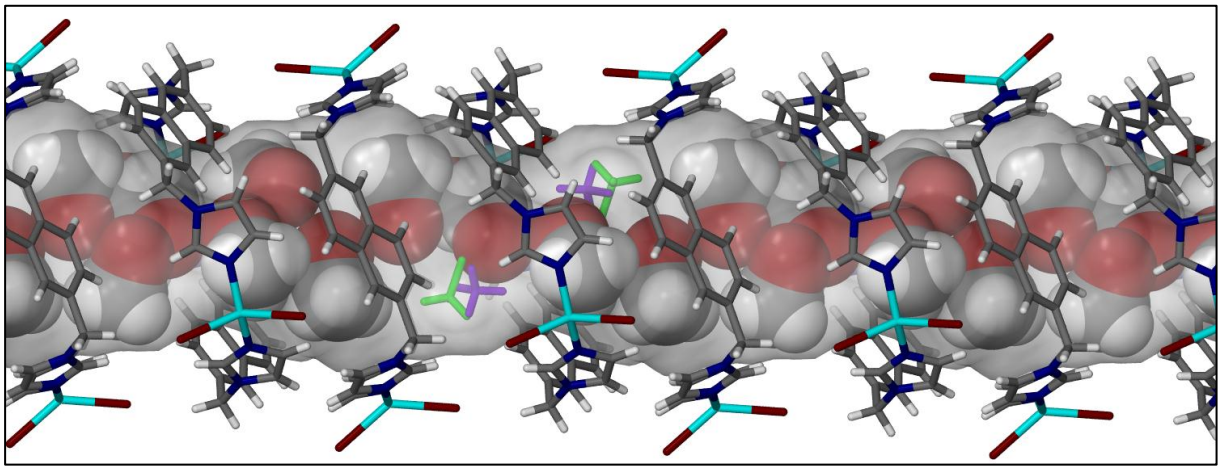

Figure 4.18 Projection of **M4·MeOH** viewed perpendicular to [001]. The methanol-filled channel passing through the stacked column of metallocycles (in capped-sticks) is shown as a semi-transparent grey Connolly surface (V = 513 Å^3 per unit cell, probe r = 1.5 Å). The location of the disordered guest is indicated in green and purple capped-sticks. The remaining guest molecules are shown in space-filling representation and only one of the positions of the disordered guests is shown. Both positions of the disordered methanol guests (shown as capped-sticks and coloured green and purple) are shown for only two locations in the middle of the figure.

4.2.3.3 M4·Me_2CO

In the crystallographic model of **M4·Me_2CO**, the ASU is comprised of half a host and two partially occupied acetone guest molecules. Both guests are symmetrically disordered across an inversion centre. The host:guest ratio is 1:2 as confirmed by electron count calculations (see table 4.3). As opposed to **M4·MeCN** and **M4·MeOH**, the shape of the acetone molecules in **M4·Me_2CO** prevents the guests from packing efficiently within the channel with V = 540 Å^3 per unit cell. Figure 4.19 shows that the most significant host-guest interaction is a C–H···O hydrogen bond between the carbonyl moiety of the guest and the 2-hydrogen of the

Im rings ($C_{donor}\cdots O_{acceptor}$ = 3.280(4) Å). Although the overall conformation of the metallocycle in **M4·Me$_2$CO** is similar to metallocycles in **M4·MeCN**, a significant change in the naphthalene "tilt" angle (from Φ = 36.32° in **M4·MeCN** to Φ = 39.09° in **M4·Me$_2$CO**) occurs upon exchanging acetonitrile for acetone. A slight elongation of the $Cu^{2+}\cdots Cu^{2+}$ distance in **M4·Me$_2$CO** accompanies these changes ($Cu^{2+}\cdots Cu^{2+}_{\mathbf{M4\cdot Me_2CO}}$ = 12.03 Å).

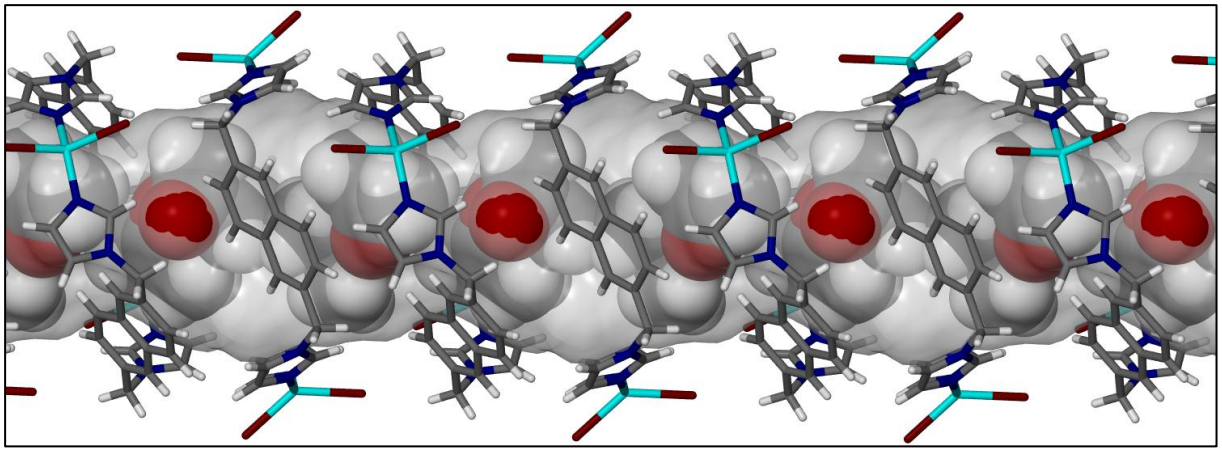

Figure 4.19 Space-filling representation of the locations of the acetone guest molecules within the channel (displayed as a semi-transparent surface with V = 540 Å^3 per unit cell, probe r = 1.5 Å) of **M4·Me$_2$CO**. The carbonyl oxygen atom of the guest protruding from the surface of the channel indicates the most significant host-guest contact. Only one arrangement of guest molecules is shown.

4.2.3.4 M4·DCM

The ASU of **M4·DCM** is comprised of half a metallocycle and two crystallographically unique half-occupancy dichloromethane guest molecules. Both guest molecules are disordered over two positions across an inversion centre at Wyckoff position *b*; the host:guest ratio is 1:2. The uptake of dichloromethane guests is presumably facilitated by a C–H···Br hydrogen bond $C_{donor}\cdots Br_{acceptor}$ = 3.76(4) Å) between the host and one of the unique guests (see Figure 4.20). The remaining guest molecule is stabilised by C–H···Cl guest-guest interactions ($C_{donor}\cdots Cl_{acceptor}$ = 3.65(6) Å**)**. Exchanging acetonitrile for dichloromethane occurs with a significant decrease in the β angle (from 119.20º to 117.63°), as well as a remarkable increase in the guest-accessible space per unit cell (from 519 to 553 Å^3 per unit cell). In order to accommodate the large chlorinated guests, metallocycles in **M4·DCM** must endure some strain by forcing the naphthalene rings from a "tilt" angle of Φ = 36.32° in **M4·MeCN** to Φ = 40.69° in **M4·DCM**. Furthermore, we speculate that the decrease in the

$Cu^{2+}\cdots Cu^{2+}$ distance (from 11.93 to 11.79 Å) is a consequence of "twisting" the naphthalene rings.

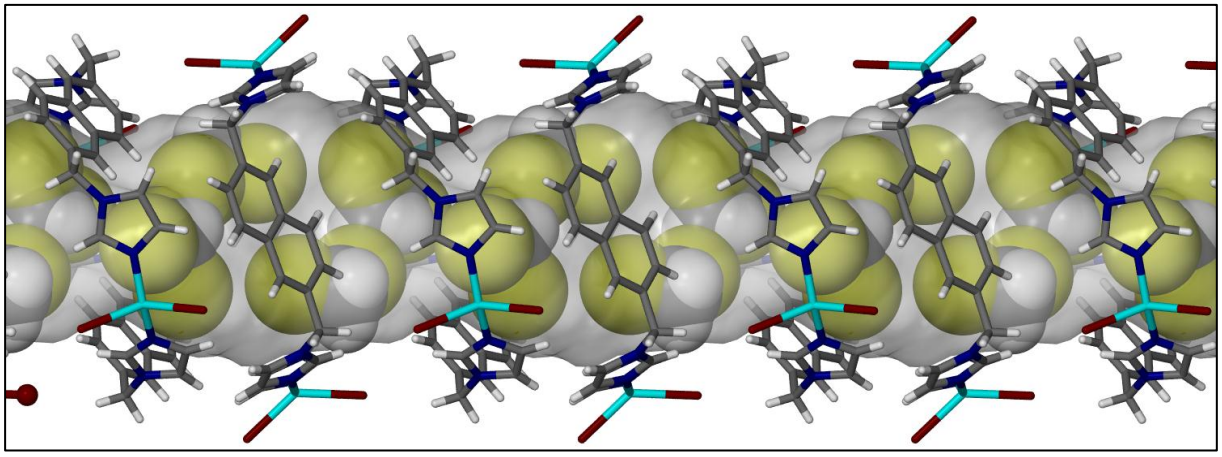

Figure 4.20 A perspective view of the channel accommodating the dichloromethane guests in the crystallographic model of **M4·DCM**. Some of the symmetry-related guest locations have been selectively omitted to avoid guest overlap as a result of the disorder in the channel. Strong host-guest interactions are indicated by guest atoms protruding from the Connolly surface (semi-transparent grey), as seen for the C–H···Br hydrogen bond.

4.2.3.5 M4·$CHCl_3$

Single-crystal diffraction analysis of crystals immersed in chloroform reveals that the metallocycles each enclose two chloroform molecules. Space group symmetry requires both guests to be disordered over two sites of equal occupancy. A host:guest ratio of 1:2 was derived from the electron count (278 e^- per unit cell) calculated using SQUEEZE. Exchanging acetonitrile for chloroform also occurs with deviation in the β angle (from 116.460(2)° to 117.680(4)°) and the naphthalene "tilt" angle (Φ = 36.2° in **M4·MeCN** and Φ = 39.5° in **M4·$CHCl_3$**).

No ordering effects (*i.e.* polar ordering) appear to be present and the arrangement of the guest molecules within the channel (Figure 4.21) is presumably determined by host-guest and guest-guest interactions. Directional guest-guest interactions are dominated by C–H···Cl hydrogen bonds with the $C_{donor}\cdots Cl_{acceptor}$ distance within the same range as that of similar interactions retrieved from the CSD.

The locations of the chlorinated guests are greatly affected by lone pair–π interactions with the *Im* rings of the host (Centroid···Cl = 3.49 – 4.02 Å). In contrast to **M4·DCM**, the

chloroform molecules occupy a large percentage of the guest-accessible space (V = 554 Å^3 per unit cell, using a probe r = 1.5 Å) within the columns formed by stacked metallocycles.

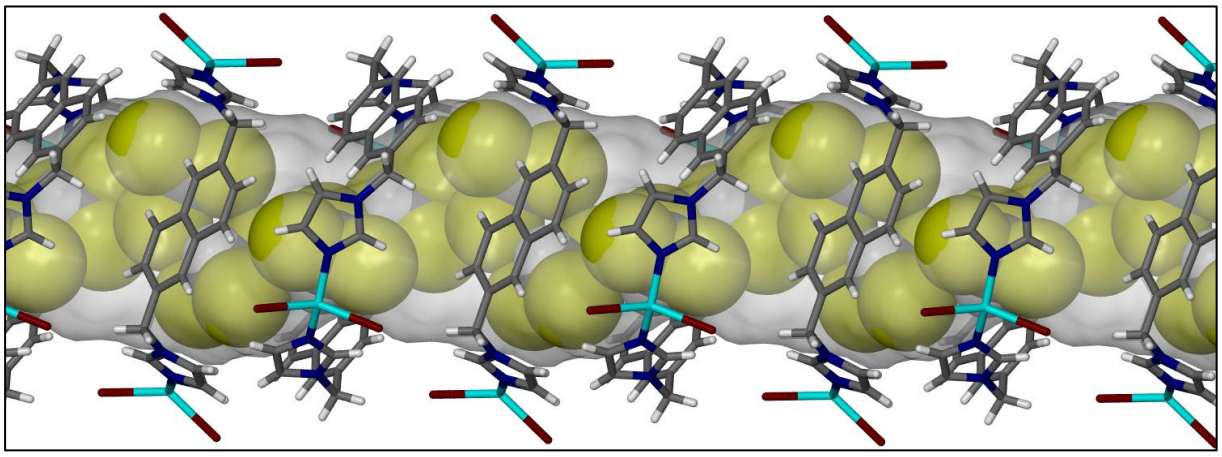

Figure 4.21 A possible arrangement of chloroform molecules within a channel (semi-transparent surface with V = 554 Å^3 per unit cell, using a probe r = 1.5 Å) of **M4·CHCl$_3$**. The specific arrangement of the chloroform molecules was obtained by omitted some of the symmetry-related disorder sites (after considering the van der Waals radii for possible guest overlap, as well as favourable interactions) in order to obtain a representation of the correct host:guest ratio. Guest molecules (shown in space-filling representation) protruding from the surface indicates strong host-guest contacts at those locations.

4.2.3.6 M4·CS$_2$

The ASU of **M4·CS$_2$** consists of half a host molecule and two half-occupancy carbon disulfide molecules, resulting in a host:guest ratio of 1:2. Symmetry-related guest positions associated across inversion centres at Wyckoff position *c* create overlap between the locations of the two unique guests (Figure 4.22). The metallocycle conformation is analogous to that observed in **M4·MeCN** with regard to the Cu^{2+}····Cu^{2+} distance, guest-accessible volume and napththalene "tilt" angle (Table 4.3). Furthermore, it appears that an electrostatic interaction with the inorganic part of the host plays a role in the consistent location of the guests close to the metal centre (Cu^{2+}···S1A = 3.797(2) Å and Cu^{2+}···S3B = 3.778(1) Å in Figure 4.22). Figure 4.23 shows a plausible arrangement of the CS$_2$ molecules within the channel, but other arrangements are also possible; some of the guest positions have been selectively deleted (to avoid guest overlap) in order to obtain a model consistent with the host:guest ratio.

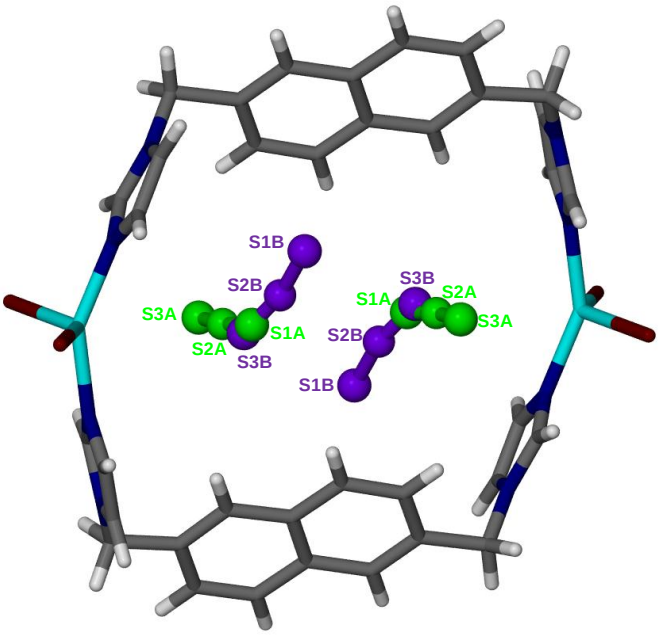

Figure 4.22 A perspective view of the guest disorder in **M4·CS$_2$**. The unique carbon disulfide guests are shown in ball-and-stick representation and coloured purple and green, respectively. Only the guest molecules are labelled. The symmetry-related instances (across an inversion centre) are shown in the same colours. The host molecule is represented using the capped-stick convention.

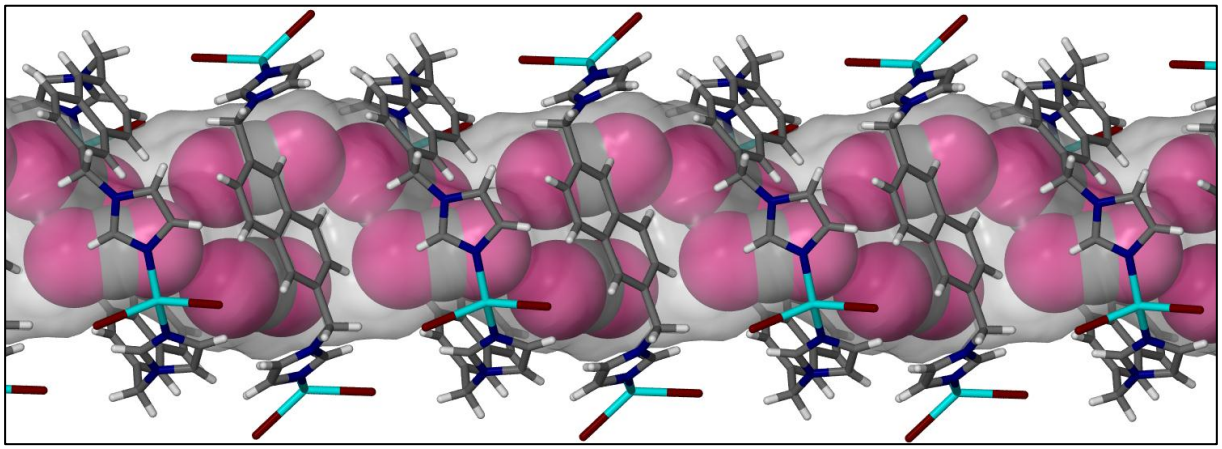

Figure 4.23 A plausible arrangement of carbon disulfide molecules within the channel of **M4·CS$_2$**.

4.2.3.7 M4·BZ

The structure obtained by exchanging acetonitrile for benzene is the most intriguing thus far since it features a substantial increase in the guest-accessible volume (from 519 to 572 Å^3 per unit cell). Consequently, significant deviation from the unit cell parameters of **M4·MeCN** occurs in **M4·BZ** (a = 27.117(6) Å, b = 14.181(3) Å, c = 12.981(3) Å, β = 116.279(1) and V =

4475.75 $Å^3$). Unlike all the abovementioned host-guest structures, **M4·BZ** does not assume a whole number stoichiometric host:guest ratio. The ASU is comprised of half a cyclic host molecule and two symmetry-independent benzene guests with occupancies of 0.5 and 0.25, respectively. Each guest is disordered over two positions of equal occupancy (see Figure 4.24(a)), resulting in a 1:1.5 host:guest ratio and the electron count (Table 4.3) within the guest-accessible space corresponds to this stoichiometry.

As might be expected for systems containing aromatic guests, guest-related interactions are dominated by π···π contacts with the naphthalene rings (C_{edge}···centroid = 3.48 Å) and *Im* rings (centroid···centroid = 3.72 Å) of the host. It is apparent from Figure 4.24 that two strong face-to-face π···π contacts between the green guests (centroid···centroid = 4.77 Å) and the green and purple guests (centroid···centroid = 4.53 Å) contribute to the overall stabilisation of the inclusion complex **M4·BZ**. In order to accommodate and strongly interact with the benzene guests, the metallocycles adapt their conformations by "twisting" the naphthalene moieties to achieve a "tilt" angle of Φ = 42.69°. As hypothesised for **M4·DCM**, excessive strain on the host conformation is prevented by a decrease in the Cu^{2+}····Cu^{2+} distance (from 11.928 to 11.669°). However, in **M4·BZ** this could also arise as a result of a weak Cu^{2+}···π host-guest contact (Cu^{2+}···centroid = 4.085 Å). Figure 4.25 indicates the locations (*e.g.* red surfaces) of the host-guest contacts that are present in **M4·BZ**.

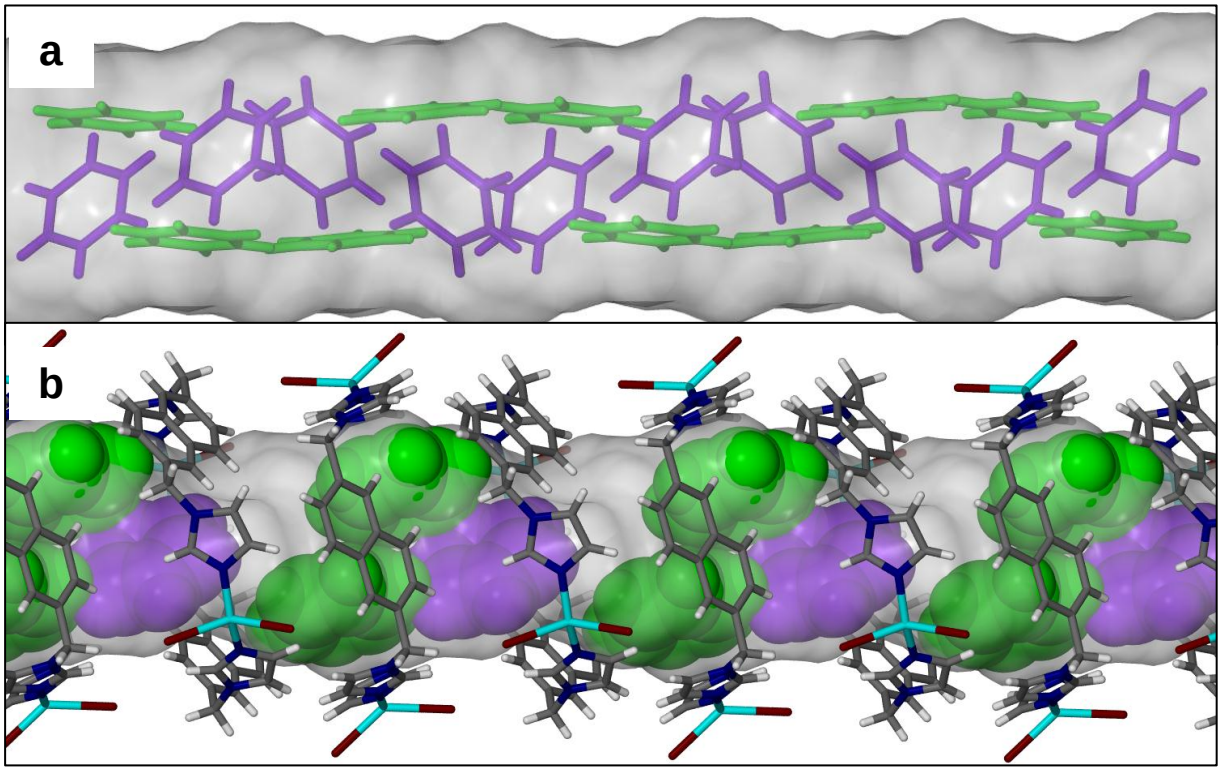

Figure 4.24 (a) Benzene-filled channel (shown as semi-transparent grey surface with V = 572 Å^3 per unit cell, using probe r = 1.5 Å) in **M4·BZ**, highlighting all the disordered sites of the guest molecules (shown as capped-sticks). The guests of occupancy 0.5 and 0.25 (and their symmetry-related instances) are shown in green and purple, respectively. Host molecules are omitted for clarity. (b) The benzene solvate **M4·BZ** viewed along [011]. Only one of the plausible arrangements of guest molecules is shown. Guest molecules are shown in space-filling representation and the same colour scheme is used as in the figure above. The green guest protrudes from the surface as a result of strong π···π and C–H···π interactions with the *Im* moieties and naphthalene rings of the host.

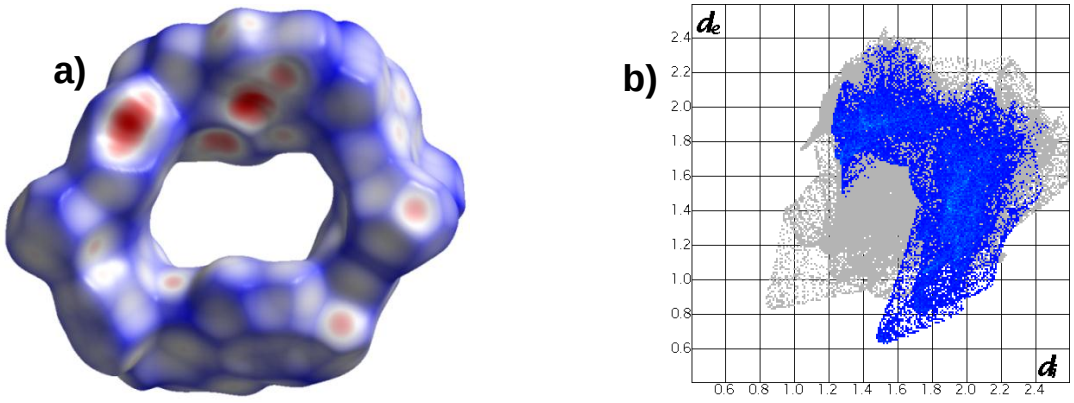

Figure 4.25 The Hirshfeld surface (a) and fingerprint plot of **M4·BZ** (b). The red regions on the interior of the ring indicate the sites of strong interactions between host and guest. The fingerprint plot reveals that 21% of the total interactions experienced by the metallocycle (*i.e.* host-host and host-guest) in **M4·BZ** are π···π contacts (shown in blue) with the benzene guest.

4.2.3.8 M4·Cy

In contrast to **M4·BZ**, the ASU of **M4·Cy** contains half a metallocycle and half a cyclohexane molecule and shows no signs of guest disorder. Thus, the structure of **M4·Cy** is consistent with a host:guest ratio of 1:1. The cyclohexane guest adopts the chair conformation throughout the structure; guests within the same channel are related via simple translational symmetry. **M4·Cy** has a guest-accessible volume (V = 533 Å^3 per unit cell) comparable to that of the acetonitrile reference structure (V = 519 Å^3 per unit cell). Furthermore, the cyclohexane molecules are not located within the rings of the metallocycles, but between adjacent metallocycles of the same stacked column (Figure 4.26). This places the guests in excellent positions for interaction with the naphthalene rings (Φ = 40.67°) via weak dispersive $\sigma\cdots\pi$ contacts (C–H$_\sigma\cdots$centroid ≈ 3.91 Å). The decrease in $Cu^{2+}\cdots Cu^{2+}$ (from 11.92 to 11.79 Å) is likely a consequence of more space being available within the complex ring, owing to the different guest locations. Guest-guest interactions appear to be absent from **M4·Cy**. A summary of the results discussed in Section 4.2.3 is shown in Table 4.3.

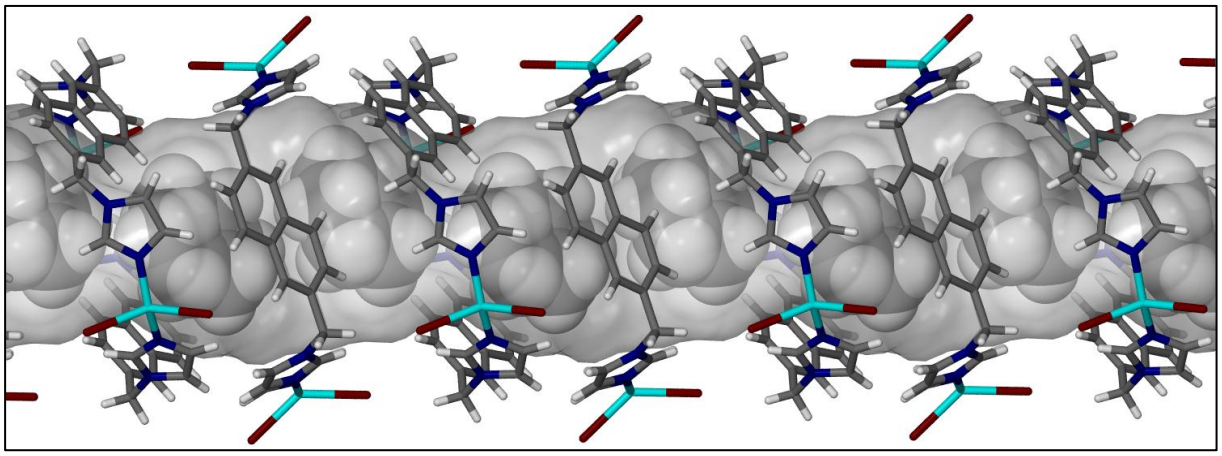

Figure 4.26 A perspective view showing the positions of the cyclohexane guest within the channel (shown as a semi-transparent surface with V = 533 Å^3 per unit cell, using a probe r = 1.5 Å) in **M4·Cy**.

Table 4.3 A summary of selected structural parameters of complexes **M4·MeOH** to **M4·Cy** (Sections 4.2.3.2-4.2.3.8).

Guest	Naphthalene "tilt" angle Φ (°)	$Cu^{2+}\cdots Cu^{2+}$ (Å)	e^- count/ unit cell	Guest-accessible volume (Å^3 / unit cell)
H_2O	41.9	11.9	208	553
MeOH	37.4	12.0	115	513
MeCN	36.2	11.9	140	519
Me_2CO	39.1	12.0	133	540
DCM	40.7	11.8	214	533
$CHCl_3$	39.5	11.9	279	554
CS_2	38.4	11.9	167	519
BZ	42.7	11.7	123	572
Cy	40.7	11.8	150	533

4.2.4 Structural support for guest-exchange involving gaseous molecules

To further probe the permeability of **M4,** single-crystals of **M4·MeCN** were exposed to I_2 vapour in a closed container. After two days the yellow-brown crystals turned darker in colour, but they were still of adequate quality for SCD. Structure elucidation revealed that the I_2 molecules are encapsulated by **M4** molecules and electron density peaks corresponding to acetonitrile were not present. The ASU of **M4·I_2** consists of half a metallocycle and one partially occupied I_2 guest. Each of the guest molecules is situated at a distance of 3.662(9) Å* from the Cu^{2+} atoms. Although this distance is too long to be considered a coordination bond, the $Cu^{2+}\cdots I$ distance and thus the consistent location of the I_2 molecules at this site is probably due to weak electrostatic interactions. The I–I bond length of 2.54 Å is an acceptable distance when compared to distances retrieved from the CSD. The naphthalene rings in **M4·I_2** are tilted at an angle of 39.19° as a result of a weak C–H···I interaction with the guest ($C_{donor}\cdots I_{acceptor}$ = 4.141(1) Å). A similar I_2 inclusion compound has been reported.[23] In principle one should be able to obtain the apohost by heating **M4·I_2** crystals, but this was not attempted owing to the poor quality of the crystals after guest exchange and being exposed to air for a few days.

* distance between the Cu^{2+} ion and the closest iodine atom

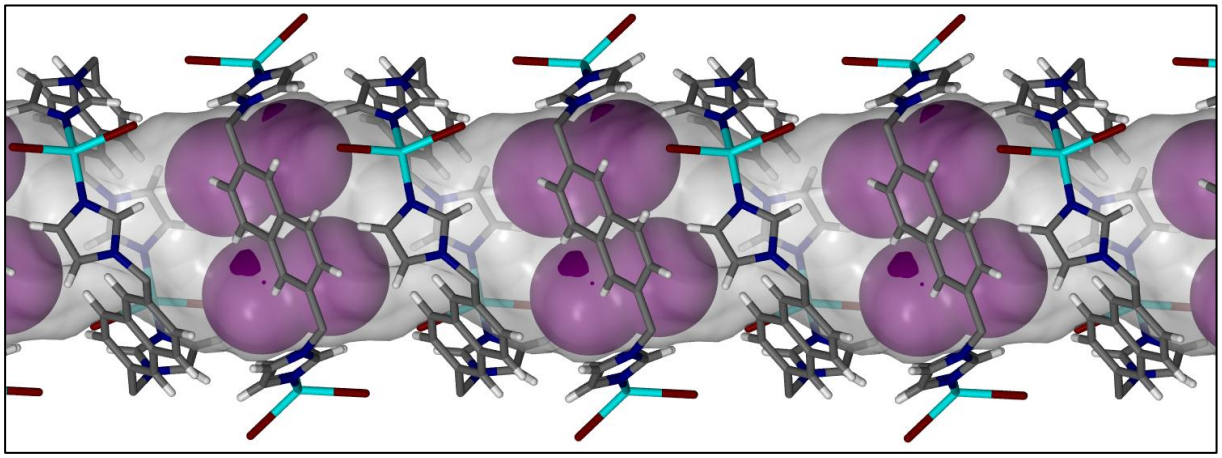

Figure 4.27 A channel (shown as semi-transparent grey surface with V = 512 Å^3 per unit cell, probe r = 1.8 Å) in **M4·I$_2$**, showing a plausible arrangement of I_2 guests. The guests shown in the figure were carefully selected from the disordered model in order to avoid guest overlap.

Our final attempt at obtaining the apohost single-crystal structure was motivated by the recent success of Hupp *et. al.*[27-29] They developed a simple method for the treatment of solvent-containing host materials to greatly increase the internal surface area (*i.e.* yield microporous materials). Experimentally, this involves extracting the included solvent molecules by subjecting the complex to supercritical CO_2 conditions.[30] The exchanged CO_2 molecules are released to the atmosphere shortly after the pressure on the crystals is released.

Crystals of **M4·MeCN** were treated with supercritical CO_2 for 4 hours. Inspection using a microscope revealed that the single-crystals were still intact. After 24 hours of exposure to the atmosphere a selected crystal was analysed by SCD at room temperature. Structure solution revealed a complex that is isostructural to **M4·MeCN** with regard to the host packing. Instead of obtaining the expected apohost structure, the channel (574 Å^3 per unit cell, probe r = 1.4 Å) formed by stacking of the **M4** metallocycles still appears to enclose diffuse electron density (140 e^- unit cell). Initially the presence of the diffused electron density was rationalised as the sorption of H_2O molecules (presumably from the atmosphere), but after closer inspection it was found that the structural parameters do not correlate with those of **M4·H$_2$O** (see Table 4.4). Moreover, in both **M4·MeCN** and **M4·H$_2$O** a continuous channel could be mapped using a probe r > 1.8 Å, but in the structure of the crystal treated with supercritical CO_2 empty space could only be mapped using a probe r < 1.5 Å. A plausible explanation is that the electron density is due to CO_2 molecules that are experiencing substantial thermal motion. If this hypothesis is correct, CO_2 molecules have

replaced the initial acetonitrile guests. It can reasonably be expected that the CO_2 guests would gradually diffuse out of the crystals when they are not exposed to CO_2 pressure.

In order to test whether **M4·MeCN** is truly porous in a practical sense, a suitable single-crystal was mounted in a gas cell to avoid gradual desorption that might take place. The device was allowed to equilibrate at a pressure of 15 bar CO_2 gas prior to successive data collections at 25 and -33 °C. Guest positions for the structure determined at 25 °C could not be located due to extensive thermal motion at this temperature. However, the cell parameters, the calculated guest-accessible volume (574 $Å^3$ per unit cell, probe r = 1.4 Å) and electron count (135 e^- per unit cell) corresponds well to the structure determined after exposure to supercritical CO_2, compared to that of **M4·H_2O** or **M4·MeCN**. Moreover, the cell parameters of **M4·CO_2** deviate significantly from those of **M4·MeCN** (see table 4.4).

Remarkably, structure determination of **M4·CO_2** at -33 °C revealed the presence of CO_2 guest molecules within the ring of **M4**. The ASU is comprised of half a metallocycle, half a CO_2 molecule (with partial occupancy – C in Figure 4.28) and another two half-occupancy CO_2 guests (A and B in Figure 4.28). The overall host:guest ratio is 1:2.5, which is in agreement with the electron count (133 e^- per 577 $Å^3$ void per unit cell) as calculated using SQUEEZE. Although the disorder of the guests allows more than one arrangement of CO_2 molecules, only one arrangement is possible when taking the van der Waals spheres into consideration. The CO_2 guests are arranged in a chain-like fashion along [001]. Within the guest chains, "T-shaped" $CO_2\cdots CO_2$ interactions form square-connected tetramers ($C{=}O_A\cdots C{=}O_B \approx 3.19$ and 2.41 Å - see Figure 4.28) which are, in turn, linked via $CO_2\cdots CO_2$ interactions ($C{=}O_C\cdots C{=}O_B \approx 3.27$ Å) to guest C. A distortion induced by these interactions is a plausible explanation for the slight deviation of the ∠O=C=O from linearity (observed for all three unique guests). Kauffman *et al.* also reported close C=O···C=O contacts as observed using X-ray diffraction and *in situ* FT-IR.[31] Furthermore, the consistent location of guest A in close proximity to the metal centre suggests that an electrostatic interaction is present between the host and the CO_2 molecule when it is in position A as shown in Figure 4.28.

All attempts at completely desorbing the CO_2 molecules by applying vacuum were unsuccessful. Although it was possible to significantly reduce the electron count upon applying vacuum for a week, residual electron density peaks were still present within the complex ring. We note that the presence of the residual electron density after evacuation could also be attributed to a small quantity of acetonitrile molecules that might not have been exchanged for CO_2. However, if acetonitrile was still present its contribution can be neglected

since it was not possible to model any acetonitrile molecules, while the positions of the CO_2 guests were resolved.

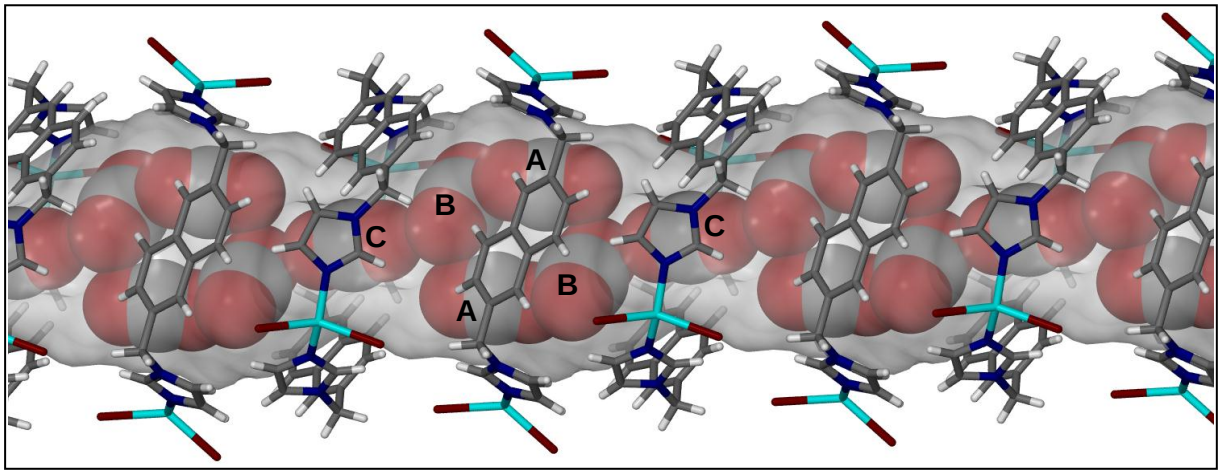

Figure 4.28 CO_2 molecules enclosed within a channel (semi-transparent grey surface with V = 577 Å^3, probe *r* = 1.4 Å) formed by the stacking of metallocycles in **M4·CO$_2$**. The unique guest molecules (and their closest symmetry related-positions) are labelled A-C. Only one of the two possible locations of guest B is shown.

In order to determine whether this exchange process is reversible, the crystal **M4·CO$_2$** was exposed to acetonitrile vapour and structure solution confirmed that the CO_2 molecules were indeed exchanged for acetonitrile. This part of the study was extended by exposing **M4·MeCN** to 11 bar acetylene and 3 bar vinyl chloride prior to X-ray data collections at 230 K, to respectively yield **M4·C$_2$H$_2$** and **M4·VCl**.

In **M4·C$_2$H$_2$**, the ASU comprises half a metallocycle and two acetylene guests; one of these guest molecules is disordered over two symmetry-related sites of equal occupancy across Wyckoff position *a* (shown in green and purple in Figure 4.29)A host:guest ratio of 1:3 is derived from the model and this ratio corresponds to the electron count of 93 e^- per unit cell (expect 84 e^- per unit cell). As for **M4·CO$_2$**, no appreciable host-guest interactions are present, but weak C–H···π guest-guest interactions (C_{donor}···Centroid ≈ 3.47 and 3.87 Å) between the two unique molecules promote guest stability (Figure 4.29). These interactions result in a guest packing motif similar to that observed in **M4·CS$_2$** (Figure 4.23).

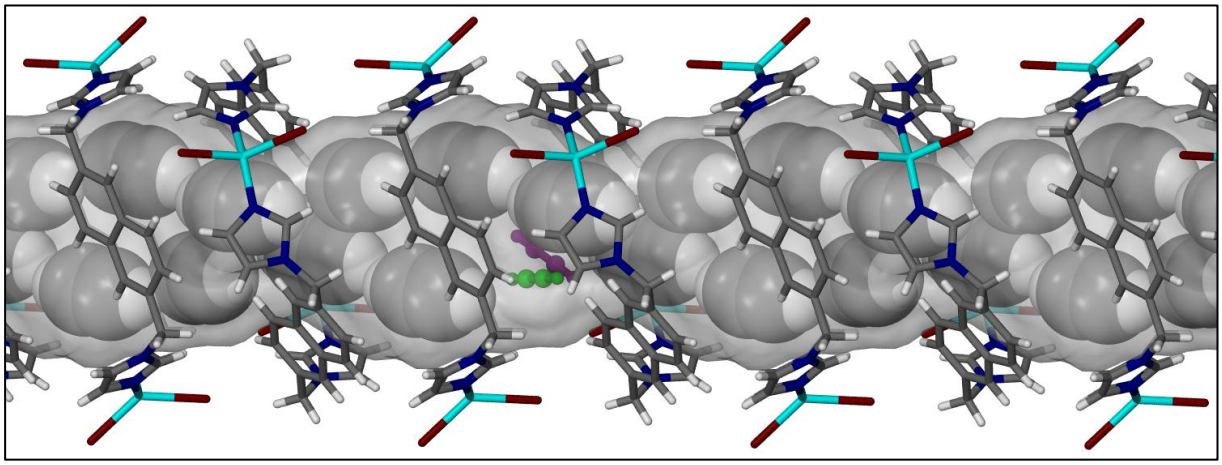

Figure 4.29 An acetylene-filled channel (V = 541 Å^3, probe r = 1.5 Å) in **M4·C$_2$H$_2$**. The guest molecules are shown in CPK colours and space-filling representation, except that one set of locations for the disordered guest is shown in green and purple. Only the positions that are symmetry-related to the green guest are shown for the rest of the channel.

In the crystallographic model of **M4·VCl** the ASU consists of half a molecule of **M4** and two half-occupancy vinyl chloride molecules (shown in green and purple in Figure 4.30). Symmetry-related guest positions across Wyckoff position *d* results in overlap of the two unique guests (Figure 4.30); the host:guest ratio is 1:2. Thus, each channel in **M4·VCl** exclusively contains either the green symmetry-related guest instances or the purple symmetry-related guest instances (Figures 4.30 and 4.31). While it appears that no considerable host-guest contacts are present in **M4·VCl**, Cl···Cl guest-guest interactions appear to stabilise the packing of the vinyl chloride molecules (Figure 4.31). All the chlorine atoms point towards the interior of the cavity in order to achieve favourable distances and angles for this interaction (*e.g.* $Cl_1\cdots Cl_1$ = 3.04 Å, $\angle$ Cl_1–Cl_1–C = 109.13°). In addition to the Cl···Cl halogen bonds, significant π···π guest-guest interactions (centroid···centroid ≈ 3.14 Å) assist in the stabilisation of **M4·VCl**.

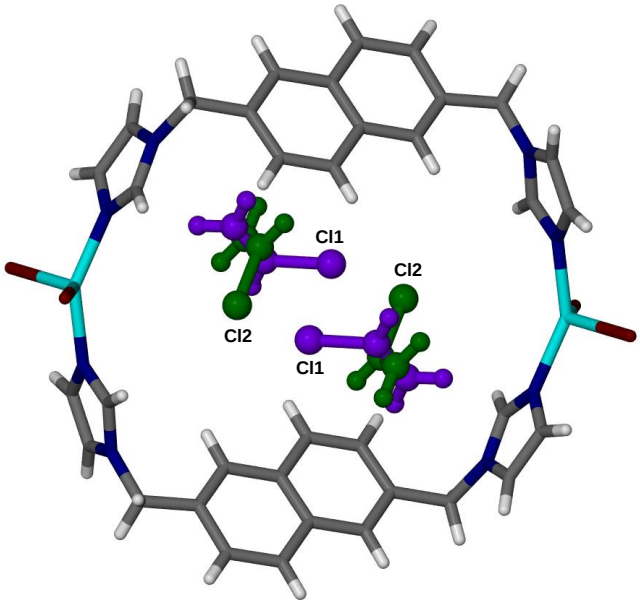

Figure 4.30 A perspective view showing the disorder of the vinyl chloride guests in **M4·VCl**. Unique guests are shown in green and purple. Only the chlorine atoms of the guest are labelled.

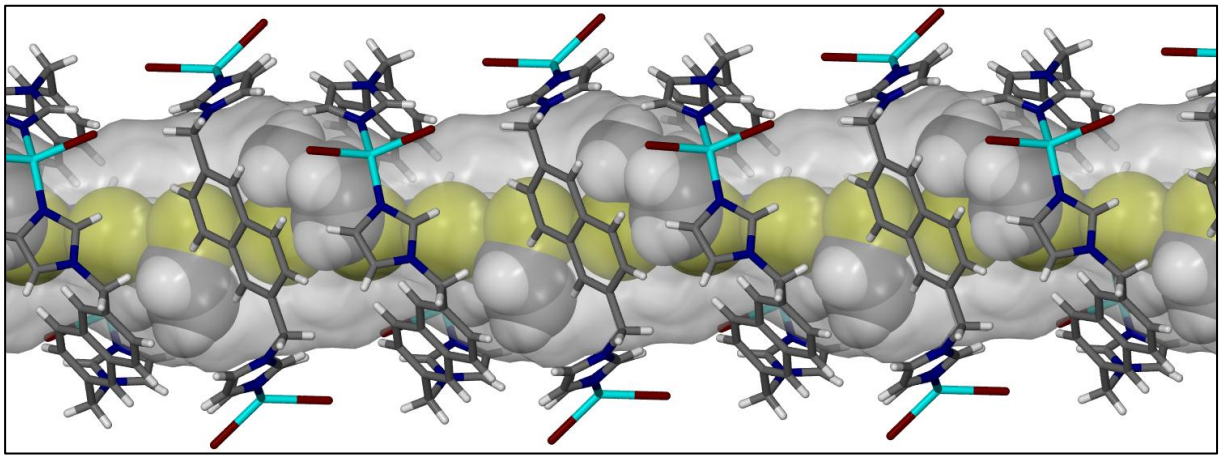

Figure 4.31 A plausible arrangement of vinyl chloride molecules within a conventional channel (shown as a semi-transparent Connolly surface with V = 572 Å^3 per unit cell, probe r = 1.5 Å) of **M4·VCl**. Although the guest molecules (in space-filling representation) are indicated in CPK colours, the specific arrangement shown here corresponds to the motif obtained from exclusively purple guests (in Figure 4.30).

4.3 Summary and general conclusions

The initial aim of this part of the study was to design and characterise novel porous metallocycles obtained from the self-assembly of ditopic coordinating ligands and transition metal salts. For this reason seven ligands having imidazole-based coordinating groups were synthesised. Only three of the ligands (**L3**, **L6** and **L7**) yielded metallocycles upon reaction with a range of transition metals salts.

The reaction of **L3** with $CoBr_2$ in acetonitrile resulted in a metallocycle **M1** and a single-crystal structure **M1·MeCN** reveals that **M1** encloses one acetonitrile molecule. All attempts at simply removing the included guest as a single-crystal to single-crystal transformation were unsuccessful. However, PXRD and DSC measurements showed that an as-yet unknown polycrystalline host phase (i.e. high temperature phase) is generated upon removal of the acetonitrile guest by heating the material at 150 °C. The host phase in **M1·MeCN** can be regenerated by exposing the high temperature phase to acetonitrile vapour.

Two conformationally different metallocycles **M2** and **M3** were obtained by layering of **L7** and $CuCl_2·2H_2O$ in benzene/methanol and solvothermal treatment of **L7** and $CuCl_2·2H_2O$ in benzene/methanol, respectively. In **M2·BZ** the metallocycle encloses one benzene molecule. The guest molecules in **M3·Mix** could not be modelled in an acceptable manner.

Slow evaporation of **L7** and $CuCl_2·2H_2O$ in acetonitrile produced yellow crystals of **M3·MeCN.** The structure **M3·Me_2CO** was obtained using an analogous experimental procedure. These complexes are very stable and desolvation of the guest appears to be unfavourable. We were unable to produce diffraction quality single crystals for a guest-exchange study. Instead, we investigated the exchange of acetonitrile for methanol, acetone, benzene, chloroform and 1,4-dioxane using solid-state UV-Vis spectroscopy and TGA. Although all the solvates of **M3** have a green reflectance band upon excitation at 320 nm, varying the guest results in slightly different reflectance band maxima.

Slow evaporation of an acetonitrile solution containing **L7** and $CuBr_2$ yielded crystals of **M4·MeCN**, which are isostructural to **M3·MeCN** with regard to the host packing. Once again the acetonitrile guest could not simply be removed from the metallocycles as a single-crystal process. However, in this instance it was possible to monitor guest-exchange processes as single-crystal to single-crystal transformations. Solvate structures **M4·H_2O**, **M4·MeOH**, **M4·Me_2CO**, **M4·DCM**, **M4·$CHCl_3$**, **M4·BZ**, **M4·CS_2** and **M4·Cy** were obtained by immersing **M4·MeCN** in the appropriate solvents. We can speculate on the mechanism of guest-exchange. Since thermally-induced desolvation coincides with the decomposition of

M4, guest-exchange is thought to proceed via an associative mechanism which involves squeezing the new guest through the aperture at one end of the channel and simultaneously releasing the acetonitrile guest at the other end.[32-33] This process is presumably facilitated by strong host-guest and guest-guest interactions. However, additional methods (such as computational studies and *in situ* Raman microspectrometry[32]) are needed to confirm these assumptions.

Finally, single crystals of **M4·MeCN** were exposed to small gaseous molecules (I_2, CO_2, C_2H_2 and vinyl chloride) with the aid of a miniature gas cell. Remarkably, it was possible to determine the binding sites of the gases in structures **M4·I_2**, **M4·CO_2**, **M4·C_2H_2** and **M4·VCl**. Apart from electrostatic association with the metal centre, which was apparent for CO_2 and I_2, no other strong host-guest interactions appear to be present in any of these structures. On the other hand, strong guest-guest interactions are present in all gas-included structures, the most prominent of which are the "T-shaped" C=O···C=O interactions in **M4·CO_2**. It also appears that desorption of the gas molecules does not occur readily and the crystals decompose after a few weeks of exposure to air; it seems that the metallocycle collapses (or dissociates) when its channels are empty. Measuring the sorption isotherms for these gases would be an important addition to the single-crystal structures, but would be difficult to interpret since the mass of the host-guest adduct will change in a complex fashion owing to the exchange taking place.

4.4 Experimental Section

4.4.1 Synthesis and characterisation

4.4.1.1 2,6-bis-(2-methyl-imidazol-1-ylmethyl)-pyridine[19] (L3)

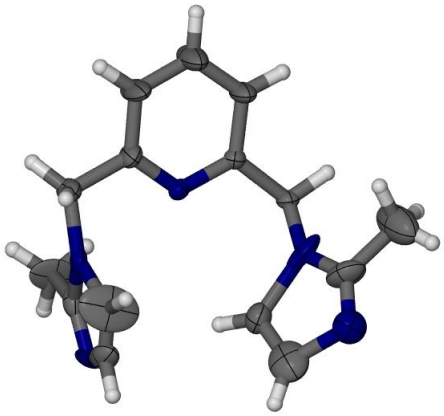

2-methyl-imidazole (8.20 g, 0.10 mol) and 2,6-bis-(bromomethyl)-pyridine (2.64 g, 0.01 mol) in 30 mL methanol were refluxed at 100 °C for 24 hrs. Whilst stirring, dry K_2CO_3 (12,00 g) was added and the reaction mixture refluxed for a further 2 hrs. The excess K_2CO_3 was filtered off prior to removing the methanol solvent under vacuum. The yellow oil that resulted was dissolved in chloroform and then washed with water. A pure product (colourless crystals, yield = 91%) was obtained by recrystallisation from a chloroform/ether solution. Characterisation was carried out by means of SCD and NMR. The NMR spectra confirmed the bulk purity of the product and can be found on the attached CD.

Crystal data for **L3**: $C_{15}H_8N_5$, M = 258.26, triclinic, space group $P\bar{1}$, a = 15.842(1), b = 10.816(1), c = 8.143(7) Å, $\alpha = \beta = \gamma = 90°$, V = 1395(2) Å^3, Z = 4, D_c = 1.230 g/cm^3, F_{000} = 532, 8571 reflections collected, 5862 unique (R_{int} = 0.0281). Final *GooF* = 1.813, *R1* = 0.1735, *wR2* = 0.4686, *R* indices based on 3626 reflections with I >2sigma(I) (refinement on F^2).

4.4.1.2 2,6-bis-(imidazol-1-ylmethyl)-naphthalene (L7)[21]

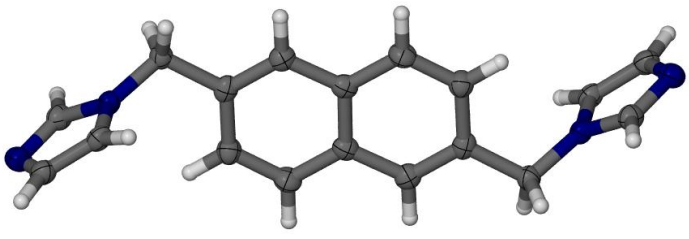

A solution containing imidazole (4,00 g, 10 mmol) and 2,6-bis-(bromomethyl)benzene (1.50 g, 1 mmol) in 100 mL methanol was refluxed at 80 °C for 16 hrs. Anhydrous K_2CO_3 (6,00 g) was added and the mixture was continuously stirred for 2 hrs. A yellow oily product resulted after the solvent was removed under reduced pressure. The oil was dissolved in chloroform and then thoroughly washed with water. The organic layer (chloroform) was extracted prior to recrystallisation from a chloroform/ether solution.

Colourless needle-shaped crystals (yield = 77%) resulted. These crystals were analysed using SCD and NMR. The NMR spectra confirmed the bulk purity and can be found on the attached CD.

Crystal data for **L7**: $C_{18}H_{16}N_4$, M = 288.35, monoclinic, space group $P2_1/n$, a = 6.217(3), b = 5.619(2), c = 20.317(8) Å, β = 91.799(6)°, V = 709.4(5) Å^3, Z = 2, D_c = 1.350 g/cm^3, F_{000} = 304, T = 100(2)K, 3749 reflections collected, 1518 unique (R_{int} = 0.0315). Final *GooF* = 1.044, *R1* = 0.0610, *wR2* = 0.1476, *R* indices based on 1128 reflections with I >2sigma(I) (refinement on F^2).

4.4.1 Crystallographic Tables

.

Table 4.4 Crystallographic data for all structures discussed in Chapter 4.

	M1·MeCN	**M2·BZ**	**M3·MeCN**	**M3·Me_2CO**
Empirical formula	$C_{34}H_{40}Br_4Co_2N_{12}$	$C_{42}H_{38}Cl_4Cu_2N_8$	$C_{40}H_{38}Cl_4Cu_2N_{10}$	$C_{42}H_{44}Cl_4Cu_2N_8O_2$
Formula weight	1054.28	923.68	927.68	961.73
Temperature/K	100(2)	100(2)	100(2)	100(2)
Wavelength/Å	0.71073	0.71073	0.71073	0.71073
Crystal system	monoclinic	monoclinic	monoclinic	monoclinic
Space group	*C*2/*m*	$P2_1/c$	*C*2/*c*	*C*2/*c*
a /Å	14.482(6)	13.181(5)	26.039(5)	26.341(5)
b /Å	22.703(9)	14.616(5)	14.354(3)	14.467(3)
c /Å	7.084(7)	10.594(4)	12.706(2)	12.746(3)
α /°	90.00	90	90	90.00
β /°	116.460(2)	97.579(6)	117.555(2)	118.294(3)
γ /°	90.00	90	90	90.00
Volume/$Å^3$	2085(2)	2023.0(12)	4210.2(14)	4276.9(15)
Z	2	2	4	4
Calculated density/g cm^{-3}	1.679	1.516	1.464	1.494
Absorption coefficient (mm^{-1})	4.669	1.358	1.307	1.291
F_{000}	1044	944	1896	1976
Reflections collected	5968	11969	12441	12566
Independent reflections	2304 [R_{int} = 0.0667]	4450 [R_{int} = 0.0665]	4579 [R_{int} = 0.1125]	4673 [R_{int} = 0.0665]
Data/restraints/parameters	2304 / 0 / 128	4450 / 0 / 238	4579 / 0 / 254	4673 / 8 / 303
Goodness-of-fit on F^2	0.863	1.184	1.100	1.221
Final *R* indices [$I>2\sigma(I)$]	*R*1 = 0.0523, *wR*2 = 0.1263	*R*1 = 0.0733, *wR*2 = 0.1866	*R*1 = 0.0714, *wR*2 = 0.1477	*R*1 = 0.0625, *wR*2 = 0.1405
R indices (all data)	*R*1 = 0.0986, *wR*2 = 0.1567	*R*1 = 0.1355, *wR*2 = 0.2283	*R*1 = 0.1731, *wR*2 = 0.1803	*R*1 = 0.1268, *wR*2 = 0.1757

Table 4.4 Continued.

	M4·MeCN	**M4·H_2O**	**M4·MeOH**	**M4·Me_2CO**
Empirical formula	$C_{40}H_{38}Br_4Cu_2N_{10}$	$C_{34}H_{40}Br_4Cu_2N_8O_{10}$	$C_{39}H_{41}Br_4Cu_2N_8O_3$	$C_{42}H_{44}Br_4Cu_2N_8O_2$
Formula weight	1105.52	1151.78	1116.52	1139.57
Temperature/K	100(2)	100(2)	100(2)	100(2)
Wavelength/Å	0.71073	0.71073	0.71073	0.71073
Crystal system	monoclinic	monoclinic	monoclinic	monoclinic
Space group	*C*2/*c*	*C*2/*c*	*C*2/*c*	*C*2/*c*
a /Å	26.433(5)	26.532(7)	26.5375(19)	26.413(2)
b /Å	14.494(3)	14.551(4)	14.4855(10)	14.6167(12)
c /Å	13.146(2)	13.062(3)	12.9626(9)	13.0538(10)
α /°	90	90	90	90
β /°	119.203(2)	118.012(3)	118.954(2)	118.6330(10)
γ /°	90	90.00	90	90
Volume/$Å^3$	4396.5(13)	4451.8(19)	4360.1(5)	4423.4(6)
Z	4	4	4	4
Calculated density/g cm^{-3}	1.670	1.718	1.701	1.711
Absorption coefficient (mm^{-1})	4.644	4.601	4.687	4.620
F_{000}	2184	2265	2212	2264
Reflections collected	12140	13712	17371	12332
Independent reflections	4734 [R_{int} = 0.0609]	5255 [R_{int} = 0.0659]	4813 [R_{int} = 0.0302]	4809 [R_{int} = 0.0243]
Data/restraints/parameters	4734 / 0 / 283	5255 / 0 / 263	4813 / 0 / 265	4809 / 0 / 297
Goodness-of-fit on F^2	0.988	0.968	1.022	0.861
Final *R* indices [$I>2\sigma(I)$]	*R*1 = 0.0515, *wR*2 = 0.1184	*R*1 = 0.0611, *wR*2 = 0.1506	*R*1 = 0.0399, *wR*2 = 0.1033	*R*1 = 0.0326, *wR*2 = 0.1014
R indices (all data)	*R*1 = 0.0920, *wR*2 = 0.1350	*R*1 = 0.1263, *wR*2 = 0.1794	*R*1 = 0.0532, *wR*2 = 0.1098	*R*1 = 0.0428, *wR*2 = 0.1120

Table 4.4 Continued.

	M4·DCM	**M4·$CHCl_3$**	**M4·CS_2**	**M4·BZ**
Empirical formula	$C_{38}H_{36}Br_4Cl_4Cu_2N_8$	$C_{37}H_{33}Br_4Cl_3Cu_2N_8$	$C_{38}H_{32}Br_4Cu_2N_8S_4$	$C_{46}H_{28}Br_4Cu_2N_8$
Formula weight	1193.27	1142.78	1175.68	1134.68
Temperature/K	100(2)	100(2)	100(2)	100(2)
Wavelength/Å	0.71073	0.71073	0.71073	0.71073
Crystal system	monoclinic	monoclinic	monoclinic	monoclinic
Space group	*C*2/*c*	*C*2/*c*	*C*2/*c*	*C*2/*c*
a /Å	26.630(8)	26.657(8)	26.580(5)	27.117(6)
b /Å	14.434(4)	14.470(4)	14.482(3)	14.181(3)
c /Å	12.998(4)	12.962(4)	12.899(3)	12.981(3)
α /°	90	90	90.00	90
β /°	117.627(4)	117.680(4)	118.785(2)	116.279(3)
γ /°	90	90	90.00	90
Volume/$Å^3$	4426(2)	4428(2)	4351.6(15)	4475.8(16)
Z	4	4	4	4
Calculated density/g cm^{-3}	1.791	1.714	1.795	1.684
Absorption coefficient (mm^{-1})	4.852	4.788	4.881	4.563
F_{000}	2344	2240	2312	2222
Reflections collected	13733	5872	12758	13308
Independent reflections	5190 [R_{int} = 0.0532]	744 [R_{int} = 0.0601]	4866 [R_{int} = 0.0372]	5286 [R_{int} = 0.0559]
Data/restraints/parameters	190 / 4 / 282	1744 / 9 / 273	4866 / 8 / 271	5286 / 0 / 253
Goodness-of-fit on F^2	1.038	1.143	1.034	1.043
Final *R* indices [$I>2\sigma(I)$]	*R*1 = 0.0578, *wR*2 = 0.1407	*R*1 = 0.0575, *wR*2 = 0.1485	*R*1 = 0.0390, *wR*2 = 0.0931	*R*1 = 0.0586, *wR*2 = 0.1455
R indices (all data)	*R*1 = 0.1018, *wR*2 = 0.1595	*R*1 = 0.0764, *wR*2 = 0.1623	*R*1 = 0.0602, *wR*2 = 0.1011	*R*1 = 0.1083, *wR*2 = 0.1682

Table 4.4 Continued.

	M4·Cy	**M4·I_2**	**M4·CO_2**	**M4·C_2H_2**
Empirical formula	$C_{42}H_{44}Br_4Cu_2N_8$	$C_{36}H_{24}Br_4Cu_2I_{0.85}N_8$	$C_{39}H_{32}Br_4Cu_2N_8O_5$	$C_{42}H_{38}Br_4Cu_2N_8$
Formula weight	1106.56	1123.22	1139.45	1101.52
Temperature/K	100(2)	100(2)	240(2)	229(2)
Wavelength/Å	0.71073	0.71073	0.71073	0.71073
Crystal system	monoclinic	monoclinic	monoclinic	monoclinic
Space group	*C*2/*c*	*C*2/*c*	*C*2/*c*	*C*2/*c*
a /Å	26.735(6)	26.605(7)	26.692(4)	26.670(3)
b /Å	14.328(3)	14.456(4)	14.581(2)	14.5591(13)
c /Å	12.906(3)	12.968(4)	13.124(2)	13.0813(12)
α /°	90	90	90	90
β /°	117.841(3)	118.576(4)	117.155(2)	118.652(2)
γ /°	90	90	90	90
Volume/$Å^3$	4371.5(18)	4380(2)	4544.9(12)	4457.5(7)
Z	4	4	4	4
Calculated density/g cm^{-3}	1.681	1.703	1.665	1.641
Absorption coefficient (mm^{-1})	4.669	5.253	4.502	4.579
F_{000}	2198	2156	2240	2176
Reflections collected	12462	13437	13443	17432
Independent reflections	5121 [R_{int} = 0.0994]	5145 [R_{int} = 0.0878]	5210 [R_{int} = 0.0281]	6190 [R_{int} = 0.0365]
Data/restraints/parameters	5121 / 0 / 254	5145 / 0 / 246	1.053	6190 / 2 / 243
Goodness-of-fit on F^2	0.917	1.064	*R*1 = 0.0470, *wR*2 = 0.1419	0.895
Final *R* indices [$I>2\sigma(I)$]	*R*1 = 0.0579, *wR*2 = 0.1283	*R*1 = 0.0695, *wR*2 = 0.1718	*R*1 = 0.0701, *wR*2 = 0.1564	*R*1 = 0.0475, *wR*2 = 0.1300
R indices (all data)	*R*1 = 0.1534, *wR*2 = 0.1717	*R*1 = 0.1506, *wR*2 = 0.2029		*R*1 = 0.0739, *wR*2 = 0.1498

Table 4.4 Continued.

	M4·VCl
Empirical formula	$C_{38}H_{35}Br_4ClCu_2N_8$
Formula weight	1085.91
Temperature/K	298(2)
Wavelength/Å	0.71073
Crystal system	monoclinic
Space group	*C*2/*c*
a /Å	26.664(3)
b /Å	14.5998(16)
c /Å	13.1153(15)
α /°	90
β /°	117.3890(10)
γ /°	90
Volume/Å^3	4533.3(9)
Z	4
Calculated density/g cm^{-3}	1.591
Absorption coefficient (mm^{-1})	4.558
F_{000}	2136
Reflections collected	8078
Independent reflections	4386 [R_{int} = 0.0256]
Data/restraints/parameters	4386 / 6 / 251
Goodness-of-fit on F^2	1.057
Final *R* indices [$I>2\sigma(I)$]	*R*1 = 0.0718, *wR*2 = 0.2267
R indices (all data)	*R*1 = 0.1050, *wR*2 = 0.2781

4.5 References

[1] J. W. Steed, J. L. Atwood, *Supramolecular Chemistry*, John Wiley & Sons Ltd, West Sussex, **2000**.

[2] R. M. Barrer, *Zeolites and Clay Minerals as Sorbents and Molecular Sieves*, London: Academic Press Inc., **1978**.

[3] D. W. Breck, in *Structure, Chemistry and Use*, John Wiley and Sons, Inc., **1974**.

[4] D. Tanaka, S. Kitagawa, *Chem. Mater.*, **2007**, *20*, 922-931.

[5] S. Kitagawa, R. Kitaura, S. I. Noro, *Angew. Chem. Int. Ed.* **2004**, *43*, 2334-2375.

[6] H. v. Bekkum, E. M. Flanigen, J. C. Jansen, Elsevier Science Publishers, B.V., **1991**.

[7] G. Ferèy, C. Serre, *Chem. Soc. Rev.* **2009**, *38*, 1380-1399.

[8] L. Dobrzańska, E. J. C. de Vries, *Inorg. Chim. Acta* **2007**, *360*, 1584-1592.

[9] L. Dobrzańska, D. J. Kleinhans, L. J. Barbour, *New J. Chem.* **2008**, *32*, 813-819.

[10] L. Dobrzańska, G. O. Lloyd, L. J. Barbour, *New J. Chem.* **2007**, *31*, 669-676.

[11] L. Dobrzańska, G. O. Lloyd, C. Esterhuysen, L. J. Barbour, *Angew. Chem. Int. Ed.* **2006**, *45*, 5856-5859.

[12] L. Dobrzańska, G. O. Lloyd, H. G. Raubenheimer, L. J. Barbour, *J. Am. Chem. Soc.* **2005**, *128*, 698-699.

[13] L. Dobrzańska, G. O. Lloyd, H. G. Raubenheimer, L. J. Barbour, *J. Am. Chem. Soc.* **2005**, *127*, 13134-13135.

[14] T. Jacobs, J. Gertenbach, D. Das, L. J. Barbour, *Aust. J. Chem.* **2010**, *63*, 573-577.

[15] G. O. Lloyd, *Crystal Engineering of Porosity (MSc Thesis), in Department of Chemistry & Polymer Science*, Stellenbosch University, **2006**.

[16] T. Jacobs, *Design and Construction of Novel Porous Materials (PhD Thesis), in Department of Chemistry & Polymer Science*, Stellenbosch University, **2007**.

[17] C. Y. Li, C. S. Liu, J. R. Li, X. H. Bu, *Cryst. Growth Des.* **2007**, *7*, 286-295.

[18] Z.-L. Jiang, R. S. Xiao, Xiao-Yu, J.-M. Yan, R.-G. Xie, *Gaodeng Xuexiao Huaxue Xuebao* **2003**, *1*, 64-67.

[19] C. H. Zhou, S. J. Guo, R. G. Xie, H. M. Zhao, *Chin. Chem. Lett.* **1996**, *7*, 321-324.

[20] D. Mihele, E. Cristea, T. O. Nicolescu, *Farmacia* **2000**, *48*, 51-56.

[21] P. D. Dhal, F. H. Arnold, *Macromolecules* **1992**, *25*, 7051-7059.

[22] C.-Y. Li, C.-S. Liu, J.-R. Li, X.-H. Bu, *Cryst. Growth Des.* **2007**, *7*, 286-295.

[23] L. Dobrzańska, G. O. Lloyd, H. G. Raubenheimer, L. J. Barbour, *J. Am. Chem. Soc.* **2006**, *128*, 698-699.

[24] P. van der Sluis, A. L. Spek, *SQUEEZE Manual* **1990**.

[25] PLATON, Utrecth University, Utrecht, The Netherlands, **2008**.

[26] Q.-K. Liu, J.-P. Ma, Y.-B. Dong, *Chem. Eur. J.* **2009**, *15*, 10364-10368.

[27] A. M. Shultz, O. K. Farha, D. Adhikari, A. A. Sarjeant, J. T. Hupp, S. T. Nguyen, *Inorg. Chem.* **2011**, *50*, 3174-3176.

[28] A. P. Nelson, O. K. Farha, K. L. Mulfort, J. T. Hupp, *J. Am. Chem. Soc.* **2009**, *131*, 458-460.

[29] O. K. Farha, J. T. Hupp, *Acc. Chem. Res.* **2010**, *43*, 1166.

[30] J. T. Hupp, O. K. Farha, *U.S. Pat. Appl. Publ.* **2011**, *20110144367*.

[31] K. L. Kauffman, J. T. Culp, A. Goodman, C. Matranga, *J. Phys. Chem. C* **2011**, *115*, 1857-1866.

[32] K. D. M. Harris, *Supramol. Chem.* **2007**, *19*, 47-53.

[33] M. D. Pluth, K. N. Raymond, *Chem. Soc. Rev.* **2007**, *36*, 161-171.

Stellenbosch University http://scholar.sun.ac.za

Chapter 5
Properties of flexible metallocycles

5.1 Introduction

The rationale for designing "doughnut-shaped" molecules is that the rigidity of the host conformation is a prerequisite for successful performance as porous materials, because flexibility would lead to a collapse of the host phase upon removing the templating solvent. On the other hand, metalloproteins take advantage of their structural flexibility, which appears to be essential for carrying out their molecular recognition functions in biological environments.[1] Much effort has been devoted to designing flexible MOFs (*i.e.* third generation MOFs such as that shown in Figure 5.1)[2] that reversibly adapt their frameworks to respond to external stimuli (e.g. guests,[1, 3-4] pressure,[5-6] light, temperature[7] and electric or magnetic fields). Depending on the system itself, an expansion or contraction (*i.e.* breathing transition)[8] of the cell volume is associated with the input stimulus.

Guest-induced flexible frameworks act as sponges and in most cases imply significant atomic displacement during transition (in the range of 2-4 Å).[9] During this process the size of the sorbed guest does not have steric influences on the swelling and only host-guest and guest-guest interactions are thought to be involved in this process.[8] While many examples of breathing transitions have been reported (the MIL-series in particular),[3, 5, 10-13] only a few examples of single-crystal to single-crystal breathing are known owing to the enormous strain on the host conformation. To the best of our knowledge, such breathing transitions have not been observed for seemingly rigid metallocycles.

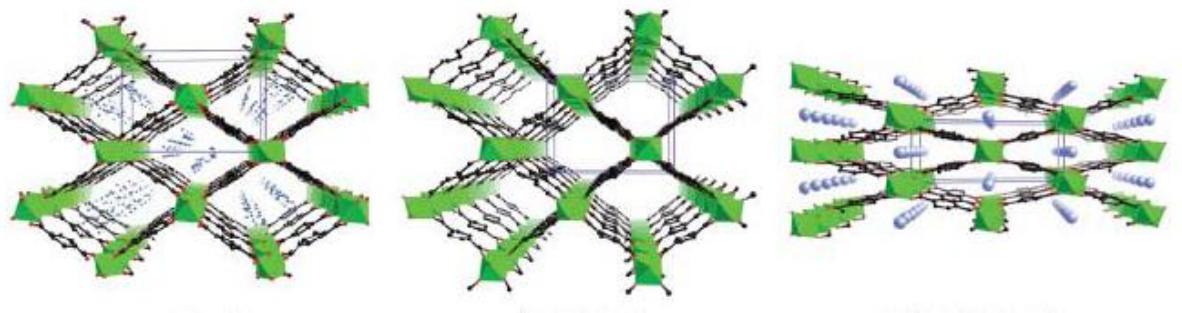

Figure 5.1 The different breathing transitions of MIL-53; a) as-synthesised "closed" phase, b) high-temperature "open" phase, and c) room temperature "hydrated" phase. This process is associated with enormous unit cell parameter changes.[9]

Stellenbosch University http://scholar.sun.ac.za

As mentioned in Chapter 4, obtaining the single-crystal structure of the apohost is not essential for industrial applications. Knowing the host conformation and the nature of the interactions of the initial (*e.g.* empty host) and the final (*e.g.* guest-induced "expanded" host), respectively, allows us to propose a mechanism that facilitates the sorption process. Unfortunately, we were unable to obtain apohost structures of metallocycles **M3** and **M4**, although "tilting" of the naphthalene rings formulates them to be excellent candidates for shape-responsive fitting[1] studies where sorption of guest molecules is facilitated by displacement of the rings. Instead, we focused our attention on metallocycle **M5**.

This work is a continuation of previous work in the Barbour Group, which reported a metallocycle obtained by reacting (in methanol) 1,3-bis(imidazolyl-1-ylmethyl)-2,4,6-trimethylbenzene (**L6**, in Scheme 5.1) with $CuCl_2{\cdot}2H_2O$ in a 1:1 molar ratio to yield $[Cu_2(\mathbf{L6})_2Cl_4]{\cdot}H_2O{\cdot}CH_3OH$, **M5·H₂O·MeOH**.[14]

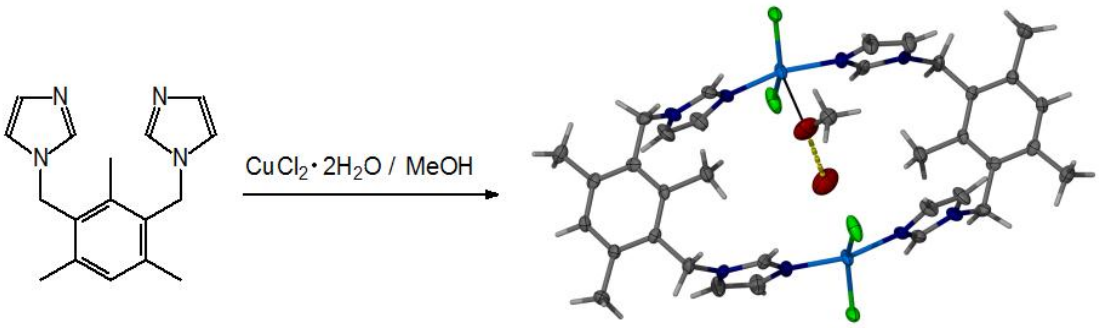

Scheme 5.1 Formation of $[Cu_2(\mathbf{L6})_2Cl_4]{\cdot}H_2O{\cdot}CH_3OH$ (**M5·H₂O·MeOH**).[14]

Each copper ion is coordinated to two anions and two **L6** ligands in a distorted square planar arrangement, with **L6** ligands situated *trans* to each other. The metallocycles are canted at an angle of approximately 40° with respect to the crystallographic *a*-axis. The packing of **M5·H₂O·MeOH** is characterised by host complexes that stack to form linear columns along [100]. The space within each complex ring is occupied by a hydrogen bonded two-membered adduct (heterodimer) consisting of one water and one methanol molecule. The solvent heterodimer is disordered over two positions across a crystallographic inversion centre. Crystals of **M5·H₂O·MeOH** were shown to undergo guest removal by mild heating and evacuation without any discernable loss of their integrity as single crystals, and a guest free structure (**M5a**) was determined by single-crystal diffraction (SCD) – see Scheme 5.2 and Figure 5.2(a). No significant change in the framework occurs upon solvent removal and

Stellenbosch University http://scholar.sun.ac.za

the space within the complex is empty (*i.e.* no appreciable electron density is present within the ring previously occupied by the solvent adduct). Thus, desolvation of **M5·H_2O·MeOH** occurs as a single-crystal to single-crystal transformation.[15-17] The program MSROLL[18-19] was used to probe the solvent-accessible space within the coordination complex. A detailed Connolly surface analysis shows that the empty structure lacks pores or channels, but displays discrete voids or pockets (volume ≈ 108 $Å^3$ using a probe radius of 1.4 Å in Figure 5.2 top). Furthermore, the framework does not appear to shrink upon removing the solvent as occurs with most of the reported coordination complexes in the literature.[4] The unoccupied space in **M5** is estimated to be approximately 6% of the total volume.

Dobrzańska *et al*. further showed that **M5** is permeable to gas molecules (CO_2, I_2, H_2, CO, CH_3, N_2) at relatively low pressures, although it is not porous in the conventional sense (*i.e.* guest molecules are not situated in continuous channels or pores).[14] Controlled CO_2 pressure single-crystal X-ray studies (as yet unpublished) indicate that the CO_2 gas molecules are located within the discrete pockets. Sorption experiments performed on the bulk material indicate host to guest ratios of 1:1 for all of the structures. Molecular mechanics simulations carried out by J. Dillen suggest that gas molecules such as CO_2 and I_2 are transferred from one pocket to another (within a stacked column) by means of a 1D diffusion mechanism.[20] The simulation implies that transport through the transiently porous material **M5** is facilitated by "flapping" of the imidazole (*Im*) rings of **L6** to create a temporary channel (*i.e.* two discrete pockets temporarily merge – see Figure 5.2(b and c)) between two successive hosts. Thus, the imidazole rings act as gates to assist the transport of the gas molecules.

Stellenbosch University http://scholar.sun.ac.za

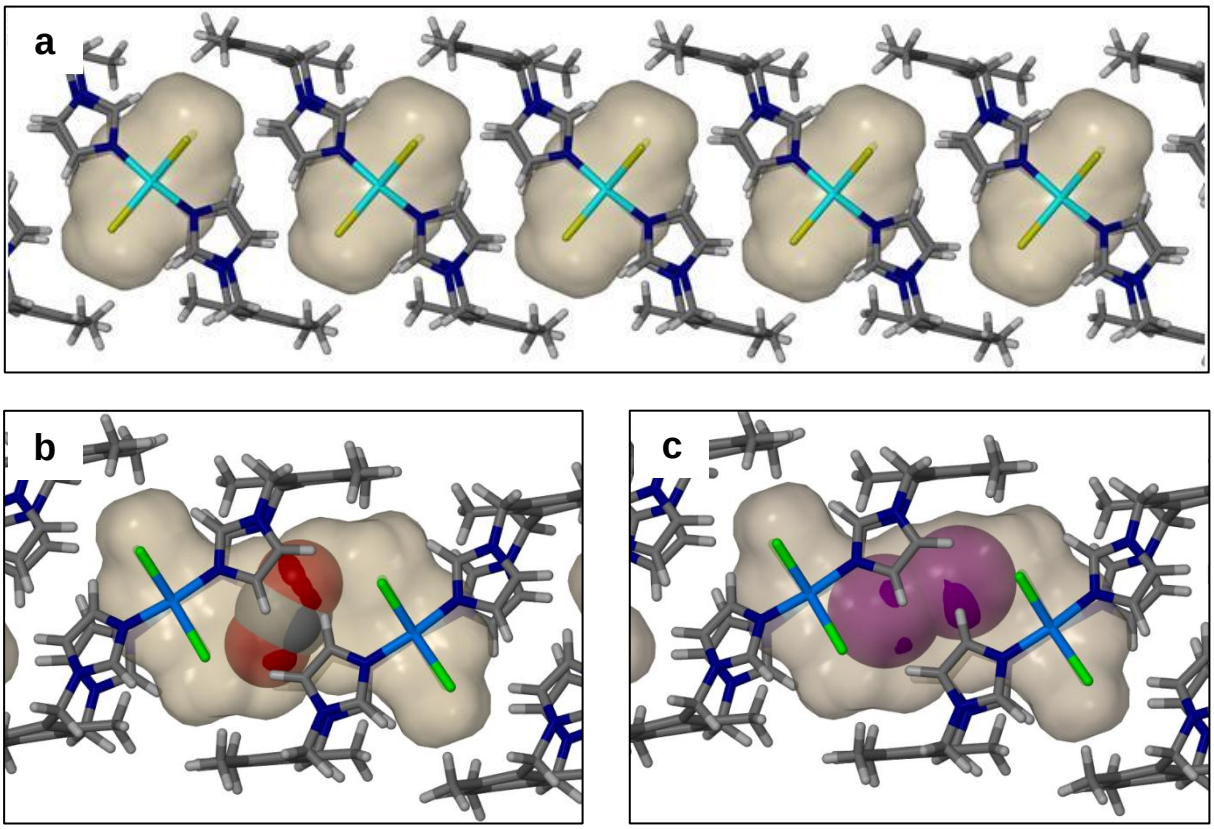

Figure 5.2 (a)Capped-stick representation of the desolvated host **M5**, illustrating the empty pockets[14] (probe *r* = 1.4 Å, volume ≈ 108 Å^3) mapped as a semi-transparent Connolly surface. Perspective views of the short-lived transition states (temporary channel between two adjacent metallocycles, shown as grey surfaces) indicating the possible mechanism of transport[20] (b) for CO_2 and (c) I_2 molecules from one void to another.

Previous studies have shown that both **M5** and [Cd_2**L**$_2Cl_4$] (see Chapter 4) are permeable to small gas molecules and that displacement of the imidazole rings plays a major part in the transport mechanism. Questions have arisen regarding the extent to which this guest-induced flexibility can be exploited.[14] We note that this system would not be considered a good candidate for commercial gas storage owing to its relatively high density (1.42 g.cm^{-3}) and low storage capacity. However, the reversible nature of gas exchange, along with the retention of monocrystallinity of **M5,** provides an excellent opportunity to study the reversible diffusion of larger guest molecules. The reversible exchange of guest molecules has industrial applications such as separation,[21] water purification[22] and drug delivery.[12]

As mentioned earlier, the retention of monocrystallinity of discrete metallocycles such as **M5** provides an opportunity to gain considerable insight into the ability of the host lattice to adapt to organic guests of different shapes, sizes and chemical properties, along with

Stellenbosch University http://scholar.sun.ac.za

information on host-guest and guest-guest interactions (see chapter 4). Measurement of the isosteric enthalpy of sorption is one of the most basic thermodynamic characterisation methods for adsorbents and is useful in optimising the sorption process.[23] Understanding the fundamental physico-chemical and structural properties such as uptake capacity, guest affinity and metallocycle flexibility induced by pressure stimuli, has the potential to enhance the industrial applications mentioned above.

In the present study, the gas sorption experiments of **M5** (initially carried out by Lloyd[21] and Dobrzańska[14] were extended by locating the guest positions of additional gases within the discrete pockets using SCD (by means of an environmental gas cell). We have thus verified the binding sites for CO_2, CO, C_2H_2 and C_2H_3Cl – Table 5.1. The host:guest ratio of the CO_2-included structure **M5·CO2** was confirmed by controlled pressure sorption measurements. The ease with which these gaseous molecules can diffuse through **M5** prompted us to investigate its permeability to larger guest molecules. Thus, the aim of this part of the study is to study structure-property relationships by determining the thermodynamic parameters associated with sorption of organic molecules, with a view to ultimately understanding the mechanism of guest transport in a transiently porous supramolecular system such as host **M5** (Scheme 5.2). To carry out such a study, the first step is to determine whether **M5** is porous to the solvents listed in Table 5.2. Information on the structural consequences of guest sorption in the unconventionally porous framework can be obtained by means of accurate single-crystal X-ray diffraction measurements. Supporting studies using sorption and thermal analyses provide valuable information on the energies associated with the sorption and desorption processes for various guest molecules.

Stellenbosch University http://scholar.sun.ac.za

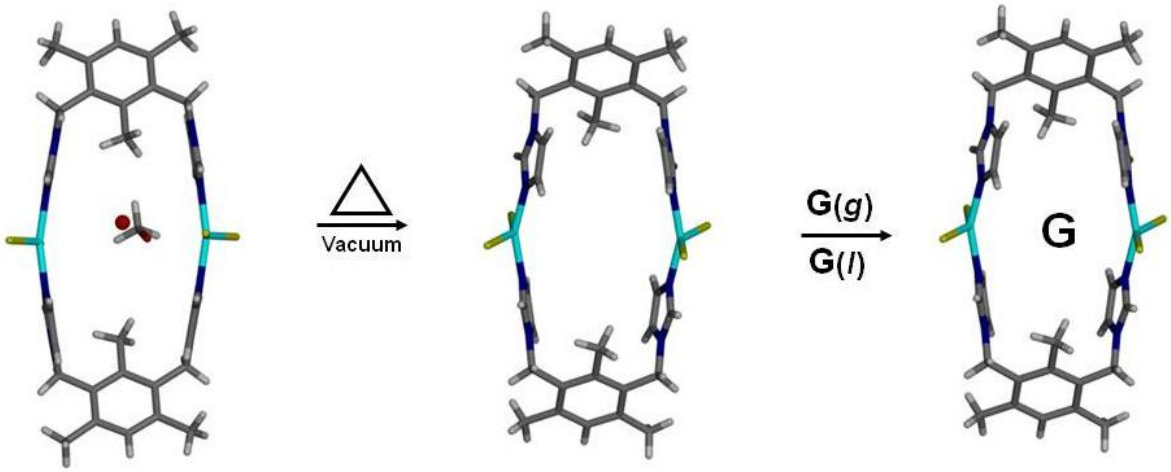

Scheme 5.2 An outline for the reversible exchange of the guests listed in Tables 5.1-5.3 using **M5** as the host. The resulting complex is indicated as **M5·G** (where G represents the included guest molecules) in each case.

The first part of the study was based on the assumption that sorption of the guests at the solid-liquid interface would yield the same complexes as at the solid-vapour interface. The guest uptake was determined as a function of the relative vapour pressure. In the second part of the study we investigated the permeability of **M5** to volatile organic *solids* in order to test the sensitivity of the host system and the size limit of guests that can permeate. Although the permeability of **M5** to many other guests was investigated (such as camphor, *p*-diiodobenzene, *p*-dibromobenzene, 4'4-bipyridyl, quinoline, quinoxaline and *p*-dimethoxybenzene), the uptake of only naphthalene and *p*-dichlorobenzene will be discussed (Table 5.3). For this part of the study we were not able to determine the thermodynamic parameters, but the experimental setup instead allowed the measurement of sorption isotherms as kinetic curves. Finally, with the aid of high quality single-crystal data of host-guest interactions, in combination with accurate molecular mechanics calculations, a possible mechanism for the transport of these large guests is discussed.

Table 5.1 Selected properties of the gas molecules used in this Chapter.

Mnemonic	Solvent	Formula	Molecular weight (g. mol^{-1})	Electron count	Critical temperature (°)
CO_2	Carbon dioxide	CO_2	44.0	22	31.1
CO	Carbon monoxide	CO	28.0	14	-140.3
C_2H_2	Acetylene	C_2H_2	26.0	14	35.1
VCl	Vinyl chloride	C_2H_3Cl	62.5	42	156.5

Table 5.2 Selected properties of the solvents used in this Chapter.

Mnemonic	Solvent	Formula	Molecular weight (g mol^{-1})	Boiling Point (ºC)	Density (g cm^{-3})	Density conversion factor	Vapour Pressure (mmHg @ 20 º)
H_2O	Water	H_2O	18.0	100.0	1.00	0.001	20.0
MeOH	Methanol	CH_3OH	32.0	64.7	0.79	0.002	97.3
Me_2CO	Acetone	C_3H_6O	58.1	56.3	0.79	0.003	183.1
MeCN	Acetonitrile	CH_3CN	41.1	81.6	0.79	0.002	72.0
DCM	Dichloromethane	CH_2Cl_2	84.9	39.8	1.33	0.003	350.0
$CHCl_3$	Chloroform	$CHCl_3$	119.4	61.2	1.48	0.004	157.1
CS_2	Carbon disulfide	CS_2	76.1	46.3	1.26	0.003	500.0
BZ	Benzene	C_6H_6	78.1	80.1	0.87	0.004	75.1
DFB	*p*-Difluorobenzene	$C_6H_4F_2$	114.3	88.82	1.17	0.004	72.0

Table 5.3 The molecular structures and selected properties of the volatile *solids* used in this Chapter.

Mnenomic	guest	Formula	Structure	Molecular weight (g. mol^{-1})	Melting Point (ºC)	Vapour Pressure (mmHg @ 20 ºC)
Naph	Naphthalene	$C_{10}H_8$	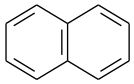	128.2	88.5	0.08
DCB	*p*-Dichlorobenzene	$C_6H_4Cl_2$	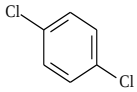	147.0	53.1	1.76

5.2 Results and discussion

5.2.1 Gas sorption studies: determination of the guest binding-site

As discussed in Section 5.1, a series of gas sorption measurements has been carried out for **M5**.[14] However, these experiments involved exposing the material to a constant pressure and the experimental setup did therefore not allow systematic monitoring of the gas uptake at gas pressures below 1 bar. Additionally, advances in single-crystal X-ray diffraction methods in combination with the development of a miniature gas cell (constructed by our group – see Chapter 2) has led to the precise determination of gas coordinates in some porous crystals. In this section we report the single-crystal structures of four gas-included complexes of **M5** (**M5·CO_2**, **M5·CO**, **M5·C_2H_2** and **M5·VCl**) and compare **M5·CO_2** with controlled pressure volumetric sorption measurements. Surprisingly, the flexible nature of **M5** facilitates the uptake of CO_2 molecules even at a gas pressure of less than 1 bar.

Adjustments of the metallocycle conformation will be discussed in terms of deviations in $Cu^{2+}\cdots Cu^{2+}$ distance and the centroid···centroid distance between opposite *Im* rings (e.g. *Im*···*Im*). Additionally, host:guest ratios as inferred from electron counts within the accessible volume were calculated using PLATON.[24] The gas-included structures will be discussed separately in the ensuing sections.

5.2.1.1 M5·CO_2

Information on the mechanism of CO_2 transport (Figure 5.2) has led us to investigate whether it is possible to create a permanent CO_2-filled channel by forcing an extra CO_2 molecule into the temporary channel (created by the transport of CO_2) connecting two adjacent pockets in

M5a. It was hypothesised that such a complex (1:2 host:guest ratio) can be obtained from exposing **M5a** to very high CO_2 pressures (*i.e.* above 50 bar) while collecting the single-crystal structure at room temperature.

M5a was exposed to 50 bar CO_2 pressure while collecting intensity data. Structure elucidation revealed the known 1:1 CO_2-included structure **M5·CO$_2$**.[21] In the crystallographic model of **M5·CO$_2$**, the host packing is identical to that observed in **M5a**, but a disordered (50:50) CO_2 guest is located within each discrete pocket (V = 126 Å^3, using probe r = 1.4 Å) of **M5·CO$_2$**. The guest positions (and disorder) are presumably due to an electrostatic interaction between the oxygen atoms of the guest and the Cu^{2+} centre, resulting in significant elongation of the $Cu^{2+}\cdots Cu^{2+}$ distance from 6.59 Å in **M5a** to 6.90 Å in **M5·CO$_2$**. Shortening of the *Im*···*Im* distance (from 5.93 to 5.61 Å) also occurs to some extent.

Low pressure CO_2 sorption and desorption isotherms were collected at three different temperatures (*e.g.* 0, 20 and 30 °C) using the ASAP2020 sorption analyser. Figure 5.3 shows that the occupancies at 900 mmHg (*i.e.* maximum experimental pressure possible) are respectively 1, 0.9 and 0.8 for isotherms collected at 0, 20 and 30 °C. The host:guest ratios derived from the sorption isotherms and the SCD structures correspond to sorption measurements previously carried out by Marais.[25] As expected for microporous materials such as **M5a**, isotherms measured at different temperatures have similar shapes (Type I isotherms). A molecular mechanics calculation carried out by G. Venter suggested an activation energy of 2.5 kJ.mol^{-1} for the uptake of CO_2.[26] The position of the CO_2 guest within the discrete pockets is shown in Figure 5.4(b).

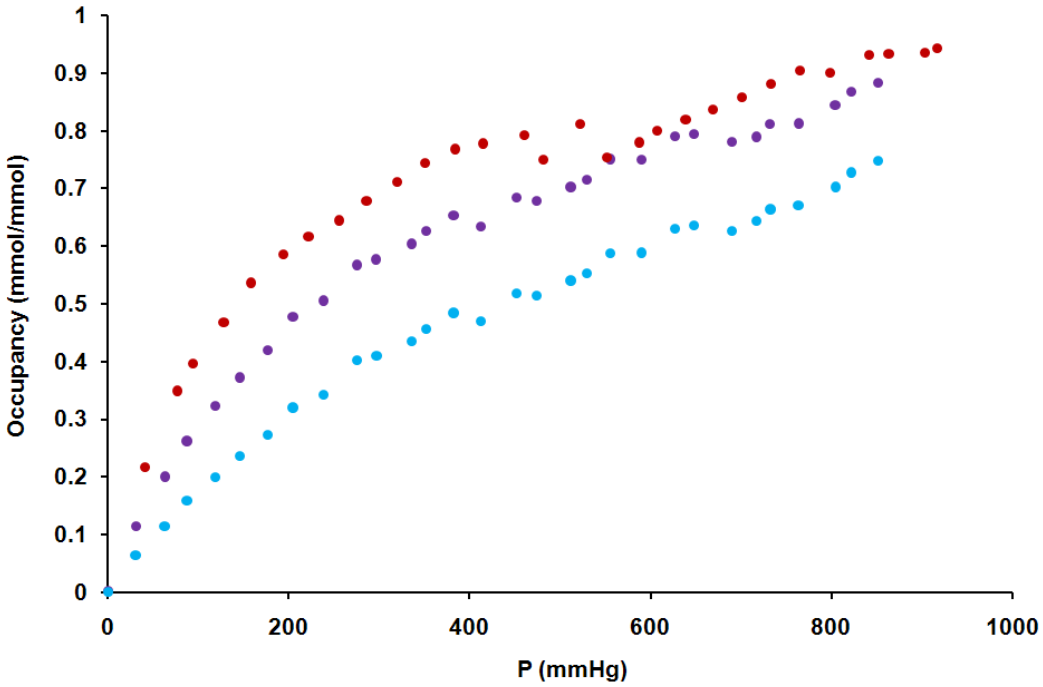

Figure 5.3 Sorption isotherms for CO_2 measured at 0 °C (red), 20 °C (purple) and 30 °C (blue). Desorption isotherms are not shown since identical isotherm paths are observed for all three temperatures (*i.e.* hysteresis does not occur).

5.2.1.2 M5·CO

The CO-included complex **M5·CO** was obtained by collecting X-ray data (consecutive measurements at room temperature and 100 K) using a crystal of **M5a** mounted in a gas cell holding 20 bar of CO gas. No significant differences were observed for the structures collected at different temperatures. Structure solution revealed that each of the pockets in **M5·CO** contains one CO molecule (disordered over two sites of equal occupancy) located at similar sites as those observed for CO_2 in **M5·CO$_2$** (Figure 5.4(a)). Like the guests in **M5·CO$_2$**, the CO molecules do not interact strongly with the host; however the location within the pocket suggests that an attractive electrostatic interaction with the metal centre influences the preferred guest positions. The uptake of CO occurs with a notable elongation of the $Cu^{2+}\cdots Cu^{2+}$ distance from 6.59 Å in **M5a** to 6.84 Å in **M5·CO** in conjunction with a 5% decrease in the *Im*···*Im* distance.

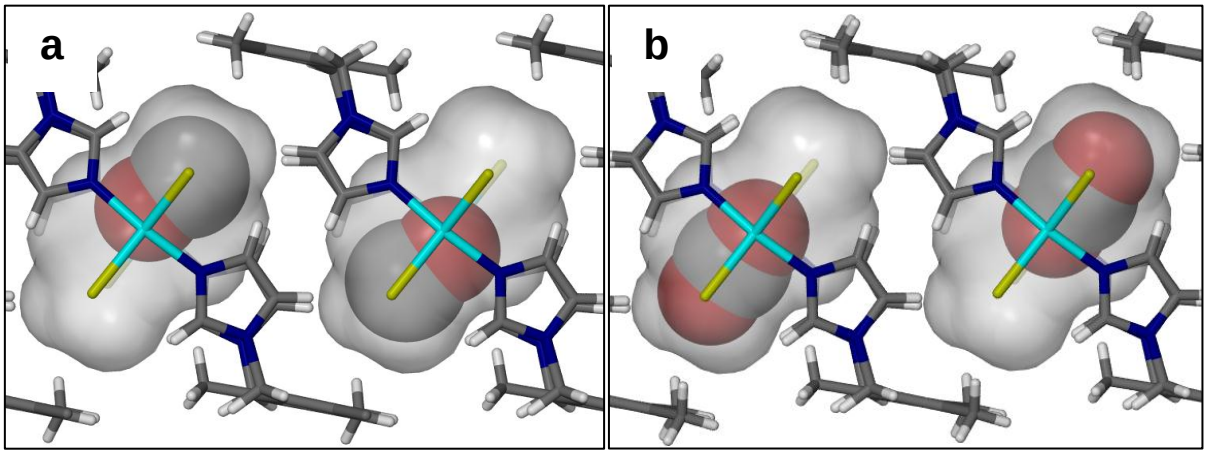

Figure 5.4 The locations of (a) the CO (V = 124 Å^3, probe r = 1.4 Å) and CO_2 (V = 126 Å^3, probe r = 1.4 Å) molecules within the discrete pockets of **M5·CO** and **M5·CO_2**, respectively.

5.2.1.3 M5·C_2H_2

The structure of **M5·C_2H_2** was determined by collecting X-ray data whilst exposing **M5a** to 11 bar acetylene gas at room temperature. The ASU of **M5·C_2H_2** comprises half a metallocycle and one acetylene guest at full occupancy. Space-group symmetry generates another guest molecule within the same pocket; guests are related via inversion symmetry and the host:guest ratio is 1:2. Unlike the gases in **M5·CO** and **M5·CO_2**, the acetylene molecules are pushed away from the metal centre (Figure 5.5) and preferentially interact with the chloride anions via a C–H···Cl hydrogen bond (C_{donor}···$Cl_{acceptor}$ = 3.779(9) Å). Therefore, a notable 8% increase in the Cu^{2+}···Cu^{2+} distance facilitates the sorption of two acetylene molecules per cavity (V = 145 Å^3, probe r = 1.4 Å).

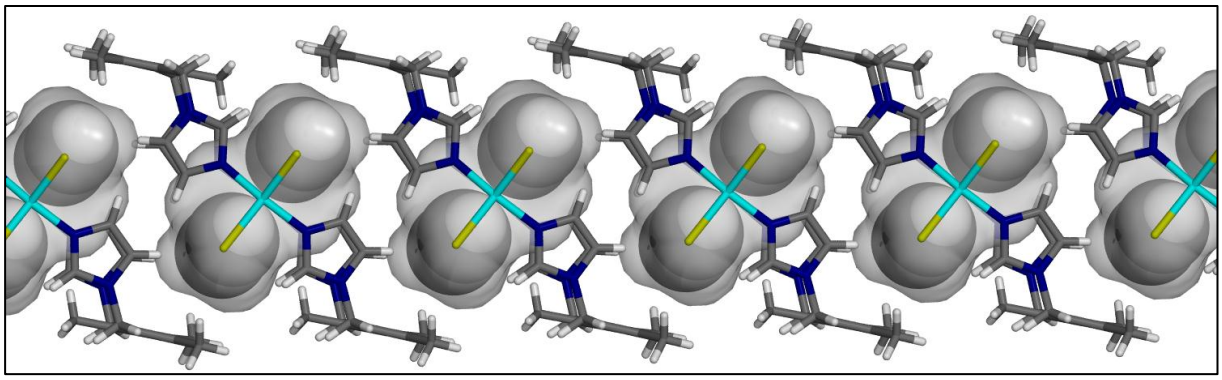

Figure 5.5 A Perspective view of the guest positions within the voids of **M5·C_2H_2**. Guest molecules are shown in space-filling representation and the metallocycles are shown as capped-sticks. A noteworthy increase in the void volume of 37 Å^3 occurs upon exposing **M5a** to acetylene.

5.2.1.4 M5·VCl

Exposing **M5a** to 5 bar vinyl chloride yielded **M5·VCl**. Structure determination revealed that the ASU consists of half a metallocycle and one vinyl chloride molecule with a site occupancy of 0.5. Space group symmetry requires the guest to be symmetrically disordered across an inversion centre. As in the previously mentioned structures, the guest molecules are located within discrete pockets ($V \approx 121$ Å^3) that can be mapped using a probe $r = 1.4$ Å. As seen in Figure 4.6, the size and shape of the cavities provide an excellent fit for vinyl chloride. It appears that no strong host:guest interactions are present in **M5·VCl.**

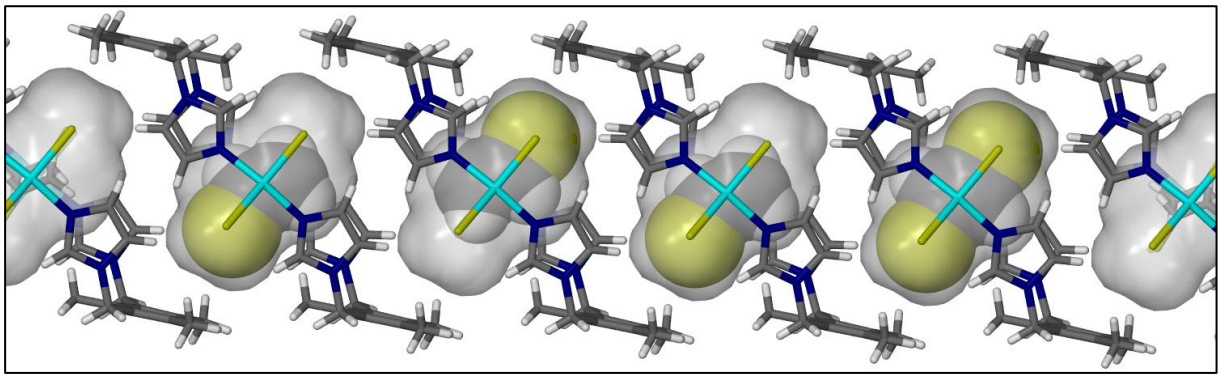

Figure 5.6 The vinyl chloride filled cavities in **M5·VCl**, showing an overlay of both positions (in space-filling representation) of the two-fold disorder in the pocket second from the right. The remaining voids are each shown with only one guest molecule each (selected arbitrarily for this illustration).

5.2.2 Permeability of M5a to organic solvents

In order to test our hypotheses regarding reversible guest exchange of organic solvents as single-crystal to single-crystal transformations, each experiment consisted of immersing several single crystals of **M5** in a small vial containing 1 ml of one of the solvents **H_2O-DFB** listed in Table 5.2. The crystals of the stable complex **M5** are not soluble in any of the organic solvents typically used for crystallisation. The systems were left overnight to equilibrate. Crystals were removed from the vial with a spatula, the tip of which was covered in paratone oil to prevent rapid desolvation during mounting prior to data collection. The host:guest ratio was calculated taking one complete metallocycle as the host (even in cases where the ASU consisted of half a metallocycle). Since both **M5·MeOH·H_2O** and **M5a** are well documented[14] and their crystal structures described in detail elsewhere, only structures with

compositions different from these parent structures will be discussed in detail in this manuscript. It is important to note that disorder of the *Im* rings occurred to a small extent in all structures. Structural adjustment (see Table 5.5 on page 180) of the metallocycle upon changing the guest was monitored in terms of the $Cu^{2+}\cdots Cu^{2+}$ distance, *Im*···*Im* distance (*i.e.* the centroid···centroid distance between imidazole rings in **L6**), the unit cell volume and the shape of the pockets, as compared to the empty metallocycle **M5a**.

5.2.2.1 M5·H_2O

It was previously noted that **M5a** does not appear to absorb water from the air.[21, 27] Upon exposure to liquid water, the space group symmetry remains unchanged for the hydrate structure **M5·H_2O** relative to that for to the empty host **M5a**. The space within the complex ring (*i.e.* empty in the case of **M5a**) is now taken up by two partially occupied water molecules and, surprisingly, the overall site-occupancies of the two water molecules only add up to 1.4 molecules per host. This might indicate that the discrete pockets in **M5a** retain some "hydrophobic" character. Both the host and the two unique guests are situated about an inversion centre. This requires only half a host to be present in the ASU, and each of the two unique guest positions to be disordered over two symmetry-related sites (*i.e.* the symmetry-related atoms must have the same site occupancy). Thus, a maximum of only two of four possible positions can be occupied at any given moment; the unique water molecules have different site-occupancy factors (O1 = 0.3 and O2 = 0.4 in Figure 5.7). Figure 5.8 shows possible arrangements of the water guests. We also note that crystals of **M5·H_2O** eventually dissolve in water after several days, while this does not occur for the other solvents investigated.

The metallocycle in **M5·H_2O** experiences a 6% decrease in the $Cu^{2+}\cdots Cu^{2+}$ distance (*i.e.* from 6.61 to 6.22 Å) and a 12% decrease in the *Im*···*Im* distance (*i.e.* from 5.91 to 5.24 Å) when compared to empty metallocycle **M5a**. The Connolly surface map (using a probe radius of 1.4 Å) reveals that the solvent-filled cavity has a volume of 92 $Å^3$. This is somewhat unexpected, since the empty pockets have a volume of 108 $Å^3$, when calculated using a probe of the same radius. Although this phenomenon is rare for rigid metallocycles such as **M5**, it has previously been observed for coordination polymers, where the framework is flexible and can therefore shrink to better accommodate the smaller guest.[1] This kind of induced-fit[28] is termed "shape-responsive fitting".[29] The mechanism of shape-responsive fitting is tied to the

host-guest interactions and shrinkage therefore occurs when a small guest can efficiently take part in strong attractive interactions with the host.[29] Water guest molecules play a part in only one primary attractive interaction (Figure 5.7) that governs the decrease in cavity size in **M5·H$_2$O**, i.e. coordination to the Cu^{2+} centre (Cu^{2+}···O2 = 2.761(2) Å).

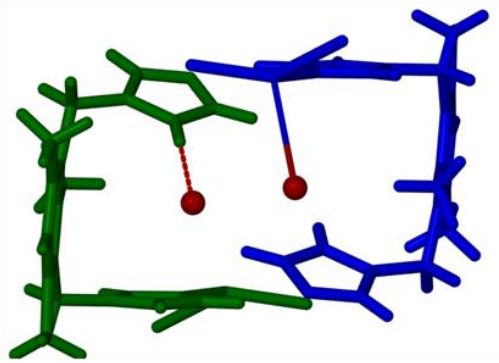

Figure 5.7 The locations of the unique water guest molecules (shown as red spheres) within the complex ring of the metallocycle. The weak coordination of O2 to the Cu^{2+} centre (Cu^{2+}···O2 = 2.761(2) Å) is shown in blue/red. The metallocycle shown in blue is above the green metallocycle, if we assume the stacked column runs into the projection plane. Only half of each of two adjacent metallocycles is shown. Hydrogen atoms of the water molecules could not be located in difference electron density maps.

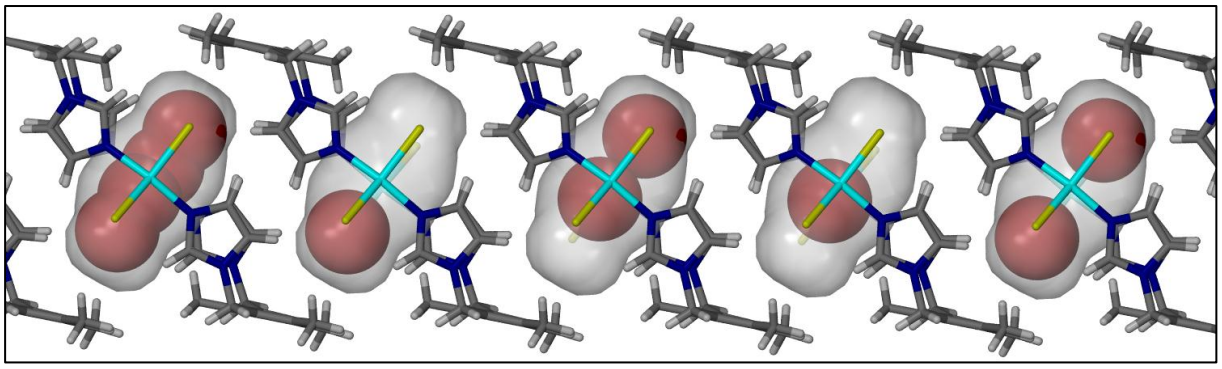

Figure 5.8 Possible placement of the water guests in **M5·H$_2$O** within a stacked column of host complexes. Guest pockets are shown as semi-transparent grey surfaces; volume = 92 Å^3 using a probe r = 1.4 Å. All of the four possible positions of the water molecules are shown simultaneously in the first (leftmost) void. Voids 2 and 4 are each shown with only one of two crystallographically unique guests and voids 3 and 5 are each shown with feasible arrangements of two water molecules per void.

5.2.2.2 M5·MeOH

Obtaining the pure methanol solvate was troublesome (ultra-purity dry methanol needed to be used), since inclusion of the methanol/water adduct appears to be more favourable, even if only a small amount of water is present. Complex **M5·MeOH** enclathrates two methanol molecules, thus having a host:guest ratio of 1:2. The ASU consists of half a metallocycle as well as two half occupied methanol guest molecules (A and B, in Figure 5.9) situated within the discrete cavity (volume of 144 $Å^3$ using a probe with r = 1.4 Å, Figure 5.10). Each of the unique methanol guests is disordered over two positions of equal occupancy. Possible arrangements of guests in **M5·MeOH** are shown in Figure 5.10. Only one of the unique **MeOH** molecules is in a favourable position for coordination to the Cu^{2+} centre, with O1···Cu1 = 2.447(6) Å (Figure 5.9).

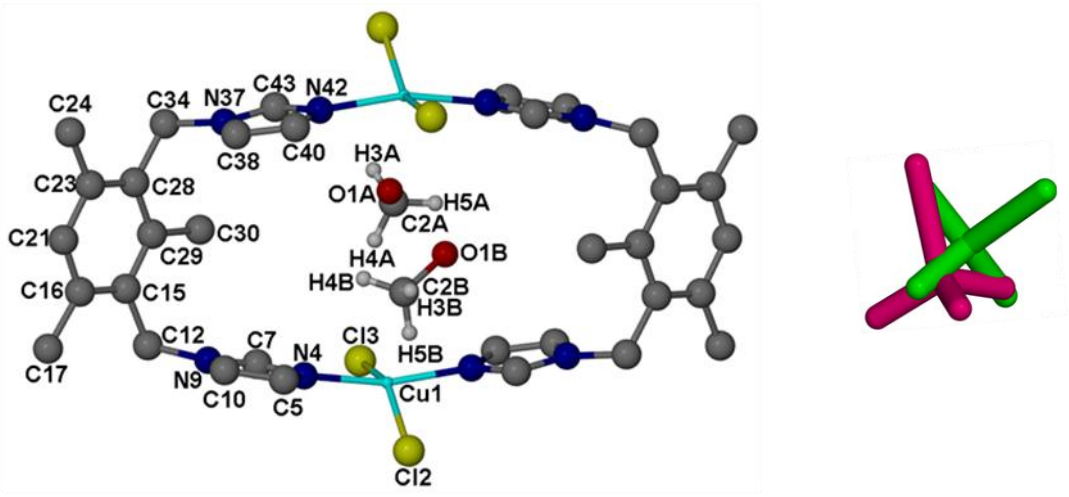

Figure 5.9 Atom numbering scheme for **M5·MeOH** (left); only the ASU is numbered. One complete host and the unique methanol guests are shown. Hydrogen atoms of the host framework are omitted for clarity. Each guest (A and B on the left) is disordered over two positions (shown in pink and green on the right).

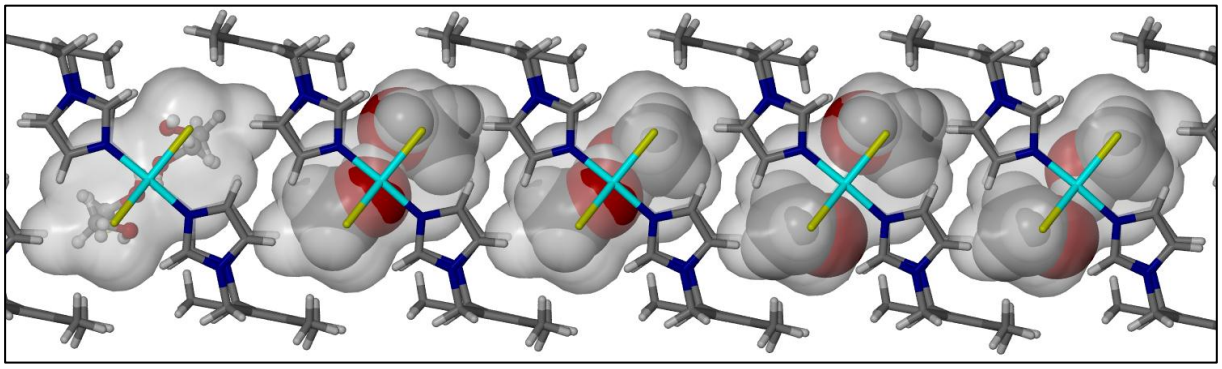

Figure 5.10 Possible positions of the disordered methanol guests (space-filled) within the semi-transparent grey Connolly surface (volume = 144 Å^3, probe r = 1.4 Å). However, we propose that only the arrangement of guest molecules in voids 2 and 5 (numbered from left to right) are plausible, when considering the guest-guest interactions.

5.2.2.3 M5·Me_2CO

The ASU of **M5·Me_2CO** (Figure 5.11) consists of half a host and one acetone guest with a site occupancy of 0.5. The acetone molecule was refined with simple bond length constraints and the overall structure converged to a final R1 = 0.054. The space group symmetry requires the acetone guest to be disordered over two sites of equal occupancy. From careful inspection of the space-filled guests (Figure 5.12) we can infer that they are distributed randomly throughout the structure with regard to their two possible orientations (*i.e.* there is no bias in favour of one guest orientation over the other within any given column).[30] Thus, guest packing trends such as partial polar ordering do not occur and there can only be one acetone molecule per pocket; the host to guest ratio is 1:1.

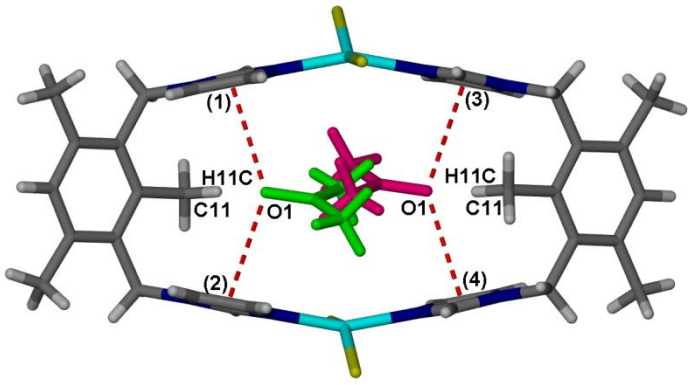

Figure 5.11 Molecular structure of **M5·MeCO**. Only selected atoms are numbered. One complete host is shown in CPK colours and the disordered guest is illustrated in green and pink. The lone pair (lp)···π interactions are indicated by red dashed lines. The imidazole rings are numbered (1) to (4).

The location of the disordered acetone guest on the two symmetry-related sites is a result of the weak hydrogen bond between the carbonyl group of the guest and the inner methyl group (labelled C11 in Figure 5.11) of the host. In the past, interactions between the electron-rich carbonyl group of the guest and imidazole (*Im*) rings of the ligand would have been overlooked, but a recent report by Mooibroek *et al.* showed the lone pair (lp)···π interaction to be of supramolecular relevance.[31] These interactions (O1···*Im*(1,2) = 3.16 Å and 3.11 Å, respectively) stabilise the acetone guest between the two imidazole rings of each **L6** ligand, and are indicated in Figure 5.11.

Figure 5.12 shows how the discrete pockets in **M5·Me$_2$CO** adapt their shape to accommodate the acetone molecule within the complex ring. Relative to the empty complex **M5**, a noteworthy increase in solvent accessible-volume (V = 152 Å^3, r = 1.4 in Figure 5.12) occurs upon saturation with the larger acetone guest. An increase (when compared to the empty host structure **M5** and the previous solvated structures) in $Cu^{2+}\cdots Cu^{2+}$ and *Im*···*Im* distances (7.04 Å and 5.85 Å, respectively) of the host in **M5·Me$_2$CO** are also observed upon saturation with acetone. These values are listed in Table 5.5 on page 180.

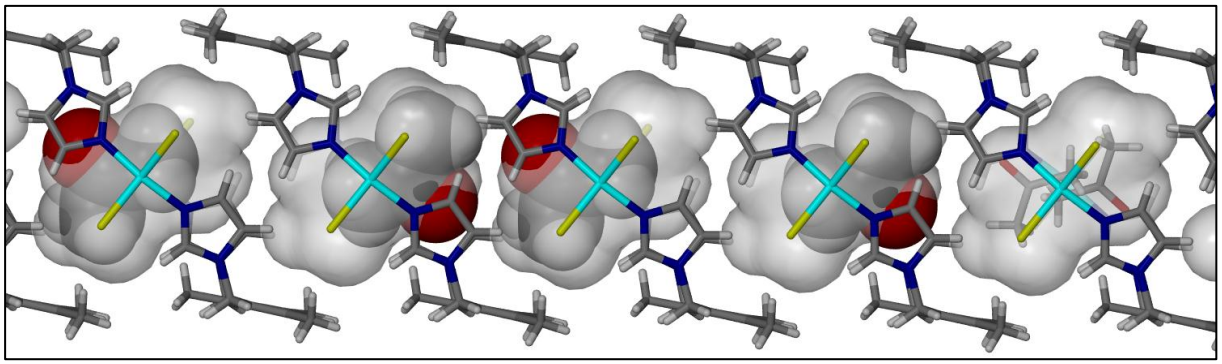

Figure 5.12 A perspective view of a column stacked along [100] showing possible positions of the acetone guests in the cavities of **M5·MeCO** (*i.e.* Connolly surface shown in semi-transparent grey, V = 152 Å^3 and r = 1.4 Å).

5.2.2.4 M5·H$_2$O·Me$_2$CO

Similar to that of the reported parent structure **M5·H$_2$O·MeOH**, the ASU of complex **M5·H$_2$O·Me$_2$CO** consists of half a host and a half-occupancy acetone/water adduct situated across an inversion centre. The guests, as well as one of the *Im* rings of each ligand are disordered over two sites. Several bond length constraints were required in order to achieve

the optimum geometry for the disordered guest and *Im* rings. Owing to the similarity to **M5·H_2O·MeOH** this structure will not be discussed in detail here.

5.2.2.5 M5·MeCN

The ASU of the acetonitrile solvate **M5·MeCN** (Figure 5.13) consists of half a host and one acetonitrile guest with a site-occupancy of 0.5. The symmetry of **M5·MeCN** requires the guest to be disordered over two equally occupied sites. Although the two disordered guests are symmetry-related, it is apparent that they cannot co-exist and only one acetonitrile molecule can therefore be present in each cavity (Figure 5.14). It is interesting to note that, despite the comparable size of acetonitrile (3.80 × 5.49 Å) to methanol (3.80 × 4.7 Å), only one acetonitrile molecule can occupy each pocket in **M5·MeCN** as compared to two methanol guests in **M5·MeOH**. Unlike the pockets in **M5·MeOH**, no increase in cavity volume with regard to the empty pockets is observed (Table 5.5, page 180). Since acetonitrile and methanol have comparable sizes, it is reasonable to presume that differences in their sorption behaviour are due to their different intermolecular interactions. We suggest that the coordination of the methanol guest allows two molecules to be accommodated in the cavity. Furthermore, guest-guest interactions enable the methanol molecules to be closer to each other. Weak attractive forces between the *Im* rings of the host and the acetonitrile guest draw the *Im*-*Im* moieties closer together than they are in the empty host **M5** (from *Im*···*Im* = 5.93 Å in **M5** to 5.48 Å in **M5·MeCN**).

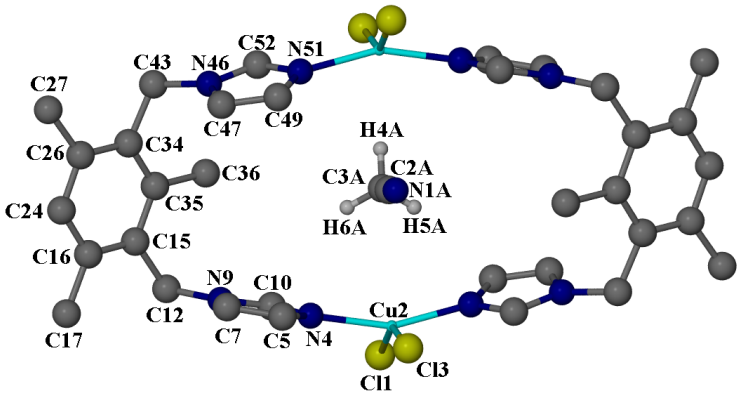

Figure 5.13 Atom numbering for the ASU of **M5·MeCN**. The guest molecule is disordered over two positions. An entire host molecule and one of the two positions for the acetonitrile guest are shown. The hydrogen atoms of the host are omitted for clarity.

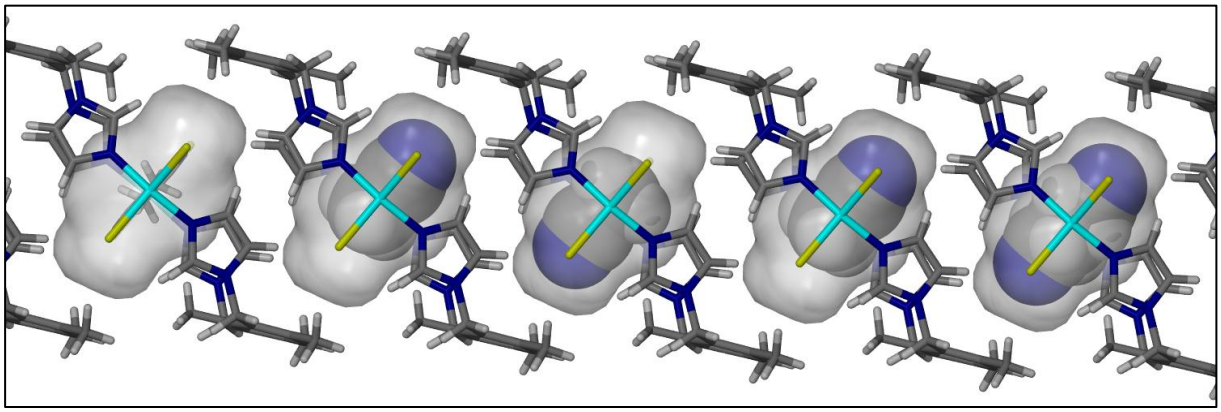

Figure 5.14 The acetonitrile solvate **M5·MeCN** viewed along [010]. The host, as well as the disordered guest molecules in the left-most cavity, are shown as capped-sticks. The four remaining guests in the cavities are shown in space-fill. Only one of the two possible sites of the disordered guest is shown in each of the three middle cavities.

5.2.2.6 M5·DCM

The ASU of **M5·DCM** (Figure 5.15) also consists of half a host and a disordered guest molecule with a site-occupancy factor of 0.5. Both host and guest are situated about an inversion centre. As noted for several of the previous structures, the space group symmetry requires the guest molecule to be disordered over two crystallographically-related sites of equal occupancy. The only significant host-guest interaction is a C–H···Cl hydrogen bond ($C33_{donor}\cdots Cl3_{acceptor}$ = 3.698(9) Å). The dichloromethane guests do not occupy the centre of the cavity, but are situated to either side in order to take part in this host-guest interaction. A perspective view (Figure 5.16) of the solvent-filled cavities shows a likely arrangement of the dichloromethane molecules.

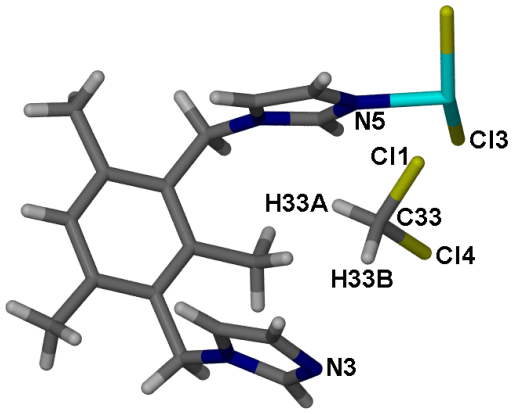

Figure 5.15 The ASU of **M5·DCM**. Only selected atoms are labelled.

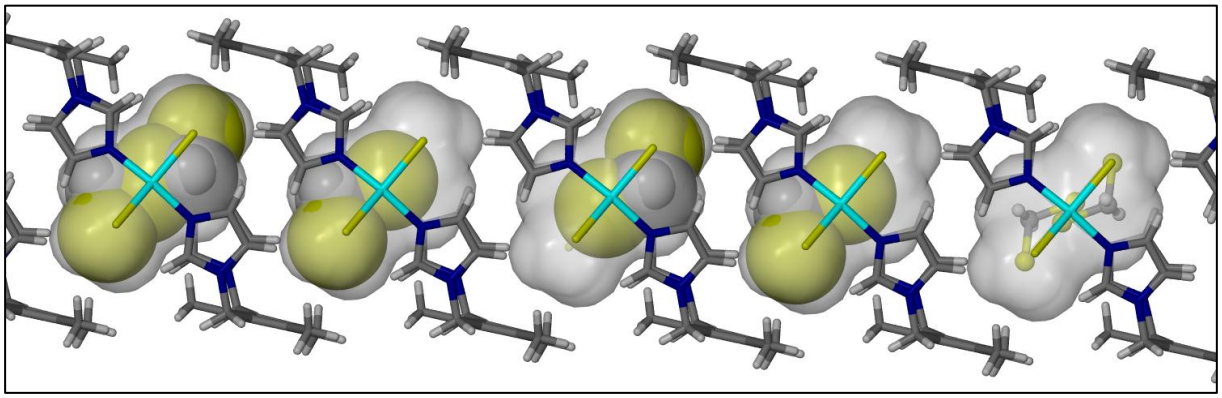

Figure 5.16 Perspective view of the discrete pockets containing dichloromethane. The disorder of the guest is shown in the far left and right as space-filled and ball-and-stick models, respectively. In all other cavities, only one of the possible sites is shown.

5.2.2.7 M5·$CHCl_3$

Unlike previous solvate structures **M5·H_2O** to **M5·DCM** (Sections 5.2.2.1 to 5.2.2.6), a noteworthy adjustment of unit cell parameters occurs upon saturation with chloroform. Although the space group symmetry remains identical, host **M5** undergoes distortion in order to accommodate the relatively large guest. *Im* rings can rotate about the Cu–N coordination bond and **L6** in **M5·$CHCl_3$** can assume either an "open" or "closed" conformation (*Im*···*Im* = 6.221 Å and 5.614 Å, respectively), depending on the close contacts present between host and guest (Figure 5.17). A molecular mechanics calculation[20] of the transport of CO_2 molecules through the crystal structure of **M5** also suggested a 1D diffusion mechanism facilitated by "flapping" of the *Im* moieties (Figure 5.18). The resulting distorted host is acentric, but the overall crystal structure of **M5·$CHCl_3$** is centrosymmetric. Space group symmetry therefore requires the ASU (Figure 5.16) to consist of one host and two chloroform guests (each with a site-occupancy factor of 0.5). Metallocycle distortion is accompanied by doubling of the *a*-axis; the unit cell parameters for **M5·$CHCl_3$** are, a = 16.6711(3) Å, b = 10.7795(2) Å, c = 22.4367(3) Å and β = 99.497° – Table 5.6. Along with doubling of the *a*-axis, chloroform inclusion induces a considerable elongation of the $Cu^{2+}\cdots Cu^{2+}$ distance within the metallocycle from 6.56 Å to 7.07 Å. There is also an increase in *Im*···*Im* when going from the conformation in **M5** to the "open" conformation in **M5·$CHCl_3$** (from 6.23 Å in **M5** to 6.56 Å in **M5·$CHCl_3$**). It appears that the mechanism of the guest inclusion process involves the displacement of the imidazole moieties. Thus, the presence of the guest provides a stimulus to open or close the imidazole "gate", yielding a complex that consists of an adaptable binding

site (*i.e.* pocket). These pockets are sensitive to the shape and size of the guest; remarkably, they can adapt their shape without any significant loss in single-crystallinity.

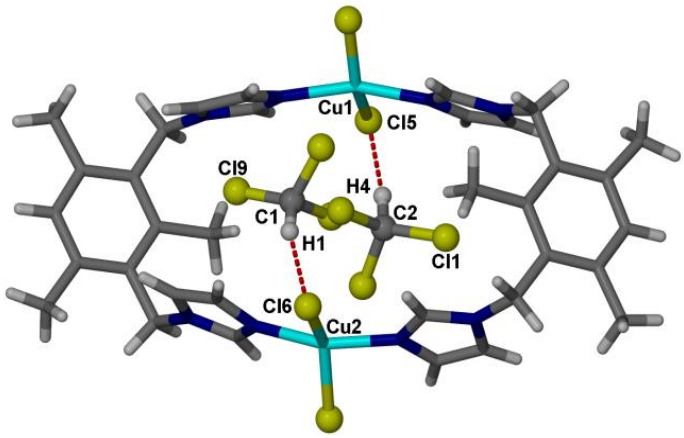

Figure 5.17 The ASU of **M5·CHCl$_3$**, with the metallocycle shown as capped-sticks and the guests shown in ball-and-stick representation. Atoms that are referred to in the text are numbered systematically. Hydrogen bonding of the guest with the chloride ions of the metallocycle (C1···Cl6 = 3.61(7) Å and C2···Cl5 = 3.62(8) Å) is indicated with red dashed lines.

It is also interesting to note that the merging of adjacent pockets of **M5** in **M5·CHCl$_3$** gives rise to a larger cavity (Figure 5.18, Bottom). Each enlarged cavity is formed between two neighbouring metallocycles and encloses two chloroform guests. Only one orientation for each guest is possible owing to the size of chloroform. Each metallocycle therefore shares a cavity with only one of its neighbouring metallocycles, but the discrete cavity is bounded by four successive metallocycles. The ends of the pockets are bounded by the *Im* groups of adjacent hosts and mesitylene rings constitute the tops and the bottoms of the discrete pockets. The hydrogen atoms of the guest penetrate the Connolly surface as a result of the strong interactions with the host. The newly formed pocket is similar to the rectangular cavity of [Cd$_2$**L**$_2$Cl$_4$] shown in Figure 4.2.[32]

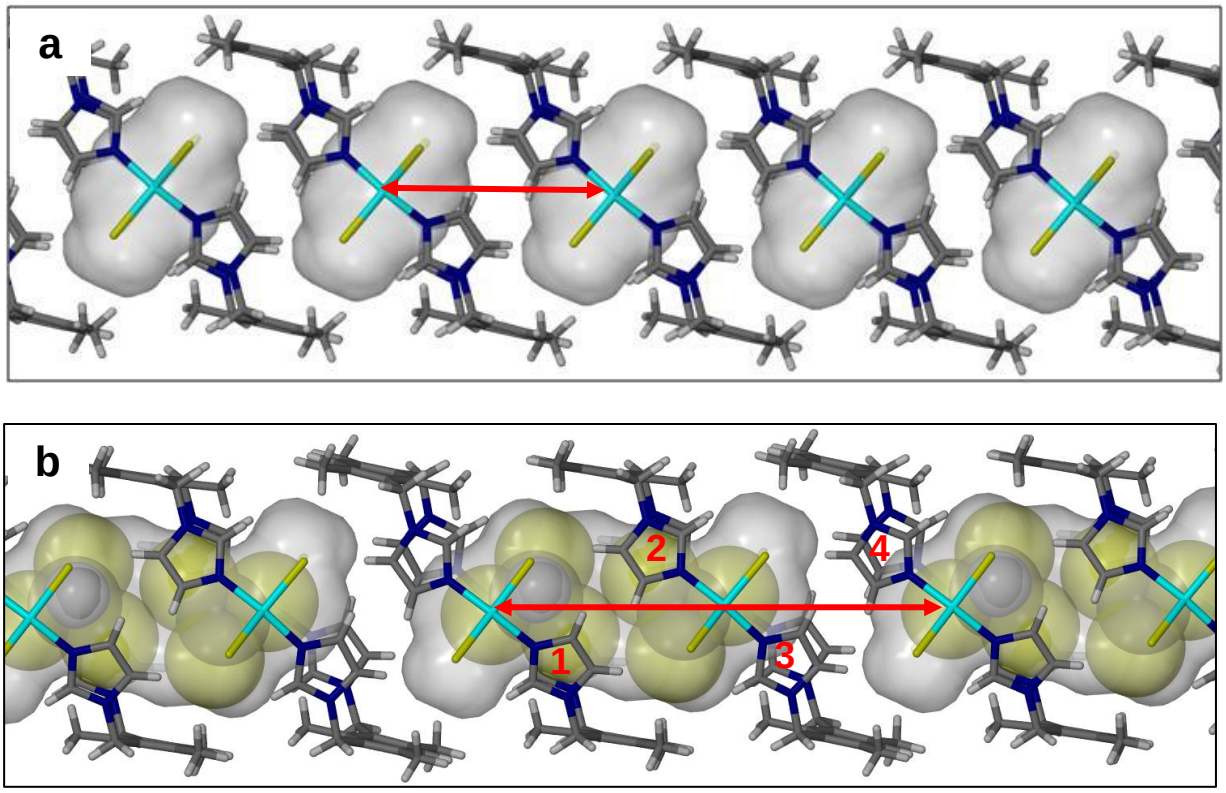

Figure 5.18 Comparison of the empty pockets in (a) **M5a** and (b) **M5·CHCl$_3$**. The empty pockets in **M5a** are shown as semi-transparent grey surfaces (V = 108 Å, probe r = 1.4 Å) and the length of the *a*-axis is indicated with a red arrow. Merging of the discrete pockets in **M5** gives rise to a much larger cavity upon saturation with chloroform. Loading with chloroform to yield **M5·CHCl$_3$** results in doubling of the *a*-axis (red arrow). *Im* rings can rotate about the Cu···N coordination bond and the **L6** ligands can assume either an "open" (indicated by 1 and 2) or "closed" (indicated by 3 and 4) conformation. The merged (*i.e.* enlarged) cavity is formed between two adjacent metallocycles and encloses two chloroform guests (shown in CPK colours and space-filled representation).

5.2.2.8 M5·CS2

The CS_2 solvate structure **M5·CS$_2$** is analogous to the unpublished CO_2-included structure initially determined by Lloyd.[21] One half occupancy CS_2 guest, together with half a host molecule, constitute the ASU. The CS_2 guest is disordered over two symmetry-related sites, but the host:guest ratio is only 1:1, as observed for most of the previously discussed solvate structures. The disorder in **M5·CS$_2$** is similar to that in **M5·MeCN** (Figure 5.14), and therefore no figure is given in this case. Apart from a weak C–H···S interaction (C_{donor} – $S_{acceptor}$ = 3.792(4) Å), no strong interactions between host and guest are found. No considerable changes in the volume of the cavity, the $Cu^{2+}\cdots Cu^{2+}$ distance or *Im*···*Im* distance occur when going from the empty host **M5** to the CS_2-included solvate **M5·CS$_2$**.

5.2.2.9 M5·BZ

Following on the success of the previous results, further studies on the permeability of **M5** were carried out using the larger organic solvent benzene.

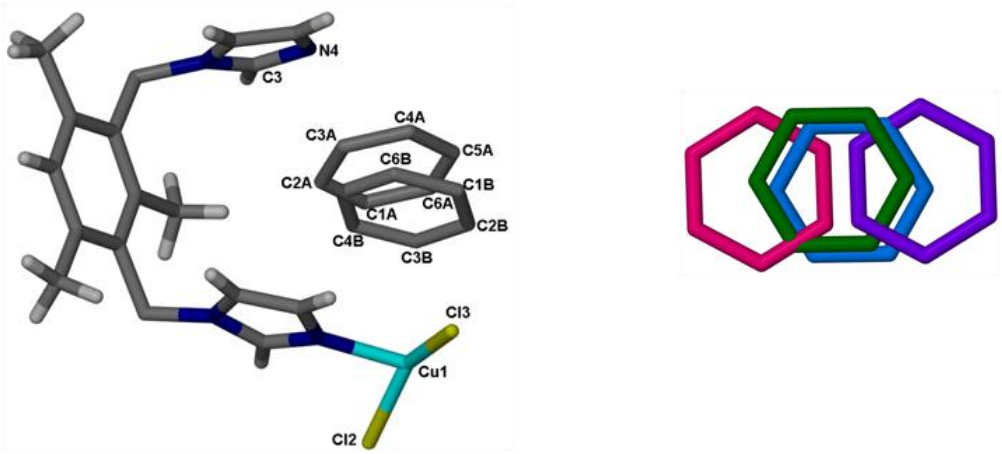

Figure 5.19 The ASU of **M5·BZ** (left), with the both the metallocycle and the guest (A and B) shown as capped-sticks. Atoms that are referred to in the text are numbered systematically. The benzene guest is disordered over four sites (shown on the right).

Unlike most of the previous structures, the ASU of the benzene solvate (Figure 5.19) consists of half a host and two partially occupied benzene guest molecules situated about an inversion centre. It is apparent from the size of the cavity and the electron count (Table 5.5) that a maximum of only one benzene guest can be accommodated per host (Figure 5.20). Two crystallographically unique benzene guests were modelled with site occupancies of 0.36 and 0.14 (guests A and B, respectively in Figure 5.19, left). The right hand side of Figure 5.19 shows the relative positions of A and B, represented as pink (site occupancy = 0.36) and green (site occupancy = 0.14) rings, respectively. Respectively, the purple and blue rings are related to the two unique rings *via* inversion symmetry. Variation in the occupancy of the guest at different positions is thought to be a result of host-guest interactions. Owing to the strong π-character of the aromatic guest, two host-guest interactions influence the occupancy: Cu^{2+}····π coordination and π···π stacking with the *Im* rings. Therefore, the higher occupancy of guest A (Figure 5.20) is mainly facilitated by π···π contacts (centroid···centroid ≈ 3.74 Å) between the benzene guest and the *Im* rings of the metallocycle. Coordination to the metal centre is the weaker interaction (Cu^{2+}···centroid ≈ 3.36 Å). A Cambridge Structural Database (CSD) search shows that the values for short contacts observed in **M5·BZ** correspond well with literature

values (Cu^{2+}····π = 3.21 – 4.62 Å and π···π = 3.63 – 4.82 Å). The inclusion of benzene is accompanied by significant elongation of the Cu^{2+}···Cu^{2+} distance (from 6.60 to 6.96 Å) of the host. Decrease in the *Im*···*Im* distance (from 5.93 to 5.88 Å) is presumed to be a consequence of strong host-guest interactions between the aromatic guest and the *Im* rings of the host. Connolly surface analysis reveals that benzene inclusion results in overlapping pockets (Figure 5.20), with cavity volume = 169 $Å^3$ (probe *r* = 1.4 Å). The structural data for **M5·BZ** are summarised in Table 5.6. Furthermore, as we had anticipated the awkwardly-shaped cyclohexane cannot diffuse through the small aperture of **M5**.

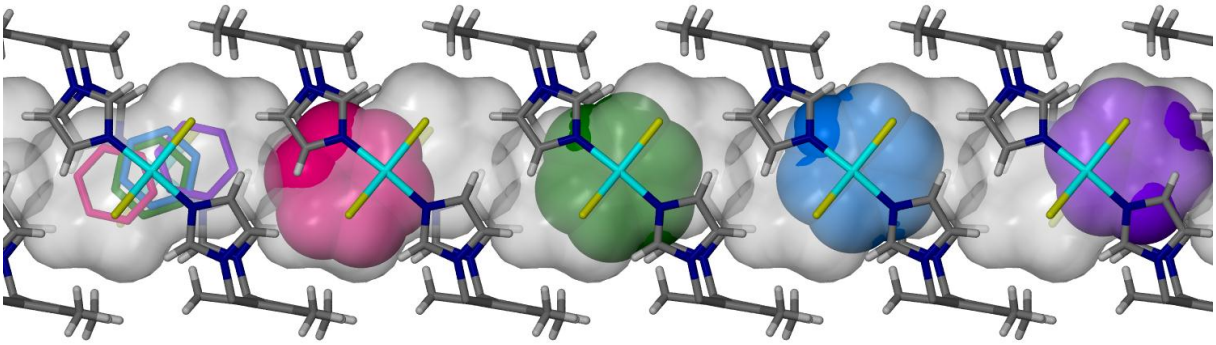

Figure 5.20 Perspective view along [010] showing the overlapping pockets in **M5·BZ**. The four-fold disorder of the benzene guest is shown in the leftmost cavity. The colours of the space-filled guests in the remaining pockets correspond to the colours in Figure 5.19.

5.2.2.10 M5·DFB

Having determined that host **M5** can accommodate a benzene guest molecule in one of four positions as observed in the crystal structure **M5·DFB**, single-crystals of **M5a** were immersed in *p*-difluorobenzene. In the *p*-difluorobenzene included structure, the ASU consists of half a host and half a guest. Thus, no guest disorder is apparent in this case, despite its structural resemblance to benzene. Inspection of the solvent-accessible volume mapped as a Connolly surface reveals discrete cavities (*V* = 151 Å, *r* = 1.5 Å in Figure 5.21), each bounded by three successive hosts within a stacked column.

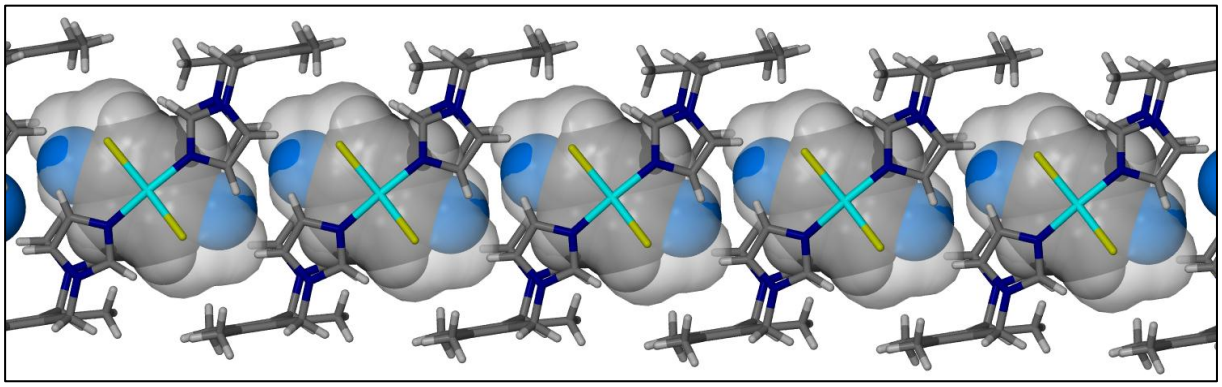

Figure 5.21 A perspective view of the *p*-difluorobenzene-filled cavities in the solvate **M5·DFB**. The host and the guest are shown as capped-sticks and space-filled models, respectively.

Fluorine atoms protruding from the Connolly surface (shown in Figure 5.21) imply interaction with the adjacent hosts within a stacked column, with $C_{donor}\cdots F_{acceptor}$ = 3.085(9)Å. It is also interesting to note that hexafluorobenzene does not appear to permeate the transiently porous metallocycle **M5a**.

5.2.3 Regeneration of the empty host: desolvation by means of thermogravimetric analysis

Thermogravimetric analysis was carried out in order to investigate the desolvation and thermal decomposition of complexes **M5·H_2O** to **M5·DFB** (Sections 5.2.2.1 to 5.2.2.10). Preparation of the saturated complex was carried out using the powdered phase of **M5**. In each case, the sample was exposed to the relevant vapour for one week before analysis. Thermal analysis results are summarised in Figure 5.22 and Table 5.5 (page 180). TGA thermograms indicate that desolvation of complexes **M5·H_2O**–**M5·DFB** occurs readily, as for the reported parent complex **M5·H_2O·MeOH**. In all cases the single-step desolvation process occurred readily, even at room temperature, indicating that gentle heating is sufficient for breaking the host-guest interactions present in complexes **M5·H_2O**–**M5·DFB**. Thus, all guests described in Section 5.2.2 can be removed as easily as they can be adsorbed. Note that decomposition of the metallocycle framework occurs above 200 °C in all cases.

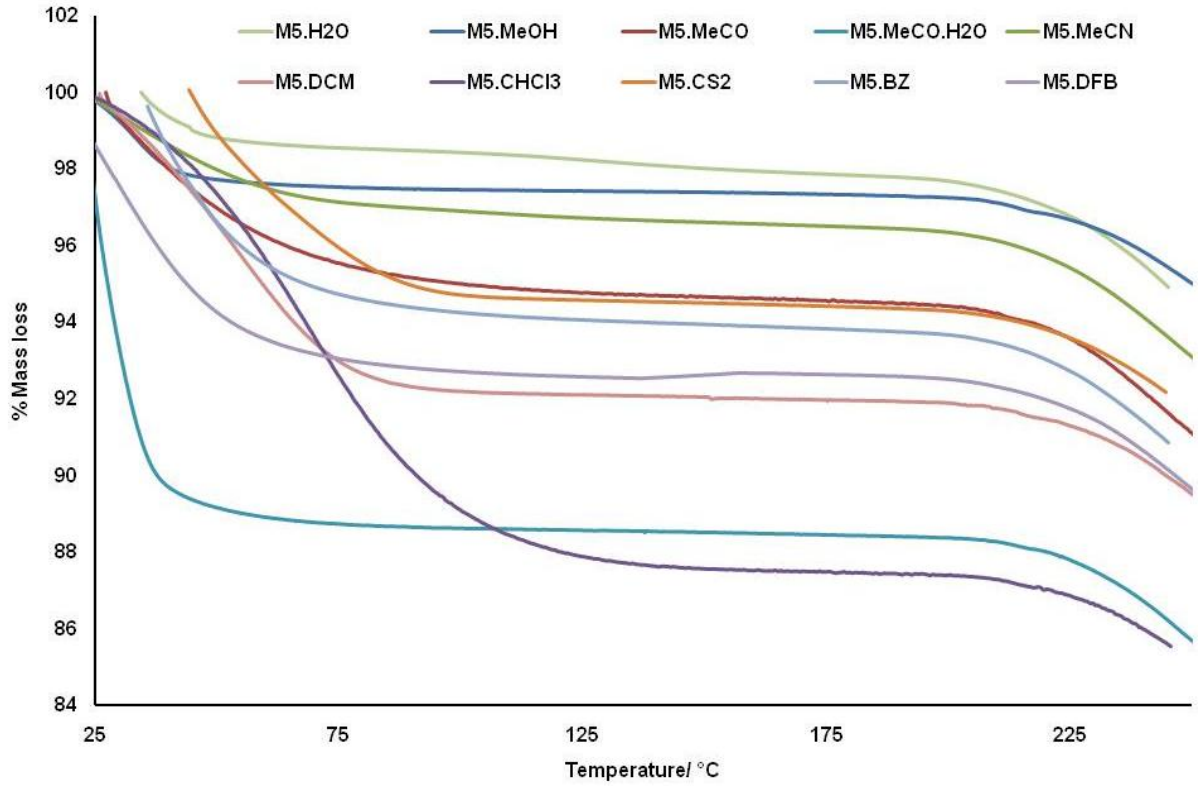

Figure 5.22 Thermogravimetric traces showing the desolvation of solvates **M5·H$_2$O**–**M5·DFB** (Table 5.5, page 180). Decomposition of the metallocycle occurs above 200 °C. In all instances the % mass loss correlates with the host:guest ratio observed in the single-crystal structure.

5.2.4 Volumetric sorption: Calculation of the thermodynamic parameters ($\Delta H°_{ad}$ and $\Delta S°_{ad}$) of sorption

During this part of the investigation, sorption isotherms were recorded at four different temperatures for each solvent vapour in order to determine the thermodynamic parameters of sorption ($\Delta H°_{ad}$ and $\Delta S°_{ad}$). The sorption isotherms will be described in terms of the IUPAC classification, though in some instances the flexible nature of the metallocycle results in isotherms that do not comply with the IUPAC categories (see Figure 5.23). Evaluation of the shape of a sorption isotherm provides useful information concerning the possible mechanism of sorption, and therefore the nature of the adsorbent (e.g. pore size, volume, area and shape). Moreover, plots of guest occupancy (*i.e.* fraction of host:guest ratio) versus the relative pressure P/P_o should reveal information on the affinity for each particular guest.

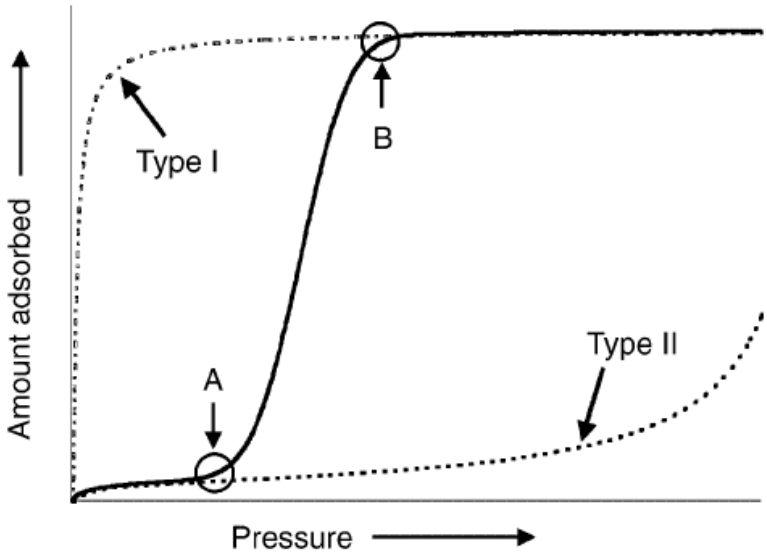

Figure 5.23 A schematic diagram indicating sorption isotherms that may result from flexible porous materials that undergo a structure transformation from nonporous to porous. Type I (micropore filling) isotherms and Type II (surface adsorption) isotherms are represented with dashed lines. The gate-opening (A) and gate-closing (B) pressures which accompany the start and end of the structure transformation are also indicated on the figure.[2]

Sorption thermodynamic data for gas-solid systems serve a useful purpose in three main areas: (1) chemical engineering (e.g. design and modelling of industrial gas separation/purification processes), (2) elucidating sorption mechanisms and (3) characterisation of energetic heterogeneity of solid surfaces.[33] However, determination of gas sorption thermodynamic data represents a challenging task and isosteric sorption values ($\Delta G°_{ad}$, $\Delta H°_{ad}$ and $\Delta S°_{ad}$) published in the literature often disagree.[33] The most accepted thermodynamic definition for $\Delta H°_{ad}$ of a pure gas or vapour is the molar enthalpy in the gas/vapour phase minus the differential enthalpy in the sorption phase. The three most widely used experimental techniques employed to obtain the isosteric sorption quantities include differentiation of sorption isotherms at constant loading pressure, direct measurement of the sorption isostere,[33] and the calorimetric method.[34] The simplest means of obtaining $\Delta H°_{ad}$ and $\Delta S°_{ad}$ is by the isosteric method,[33] which involves the measurement of at least three isotherms at different temperatures for any given system, and subsequent application of the Clausius-Clapeyron equation. Thus, the Clausius-Clapeyron equation relates $\Delta H°_{ad}$ and $\Delta S°_{ad}$ to the change in pressure with temperature in the following manner:[35]

$$\frac{d(lnP)}{d(T)} = \frac{\Delta H}{RT^2}$$

As mentioned above, data obtained from the isosteric method can be used to determine $\Delta H°_{ad}$, and $\Delta S°_{ad}$ based on the following physico-chemical principles of a system at equilibrium: Consider the guest inclusion/removal reaction,

$$m\mathbf{H}\,(s) + n\mathbf{G}\,(g) \rightleftharpoons \mathbf{H}_m\mathbf{G}_n\,(s)$$

The equilibrium constant for this reaction is:

$$K = \frac{[\mathbf{H}_m\mathbf{G}_n]}{[\mathbf{H}]^m[\mathbf{G}]^n}$$

This equation simplifies to (**H** and $\mathbf{H}_m\mathbf{G}_n$ are solids)

$$K = [\boldsymbol{G}]^{-n}$$

The equilibrium constant is related to the thermodynamic parameters of a reaction by

$$\Delta G = -RT\ ln\ K = \Delta H - T\Delta S$$

Therefore,

$$-RT\ ln\ [\mathbf{G}]^{-n} = \Delta H - T\Delta S$$

The chemical activity of **G** can be approximated as its pressure, considering that only vaporous guests ($\mathbf{H_2O}$-**DFB** in Table 5.2) are used in this study. Thus,

$$n RT \ln P = \Delta H - T\Delta S$$

$$n \ln P = \Delta H/RT - \Delta S/T$$

When the value of n is standardised to one mole of gas, the linear plot of $ln\ P$ as a function of $1/T$ has a gradient of $\Delta H/R$. ΔH is then defined as the isosteric enthalpy of sorption ($\Delta H°_{ad}$). Similarly, the value for the isosteric entropy of sorption ($\Delta S°_{ad}$) is obtained from the negative of the vertical intercept of the plot of $ln\ P$ versus $1/T$.

Physisorption is necessarily exothermic and therefore evolves heat. When considering the equation:

$$\Delta G^\circ_{ad} = \Delta H^\circ_{ad} - T\Delta S^\circ_{ad}$$

the change in enthalpy, ΔH°_{ad}, must be negative since the change in ΔS°_{ad} is negative owing to the adsorbed molecules being in a more ordered state in the host framework than in the supernatant gas phase.[36] The ΔH°_{ad} value at zero equilibrium loading pressure gives an indication of the affinity that a host system has for a guest and can be related to various interaction energies.[36] Some of the most important interactions involved include dispersion and short range repulsion, polarisation and electrostatic energies.[36] Furthermore, isosteric sorption parameters can be an indication of the degree of adsorbent surface heterogeneity.[37]

In this part of the work, sorption characteristics of **M5·H_2O–M5·$CHCl_3$** and **M5·BZ** (section 5.2.2) were investigated by means of volumetric sorption experiments at the solid-vapour interface. All studies were performed using **M5a** and pure components of the vapours **H_2O–$CHCl_3$** and **BZ**. Unless otherwise stated, equilibrium sorption isotherms were determined at four different temperatures (0, 10, 20 and 30 °C). The amount of guest absorbed is expressed as the fraction mol guest per mol of host (occupancy) in all isotherms. The resultant host:guest ratios are compared with those obtained from single-crystal structures **M5·H_2O–M5·$CHCl_3$** and **M5·BZ** as described in detail in Section 5.2.2.

Values (in kJ mol^{-1}) for ΔH°_{ad} and ΔS°_{ad} at a particular occupancy were calculated with standard deviations obtained from regression analysis of the linear fits of $n\ln P$ vs $1/T$. The Gibbs free energy of sorption (ΔG°_{ad}) was not calculated considering that the standard deviation on ΔS°_{ad} is not within the required margin of error. Desorption data points were not collected since it was assumed that no vapour-induced structural phase changes occurred (*i.e.* that the isotherms show no hysteresis) whilst conducting the sorption experiments. The data points above $P/P_0 = 0.8$ were ignored owing to significant capillary condensation of the guest above this level. Sorption isotherms obtained for all guests (**H_2O–$CHCl_3$** and **BZ)** will be discussed in separate sections 5.2.4.1 – 5.2.4.7.

5.2.4.1 H_2O

Sorption isotherms for water were measured in the temperature range 5 – 20 °C (Figure 5.24) since sufficient absolute *P* could not be achieved above this temperature range. The rather

small initial sorption of water below $P/P_0 \approx 0.2$ indicates weak interactions between host and guest and suggests some hydrophobic character of **M5**. MOF-type hosts[1, 38] and organic hosts[39] possessing hydrophobic cavities have previously been reported. In most of these cases the material displayed selective properties: either an affinity for water[40] over organic solvents[41] or a preferential sorption of organic solvent[42] over water.[43] In the instances where water is sorbed, an initial nonwetting or hydrophobic character is detected prior to any significant uptake.[38] Above this relative pressure, the sorption continues at approximately the same rate, but never reaches a plateau. Surprisingly, a maximum host:guest ratio of only 1:1.4 was reached at $P/P_0 \approx 0.8$. The same ratio was determined from both the TGA thermogram (section 5.2.3) and the single-crystal structure **M5·H$_2$O** (in section 5.2.2.1)

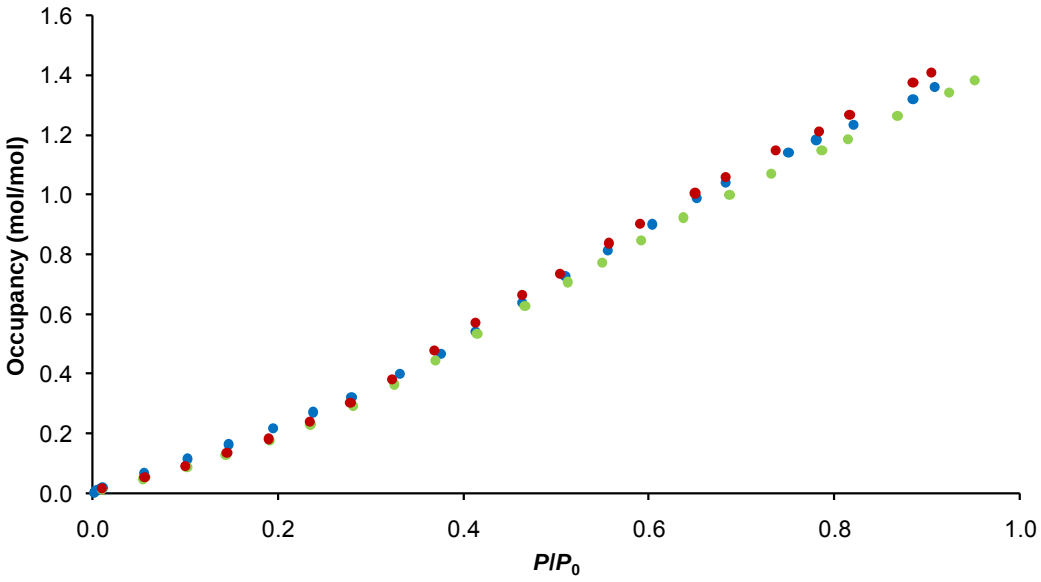

Figure 5.24 The sorption isotherms for water at temperatures 5 (red), 10 (green) and 20 °C (blue) plotted as occupancy against the relative pressure P/P_0.

5.2.4.2 MeOH

The isotherms for sorption of methanol at the different temperatures are shown in Figure 5.25. It is evident that host **M5** is permeable to the strongly polar solvent methanol, with saturation reached at an occupancy of two methanol molecules per host. This is consistent with the host:guest ratio of 1:2 observed for the single-crystal structure **M5·MeOH** (described in section 5.2.2.2), suggesting that this complex can also be generated upon exposure to methanol vapour. Further investigation using SCD and PXRD needs to be carried out to

confirm this, but for the purpose of this study it was assumed that complexes arising from the solid-vapour and solid-liquid interfaces are identical.

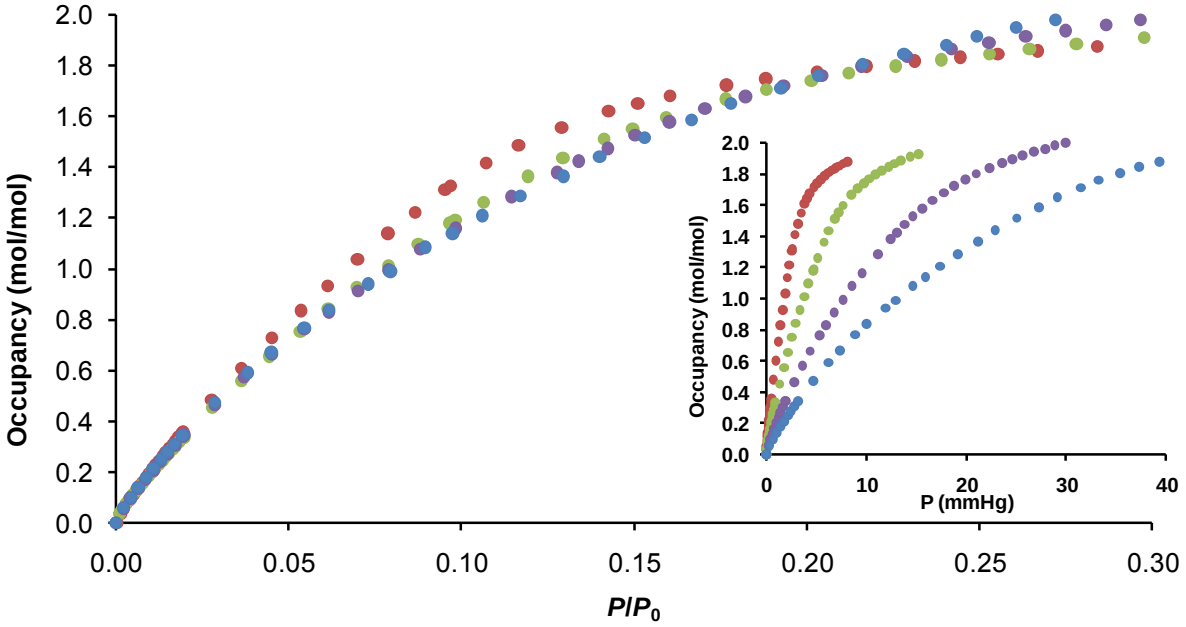

Figure 5.25 Isotherms for methanol sorption at different temperatures (red: 0 °C; green: 10 °C; purple: 20 °C and blue: 30 °C) plotted as occupancy against the relative pressure P/P_0. The abscissa is shown to P/P_0= 0.3. An inset of the methanol sorption isotherm plotted as the occupancy versus the absolute pressure is shown to compare the uptake of methanol at the different temperatures.

Saturation of the cavities occurs at $P/P_0 \approx 0.4$ and higher occupancies are observed with decreasing temperature (Figure 5.25). The key parameters related to the sorption of methanol are listed in Table 5.4. There is no evidence of steps corresponding to the sorption of the individual methanol molecules; occupancy of 0.5 (one guest per pocket) corresponds to $P/P_0 \sim$ 0.09. Sorbent **M5** has a very high affinity for methanol since sorption takes place at very low values of P/P_0. This process is usually associated with enhanced sorbent-sorbate interactions.[33] Refer to section 5.2.2.2 for more information on the intermolecular interactions between host **M5** and the methanol guest molecules. The shape of the methanol sorption isotherms conforms to a typical type I isotherm, despite the host lacking conventional pores.

By plotting $n\ln P$ against $1000/T$ (Figure 5.26), values of $\Delta H°_{ad}$ and $\Delta S°_{ad}$ for the sorption of methanol can be derived from the slope and the intercept, respectively. The almost parallel lines (representing occupancies of 0.5, 0.8, 1.1, 1.4 and 1.7 in Figure 5.26) resulting

from the *n*ln*P* against 1000/*T* plot suggests that isosteric energy values will be similar when taking into account the standard deviation. Values for $\Delta H°_{ad}$ and $\Delta S°_{ad}$ of -99 kJ mol^{-1} and 0.05 kJ mol^{-1}, respectively, are obtained for an occupancy of 0.2 (Table 5.4). These values are consistent with literature values for thermodynamic parameters related to the sorption of methanol using flexible MOF type absorbents.[38]

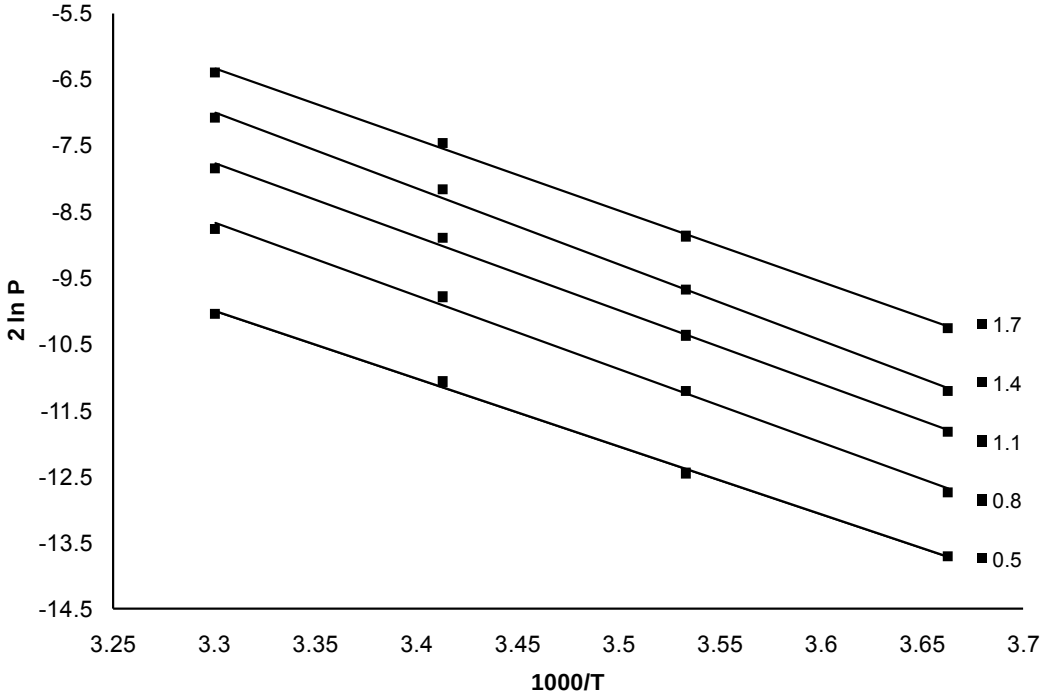

Figure 5.26 Plots of *n*ln*P* versus 1000/*T* for the sorption of methanol using sorbent **M5**. Each line represents a specific occupancy (1.7, 1.4, 1.1, 0.8, 0.5 in this case). Values for $\Delta H°_{ad}$ and $\Delta S°_{ad}$ are derived from the slope and intercept, respectively.

The large negative value of $\Delta H°_{ad}$ (Figure 5.27) is also an indication of the host's affinity for methanol. At guest occupancies ranging between 0 and 0.3, $\Delta H°_{ad}$ becomes more favourable, reaching a minimum at 0.2 guest occupancy (Figure 5.27). This is counter to what is expected when strong lateral interactions are present between the sorbed guest molecules. In most reported cases $\Delta H°_{ad}$ increases with increasing capacity of sorbate (*i.e.* methanol). The trend of decreasing $\Delta H°_{ad}$ with increasing capacity of sorbate, reaching a minimum value, has previously been reported for the sorption of CO_2[25] using the same host. It was suggested that sorbent-sorbate interactions act cooperatively until a maximum affinity is reached at the minimum value for $\Delta H°_{ad}$. Values of $\Delta H°_{ad}$ increase by only a small amount when guest occupancy approaches complete filling (two molecules per cavity as depicted in

Figure 5.10). We note that the discrete nature of the sorption sites (*i.e.* pockets) prevents guest-guest interaction between methanol molecules in neighbouring pockets. However, repulsive interactions between methanol guests located in the same pocket are considered to be the primary factor contributing to the unfavourable values for $\Delta H°_{ad}$ upon saturation. As previously mentioned, the change in $\Delta S°_{ad}$ is negative owing to the sorbed methanol molecules taking on a more ordered state.

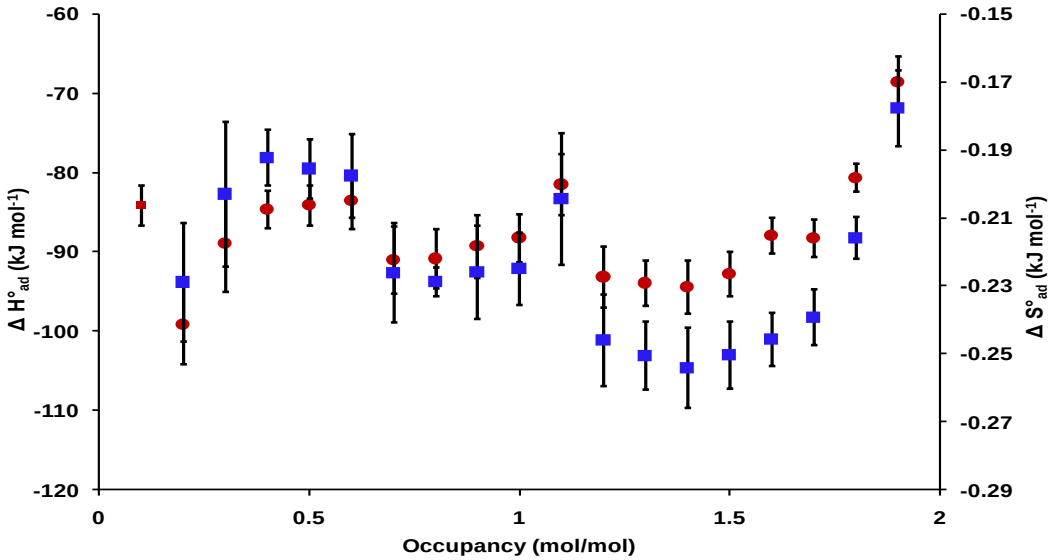

Figure 5.27 Plot showing the relationship between the thermodynamic parameters $\Delta H°_{ad}$ (red) and $\Delta S°_{ad}$ (blue) and the occupancy of methanol sorption. The standard deviation was obtained by means of regression analysis of the linear fits of $n\ln P$ versus $1/T$.

5.2.4.3 Me_2CO

The results of the volumetric sorption of acetone vapour are shown in Figure 5.28. Isotherm profiles for acetone are quite different (with respect to the sorption of methanol), having a clear step (inflection) at ~0.02 P/P_0, corresponding to 0.2 occupancy. This suggests that acetone guests cannot easily penetrate the small aperture of the cavity.[4] Steps at low P/P_0 in type I isotherms are common for flexible coordination polymers. In previous work the presence of steps has been attributed to the so-called "breathing effect" which is associated with a structural change (e.g. from an initial nonporous to a porous framework).[8, 12-13] We propose that the inflection at ~0.02 P/P_0 can be associated with a "gating pressure" that forces open opposite *Im* moieties, facilitating the proposed 1D-diffusion of acetone.[20] Moreover, this is also an indication that host **M5** has a lower affinity for acetone than for methanol.

The same conclusions can be derived by calculating $\Delta H°_{ad}$, having a minimum value (-48 kJ mol^{-1} at 0.2 saturation, Figure 5.29) at the "gating pressure".[44-45] Similar $\Delta H°_{ad}$ values for acetone can be found in the literature.[46] The host:guest ratio approaches 1:1 at ~0.1 P/P_0, following a steep sorption profile. The steep increase in sorption is probably a result of increased lp···π interactions (**M5·MeCO** in 5.2.2.3) between host and guest. Unlike the host:guest ratio in **M5·MeOH**, the ratio remains 1:1 when continuously exposed to acetone vapour. This is to be expected, considering that the single-crystal structure of the solvated complex **M5·MeCO** yields the same ratio. The decrease in $\Delta H°_{ad}$ upon saturation with acetone vapour is attributed to the increase in unfavourable repulsive interactions between host and guest.

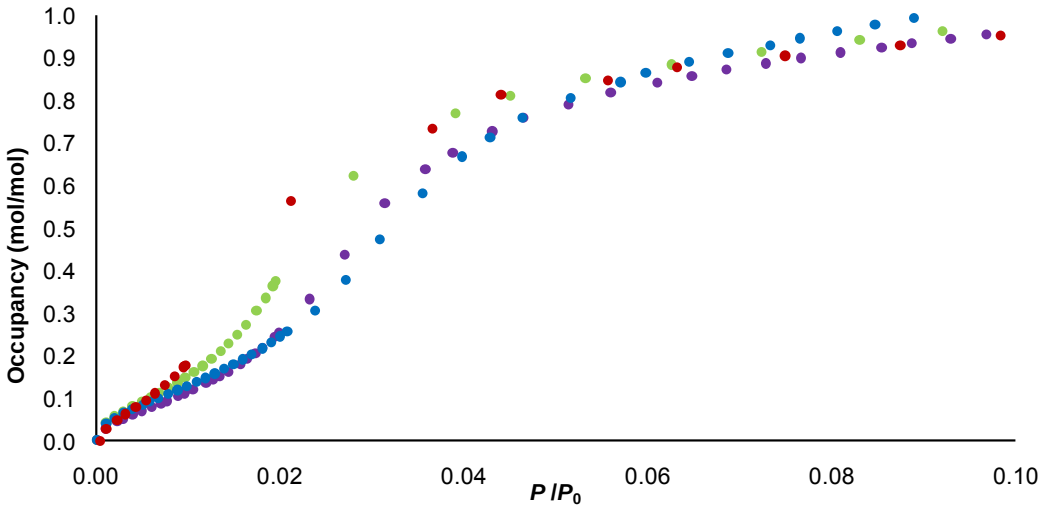

Figure 5.28 Acetone sorption on **M5** at different temperatures (red: 0 °C; green: 10 °C; purple: 20 °C and blue: 30 °C) plotted as occupancy against the relative pressure P/P_0. The abscissa is shown to P/P_0 = 0.1 owing to full occupancy (host:guest = 1:1) being reached at this pressure.

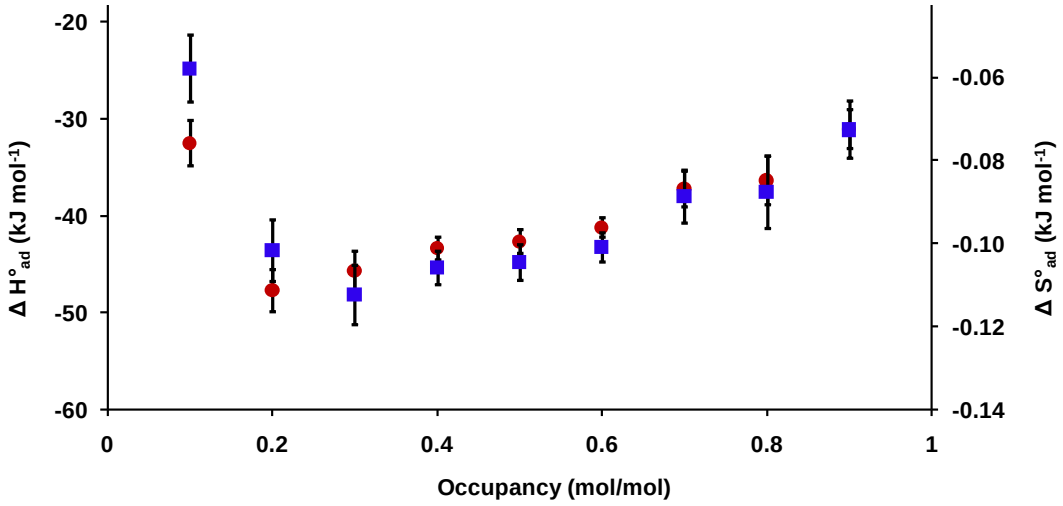

Figure 5.29 The relationship between the thermodynamic quantities ($\Delta H°_{ad}$ in shown red and $\Delta S°_{ad}$ shown in blue) and occupancy for the sorption of acetone. The standard deviation was obtained by means of regression analysis of the linear fits of $n\ln P$ versus $1/T$.

5.2.4.4 MeCN

As discussed in 5.2.2.4, a host:guest ratio of 1:1 is expected in the case of acetonitrile. Sorption results confirm this with a ratio of 1:1 being achieved at ~0.1 P/P_0 (Figure 5.30). Similar to the sorption of methanol, a classical type I isotherm is recorded for acetonitrile as the sorbate. The steep slope at very low P/P_0 shows that **M5** exhibits a high affinity for acetonitrile as a result of favourable attractive host-guest interactions. However, calculation of $\Delta H°_{ad}$ (Figure 5.31) reveals a much lower affinity for acetonitrile than for methanol, despite the comparable size of acetonitrile to methanol as mentioned in 5.2.2.4. We propose that the stronger affinity is a consequence of methanol guests coordinating to the Cu^{2+} centre as seen in **M5·MeOH** while no strong interactions between host and guest results from the sorption of acetonitrile (**M5·MeCN**). Moreover, $\Delta H°_{ad}$ values (Figure 5.31) show no significant minimum before gradually increasing as a result of unfavourable host-guest interactions. Selected $\Delta H°_{ad}$ and $\Delta S°_{ad}$ values are listed in Table 5.4.

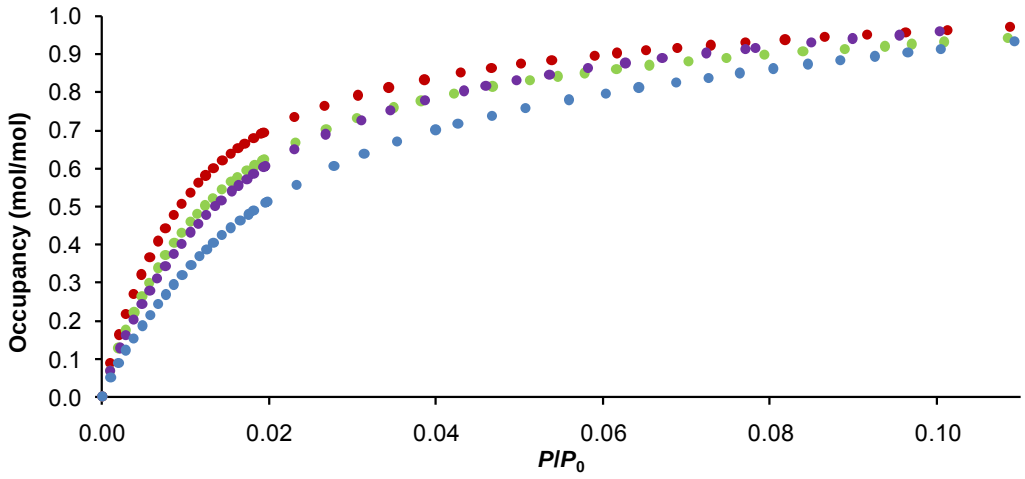

Figure 5.30 The occupancy versus relative pressure P/P_0 isotherm for acetonitrile sorption using adsorbent **M5** at different temperatures (red: 0 °C; green: 10 °C; purple: 20 °C and blue: 30 °C). A host:guest of 1:1 (i.e. saturation) is reached at P/P_0 = 0.12. The abscissa is therefore only shown to P/P_0 = 0.1

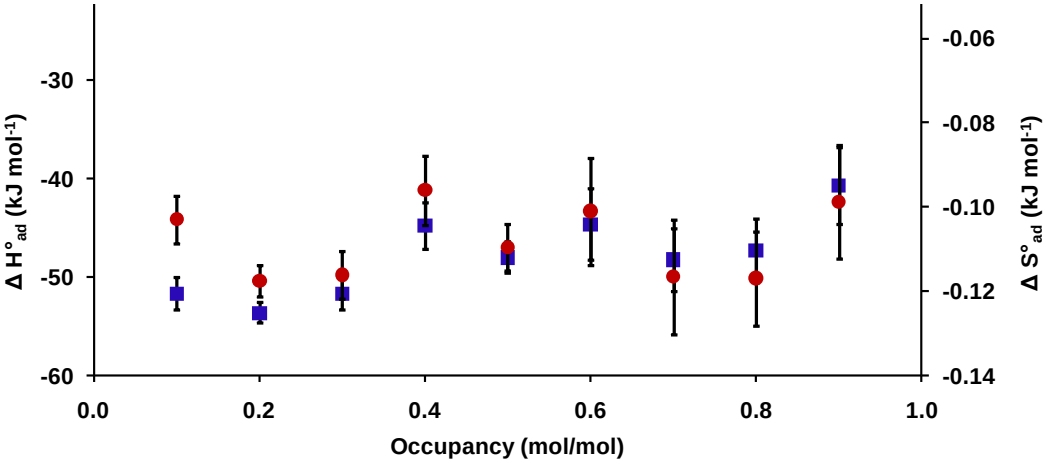

Figure 5.31 The values for $\Delta H°_{ad}$ (red) and $\Delta S°_{ad}$ (blue) versus occupancy for the sorption of acetonitrile.

5.2.4.5 DCM

Figure 5.32 shows the sorption isotherms measured for dichloromethane at four different temperatures. These are excellent examples of classical type I sorption isotherms. In both cases the product has a host:guest ratio of 1:1 when completely filled (*i.e.* one DCM per pocket). Characteristic of strong host-guest affinity, the sorption profile illustrates a very steep gradient between zero guest capacity and $P/P_0 \approx 0.04$, with 90% of the pockets filled at 0 °C. This is unexpected given that dichloromethane is a much larger guest than acetonitrile (70% filled at 0 °C).

Toward saturation, the dichloromethane uptake increases very slowly to reach an almost horizontal plateau between $P/P_0 \approx 0.04 - 0.2$. The differences in the sorption process for

dichloromethane are also reflected in the values of $\Delta H°_{ad}$ (Figure 5.33). Figure 5.33 shows an approximately linear decrease in $\Delta H°_{ad}$ values, reaching a minimum of -49 kJ mol^{-1} at occupancy = 0.8 before increasing toward saturation. Previous studies[47] reported $\Delta H°_{ad}$ values within the same range, when considering the margin of error. The large negative nature of $\Delta H°_{ad}$ implies that **M5** has an increasing affinity for the chlorinated solvent as a result of enhanced attractive host-guest interactions. The interaction between dichloromethane and the chloride anions of the host framework (**M5·DCM** in section 5.2.2.6) is thought to be one of the primary interactions contributing to the high affinity and large negative value for $\Delta H°_{ad}$. Interaction of the chloride anions of the host framework with a gaseous guest was previously reported for a similar metallocycle.[32]

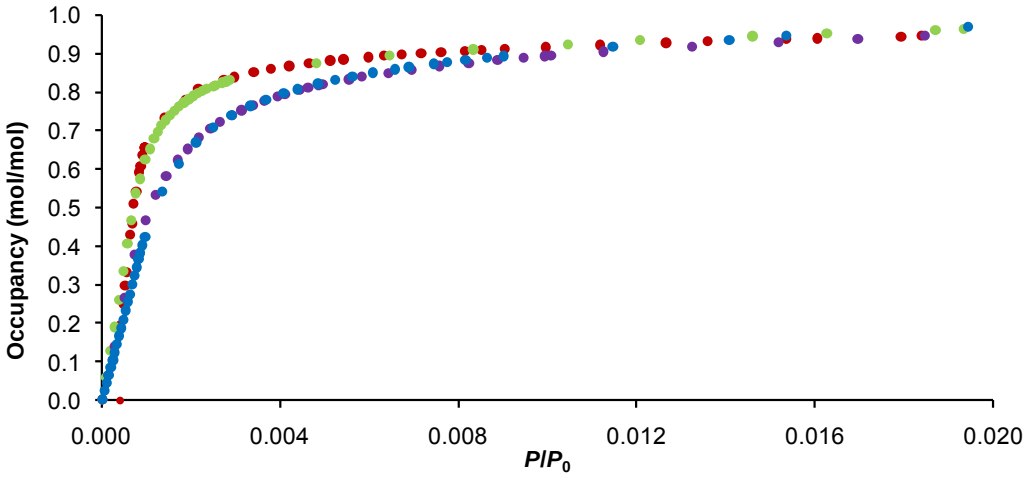

Figure 5.32 Isotherms for the sorption of dichloromethane. The colours of the different isotherms correspond to those in Figure 5.30. The abscissa is only shown to $P/P_0 = 0.02$.

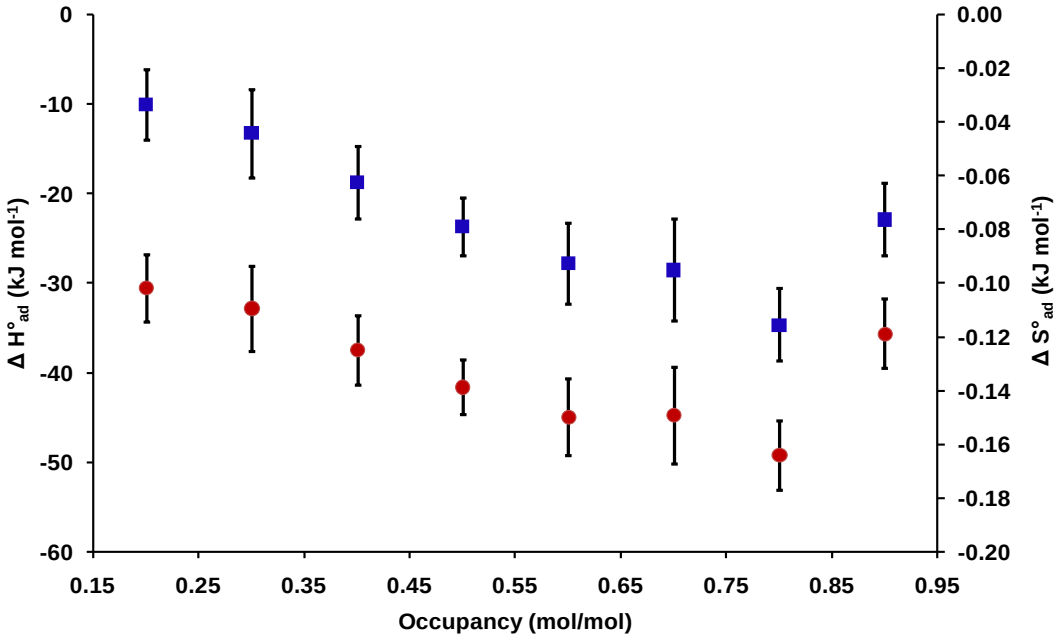

Figure 5.33 Plot showing the relationship between the thermodynamic parameters $\Delta H°_{ad}$ (red) and $\Delta S°_{ad}$ (blue) and the occupancy for dichloromethane sorption. The standard deviation was obtained by means of regression analysis of the linear fits of $n\ln P$ versus $1/T$.

5.2.4.6 $CHCl_3$

The curious sorption trends observed for dichloromethane led us to investigate chloroform as a potential sorbent. As discussed in section 5.2.2.7, a host:guest ratio of 1:1 is inferred from the crystallographic studies. This ratio was not reached throughout the chosen experimental relative pressure range. However, the guest:host ratio still increases at $P/P_0 = 0.8$. The inset in Figure 5.34 reveals that no significant sorption takes place until the "gating pressure"[44-45] at $P/P_0 \approx 0.005$, above which the steep isotherm is an indication of strong affinity for the chlorinated solvent, owing to the increased host-guest attractive interactions. As seen in the solvated crystal structure **M5·CHCl$_3$,** the C–H···Cl hydrogen bond between guest and host is the primary interaction, most likely contributing to the sudden increase in affinity. Interestingly, the steep uptake stage is interrupted by another step in the region of occupancy ≈ 0.45. In most cases the presence of sub-steps in type I isotherms is associated with a structural change, as previously mentioned in section 5.2.4.3.[8, 12-13] The solvated crystal structure **M5·CHCl$_3$** reveals that no structural transformation occurs upon saturation with chloroform vapour. The small step at occupancy ≈ 0.45 is probably the result of a host conformational change (*i.e.* distortion) that induces doubling of the *a*-axis (Figure 5.18).

Figure 5.34 shows that after an initial rapid guest uptake, above occupancy ≈ 0.5 the isotherms ascend slowly. A plausible explanation for the sudden slow uptake is that guest-guest repulsive interactions within the cavities give rise to energetically unfavourable conditions, thus hindering guest uptake to reach the maximum 1:1 ratio. Note that discrete pockets are formed between two hosts in **M5·CHCl$_3$** and not within the complex ring as observed for **M5·H$_2$O–M5·MeOH.** Above occupancy ≈ 0.5 a second chloroform guest is forced into the enlarged pockets, thus giving rise to these energetically unfavourable guest-guest interactions.

Trends observed with regard to the thermodynamic parameters (Figure 5.35) support the above-mentioned assumptions. The initial large negative value for $\Delta H°_{ad}$ (-50 kJ mol^{-1} at occupancy = 0.1) increases rapidly as expected for a host comprised of a heterogeneous surface, where guest-guest repulsive interactions increase as a function of increased guest occupancy (Figure 5.35).[37] Furthermore, between 0.6 and 0.7 guest occupancy, $\Delta S°_{ad}$ values become positive (Figure 5.35) which usually indicates that the sorption reaction is not spontaneous since this will result in a positive value for ΔG. Consequently, the desorption reaction will become more energetically favourable above these relative pressures. Although this is to be expected for systems involving diffusion along a concentration gradient (*i.e.* physisorption), this trend is not observed to a significant extent for the sorption of **MeOH**, **Me$_2$CO** and **MeCN**.

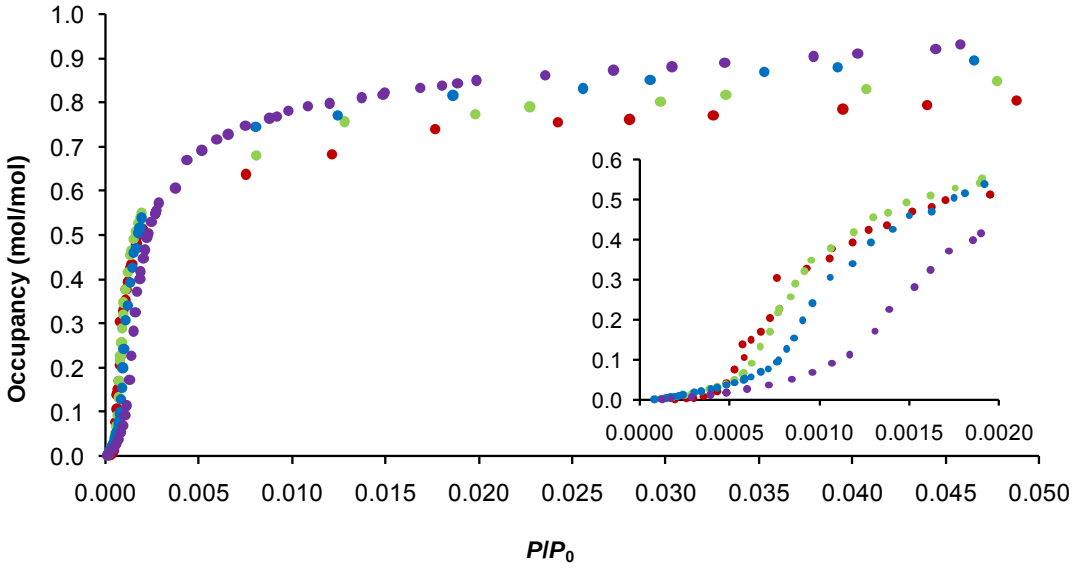

Figure 5.34 The sorption profile for chloroform is shown at four different temperatures. Colours indicating the different temperatures correspond to those used in Figure 5.27. The inset shows how sorption of **CHCl$_3$** is hampered below 0.0015 P/P_0.

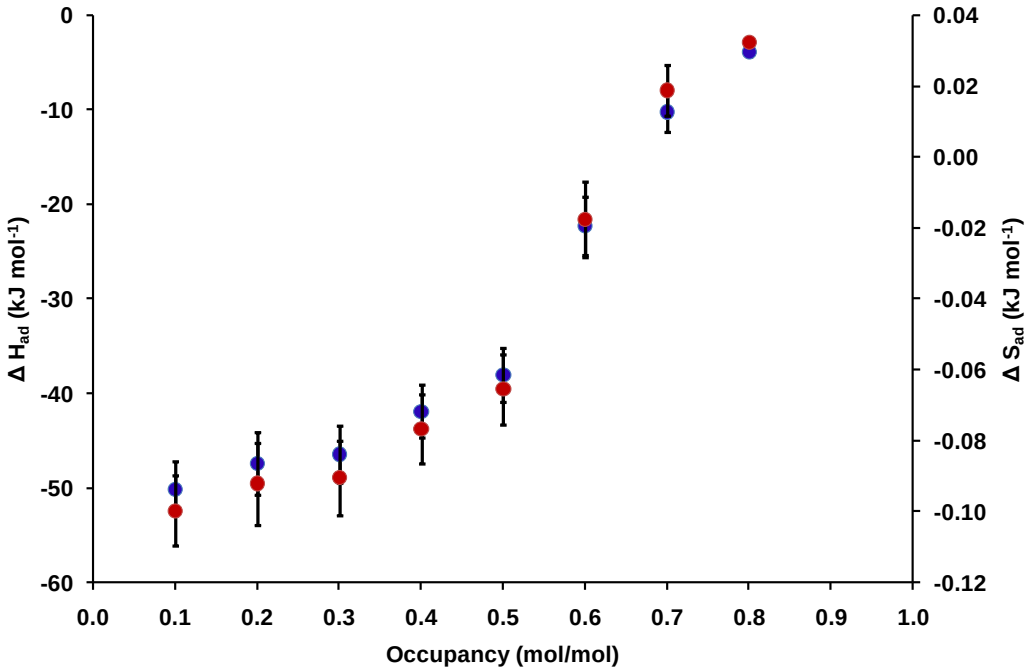

Figure 5.35 A plot of the thermodynamic parameters (red: $\Delta H°_{ad}$, blue: $\Delta S°_{ad}$) for the sorption of chloroform vapour.

5.2.4.7 BZ

Sorption isotherms (Figure 5.36) for benzene only show increased occupancy at lower temperature between $P/P_0 \approx 0 - 0.04$ for the temperature range 0 – 30 °C. Similar to the sorption of acetone and chloroform, sorption of benzene is hampered until the "gating pressure"[44-45] is reached at $P/P_0 \approx 0.02$. This step in the isotherm is not associated with a structural change, but is most likely the consequence of strong host-guest interactions that are implemented cooperatively. The major interactions contributing to the abrupt increase in affinity are thought to be the Cu···π and π··· π interactions between host and guest. A host:guest ratio of 1:1 is reached after an almost horizontal plateau between $P/P_0 \approx 0.06 - 0.2$. This corresponds well with the ratios obtained from the TGA thermogram in section 5.2.3 and the single-crystal structure **M5·BZ** in section 5.2.2.9.

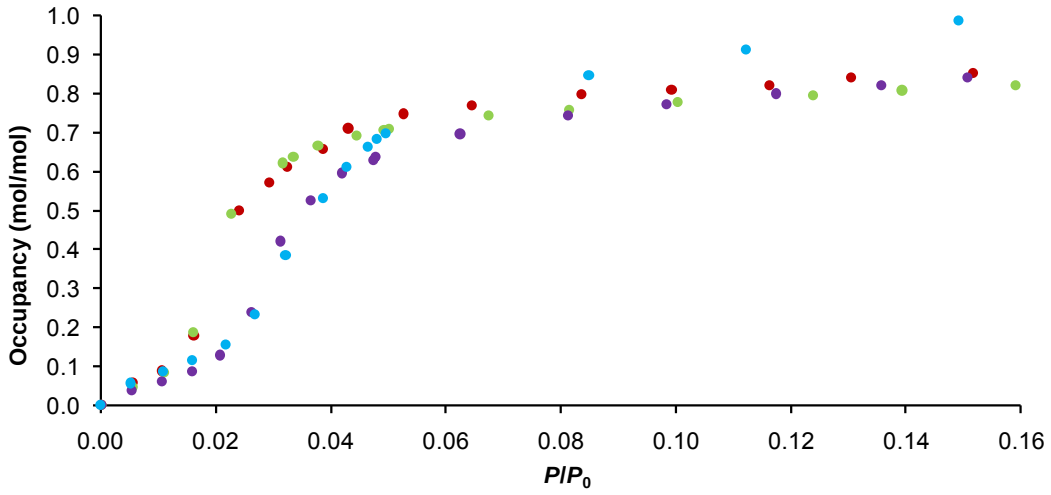

Figure 5.36 Sorption isotherms for the sorption of benzene, measured in the temperature range 0 – 30 °C.

As expected for a homogeneous surface, the calculated $\Delta H°_{ad}$ values increase rapidly above occupancy = 0.5 when repulsive interactions contribute to the energy values (Figure 5.37). Comparing calculated $\Delta H°_{ad}$ values for benzene (Figure 5.37) with the values (-50 to -45 kJ mol^{-1}) obtained from a study using activated carbon as the adsorbate,[48] implies a strong affinity for benzene.

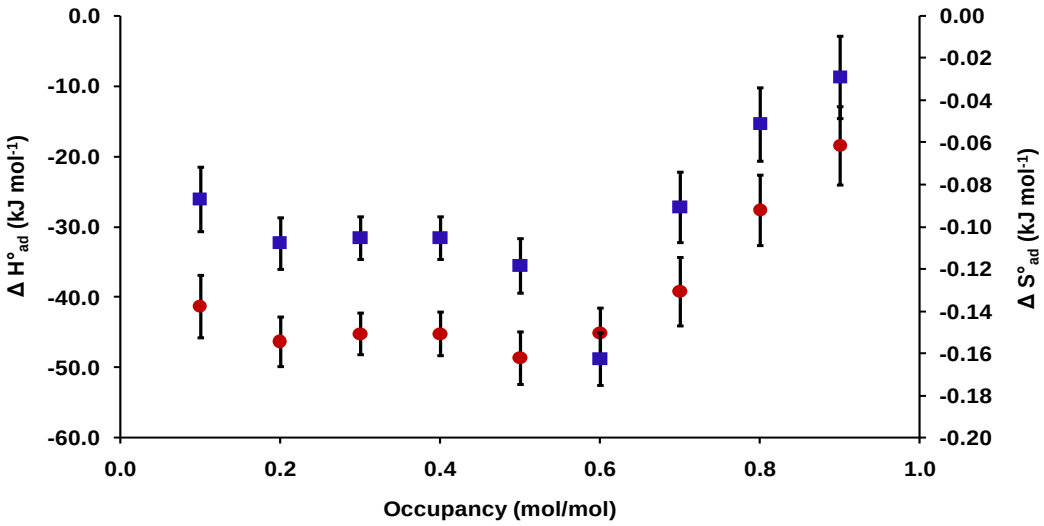

Figure 5.37 The $\Delta H°_{ad}$ (red) and $\Delta S°_{ad}$ (blue) values for the sorption of benzene.

Table 5.4 A summary of the thermodynamic parameters for sorption of **H_2O–$CHCl_3$** and **BZ**. Values (in kJ mol^{-1}) for $\Delta H°_{ad}$ and $\Delta S°_{ad}$ at an occupancy of 0.2 are given and standard deviations were obtained from regression analysis of the linear fits of $n\ln P$ vs $1/T$.

	guest	$\Delta H°_{ad}$ (kJ/Mol)	standard deviation $\Delta H°_{ad}$	$\Delta S°_{ad}$ (kJ/Mol)	standard deviation $\Delta S°_{ad}$
H_2O	water	-27.4	4.1	-0.05	0.01
MeOH	methanol	-99.1	5.0	-0.23	0.02
Me_2CO	acetone	-47.7	2.2	-0.10	0.01
MeCN	acetonitrile	-53.6	1.0	-0.12	0.00
DCM	dichloromethane	-30.5	3.7	-0.03	0.01
$CHCl_3$	chloroform	-47.4	3.3	-0.09	0.01
BZ	benzene	-46.3	3.5	-0.11	0.01

5.2.5 Sorption of volatile organic solids

Studies of the permeability to organic vapours by porous as well as seemingly nonporous materials have received much attention in the field of supramolecular chemistry. However, thus far there have been very few reports[49] on physisorption (*i.e.* thermodynamic and/or kinetic processes) of volatile organic solids larger than iodine; most of the studies utilise carbon nanotubes and MOFs with large permanent pores.[50-51] In order to determine whether **M5** is porous to even larger guests, we investigated several volatile organic solids (Figure 5.38) as potential sorbates.

Single-crystals of **M5a** were sealed in the presence of freshly ground crystals of the targeted guest, taking special care to allow crystals of **M5a** to be in contact with the excess naphthalene or *p*-dichlorobenzene. In both cases the crystals remained intact such that their structures could be determined using single-crystal X-ray diffraction. The permeability to these guests (listed in Table 5.3) was further investigated kinetically using an in-house constructed gravimetric system based on an instrument that was previously used for such measurements.[52] Data obtained from the sorption experiments were plotted as the occupancy (mol guest/mol host) versus the measurement time.

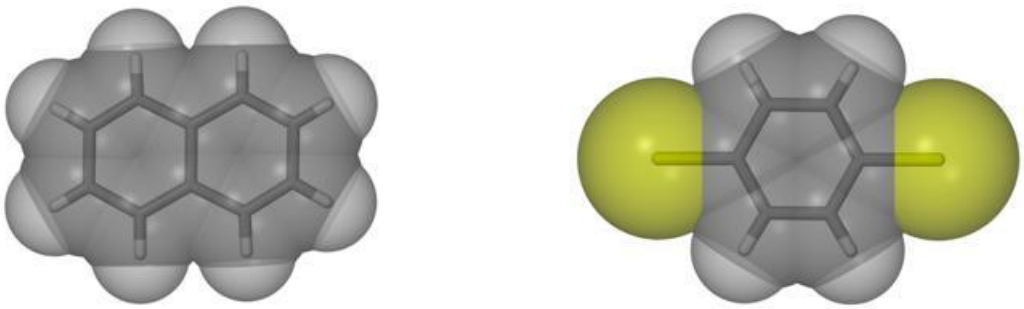

Figure 5.38 Idealised van der Waals representations of naphthalene and *p*-dichlorobenzene. The accessible space in **M5a** is 108 Å^3, whereas naphthalene and *p*-dichlorobenzene have molecular volumes of 126 and 115 Å^3, respectively.

The ASU (Figure 5.39(b)) of the naphthalene-included complex (**M5·Naph**) consists of half a metallocycle and half the atoms of a naphthalene guest molecule, each at half occupancy. The *Im* moiety of the unique component of the metallocycle is disordered over two positions of equal occupancy. The dihedral angle between the two possible orientations of the disordered *Im* ring is 26.49(1)°. It was initially surprising to note that the guest is not located within the complex ring; the naphthalene guest is instead situated between two neighbouring hosts of a stacked column (Figure 5.43(b)). Although a similar arrangement of host and guest is observed in the chloroform solvate structure **M5·CHCl$_3$** (Section 5.2.2.7), the naphthalene guest in **M5·Naph** is much larger than chloroform and only one guest can be accommodated per pocket. Therefore, each metallocycle shares a guest with only one neighbouring metallocycle in order to avoid repulsive van der Waals contacts between nearby guests (Figure 5.43(b)). Thus, an enlarged pocket is formed between two hosts by means of a similar mechanism explained for sorption of chloroform in Section 5.2.2.7. The formation of the merged cavity supports the previously suggested mechanism of transport (see Figure 5.2).[20] In **M5·CHCl$_3$** the metallocycles accommodate the chloroform guest by doubling the *a* axis, but in **M5·Naph** no doubling of the axis occurs. A host:guest ratio of 2:1 is observed in the single-crystal structure **M5·Naph.**

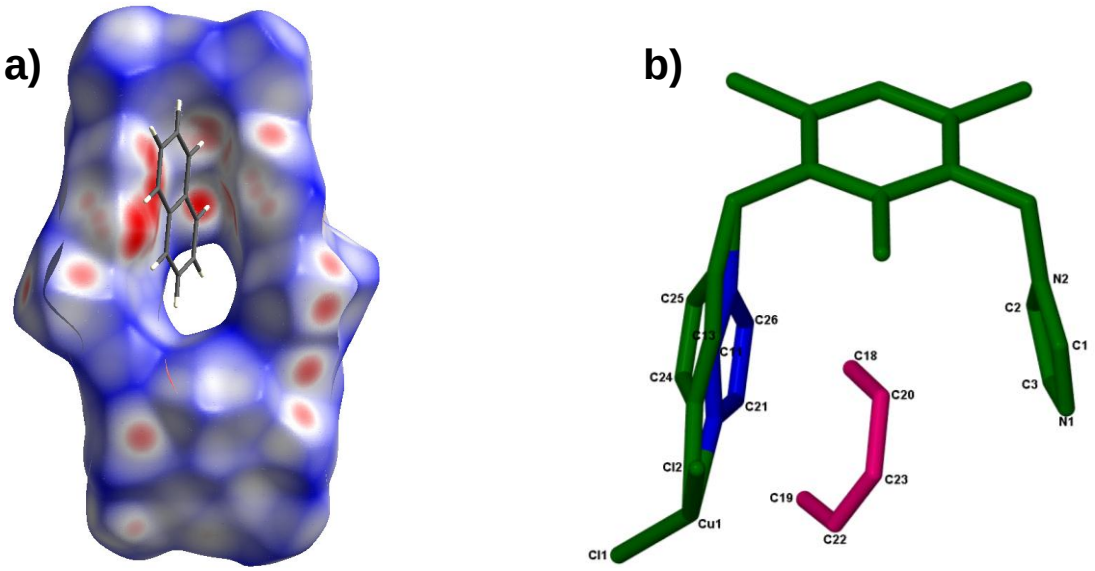

Figure 5.39 (a) Hirsfeld surface analysis (right) was carried out for the metallocycle and the position of the naphthalene guest is illustrated; red surfaces reveal strong interactions between host and guest. (b)The ASU (situated about an inversion centre) of the naphthalene-included structure **M5·Naph** is shown as capped-sticks. Only selected atoms are numbered. The disordered positions of the *Im* rings are shown in blue ("closed") and green ("open"). The guest is represented in pink and hydrogen atoms are omitted for clarity.

As might be expected for systems containing naphthalene, host-guest contacts in **M5·Naph** mainly consist of π-π stacking of the guest and *Im* moieties of the host (centroid···centroid ≈ 3.63 Å and $C20_{donor}$···centroid ≈ 3.19 Å). The host-guest interactions can be mapped on the Hirshfeld surface of the host, using the program CrystalExplorer; red surfaces represent strong interactions (Figure 5.39(a)). Removal of naphthalene from **M5·Naph** occurs readily at room temperature as seen in the TGA thermogram shown in Figure 5.40. The percentage mass loss on the TGA thermogram also corresponds to a host:guest ratio of 2:1. Furthermore, the DSC thermogram (Figure 5.48) reveals two endothermic peaks. The sharp peak at ~80 °C corresponds to the melting point of naphthalene (Table 5.3) and the broad peak at ~110 °C is thought to be a host distortion as a consequence of naphthalene diffusing out of the cavities. Thus, the metallocycle in **M5·Naph** reverts to the conformation in the empty host phase **M5a**.

Sorption of naphthalene using host **M5** was investigated using a gravimetric sorption instrument. The abrupt uptake between 0 and 100 min is an indication that the solid-vapour reaction proceeds readily. A host:guest ratio of 2:1, as observed in the single-crystal structure **M5·Naph**, is reached after a time of 700 min. Complete filling (mass of empty host sample = 59.2 mg, one naphthalene shared between two hosts = 4.5 mg) is achieved after a gradual rise

towards an almost horizontal plateau between 300 and 700 min. Using this kinetic approach one can postulate the mechanism of sorption, but this forms part of future studies.

It is also interesting to note that metallocycle **M5** does not appear to be permeable to decahydronaphthalene, anthracene, phenanthrene or any of the quinoline-based compounds. A plausible explanation for decahydronaphthalene not being sorbed is its irregular shape when compared to the planar molecular shape of naphthalene.

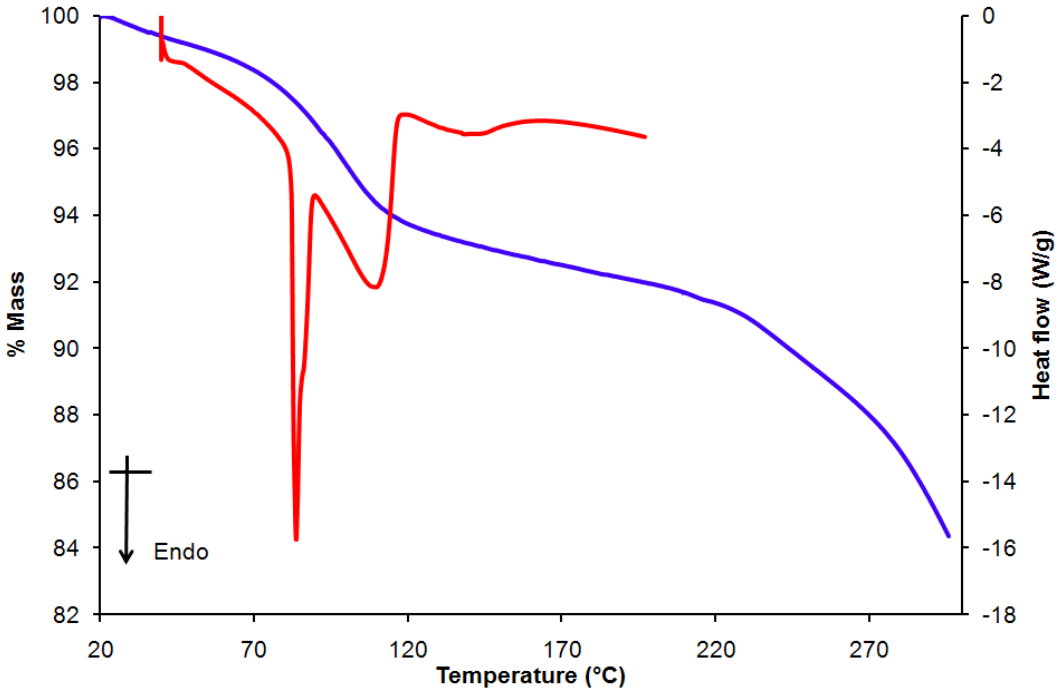

Figure 5.40 Thermoanalytical data for desorption of **M5·Naph**. The TGA thermogram is shown in blue and the DSC thermogram in red. Desorption of napthalene results in a mass loss of approximately 6.41%. Decomposition of the metallocycle occurs above 200 °C.

Owing to its molecular volume, which is comparable to that of naphthalene, as well as its high vapour pressure at room temperature, the permeability to p-dichlorobenzene (Table 5.3) was tested in a manner similar to that described for naphthalene in the previous section (See Figures 5.41 and 5.42). Kinetic sorption measurements (Figure 5.42) revealed a surprising trend towards a 1:1 host:guest ratio. However, the precise 1:1 ratio was not reached during the measurement time allowed. The sorption isotherm shown in Figure 5.42 is indicative of a high affinity for *p*-dichlorobenzene and the solid-vapour reaction proceeds readily. This is suggested by the steep gradient (time = 0 – 20 min) on the kinetic curve in Figure 5.42.

Following the steep gradient, the almost horizontal sorption profile reaches an occupancy of 0.9 after approximately 1000 min.

Single-crystals exposed to *p*-dichlorobenzene vapour for several days were of sufficient quality for SCD and the structure was easily elucidated. Although the space-group symmetry ($P2_1/c$) of the empty metallocycle **M5** is maintained, the ASU is comprised of half a metallocycle and half a *p*-dichlorobenzene guest molecule. Thus, the host:guest ratio from the crystallographic data is consistent with that implied by the sorption isotherm (~ 1:1). Calculation of the accessible space (*i.e.* Connolly surface, using a probe r = 1.8 Å in Figure 43c) in **M5·DCB** reveals a void volume ≈ 1196 $Å^3$ per unit cell. Figure 5.43c illustrates the tight fit of the guest molecules within the empty space. Instead of forming a temporary channel (*e.g.* merged cavity as observed for **M5·Naph**) between neighbouring metallocycles, the hosts accommodate the large guests by creating a permanent *p*-dichlorobenzene-filled channel. The reversibility of this host deformation (i.e. metallocycle conformation in **M5·DCB** to conformation in **M5**) is suggested by the broad endotherm in the DSC thermogram (Figure 5.41). We suspect that the strong guest-guest interactions (Cl···Cl = 3.823 Å, ∠C–Cl···Cl = 110.67°) of the halogenated guest play a major role in both the tight fit in the channel (*i.e.* 1:1 host:guest ratio), and the strong affinity for *p*-dichlorobenzene. Strong host-guest interactions (π···π stacking: centroid···centroid ≈ 3.642 Å; C–H···π hydrogen bond: C_{donor}···centroid ≈ 3.532 Å) also contribute to the strong affinity for *p*-dichlorobenzene. Unlike most of the guests investigated in the present study, *p*-dichlorobenzene does not desorb readily at room temperature. The chlorinated guest can only be removed by heating above 70 °C (Figure 5.41), which comports with the assumptions made from the strong guest-guest interactions present in the SCD structure of **M5·DCB**.

Host **M5** was additionally exposed to several other volatile organic solids (*p*-dibromobenzene. *p*-diiodobenzene and *p*-dimethoxybenzene). Of these, only *p*-diiodobenzene is not absorbed. However, sorption of the larger guests does not leave the crystals intact and high resolution PXRD data will be required in order to obtain structural information for the complexes.

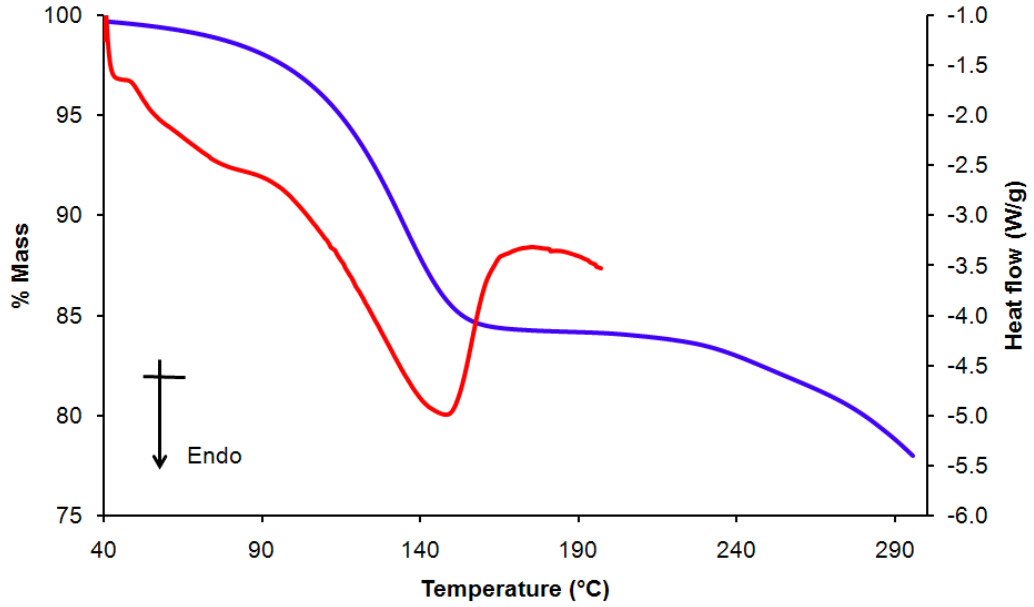

Figure 5.41 Thermoanalytical data for desorption of **M5·DCB**. The TGA thermogram is shown in blue and the DSC thermogram in red. Desorption of *p*-dichlorobenzene results in a mass loss of 15.83%. Decomposition of the metallocycle occurs above 200 °C.

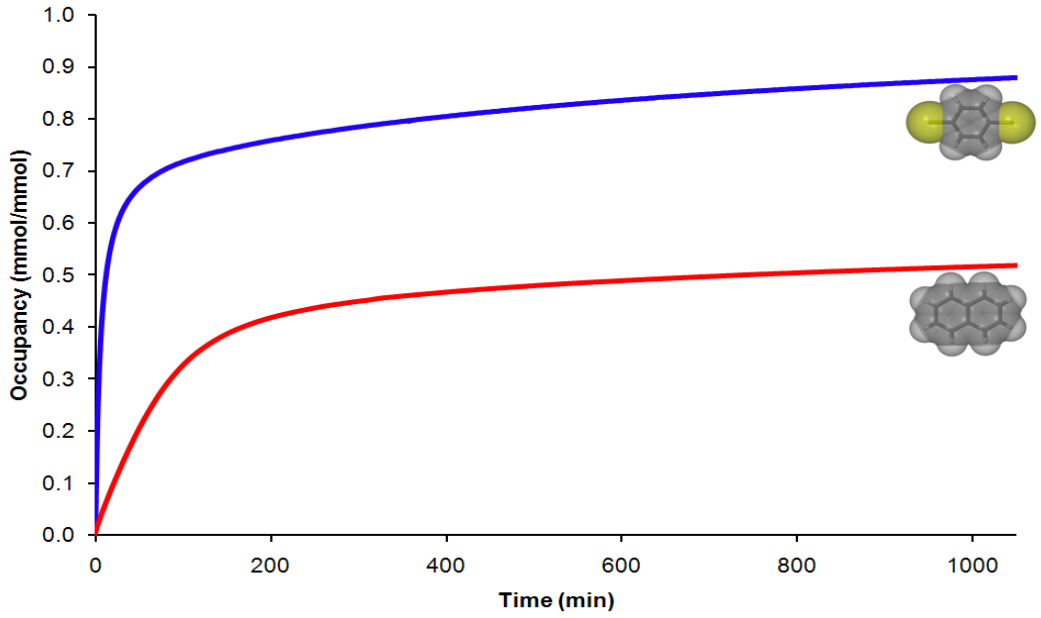

Figure 5.42 Kinetic isotherms (measured at room temperature) for naphthalene (red) and *p*-dichlorobenzene (blue) at guest vapour pressures of 0.08 and 1.76 mmHg, respectively. Sorption isotherms were measured using an in-house constructed gravimetric system.[52] Full occupancy for naphthalene uptake (host:guest ratio = 2:1) is reached after approximately 700 min. Full occupancy for *p*-dichlorobenzene uptake (host:guest ratio = 1:1) is not reached in the experimental time allowed.

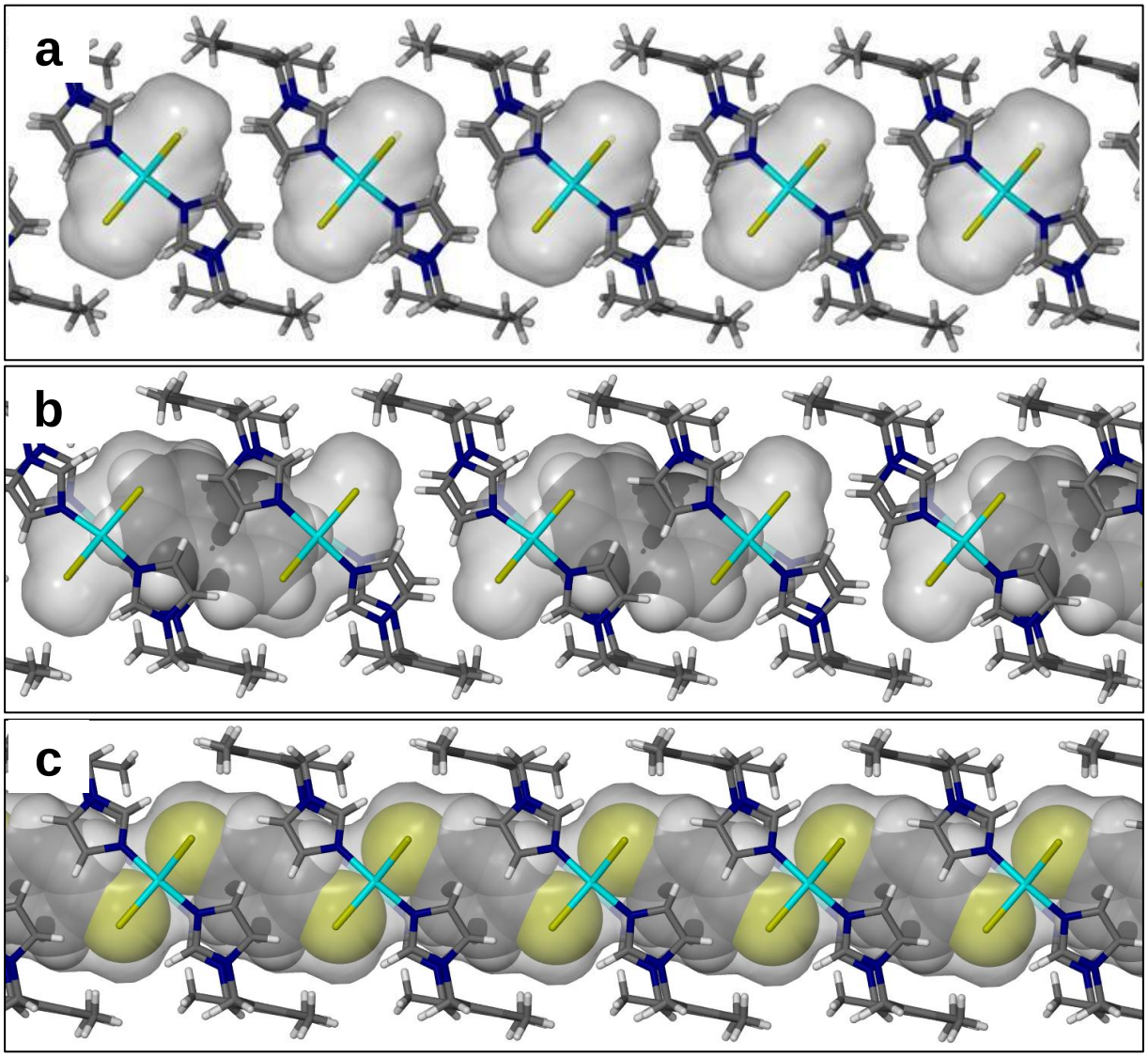

Figure 5.43 A perspective view along [101] of the stacked columns showing the guest-accessible volumes (grey transparent surface) in (a) **M5a (***V* = 107 Å^3 and probe *r* = 1.4 Å) (b) **M5·Naph (***V* = 296 Å^3 and probe *r* = 1.4 Å) (c) **M5·DCB (***V* = 1196 Å^3/ cell and probe *r* = 1.8 Å). The guests are represented as van der Waals surfaces and the metallocycles as CPK capped-sticks. In both **M5·Naph** (b) **M5·DCB** (c) strong host-guest interactions are present between the *Im* rings as indicated by the van der Waals surface of the guests protruding slightly from the Connolly surface. Remarkably, the accessible space in **M5·Naph** and **M5·DCB** is correspondingly 16% and 59% of the total volume.

5.3 General conclusions and future studies

Metallocycle **M5** was shown to be an excellent candidate for further advances in gaining precise structural detail of absorbed gas molecules, in view of the fact that **M5a** retains monocrystallinity upon desolvation and responds to even low external pressures. In addition to the flexibility of **M5**, its relatively low symmetry facilitates accurate modelling of disordered guest molecules over several positions when compared to high symmetry systems where modelling of disordered guests can be very difficult. This allowed us to accurately characterise complexes **M5·CO_2**, **M5·CO**, **M5·C_2H_2** and **M5·VCl** (Table 5.1) and deduce host:guest ratios that corresponded to the low pressure sorption isotherms.

A series of experiments was conducted in order to investigate the reversible sorption of a range of larger organic guests using discrete metallocycle **M5** (Scheme 5.2). Relatively insignificant deviations in the lattice parameters and atomic coordinates of structures **M5a**–**M5·DFB** were observed upon exposure to organic guest vapours **H_2O**–**DFB** (Table 5.2). Structure elucidation together with electron count calculations (Table 5.5, page 180) revealed that all of the investigated solvents are indeed included in the crystal structures as depicted in Scheme 5.2. At the same time it is remarkable that the same crystal can be dipped into another solvent listed in Table 5.2, and full occupancy is reached after several hours. Thus, desolvation of **M5·H_2O·MeOH** is not required (Scheme 5.2), since guest exchange occurs readily. Several solvate structures resulted and, in most cases, the guest molecules were found within a discrete cavity of which the Connolly surface could be mapped using a probe radius of 1.4 – 1.8 Å. In principle, the host framework remains unaltered, but undergoes progressive adjustment of its structure to accommodate the uptake of organic guests **H_2O**–**DBF** (Table 5.2). During the process of guest uptake, the average size and shape of the cavity changes, increasing smoothly from 108 $Å^3$ for **M5a** to 147 $Å^3$ for **M5·MeOH** to 152 $Å^3$ for **M5·Me_2CO** (Table 5.5 page 180). In contrast to the structures **M5·H_2O**–**M5·DCM**, the chloroform guests were not located within the complex ring in **M5·$CHCl_3$**; instead two chloroform molecules were enclosed in an enlarged cavity (between two neighbouring metallocycles) formed by merging two discrete pockets. Volumes of the solvent-filled cavities are significantly larger than those of the parent structures, almost certainly as a result of the shape and size of the newly adsorbed guest molecules. Furthermore, a significant increase (when compared to the empty structure **M5**) in Cu···Cu distance and *Im*···*Im* distance (Table 5.5, page 180) is observed upon saturation with organic solvents **H_2O**–**DFB**. Host-guest

interactions also play a major role in guest uptake, the position of the guest within the discrete pocket, and the host:guest ratio. Removal of the guest molecules always resulted in desolvated complex **M5a**.

Sorption isotherms for each of the guests **H_2O–BZ** were measured at four different temperatures using a volumetric instrument. Evaluation of thermal effects on the sorption of guest vapours indicated that increasing the temperature from 0 – 30 °C decreases the uptake capacity at any particular pressure in all cases. The resulting saturated complexes were identical to those obtained in the SCD study in all cases. Data obtained from the isotherms were used to determine thermodynamic parameters by means of the isosteric procedure. Values for $\Delta H°_{ad}$ and $\Delta S°_{ad}$ (Table 5.4) correspond well with previously reported values using zeolites and/or coordination polymers. Host **M5** was found to have the highest affinity for **MeOH**, followed by **MeCN** > **Me_2CO** > **$CHCl_3$** > **BZ** > **DCM** > **H_2O**. As mentioned above, host-guest interactions are considered the primary driving force in all instances, specifically where a high affinity is observed. Affinity of host **M5** for various guests could additionally be tested by carrying out competition experiments. This entails exposing **M5** to vapour mixtures and unravelling the composition of the resultant complex by carrying out single-crystal X-ray diffraction analysis (in addition to supporting analyses such as NMR, IR and GC-MS). The complex can therefore consist of a mixture of guests or it can preferentially absorb one guest above the other, depending on the affinity for the particular guests.

We have also provided convincing support for the proposed mechanism of guest transport through seemingly nonporous metallocycle **M5**. This mechanism involves the 1D-diffusion of guest molecules from one discrete pocket to another by spontaneously creating a temporary channel between two neighbouring hosts within a stacked column. The working principle of the 1D-diffusion is thought to be the flexibility of the *Im* rings of each **L6** ligand. Thus, the *Im* rings act as a gate to facilitate and control the permeability of guests. The gates are therefore "open" when a guest is present, and "closed" in the empty host structure **M5**. The extent of this flexibility was tested using larger guests such as naphthalene and *p*-dichlorobenzene. Surprisingly, even these larger organic solids can undergo this suggested 1D-diffusion[20] from one cavity to another within a stacked column, despite the relatively low vapour pressure of the guests naphthalene and *p*-dichlorobenzene. At the same time it is also remarkable that the crystals remain intact (*i.e.* SCD data could be collected), bearing in mind the enormous strain that the metallocycle must endure to accommodate the large guests (the empy space in **M5a** has a volume of 108 $Å^3$, but naphthalene has a molecular volume of 126

Å^3). Host:guest ratios of 2:1 and 1:1 were reached in **M5·Naph** and **M5·DCB**, respectively. In the naphthalene-included crystal structure **M5·Naph**, the *Im* rings are tilted at a dihedral angle of 26.49(1)° with respect to the position in the empty structure. The structural data obtained from **M5·Naph** and **M5·DCB** support the suggested mechanism of transport calculated for CO_2 and I_2 (part of a previous study on gas sorption).[20] Sorption isotherms for the organic solids were measured using a locally-constructed gravimetric system and were found to be consistent with the SCD data. Furthermore, molecular mechanics calculations of naphthalene and *p*-dichlorobenzene diffusion through the crystal of **M5** are in progress and will hopefully provide convincing support for the adaptable binding-site hypothesis as a mechanism of guest transport, which was also suggested for the permeability of CO_2 and I_2.

It would be interesting to study the permeation of long alkyl chains, considering that (if adsorbed) these guests should cause the *Im* rings to be "open" *throughout* the structure, thus creating a continuous channel as observed in **M5·DCB**. However, using alkyl chains sometimes results in incommensurate structures (*i.e.* the host and guest have different periodicities).[53] In this case, it would be difficult to model the guest molecules, but such investigations will form part of future studies on the permeability of **M5**.

Table 5.5 A summary of the SCD data, thermal analysis and volumetric sorption data obtained from the present study. Electron count predictions are shown in brackets.

Solvate	% Mass loss (TGA)	Host : Guest (TGA)	Host : Guest (SCD)	Cu–Cu (Å)	*Im–Im* (Å)	Void Volume (Å^3)	Electron Count (calc)	Host : Guest (Sorption)
Empty Host	-	-	-	6.59	5.93	108	- (0)	-
H_2O	2.65	1:1.4	1:1.4	6.17	5.18	92	27 (26)	1:1.4
Methanol	4.03	1:2	1:2	6.61	5.71	147	37 (36)	1:2
Acetone	3.39	1:1	1:1	7.04	5.85	152	30 (32)	1:1
Acetonitrile	3.34	1:1	1:1	6.68	5.48	107	25 (22)	1:1
Dichloromethane	8.01	1:1	1:1	6.89	5.69	125	38 (41)	1:1
Chloroform	12.46	1:1	1:1	7.07	6.23	298	112 (116)	1:1
Carbon Disulfide	5.53	1:1	1:1	6.73	5.53	108	33 (38)	1:1
Benzene	8.95	1:1	1:1	6.96	5.88	169	42 (47)	1:1
p-Difluorobenzene	7.37	1:1	1:1	7.06	5.87	151	58 (58)	-
Naphthalene	2.86	2:1	2:1	6.97	6.04	296	32 (34)	2:1
p-Dichlorobenzene	15.83	1:1	1:1	7.31	6.30	1196[*]	83(74)	1:1

[*] Calculated as the section of the channel per unit cell

5.6 Experimental section

5.6.1 Synthesis and characterisation

5.6.1.1 1,3-bis(imidazol-1-ylmethyl)-2,4,6-trimethylbenzene (L6)[14]:

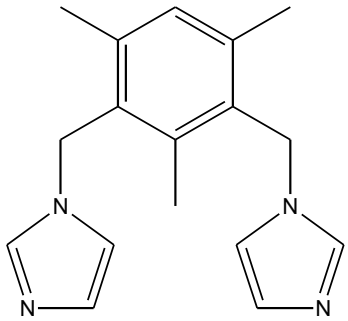

To a solution of imidazole (6.71g 100mmol) in 100 ml methanol were added 2.32g of 1,3-bis(dichloro-1-ylmethyl)-2,4,6-trimethylbenzene. The mixture was heated under relux at 70 ºC. The reaction was followed by accurate spotting of the product against the starting material on a TLC plate and found to be complete after 24 hrs. Excess solvent was removed under reduced pressure and gentle heating before precipitation of the product by adding an ample amount of a 10% K_2CO_3 solution. After washing with ethyl acetate, the pure product was filtered and left to dry overnight.

Crystals of this complex were grown under solvothermal conditions (heated at 80 ºC for 24 hrs before cooling to room temperature over a period of 36 hrs) by adding a solution 15.2 mg (0.089 mmol) of $CuCl_2 \cdot 2H_2O$ in 2 ml of methanol to a solution of 25 mg (0.089mmol) **L6** in 3 ml of methanol. Immediate precipitation took place, but green plate-shaped crystals suitable for SCD were present after the solvothermal handling. The solvent-free complex (**M5a**) was obtained by evacuating the crystals for 3 hrs at 60 ºC under reduced pressure. Both products were characterised by means of PXRD, SCD and thermal analysis. The PXRD of the green precipitate is representitive of the powder pattern simulated from the SCD structure.

5.7 Crystallographic data

Table 5.6 Crystallographic data for all the structures discussed within Chapter 5.

	M5·H_2O	**M5·MeOH**	**M5·MeCN**	**M3·Me_2CO**
Empirical formula	$C_{34}H_{38}Cl_4Cu_2N_8O_{1.40}$	$C_{18}H_{23}Cl_2CuN_4O$	$C_{36}H_{25}Cl_4Cu_2N_9$	$C_{19}H_{23}Cl_2CuN_4O_1$
Formula weight	850.00	445.84	852.88	444.43
Temperature/K	100(2)	100(2)	100(2)	100(2)
Wavelength/Å	0.71073	0.71073	0.71073	0.71073
Crystal system	monoclinic	monoclinic	monoclinic	monoclinic
Space group	$P2_1/c$	$P2_1/c$	$P2_1/c$	$P2_1/c$
***a* /Å**	8.333(4)	8.4261(10)	8.3483(11)	8.386(3)
***b* /Å**	10.394(5)	10.7068(13)	10.5979(14)	10.778(4)
***c* /Å**	22.167(10)	21.974(3)	22.200(3)	22.282(8)
α /°	90	90	90	90
β /°	98.264(7)	99.441(2)	98.700(2)	99.205(4)
γ /°	90	90	90	90
Volume/Å^3	1900.1(15)	1955.5(4)	1941.5(4)	1988.0(12)
Z	2	4	2	4
Calculated density/g cm^{-3}	1.486	1.514	1.459	1.485
Absorption coefficient (mm^{-1})	1.441	1.405	1.409	1.380
***F*$_{000}$**	870	920	860	917
Reflections collected	11053	8063	7967	10353
Independent reflections	4090 [R_{int} = 0.0505]	4118 [R_{int} = 0.0316]	2633 [R_{int} = 0.0360]	4167 [R_{int} = 0.0730]
Data/restraints/parameters	4090 / 0 / 239	4118 / 2 / 240	2633 / 1 / 226	4167 / 4 / 257
Goodness-of-fit on F^2	1.015	0.996	1.247	0.997
Final *R* indices [I□>□2σ(I)]	$R1$ = 0.0459, $wR2$ = 0.0931	$R1$ = 0.0541, $wR2$ = 0.1594	$R1$ = 0.0499, $wR2$ = 0.1344	$R1$ = 0.0537, $wR2$ = 0.1078
R indices (all data)	$R1$ = 0.0713, $wR2$ = 0.1039	$R1$ = 0.0744, $wR2$ = 0.1834	$R1$ = 0.0607, $wR2$ = 0.1418	$R1$ = 0.1378, $wR2$ = 0.1373

Table 5.6 Continued.

	M5·DCM	**M5·$CHCl_3$**	**M5·CS_2**	**M3·BZ**
Empirical formula	$C_{18}H_{22}Cl_2Cu_2N_4$	$C_{35}H_{41}Cl_7Cu_2N_8$	$C_{35}H_{40}Cl_4Cu_2N_8S_2$	$C_{40}H_{32}Cl_4Cu_2N_8$
Formula weight	456.33	948.99	905.75	898.12
Temperature/K	100(2)	100(2)	100(2)	328(2)
Wavelength/Å	0.71073	0.71073	0.71073	0.71073
Crystal system	monoclinic	monoclinic	monoclinic	monoclinic
Space group	$P2_1/c$	$P2_1/c$	$P2_1/c$	$P2_1/c$
***a* /Å**	8.3498(11)	16.671(2)	8.3483(11)	8.410(2)
***b* /Å**	10.6457(14)	10.7795(15)	10.5979(14)	10.882(3)
***c* /Å**	22.378(3)	22.437(3)	22.200(3)	22.099(5)
α /°	90	90	90	90
β /°	99.387(2)	99.497(2)	98.700(2)	99.049(3)
γ /°	90	90	90	90
Volume/Å^3	1962.5(4)	3976.7(10)	1941.5(4)	1997.3(8)
Z	4	4	2	2
Calculated density/g cm^{-3}	1.544	1.585	1.549	1.493
Absorption coefficient (mm^{-1})	1.524	1.578	1.516	1.373
***F*$_{000}$**	936	936	928	913
Reflections collected	10291	22657	8911	11302
Independent reflections	4184 [R_{int} = 0.0339]	8607 [R_{int} = 0.0416]	3309 [R_{int} = 0.0299]	4292 [R_{int} = 0.0343]
Data/restraints/parameters	4184 / 2 / 256	8607 / 0 / 455	3309 / 0 / 247	4292 / 0 / 240
Goodness-of-fit on F^2	1.014	1.032	1.016	1.134
Final *R* indices [I□>□2σ(I)]	$R1$ = 0.0412, $wR2$ = 0.1008	$R1$ = 0.0546,$wR2$ = 0.1446	$R1$ = 0.0325, $wR2$ = 0.0774	$R1$ = 0.0655, $wR2$ = 0.1481
R indices (all data)	$R1$ = 0.0636, $wR2$ = 0.1153	$R1$ = 0.0920,$wR2$ = 0.1709	$R1$ = 0.0436, $wR2$ = 0.0836	$R1$ = 0.0844, $wR2$ = 0.1572

Table 5.6 Continued.

	M5·DFB	**M5·Naph**	**M5·DCB**	**M5·CO_2**
Empirical formula	C_{38} $H_{43}Cl_4Cu_2F_2N_8$	$C_{39}H_{44}Cl_4Cu_2N_8$	$C_{40}H_{44}Cl_6Cu_2N_8$	$C_{35}H_{40}Cl_4Cu_2N_8O_2$
Formula weight	911.77	893.70	976.61	874.67
Temperature/K	100(2)	100(2)	100(2)	296(2)
Wavelength/Å	0.71073	0.71073	0.71073	0.71073
Crystal system	monoclinic	monoclinic	monoclinic	monoclinic
Space group	$P2_1/c$	$P2_1/c$	$P2_1/c$	$P2_1/c$
***a* /Å**	8.424(2)	8.2957(16)	8.383(2)	8.413(2)
***b* /Å**	10.944(3)	10.770(2)	10.868(3)	10.719(3)
***c* /Å**	22.094(6)	22.516(4)	22.633(6)	22.501(6)
α /°	90	90	90	90
β /°	99.735(5)	99.655(2)	79.007(3)	99.324(3)
γ /°	90	90	90	90
Volume/Å^3	2007.5(9)	1983.1(7)	2024.3(9)	2002.3(10)
Z	2	2	2	2
Calculated density/g cm^{-3}	1.508	1.497	1.602	1.451
Absorption coefficient (mm^{-1})	1.372	1.382	1.489	1.371
***F*$_{000}$**	936	920	1000	897
Reflections collected	4987	7793	11065	11507
Independent reflections	3790 [R_{int} = 0.0330]	2571 [R_{int} = 0.0333]	4356 [R_{int} = 0.0382]	4319 [R_{int} = 0.0253]
Data/restraints/parameters	3790 / 0 / 257	2571 / 0 / 283	4356 / 0 / 256	4319 / 0 / 248
Goodness-of-fit on *F*^{2}	1.054	1.163	1.091	0.994
Final *R* indices [*I*□>□2σ(*I*)]	*R*1 = 0.0642, *wR*2 = 0.1618	*R*1 = 0.0488, *wR*2 = 0.1452	*R*1 = 0.0548, *wR*2 = 0.1125	*R*1 = 0.0333, *wR*2 = 0.0830
R indices (all data)	*R*1 = 0.1012, *wR*2 = 0.1883	*R*1 = 0.0613, *wR*2 = 0.1535	*R*1 = 0.0746, *wR*2 = 0.1201	*R*1 = 0.0498, *wR*2 = 0.0914

Table 5.6 Continued.

	M5·CO	**M5·C_2H_2**	**M5·VCl**
Empirical formula	$C_{35}H_{34}Cl_4Cu_2N_8O$	$C_{19}H_{22}Cl_2CuN_4$	$C_{36}H_{43}Cl_5Cu_2N_8$
Formula weight	851.58	440.85	891.80
Temperature/K	296(2)	100(2)	218(2)
Wavelength/Å	0.71073	0.71073	0.71073
Crystal system	monoclinic	monoclinic	monoclinic
Space group	$P2_1/c$	$P2_1/c$	$P2_1/c$
***a* /Å**	8.3965(7)	8.4815(9)	8.3742(6)
***b* /Å**	10.7207(9)	10.6766(11)	10.6947(8)
***c* /Å**	22.3423(18)	22.732(2)	22.3020(15)
α /°	90	90	90
β /°	98.9880(10)	100.2210(10)	98.9290(10)
γ /°	90	90	90
Volume/Å^3	1986.5(3)	2025.8(4)	1973.2(2)
Z	2	4	2
Calculated density/g cm^{-3}	1.424	1.445	1.501
Absorption coefficient (mm^{-1})	1.378	1.352	1.454
F_{000}	868	908	916
Reflections collected	11327	11523	5326
Independent reflections	4282 [R_{int} = 0.0235]	4353 [R_{int} = 0.0319]	3623 [R_{int} = 0.0211]
Data/restraints/parameters	4282 / 0 / 238	4353 / 0 / 239	3623 / 0 / 248
Goodness-of-fit on F^2	0.985	1.034	1.022
Final *R* indices [I□>□2σ(I)]	$R1$ = 0.0386, $wR2$ = 0.1210	$R1$ = 0.0363, $wR2$ = 0.0915	$R1$ = 0.0376, $wR2$ = 0.0845
R indices (all data)	$R1$ = 0.0562, $wR2$ = 0.1366	$R1$ = 0.0498, $wR2$ = 0.0977	$R1$ = 0.0552, $wR2$ = 0.0922

5.6 References

[1] R. Matsuda, R. Kitaura, S. Kitagawa, Y. Kubota, T. C. Kobayashi, S. Horike, M. Takata, *J. Am. Chem. Soc.* **2004**, *126*, 14063-14070.

[2] S. Kitagawa, R. Kitaura, S. I. Noro, *Angew. Chem. Int. Ed.* **2004**, *43*, 2334-2375.

[3] S. Bourrelly, B. Moulin, A. Rivera, G. Maurin, S. Devautour-Vinot, C. Serre, T. Devic, P. Horcajada, A. Vimont, G. Clet, M. Daturi, J. C. Lavalley, S. Loera-Serna, R. Denoyel, P. L. Llewellyn, G. Ferèy, *J. Am. Chem. Soc.* **2010**, *132*, 9488-9498.

[4] S. Ghosh, S. Bureekaew, S. Kitagawa, *Angew. Chem. Int. Ed.* **2008**, *47*, 3403-3406.

[5] A. H. Fuchs, A. Boutin, M. A. Springuel-Huet, A. Nossov, A. Gedeon, T. Loiseau, C. Volkringer, G. Ferèy, F. X. Coudert, *Angew. Chem. Int. Edit.* **2009**, *48*, 8314-8317.

[6] P. A. Wright, S. R. Miller, G. M. Pearce, F. Bonino, S. Chavan, S. Bordiga, I. Margiolaki, N. Guillou, G. Ferey, S. Bourrelly, P. L. Llewellyn, *J. Am. Chem. Soc.* **2008**, *130*, 15967-15981.

[7] C.-F. Zhuang, J. Zhang, Q. Wang, Z.-H. Chu, D. Fenske, C.-Y. Su, *Chem. Eur. J.* **2009**, *15*, 7578-7585.

[8] G. Ferèy, C. Serre, *Chem. Soc. Rev.* **2009**, *38*, 1380-1399.

[9] G. Ferèy, *Chem. Soc. Rev.* **2008**, *37*, 191-214.

[10] T. Devic, P. Horcajada, C. Serre, F. Salles, G. Maurin, B. Moulin, D. Heurtaux, G. Clet, A. Vimont, J. M. Greneche, B. Le Ouay, F. Moreau, E. Magnier, Y. Filinchuk, J. Marrot, J. C. Lavalley, M. Daturi, G. Ferèy, *J. Am. Chem. Soc.* **2010**, *132*, 1127-1136.

[11] C. Serre, C. Mellot-Draznieks, S. Surble, N. Audebrand, Y. Filinchuk, G. Ferèy, *Science* **2007**, *315*, 1828-1831.

[12] T. K. Trung, N. A. Ramsahye, P. Trens, N. Tanchoux, C. Serre, F. Fajula, G. Férey, *Microporous Mesoporous Mater.* **2010**, *134*, 134-140.

[13] C. Volkringer, T. Loiseau, N. Guillou, G. r. Férey, M. Haouas, F. Taulelle, N. Audebrand, I. Margiolaki, D. Popov, M. Burghammer, C. Riekel, *Cryst. Growth Des.* **2009**, *9*, 2927-2936.

[14] L. Dobrzańska, G. O. Lloyd, H. G. Raubenheimer, L. J. Barbour, *J. Am. Chem. Soc.* **2006**, *128*, 698-699.

[15] L. Dobrzańska, G. O. Lloyd, C. Esterhuysen, L. J. Barbour, *Angew. Chem. Int. Ed.* **2006**, *45*, 5856-5859.

[16] P. K. Thallapally, L. Dobrzańska, T. R. Gingrich, T. B. Wirsig, L. J. Barbour, J. L. Atwood, *Angew. Chem. Int. Ed.* **2006**, *45*, 6506-6509.

[17] T. Jacobs, J. Gertenbach, D. Das, L. J. Barbour, *Aust. J. Chem.* **2010**, *63*, 573-577.

[18] M. L. Connolly, *Science* **1983**, *221*, 709-713.

[19] M. L. Connolly, *J. Mol. Graphics* **1993**, *11*, 139-143.

[20] J. Dillen, Department of Chemistry and Polymer Science, Stellenbosch University

[21] G. O. Lloyd, *Crystal Engineering of Porosity (MSc Thesis), in Department of Chemistry & Polymer Science*, Stellenbosch University, **2006**.

[22] M. H. El-Naas, S. Al-Zuhair, M. A. Alhaija, *Chem. Eng. J.* **2010**, *162*, 997-1005.

[23] H. Li, M. Xu, Z. Shi, B. He, *J. Colloid Interface Sci.* **2004**, *271*, 47-54.

[24] PLATON, Utrecth University, Utrecht, The Netherlands, **2008**.

[25] C. G. Marais, MSc Thesis at the Department of Chemistry and Polymer Science, Stellenbosch University, **2008**.

[26] G. Venter, University of Cape Town, **2011**.

[27] L. Dobrzańska, G. O. Lloyd, H. G. Raubenheimer, L. J. Barbour, *J. Am. Chem. Soc.* **2005**, *128*, 698-699.

[28] J. W. Steed, J. L. Atwood, *Supramolecular Chemistry*, John Wiley & Sons Ltd, West Sussex, **2000**.

[29] E. J. Cussen, J. B. Claridge, M. J. Rosseinsky, C. J. Kepert, *J Am Chem Soc* **2002**, *124*, 9574-9581.

[30] T. Jacobs, M. W. Bredenkamp, P. H. Neethling, E. G. Rohwer, L. J. Barbour, *Chem. Commun.* **2010**, *46*, 8341-8343.

[31] T. J. Mooibroek, P. Gamez, J. Reedijk, *CrystEngComm* **2008**, *10*, 1501-1515.

[32] T. Jacobs, *Design and Construction of Novel Porous Materials (PhD Thesis), in Department of Chemistry & Polymer Science*, Stellenbosch University, **2007**.

[33] F. Rouquerol, J. Rouquerol, K. Sing, *Adsorption by Powders and Porous Solids* **1999**, *Academic Press, San Diego*.

[34] S. Sircar, A. L. Myers, J. A. Dunne, R. Mariwala, M. Rao, R. J. Gorte, *Langmuir* **1996**, *12*, 5888.

[35] P. W. Atkins, Oxford University Press, Oxford, **1999**.

[36] D. W. Breck, *Zeolites Molecular Sieves*, John Wiley & Sons, New York, **1974**.

[37] R. M. Barrer, *Zeolites and Clay Minerals as Sorbents and Molecular Sieves*, London: Academic Press Inc., **1978**.

[38] S. Bourrelly, B. a. Moulin, A. Rivera, G. Maurin, S. Devautour-Vinot, C. Serre, T. Devic, P. Horcajada, A. Vimont, G. Clet, M. Daturi, J.-C. Lavalley, S. Loera-Serna, R. Denoyel, P. L. Llewellyn, G. R. Férey, *J. Am. Chem. Soc.* **2010**, *132*, 9488-9498.

[39] P. K. Thallapally, G. O. Lloyd, J. L. Atwood, L. J. Barbour, *Angew. Chem. Int. Ed.* **2005**, *44*, 3848-3851.

[40] J.-Z. Gu, W.-G. Lu, L. Jiang, H.-C. Zhou, T.-B. Lu, *Inorg. Chem.* **2007**, *46*, 5835-5837.

[41] B. Chen, Y. Ji, M. Xue, F. R. Fronczek, E. J. Hurtado, J. U. Mondal, C. Liang, S. Dai, *Inorg. Chem.* **2008**, *47*, 5543-5545.

[42] J.-P. Zhang, X.-M. Chen, *J. Am. Chem. Soc.* **2008**, *130*, 6010-6017.

[43] L. Pan, B. Parker, X. Huang, D. H. Olson, Lee, J. Li, *J. Am. Chem. Soc.* **2006**, *128*, 4180-4181.

[44] R. Kitaura, K. Seki, G. Akiyama, S. Kitagawa, *Angew. Chem. Int. Ed.* **2003**, *42*, 428-431.

[45] T. K. Maji, G. Mostafa, R. Matsuda, S. Kitagawa, *J. Am. Chem. Soc.* **2005**, *127*, 17152-17153.

[46] N. Peybernes, C. Marchand, S. L. Calve, P. Mirabel, *Phys. Chem. Chem. Phys.* **2004**, *6*, 1277-1284.

[47] W. G. Shim, J. W. Lee, H. Moon, *Journal of Chemical & Engineering Data* **2003**, *48*, 286-290.

[48] B. Bilinski, *Journal of Colloid and Interface Science* **2000**, *225*, 105-111.

[49] M. Meilikhov, K. Yusenko, R. A. Fischer, *Dalton Trans.* **2010**, *39*, 10990-10999.

[50] D. Liu, J.-P. Lang, B. F. Abrahams, *J. Am. Chem. Soc.* **2011**, *doi./10.1021/ja203053y*.

[51] N. M. D. Brown, B. J. Meenan, G. M. Taggart, *Spectrochim. Acta, Part A* **1991**, *47*, 219-232.

[52] L. J. Barbour, K. Achleitner, J. R. Greene, *Thermochim. Acta* **1992**, *205*, 171-177.

[53] B. Toudic, P. Garcia, C. Odin, P. Rabiller, C. Ecolivet, E. Collet, P. Bourges, G. J. McIntyre, M. D. Hollingsworth, T. Breczewski, *Science* **2008**, *319*, 69-71.

Stellenbosch University http://scholar.sun.ac.za

Chapter 6
Summary and conclusion

As it is practiced today, supramolecular chemistry is an interdisciplinary field whereby individual molecules are combined to form new chemical species that have physical and chemical properties different from those of the initial "building units". Much of the current research in supramolecular chemistry is aimed at creating "crystals by design" using crystal engineering strategies. Although crystal engineering strategies are as yet not at a level where accurate structure prediction is possible, by controlling the non-covalent interactions, it has rapidly evolved to the rational design of materials with desired properties.[1] The work presented in this manuscript involves a range of research objectives in supramolecular chemistry that were uncovered and explained. Both organic and metal-organic hosts were strategically designed to form hosts with "awkwardly" shaped molecular conformations. The rationale behind the "smart" creation of such compounds is that the limited self-complementarity precludes close-packing of molecules in the solid-state, yielding functional porous materials. In particular, the importance and cooperative nature of both strong and weak intermolecular forces (which aid in conformational flexibility of seemingly rigid host-guest systems) are highlighted throughout *Chapters 3-5*.

Chapter 3 describes modification of a known oxacalix[4]arene compound **C1** by incorporating 2,3-naphthalene and 2,7-naphthalene moieties to yield two novel derivatives, namely 4,6,21,23-tetranitro-2,8,19,25-tetraoxacalix[2]arene[2]naphthalene (**C2**) and 4,6,18,20-tetranitro-2,8,16,22-tetraoxacalix[2]arene[2]naphthalene (**C3**). Alteration of the molecular structure of **C1** produced elongated arms in **C2** and a larger cavity in **C3**. In order to study the effect of these structural modifications on inclusion capability, compounds **C1-C3** were dissolved in a range of high-boiling solvents in an attempt to obtain crystals suitable for single-crystal X-ray diffraction. Compounds **C1-C3** have similar saddle-shaped conformations in the solid state. As was previously suggested for **C1** molecules in solution, the molecules in **C1a** assume saddle-shaped conformations and do not enclose solvent molecules in the solid state. Furthermore, two concomitant conformational polymorphs **C1a** and **C1c** crystallised from a DMSO solution. Polymorph **C1c** crystallises in $P2_1$ (compared to $P2_1/n$ in **C1a**) and the molecules assume distorted saddle-shaped conformations, resulting in a less dense packing arrangement than that observed for **C1a**.

Compound **C2** yielded solvate structures with DMF, DMAC, NMP and NBZ and crystallisation from DMSO produced an apohost phase. The conformation of the host

molecule is approximately C-shaped (closed) in the apohost structure **C2a** and V-shaped (open) in the solvate structures **C2·DMF** to **C2·NBZ**. The apohost phase does not have any space available to accommodate solvent molecules, but in the solvate structures the solvent molecules are located between the two naphthalene arms such that the host functions as a molecular tweezer and utilises low energy bond angle distortions to "open" or close" the naphthalene arms (pincers) in its empty or complexed forms. The increase in the distance and the dihedral angle between the naphthalene arms is the greatest in **C2·NBZ** (4.00 Å and 9.59(5)° in **C2a** compared to 6.95 Å and 30.73(1)° in **C2·NBZ**). Solvates **C2·DMF**, **C2·DMAC** and **C2·NMP** are isoskeletal with respect to the host packing and a host:guest ratio of 1:1 is inferred from the TGA thermograms in all cases. The apohost phase **C2a** is obtained by desolvation of the isoskeletal solvates. Unlike the isostructural solvates, **C2·NBZ** comprises two nitrobenzene guests per host and has a different host packing arrangement. One of the nitrobenzene molecules is located between the pincer arms, while the remaining guest molecule is situated interstitially. The TGA thermogram of **C2·NBZ** displays a one-step mass loss which corresponds to an endotherm on the DSC thermogram. Desolvation of **C2·NBZ** results in an as yet unknown apohost phase which transforms to **C2a** upon heating at 150 °C. The only significant host-guest interactions present in the solvate structures are weak C–H···O bifurcated hydrogen bonds. Although DMSO is capable of participating in a similar host-guest interaction, we suggest that the non-planarity of the solvent overrides this consideration and an apohost structure is obtained.

Single crystals of compound **C3** were obtained from DMF and structure solution of **C3a** revealed that no solvent molecules are present, and that the host adopts a more planar saddle-shaped conformation than was observed for the apohost in **C2a**. It was inferred from this study that elongating the arms of **C1** results in a molecular tweezer that can encapsulate planar guest molecules in the solid-state; increasing the cavity ring-size of **C1** precludes the inclusion of guests owing to the more planar saddle-shaped host conformation, which results in an interdigitated packing arrangement.

Chapter 4 describes the self-assembly of novel guest-included metallocycles by utilising imidazole-derived coordinating ligands (**L1**-**L7**) and transition metal salts. The rational design of these complexes is based on the strong coordination bond that forms between the N-donor atom and the metal ion, which should introduce some rigidity to the complex, thus allowing single-crystal to single-crystal desolvation of the encapsulated guest molecules to yield a porous material. The insolubility of the host material is also considered to

be an important factor for these processes to occur in a single-crystal to single-crystal fashion. Although the choices of donor-ligands and metal ions are essentially limitless, we have had much success in forming discrete 0D metallocycles rather than polymeric chains when using imidazole-based organic ligands and Cu^{2+}, Cd^{2+} and Co^{2+} ions. During this study, seven ligands **L1**-**L7** were synthesised and reacted with a variety of metal salts in various solvent systems.

Four novel metallocycles (**M1**-**M4**) were produced and characterised using SCD, thermal analyses and PXRD. The host packing arrangement results in discrete cavities in **M1·MeCN** and **M2·BZ** and continuous channels in crystals **M3·MeCN** and **M4·MeCN**. The solvents from which the metallocycle crystals were grown were included within the molecular apertures in all instances. Desorption of metallocycles **M2·BZ**, **M3·Mix**, **M3·MeCN** and **M4·MeCN** occurs at temperatures above 190 °C and coincides with the decomposition of the metallocycle. This is particularly surprising for **M3·MeCN** and **M4·MeCN** because no strong host-guest interactions appear to be present and we speculate that both host-guest and guest-guest contacts stabilise these inclusion compounds. Consequently, apohost phases for **M2·BZ** and **M3·MeCN** could not be characterised using SCD and no additional experiments were carried out using **M2·BZ**. Although guest release for **M1·MeCN** occurs at mild temperatures, single-crystallinity is not maintained as a result of a concomitant phase transformation. Exposing the desorbed phase of **M1** to acetonitrile vapour produces the initial **M1·MeCN** phase and the phase transformation is also apparent from the acetonitrile sorption isotherm.

Since it was not possible to obtain "empty" porous single-crystals of any of the metallocycles studied, the permeabilities of **M3·MeCN** and **M4·MeCN** were investigated by means of reversible guest-exchange. Owing to the small crystals produced for **M3·MeCN**, guest-exchange processes could not be monitored using SCD. However, solid-state UV-Vis revealed minor variation in the reflectance band maxima (and consequently vague colour changes) upon exchanging acetonitrile for other solvent vapours. TGA confirmed the host:guest ratios of the complexes formed.

In contrast to **M3·MeCN**, it was possible to study the permeability of **M4·MeCN** as a single-crystal to single-crystal process. Remarkably, an additional eight solvate structures (**M4·H2O**, **M4·Me_2CO**, **M4·MeOH**, **M4·DCM**, **M4·CHCl3**, **M4·CS2**, **M4·BZ** and **M4·Cy**) of **M4**, despite the difficulty desorbing the acetonitrile solvent using heat. In most instances several host-guest, as well as guest-guest interactions facilitate the uptake process, which is presumed to occur via an associative mechanism.[2-3] This involves the simultaneous release of acetonitrile at one end of the crystal and guest uptake at the other end. Although the host

packing arrangement remains unaltered in principle, significant variation in the solvent-accessible volume (*e.g.* V = 519 Å^3 per cell in **M4·MeCN** and V = 572 Å^3 per cell in **M4·MeBZ** using a probe r = 1.5 Å) and the naphthalene "tilt" angle (*e.g.* Φ = 36.2° in **M4·MeCN** and Φ = 42.7° in **M4·BZ**) occurs upon guest-exchange. Moreover, the shape of cyclohexane appears to be a highly suitable for the channels in **M4**, since it is the only guest that does not show any disorder or high thermal parameters, which may indicate that the other guest molecules can move around slightly within the channels.

The permeability of **M4** was tested by exposing a single crystal of **M4·MeCN** to small gaseous molecules (I_2, CO_2, C_2H_2 and vinyl chloride) with the aid of a miniature gas cell. Remarkably, it was possible to determine the binding sites of the gases in structures **M4·I2**, **M4·CO2**, **M4·C2H2** and **M4·VCl**. Electrostatic association with the metal centre are apparent for CO_2 and I_2. On the other hand, strong guest-guest interactions are present in all of the gas-included structures. The most prominent of these guest-guest interactions are the "T-shaped" C=O···C=O interactions in **M4·CO2**. It also appears that desorption of the gas molecules does not occur rapidly.

Although **M4·MeCN** is not porous in the conventional sense (the channels cannot be emptied and refilled with the same or different guests), it displays permeability by means of guest exchange rather than reversible sorption by empty pores. Since permeability goes hand-in-hand with porosity and **M4·MeCN** therefore possesses a form of porosity. Supporting studies provided by reliable computational and sorption techniques should provide valuable information regarding the effects of the interactions involved and the dynamics of the system.

Chapter 5 comprises an investigation of the physico-chemical aspects of sorption to ultimately achieve a better understanding of the mechanism of transport in a seemingly nonporous metallocycle. For this reason, the single-crystal to single-crystal permeability to a variety of gaseous guests, solvents and volatile *solids* was tested. Remarkably, even guests as large as naphthalene and *p*-dichlorobenzene are accommodated within the vacant space of metallocycle **M5**. This resulted in the characterisation of three novel gas-included structures (**M5·CO**, **M5·C_2H_2** and **M5·VCl**), nine new solvent-included structures (**M5·H2O**, **M5·MeOH**, **M5·MeCN**, **M5·Me_2CO**, **M5·DCM**, **M5·CHCl3**, **M5·CS_2**, **M5·BZ** and **M5·DBF**) and two *solid-included* structures (**M5·Naph** and **M5·DCB**). In principle, the host framework remains unaltered, but undergoes progressive adjustment of its structure to accommodate the uptake of the guests. The host displays remarkable shape-responsive fitting; the void volume in **M5a** (108 Å^3) decreased to 92 Å^3 in **M5·H2O** to better accommodate (*e.g.*

favourable host-guest interactions) the smaller water molecules. The average size and shape of the cavity adapts to accommodate the larger guests by increasing smoothly from 108 $Å^3$ for **M5a** to 147 $Å^3$ for **M5·MeOH** to 169 $Å^3$ for **M5·BZ**. Host-guest interactions also play a major role in guest uptake, the position of the guest within the discrete pocket, and the host:guest ratio. Removal of the guest molecules always results in desolvated complex **M5a** (*i.e.* a reversible process).

Interestingly, the uptake of chloroform or naphthalene occurs in conjunction with the formation of a larger cavity which is created by merging two adjacent discrete pockets. The mechanism of transport involves the 1D-diffusion of guest molecules from one discrete pocket to another by spontaneously creating a temporary channel between two neighbouring hosts within a stacked column. The working principle of the 1D-diffusion process is thought to involve the flexibility of the methylene-bond and the *Im*–metal bond. Thus, the *Im* rings act as gates to facilitate the permeability to the guests. The gates are therefore "open" when a guest is present between two successive metallocycles, and vibrates between the "open" and the "closed" states in the empty host structure **M5a**. Remarkably, inclusion of *p*-dichlorobenzene "opens" all the imidazole rings in the structure such that continuous *p*-dichlorobenzene-filled channels are produced.

As part of this study, controlled-pressure vapour-sorption isotherms of water, methanol, acetonitrile, acetone, dichloromethane, chloroform and benzene were measured at four different temperatures in order to confirm the host:guest ratios obtained from the single-crystal structures and also to calculate the thermodynamic parameters of sorption ΔH_{ad} and ΔS_{ad}. Host **M5** was found to have the highest affinity for **MeOH**, followed by **MeCN** > **Me2CO** > **CHCl3** > **BZ** > **DCM** > **H2O**. The relatively low volatilities of naphthalene and *p*-dichlorobenzene did not allow us to measure the sorption isotherms using the controlled pressure method; instead we were able to measure the uptake of naphthalene and *p*-dichlorobenzene as kinetic isotherms. Host:guest ratios of 2:1 and 1:1 were reached in **M5·Naph** and **M5·DCB**, respectively.

In conclusion, the findings herein bring us a few steps closer to understanding and constructively applying the processes that influence the cooperativity in flexible host:guest systems (*i.e.* adaptable binding-sites) and provide us with a foundation for further exploration aimed at producing crystals tailored for specific applications.

References

[1] D. V. Soldatov, I. S. Terekhova, *J. Struc. Chem.* **2005**, *46*, S1-S8.

[2] M. D. Pluth, K. N. Raymond, *Chem Soc Rev* **2007**, *36*, 161-171.

[3] K. D. M. Harris, *Supramol. Chem.* **2007**, *19*, 47-53.